INCISED VALLEYS IN THE FERRON SANDSTONE

STRATIGRAPHY, PROVENANCE, TIMING AND CONTROL OF INCISED VALLEYS IN THE FERRON SANDSTONE

By: DAVID KYNASTON, B.Sc.

A Thesis Submitted to the School of Graduate Studies in Partial Fulfillment of the Requirements for the Degree Doctor of Philosophy

McMaster University Doctor of Philosophy (2019)

Hamilton, Ontario, Canada (School of Geography and Earth Sciences)

TITLE: Stratigraphy, Provenance, Timing and Control of Incised Valleys in The Ferron Sandstone

AUTHOR: David Kynaston

Bachelor of Science (Honours), Earth and Environmental Sciences

McMaster University, 2014

SUPERVISOR: Dr. Janok P. Bhattacharya, Professor and Susan Cunningham Research Chair in Geology

NUMBER OF PAGES: 242

ABSTRACT

This thesis evaluates the nature, provenance, geometry and morphology of incised valley fills to test assumptions made by valley models using ancient examples from well exposed outcrops, in the late Turonian Ferron Sandstone Member of the Mancos Shale Formation in southeastern Utah. The relevance of this work will have particular significance to long wavelength cycles of fluvial landscapes and valley morphology, non-marine reservoir characterization and significant implications for non-marine response to high frequency allogenic cycles such as climate change and changes in relative sea-level.

This study illustrates the stratigraphic complexity of valley fill deposits at three levels of spatial resolution. At channel scale within the lower backwater, facies architecture and paleohydraulic analysis are used to predict the degree of shale drape coverage of point bars in a tidally-influenced incised channel. At channel belt scale the study documents a tidally incised, mudstone prone trunk-tributary valley fill and overlying highstand fluvial succession within a stratigraphic framework of fluvial aggragation cycles. 3D photogrammetry models and a high resolution GPS survey are used to restore the morphology of a trunk-tributary valley floor, revealing a surface of tidal ravinement and tidal drainage morphology. At a regional scale, this study radically revises the paleogeographic mapping of the Ferron trunk system, spanning over 1,600 km^2. Provenance analysis reveals Ferron Notom trunk valleys were filled at times by sediment from the Mogollon Highlands of Arizona to the southwest, and alternately by sediment from the Sevier Thrust Front to the northwest. Evidence shows the Ferron trunk rivers, previously hypothesized to be an avulsive axial drainage, to be more analogous to Quaternary examples.

ACKNOWLEDGEMENTS

I wish to express my sincere gratitude to my academic supervisor, Dr. Janok Bhattacharya for his continued support, patience and enthusiasm; not to mention encouraging this journey in the first place. I am also grateful for the invaluable guidance of my supervisory committee members, Dr. Carolyn Eyles and Dr. Eduard Reinhardt throughout my research.

The arduous task of conducting field geology in the Utah desert is not for those who possess a delicate and leisurely work ethic. It was my privilege to have been assisted by undergraduates Harrison Martin, Matthew Leung, Kristin Dosen, Mitchell Davidson and fellow graduate student Stephanie Kimmerle; all of whom made my summers in the field more productive and enjoyable than I could have ever imagined.

This research was funded with the generous support of the Susan Cunningham Research Chair at McMaster University, Quantitative Sedimentology Laboratories, with funding from NSERC, BP, INPEX, Ecopetrol, Nexen, Exxon Mobil, Anadarko, Bhpbilliton, Pioneer and Shell. Permission for this research was provided by the U.S. Bureau of Land Management with assistance from the Hanksville field office.

The development of ideas and discussions offered in this thesis was strengthened by the feedback and suggestions from poster presentations, talks given and field trips taken at several international and region conferences including AAPG Eastern Section, AAPG Annual Conventions and the International Sedimentological Congress.

Last, I wish to thank my wife and children. Few newlyweds would appreciate departing their honeymoon separately so your spouse could return to the desert for fieldwork. There was a time when I had spent as much of my daughter's lifetime in the field as home with her and my son has yet to know a father who is not buried in papers. My family's sacrifice of my time has driven this work. My wife's never-ending love and support has made it possible.

PREFACE

This Ph.D. dissertation is composed of five chapters. Chapters 2, 3, and 4 constitute the main body of the dissertation; each of these three chapters is written as a peer-reviewed journal paper. Chapter 2 documents the heterogeneity of fluvial deposits in a tidally-influenced channel, and predicts the degree of shale drape coverage within the fluvial to marine transition zone. Chapter 3 spatially restores the morphology of a mudstone prone, tidally-influenced tributary valley and presents evidence of autogenic versus allogenic controls of fluvial aggradation cycles based on chronostratigraphic timing and lateral extent. Chapter 4 presents radically revised paleogeographic mapping of the Ferron trunk system, using provenance analysis; and documents how terraces deposited by separate trunk channels may fill the same incised valley deposit.

Declaration of Academic Acheivement

Chapter 2:

Kynaston, David and Bhattacharya, Janok P. (2019) Mudstone Dimensions Within the Backwater Zone and Paleohydraulics in a Tidally Influenced Tributary Valley Fill, Cretaceous Ferron Sandstone, Utah: *AAPG Bulletin*, to be resubmitted.

David Kynaston (dissertation author) is the main researcher, first author and corresponding author of this paper. David Kynaston collected 95% of the field data and Dr. Janok P. Bhattacharya collected 5% of the field data and the outcrop photos. All calculations, plots, tables and figures were produced by David Kynaston as well as the writing of the manuscript. Dr. Bhattacharya edited the manuscript and provided thoughtful input regarding interpretation and discussion. Further input has been offered and incorporated from anonymous reviewers from AAPG Bulletin. This Manuscript is in preparation to be resubmitted.

Chapter 3:

Kynaston, David and Bhattacharya, Janok P. (2019) Facies Architecture and Time Stratigraphic Relationships of Confined Tributary Valley Fills and Unconfined Fluvial Systems within the Backwater, Ferron-Notom Delta, Utah : *Journal of Sedimentary Research* to be submitted.

David Kynaston (dissertation author) is the main researcher and first author of this paper. David Kynaston collected all field data and the photographs. Dr. Bhattacharya originally discovered the study area and hypothesized the tributary valley. All calculations, plots, tables and figures were produced by David Kynaston,as well as the writing the manuscript. Dr. Bhattacharya edited the manuscript and guided the discussion.

Chapter 4:

Kynaston, David; Matthews, William; Bhattacharya, Janok P.; Singer, Brad S.; Jicha, Brian R.; Ferron, Curtis and Howell, John (2019) Paleogeographic Reconstruction and Provenance Analysis of a Compound Incised Valley, Turonian Ferron Sandstone, Utah: *Journal of Sedimentary Research* to be submitted.

David Kynaston (dissertation author) is the main researcher, first author of this paper and collected all field data and photography. The sampling of all Ferron Notom outcrops was collected by David Kynaston. The two Ferron Sandstone samples from the Vernal delta were collected by John Howell. The concentration of heavy minerals to be processed for U-Pb zircon analysis for the Ferron Notom samples (N=13) were extracted by David Kynaston, while Curtis Ferron extracted the concentrations from the Vernal samples. David Kynaston performed all petrographic analysis in the study. U-Pb zircon geochronology and sample preparation was performed by William Matthews, who did 80% of the laser ablation sequence targeting, and also did 80% of the U-Pb data reduction. David Kynaston did the remaining 20% of ablation targeting and U-Pb data reduction. Curtis Ferron scripted the original python coding for the MDS relative probability and cumulative probability plots and assisted David Kynaston in producing those figures. David Kynaston produced all the remaining figures and coded the python script for the regional detrital analysis. Brian Jicha and Brad Singer processed and dated the bentonites from existing samples and one collected by David Kynaston. Dr. Bhattacharya edited the manuscript and guided the discussion.

TABLE OF CONTENTS

LIST OF FIGURES

LIST OF TABLES

CHAPTER 1

INTRODUCTION

1.1 Overview

Over 60% of the world's population lives within 100 km of the coastline at an elevation less than 10 m above sea level (Vitousek, 1997). The majority of the current human population therefore has a significant and inherent interest in the role that changing sea level plays in predicting the future of land and fresh water resources. With increasing global awareness of anthropogenic influence on climatic forcing, it is imperative to understand the stratigraphic rock record as it is the longest scientific account of life on earth (Burke, 1990). Rivers respond to changes in base level by incising or filling with sediment in order to achieve equilibration in their along-flow profile. Fluvial and estuarine deposits have excellent preservation potential and count for as much as 25% of all off-structure hydrocarbon reservoirs worldwide (Boyd et al., 2006). Due to the dynamic nature of the rivers that deposited them, the study of fluvial aquifers and hydrocarbon reservoirs are a challenging and complex field and often are oversimplified or overlooked due to this complexity. The greatest issue in understanding fluvial sandbodies is the internal organization and lithological variability caused by autogenic and allogenic processes, such as avulsion, migration and changes in base level

The purpose of this dissertation is to document and analyse outcrop exposures of ancient fluvial systems in order to identify autogenic and allogenic processes that control fluvial deposition. There are many previous examples of incised valley studies that look solely at the organization of trunk valleys (Shanley and McCabe, 1994; Zaitlin et al., 1994; Dalrymple et al., 2003b; Boyd et al., 2006; Strong and Paola, 2008), but do not represent tributary valleys within that system. This work looks to provide context for tributary valleys within a well-documented compound incised valley system (Li et al., 2010; Zhu et al., 2012; Li and Bhattacharya, 2013; Ullah et al., 2015; Kimmerle and Bhattacharya, 2018).

The scope of the research will center on incised valley deposits of the Turonian Ferron Sandstone Member of the Mancos Shale Formation in Southern Utah. By examining these deposits at various scales of resolution, we show multiple levels of complexity that have been oversimplified or overlooks by current incised valley models. The focus of investigation looks at the stratigraphic organization of confined and unconfined fluvial channel sandstones, and channelized to overbank mudstones within or near the backwater limit of a coastal plain incised valley system. Key concepts of this research include the effects of backwater within lowstand fluvial systems, fluvial depositional cycles, and incised valley morphology.

The backwater is the effect of a standing body of water on river that feeds it at the point that the base of the river channel is at or below the elevation of the standing body's surface due to the incompressibility of water. The length to which that effect is propagated upstream is known as the backwater length (L_b) (Fig. 1.1), and is defined as the height of the fluvial channel (h_f) divided by the channel gradient or slope (S).

Backwater effects may include a distinctly tidal signal, and may allow for brackish water to be present.

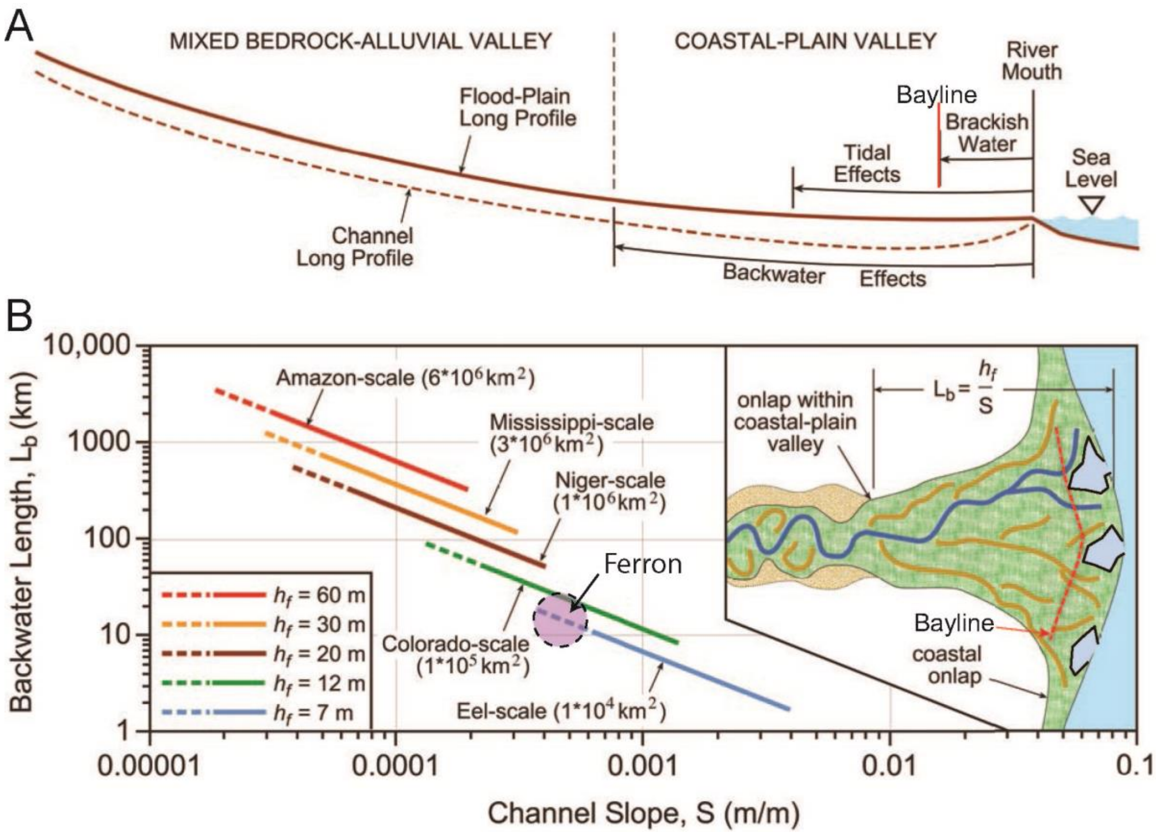

Figure 1.1: Backwater concept. A) Profile view of backwater effects relative to channel axis (*modified from* : Li, 2006; Blum et al., 2013). B) Plan view of the backwater length versus channel slope for modern rivers. The interpreted position of the Ferron system is plotted.

The backwater length (L_b) marks a distinct reduction in stream velocity. Consequently the upper backwater is typically a location of large-scale sand deposition in laterally accreting point bar deposits that may show mudstone draping (Durkin et al., 2015; Horner et al., 2019a). At half the backwater length, channels decrease the degree of lateral point bar migration, there is increased erosion of the trunk channel in response to flood stage drawdown and an increase in mud sequestration due to tidal modulation of fluvial currents (Chatanantavet et al., 2012; Colombera et al., 2016). Current reversals (Visser, 1980) and marine sediments are found in the most distal reaches, depending on the current velocity and tidal range.

We address specific scientific problems of understanding thin bedded fluvial deposits in their sequence stratigraphic context, the nature of mudstone deposits within fluvial cycles, and valley evolution as it relates to specific drainage sources. Fluvial cycles are typically distinguished as either autogenic, such as channel avulsion, or allogenic, such as aggradational channel patterns and valley incision. Floodplain deposition and paleosol development are the basis of a far more complex stratigraphic framework than channel stacking patterns, but reveals insights into non-marine deposition with or without preserved channel sandstones.

Valley morphology and plan view reconstruction is particularly important to constraining the dimensions and connectivity of fluvial reservoirs. With recent improvements in geochronology (Jicha et al., 2016; Matthews and Guest, 2017), provenance analysis of detrital zircons and absolute age dating of sanidine crystals from bentonite deposits allow the sequential timing, source and lateral extent of regional scale drainage networks to be mapped, revealing the evolution of ancient incised systems.

1.2 Dissertation Contents

This thesis is organized into five chapters. The main body of the thesis is composed of Chapters 2, 3 and 4, which consist of peer-reviewed journal articles prepared for publication. Chapter 2, submitted to AAPG Bulletin, has been reviewed and encouraged to resubmit.

Many of the reviewers concerns have been addressed in this new version. Chapters 3 and 4 contain a degree of overlap concerning the chronostratigraphic data provided by the bentonite beds. This was necessary to explain the timing of stratigraphic sequences at both individual tributary valley scale as well as regional compound valley scale. Modifications may be made once one or the other is published first.

Chapter 2 examines the heterogeneity of fluvial deposits within the fluvial to marine transition zone (FMTZ) and documents a tidally influenced fluvial channel in a late stage valley fill. Closely spaced measured sections show stacked fining upward channels filling a valley incised into older marine sediments. Paleohydraulic analysis and bedding geometries are used to restore the paleogeography of a meandering, low to moderately sinuous paleochannel. The workflow is designed to predict the degree of shale drape coverage of point bars within specific fluvial reaches of the backwater and proposes an improved model of mudstone dimensions applied to tributary fluvial systems within the FMTZ.

Chapter 3 documents a tidally incised, mudstone prone trunk-tributary valley fill and overlying highstand fluvial succession within a stratigraphic framework of FACs. 3D photogrammetry models and a high resolution GPS survey, are used to restore the morphology of a trunk-tributary valley floor, revealing a surface of tidal ravinement and tidal drainage morphology similar to that found in Pleistocene sediments and modern analogues. Age dating of bentonite beds confirms previous assumptions of Milankovitch scale sequence duration (15 ± 5 ka) of the youngest sequence in the Ferron-Notom, and supports evidence that FACs are a result of autogenic processes, while FAC-sets may be allogenic in nature due to their sub-avulsion frequency and lateral extent (>10 km).

Chapter 4 presents a robust detrital zircon (DZ) dataset collected from the Ferron Sandstone with a total zircon sample size of 2953 concordant dates. These samples were taken from valley terraces of the youngest compound valley in the Ferron Notom delta confining a stratigraphic valley area of ~100 km^2. Ferron Notom valleys were found to have been filled at times by sediment from the Mogollon Highlands of Arizona to the southwest, and alternately by sediment from the Sevier Thrust Front to the northwest. This study radically revises the paleogeographic mapping of the Ferron trunk system, from the avulsive axial drainage that was previously hypothesized, to a drainage pattern more analogous to Quaternary examples.

Chapter 5 offers a summary of conclusions drawn from Chapters 2, 3, and 4, and suggests future work that is related to the studies described above.

Chapter 2

MUDSTONE DIMENSIONS WITHIN THE BACKWATER ZONE AND PALEOHYDRAULICS IN A TIDALLY INFLUENCED TRIBUTARY VALLEY FILL, CRETACEOUS FERRON SANDSTONE, UTAH

Abstract

This study addresses the heterogeneity of fluvial deposits within the fluvial to marine transition zone and documents a tidally-influenced fluvial channel in a late stage valley fill of the Turonian Ferron Sandstone Member in central Utah. Six measured sections show stacked fining-upward channels filling a valley incised into older marine sediments. The lower valley shows tidally influenced deposits, while channel reconstruction shows high sinuosity meandering channel deposits in the upper part of the valley and five storey successions of 5th order bounding surfaces separating point bar deposits within the valley fill. This 27.9 ± 2.9 m wide channel confined within the valley has a bankfull flow depth of 2.5 ± 1.0 m, with a paleodischarge between 20 ± 2 and 37 ± 8 m^3/s. Systematic paleohydraulic analysis and bedding geometries allowed for a plan-view reconstruction of a meandering, low to moderately sinuous paleochannel. A tributary valley fill within the backwater is compared to trunk valley fills and upper distributary channel fills to show that the former has a higher ratio of point bar deposits that are draped by mudstones; and that the tributary mudstone drapes tend to cover a greater surface area of each individual point bar deposit.

An improved model of mudstone dimensions applied to tributary fluvial systems within the backwater limit incorporates both inter-formational and intra-formational mudstones that affect the nature of channel fill and the flow characteristics of potential hydrocarbon reservoirs. These tidally influenced channel deposits represent outcrop analogs useful in the reservoir characterization of heterogeneous tide influenced reservoirs such as the McMurray Formation in Alberta, that host vast bitumen resources in the Athabasca Oil Sands.

2.1 Introduction

The facies architecture of inclined heterolithic stratification (IHS) is a key heterogeneity that affects fluid flow and recovery in point bar reservoirs, such as the supergiant oil sand reserves within the McMurray Formation in Alberta (Mossop and Flach, 1983), or the Kern River Formation in the San Joaquin Valley, California (Coburn et al., 2002). Heterogeneity of fluvial reservoirs within the fluvial to marine transition zone (FMTZ) is important in understanding these reservoirs. Such deposits have been the focus of interest for oil and gas extraction because of their low permeability and the complexity of their structure (Thomas et al., 1987). The outcrop in this study is a tidally-influenced channel within the Notom Delta complex of the Ferron Sandstone Member, which forms part of the Upper Cretaceous Mancos Shale Formation in central Utah, and represents an analogue for reservoirs with recognizable tidal signatures.

Mudstones within fluvial deposits may have considerable impact on reservoir quality and their architecture can only be predicted accurately if they are recognized in core or well logs, as they are often below seismic resolution. The conceptual model of Lynds and Hajek (2006) for braided fluvial reservoirs can be used to predict mudstone dimensions, including maximum thickness, maximum width and maximum length; but has not been applied to model mud sequestration in reservoirs deposited by single thread meandering channels (Miall, 1977), especially within the tidal backwater limit. The backwater limit is defined as the horizontal distance of a stream that experiences an adjustment in flow due to the downstream interaction with a standing body of water, calculated by the channel depth divided by the slope (Paola and Mohrig, 1996). The tidal backwater limit is represented by the tidal range over the slope of the coastal plain and is the distance over which a tidal signal effects distributary channels and linked upstream reaches and may coincide with the landward limit of marine water, referred to as the bayline. Knowledge of the backwater allows the possibility of predicting facies variability. Backwater effects include decreased lateral migration of point bars, increased erosion of the trunk channel in the lower backwater in response to flood stage drawdown, an increase in mud sequestration and an increase in lateral continuity of shale drapes (Chatanantavet et al., 2012; Blum et al., 2013; Colombera et al., 2016; Fernandes et al., 2016). As a result of the tidal backwater, deposits may be dominated by inclined heterolithic strata (), defined by Thomas, et al. (1987) as, “parallel to sub-parallel strata occurring within lithologically homogeneous and heterogeneous units of waterlain siliciclastic sedimentary sequences”, to describe laterally accreting beds of alternating sands and shales. The waxing and waning of tidal forces can create rhythmic variations in flow discharge and flow velocity, and so it follows that channels with lower flow discharges may be more sensitive to tidal effects than channels with higher discharges (Dalrymple, 2010a).

Previous studies in the distributary channel deposits of the Last Chance Delta of the Ferron Sandstone Member (Novakovic et al., 2002; Corbeanu et al., 2004) observed fluvial point bar deposits in an upper delta plain in 3D, using ground penetrating radar, outcrop and core data, and described laterally stacked, inclined bedsets with laterally extensive mud drapes on the bedset surfaces. This heterogeneity and complex internal IHS architecture is contrary to the simple upward fining trend of sandstone channel storey models (Cant and Walker, 1976; Miall, 1977), in which the deposits of a single channel fill define a single channel depth wherein mudstones are sequestered in bar top, channel abandonment and floodplain facies. This complex geometry was interpreted to be a function of tidal influence (Thomas et al., 1987; Corbeanu et al., 2004) and complicates the connectivity and continuity of fluvial sandstone bodies in reservoirs (Larue and Hovadik, 2006). The connectivity of fluvial deposits can greatly influence recovery factors, and is a function of both the ratio of net sandstone to gross rock volume (Larue and Hovadik, 2006), and migration of the river by translation and/or expansion through time (Willis and Tang, 2010). Similar studies of the Ferron Sandstone looked at bar scale architecture and mapped the draping of mudstones on 3rd order surfaces in 2D outcrop exposures (Campbell, 2013; Kimmerle and Bhattacharya, 2017). Such high resolution architectural analysis allows the estimation of bar surface area relative to mudstones that directly overlie it. Mudstone and bar length outcrop measurements, within tidally influenced valley fill deposits, were converted to length and width values with respect to the paleo-current direction (Biber et al., 2017). This allows the estimation of bar surface area and percentage coverage.

This paper addresses the following aspects of tidally-influenced fluvial deposits:

1. The facies, architecture, grain size distributions and paleohydraulic estimation of a tidally-influenced tributary channel.
2. The dimensions of mudstones, ratio of bar surfaces covered and percent of bar coverage by mudstones in a tidally-influenced tributary.
3. The comparison of tidally-influenced tributary bar drapes with their associated trunk channels, and unconfined distributary channels.
4. An improved model of mudstone deposition in a tidally-influenced tributary channel within the lower backwater.

The study outcrop is stratigraphically located within the youngest sequence of the Ferron Sandstone, and is in the uppermost fill of an incised valley deposit (Li et al., 2010). The depth of channel incision of this tributary is greater than double the maximum flow depth observed in a single channel storey in outcrop, and therefore fulfills the criteria required to be considered an incised valley (Zaitlin et al., 1994). This incised valley shows paleocurrents that run at a high angle to regional paleocurrents within a well-documented, much larger trunk valley in the Ferron (Li et al., 2010; Li et al., 2011a; Li and Bhattacharya, 2013; Li and Bhattacharya, 2014; Ullah et al., 2015; Kimmerle and Bhattacharya, 2018).

Previous work on tributary valleys discuss how associated trunk channels may cause damming of tributary channel mouths, causing tributary valleys to be much more mudstone rich than their trunk valley (Kvale and Archer, 2007). This paper examines the geometries of a minor incised tributary valley, composed of multiple stacked channel deposits, within a compound valley in the Ferron Sandstone Notom Delta and discusses the nature and extent of IHS within a tidally influenced channel. Paleohydraulics of the formative channels were calculated to estimate paleodischarge and the facies architecture was used to reconstruct fluvial style and migration patterns.

2.2 Geological Setting, Recent Work, and Study Area

The peak of thrust faulting during the Sevier Orogeny in Utah was in the Late Cretaceous, having created a fully mature foredeep basin in response to thin skinned crustal shortening (Decelles et al., 1995; Willis, 1999; DeCelles and Coogan, 2006). The Mancos Shale was deposited in the Western Interior Basin as it filled due to high rates of synorogenic sedimentation, subsidence and eustatic sea level rise (Fig. 2.1A). Three clastic deltaic wedges comprise the Turonian Ferron Sandstone Member of the Mancos Shale; the Last Chance, Vernal, and Notom Deltas (Uresk, 1978; Hill, 1982; Bhattacharya and Tye, 2004; Corbeanu et al., 2004; Fielding, 2011) (Fig. 2.1B).

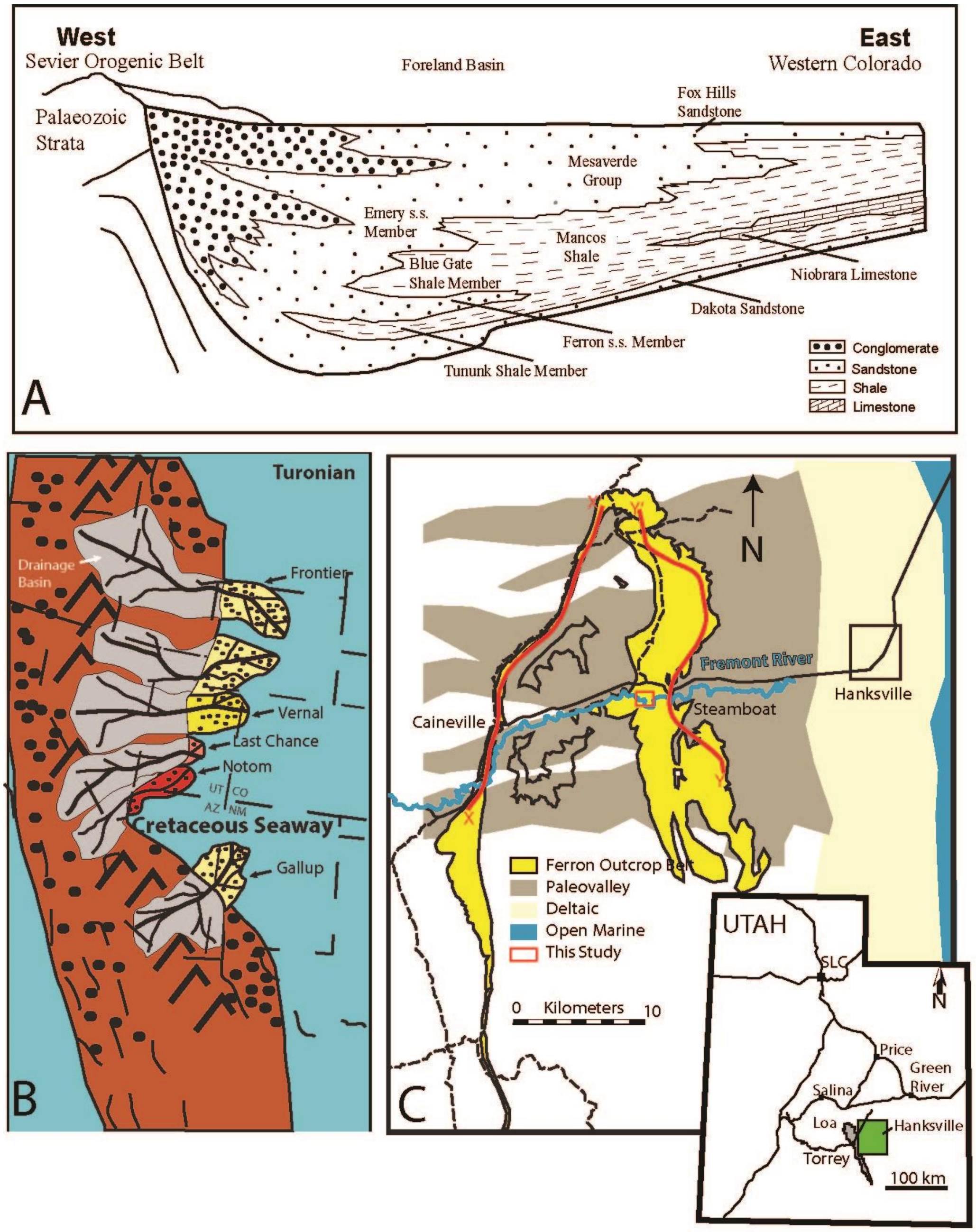

Figure 2.1: A) Regional stratigraphic cross section of the Mancos Shale showing the relative location of the Ferron Sandstone Member, the overlying Bluegate Shale Member, and the underlying Tununk Shale (Modified from: Armstrong, 1968). B) The Western Interior Seaway and location of the Notom Delta relative to present day state boundaries

(modified from: Bhattacharya and Tye, 2004; *Based on:* Gardiner, 1995). C) The study area within Utah (Kimmerle et al., 2018). Cross section locations (Fig. 2.4 and 2.5) are indicated by red lines. The red box indicates the study area satellite photo location (Fig. 2.3).

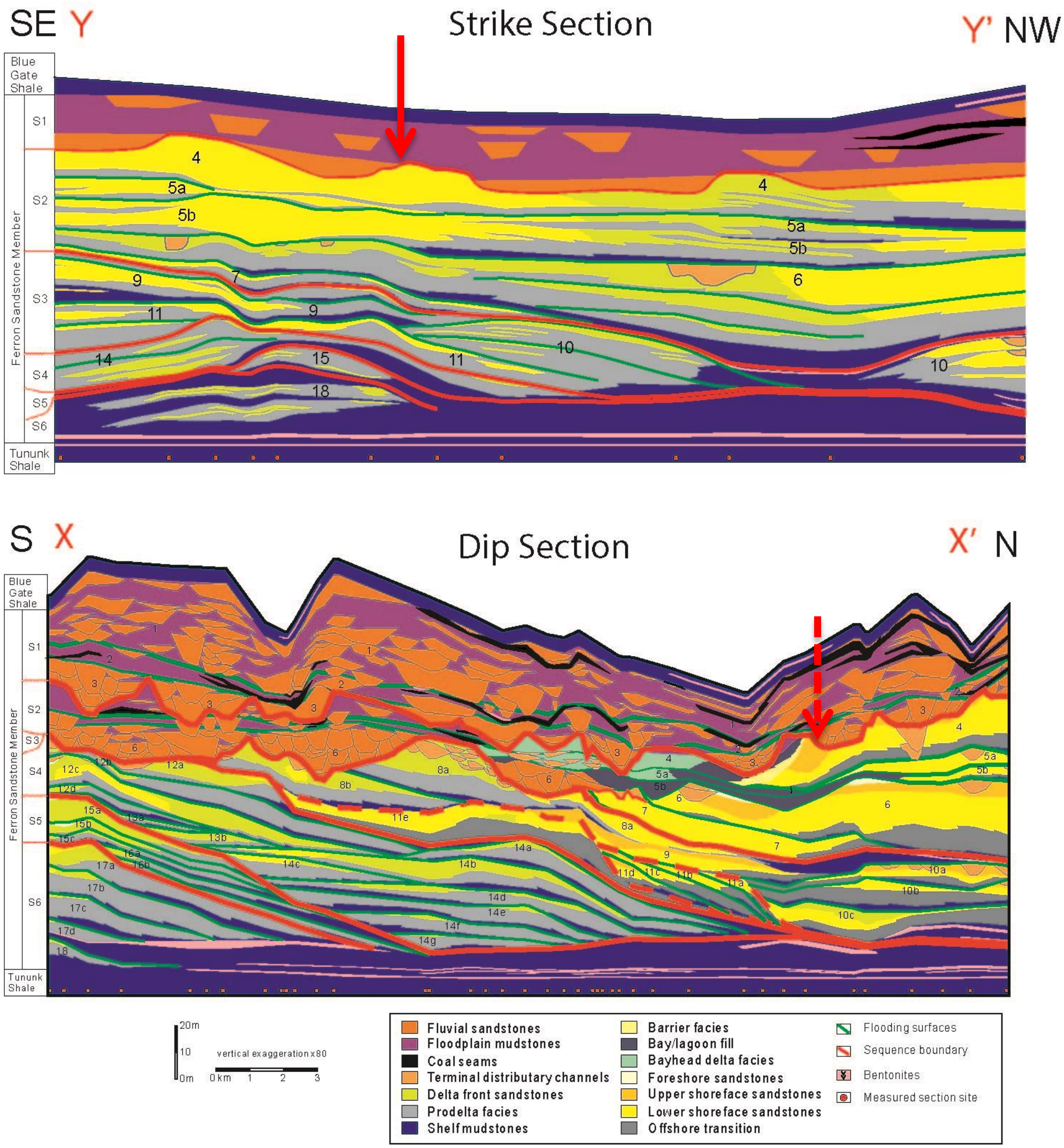

Figure 2.2: Upper) Strike cross section Y-Y' in figure 2.3, showing the study interval. Approximate location of study outcrop is indicated by the red arrow. Focus is on fluvial strata in sequence 1 (modified from: Zhu et al, 2012). Lower) Dip oriented cross section X- X' in figure 2.3, showing the projected study interval (*modified from*: Zhu et al, 2012 and Richards, 2018).

The Ferron-Notom Delta overlies the Tununk Shale Member of the Mancos Shale and shows a gradational contact. Above the Notom Delta is a sharp contact with the overlying Bluegate Shale Member. The Notom Delta is composed of 6 sequences, which are further divided into 18 parasequence sets and 42 parasequences (Li et al., 2011a; Zhu et al., 2012) (Fig. 2.2). The lower four sequences are composed of shoreface and heterolithic deltaic facies, while the upper two sequences show incision of lowstand compound incised valleys truncating underlying deltaic and shoreface deposits (Li et al., 2010; Li and Bhattacharya, 2013; Famubode and Bhattacharya, 2016). The youngest incised valley is filled with terrace deposits forming three distinct stages; from youngest to oldest, so named V1, V2, and V3 (Li and Bhattacharya, 2013).

Recent studies (Li et al., 2010; Fielding, 2011; Zhu et al., 2012), have mapped the extent of the Ferron Notom Delta outcrop (Fig. 2.1C); across regional strike and dip cross-sections (Fig. 2.2), indicating several sequence boundaries. The deposit is stratigraphically located within the youngest sequence of the Ferron sandstone (Li et al., 2010) and is in the uppermost fill of a valley deposit that incises Parasequence 4 of Sequence 2.

The study area lies directly south of Factory Butte near Hanksville, Utah; and north of the Freemont River. The valley deposit is well exposed and shows multiple stacked channel deposits. Paleocurrent directions suggest it is a tributary to the main trunk valley system (Fig. 2.3) mapped in previous studies (Kimmerle and Bhattacharya, 2018).

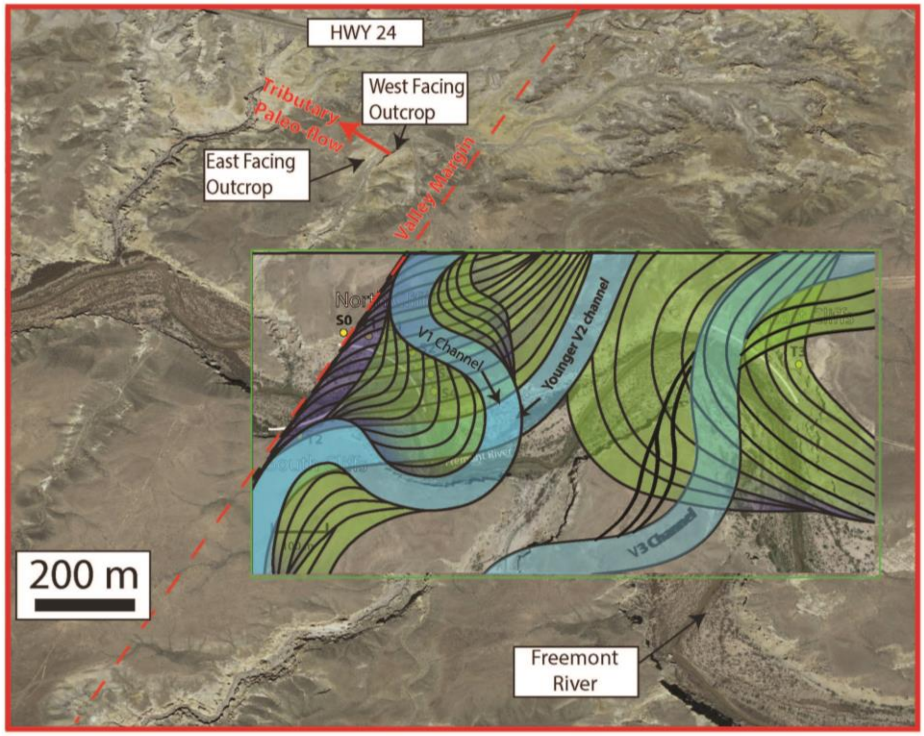

Figure 2.3 Satellite imagery of study area (Fig. 2.1) and paleogeographic map from Kimmerle and Bhattacharya (2018) (green box) shows relative position of the interpreted trunk valley margin and trunk channels to the tributary outcrop and predominant paleocurrent direction from this study (red arrow).

2.3 Methods

Measured sections and facies descriptions include the identification of trace fossils, grain size estimates, sedimentary structures, bioturbation index (BI) and paleocurrent directions. These were made in the field using a Jacob's Staff with an Abney level, hand lens and grainsize card. Estimates of mudstone clay content were made by relative comparison of colour, texture and swelling in the field. Net to gross sandstone ratios (NTG) were calculated by multiplying these estimates by their relative thicknesses within measured sections for individual facies and reported as a range to capture facies variability and estimation error.

An SX Blue differential GPS system was used for location accuracy and image control points. Outcrop images were produced by stitching digital camera imagery in photo mosaic software, and by acquiring vertical drone imagery used to create a point cloud and triangular mesh using Pix4D photogrammetry software (Nieminski and Graham, 2017). This was then used to extract an orthophoto parallel to the outcrop (Fig. 2.4A and 2.4B). These outcrop exposures are separated by a distance of approximately 20 m. These photos were used to identify and correlate bedding and facies architecture diagrams (Fig. 2.5) with the measured sections superimposed. Topographic reconstruction of the channel over time was estimated using bedding geometries and measured paleocurrents.

3rd, 4th and 5th order surfaces (Miall, 1994) were correlated (Fig. 2.6A). Smaller scale, <3rd order surfaces that define cross-set boundaries were not correlated. The surfaces are ranked between elements 1 through 7 (Fig. 2.6). 1st order surfaces show the continuous sedimentation of individual lamina within a crossbed set. 2nd order bounding surfaces indicate boundaries of individual beds that are groups of micro to mesoforms that show a change in flow conditions such as the surface that marks the change from dunes to ripples. Neither 1st, nor 2nd order surfaces show significant internal erosion (Fig. 2.6B). For the purpose of simplicity, these lower order surfaces are not shown but were identified in measured sections. Individual beds were walked out in the field and sampled between correlated measured sections to document the lateral variability (or uniformity) of grain size. 3rd order bounding surface cross cut 2nd order surfaces within macroforms. These 3rd order surfaces bound lateral accretion deposits and downstream accretion deposits and define bed sets. The orientation and variability of accretion direction with respect to overall paleotransport is used to distinguish point bars from braid bars and is used in this study to determine whether this system is a meandering or braided channel. 4th order surfaces tend to be the surface of macroforms or the basal scour surface within bars, and represent changes in flow direction or bar migration style. Both 3rd and 4th order surfaces are characterized by very low depositional dip. 5th order surfaces separate major sandstone sheets and channel storeys, whereas 6th order surfaces separate paleovalleys containing at least two channel storeys. 5th and 6th order surfaces are the most laterally extensive. A 7th order surface is identified as a surface that is higher in order than a 6th order surface and is interpreted to represent a compound valley margin (Fig. 2.6C).

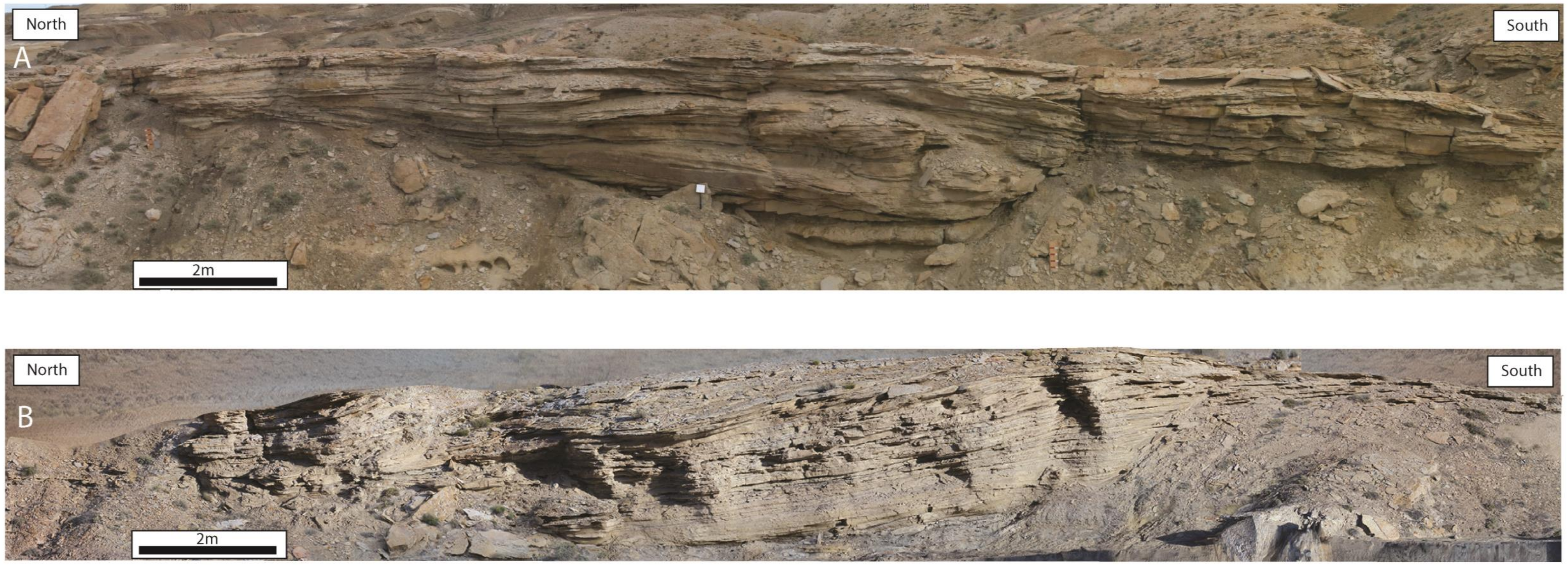

Figure 2.4: A) Photomosaic of west facing outcrop. Talus covers mudstone and marine units while vertically oriented exposures are fluvial channel deposits. B) Orthopane image of east facing outcrop extracted from a 3D model generated from UAV imagery of east using Pix4D software.

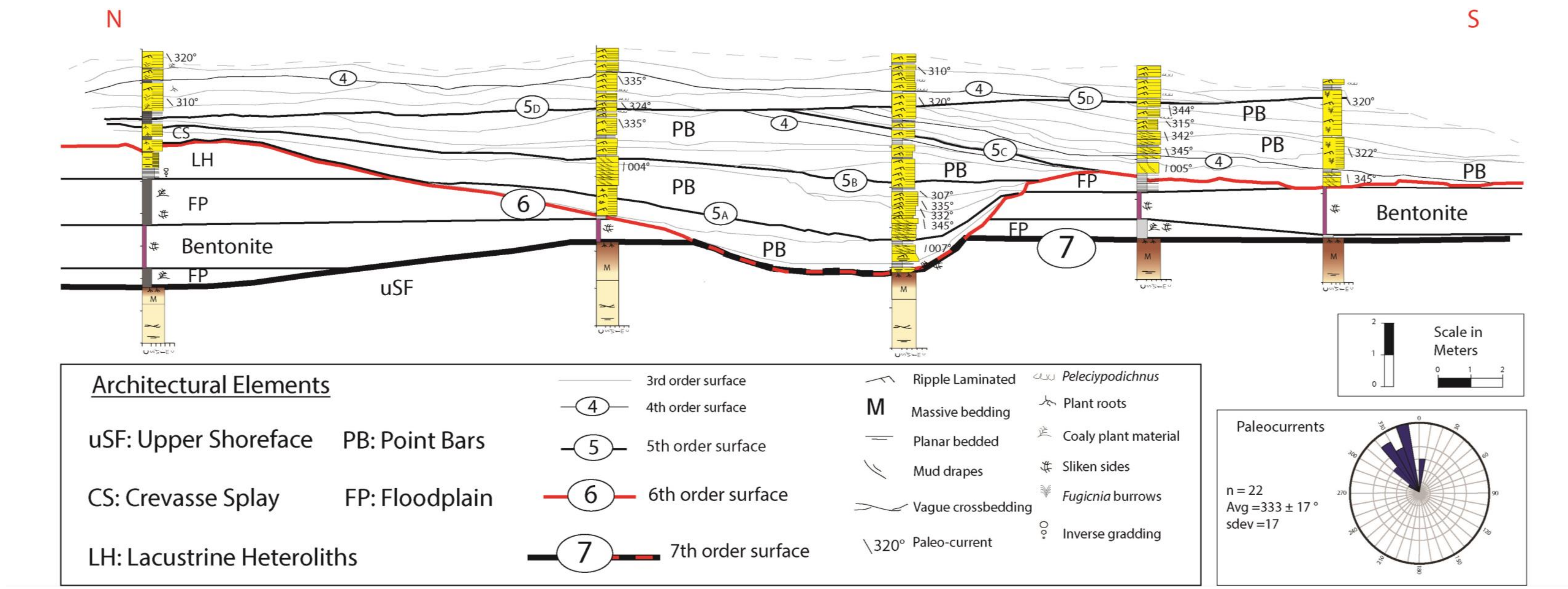

Figure 2.5: Bedding diagram of the west facing outcrop (Fig. 2.4) showing 6th order bounding surface (red) of the channel incision and 7th order composite surface (red and black dashed) shows the valley incision separating associated flood plain deposits and the underlying marine deposits. Four 5th order surfaces indicate individual fining upward channel storeys. 3rd and 4th order surfaces delineate the tops of point bars. Rose diagram indicates paleocurrent direction of fluvial deposits above the 6th order bounding surface.

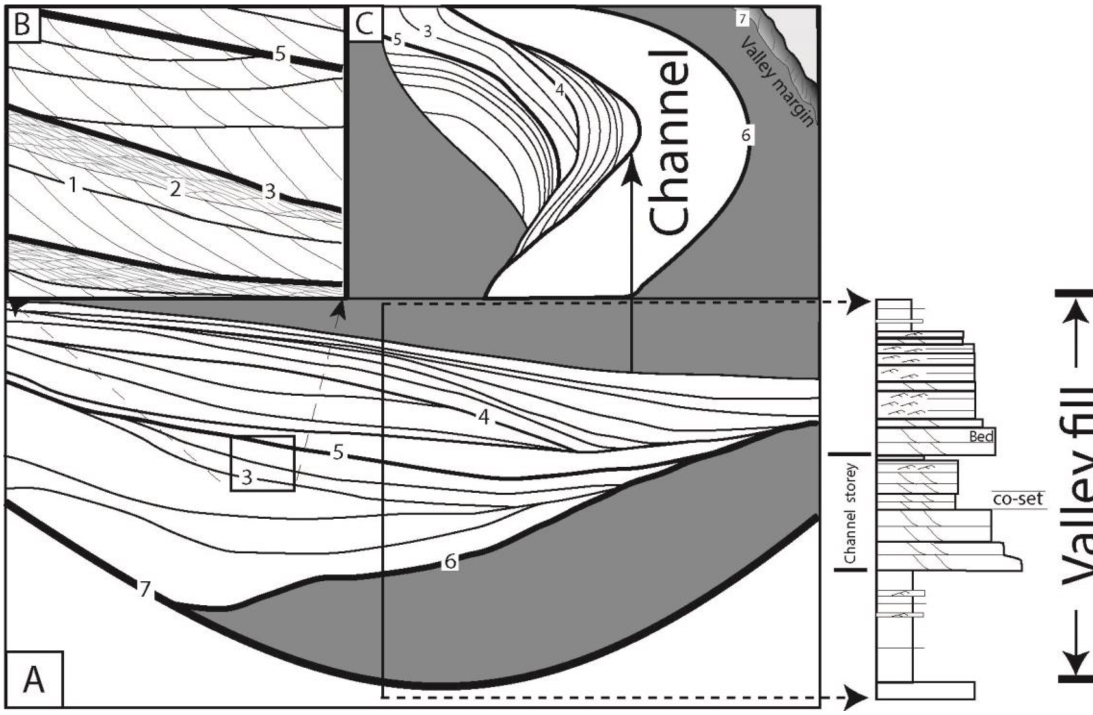

Figure 2.6: Surface hierarchy for this study based on Miall (1985).

Mudstone dimensions were collected from those that directly overlie barforms, defined as the total length in outcrop that covers a 3rd or 4th order surface. The 3rd or 4th order surface length across the outcrop face is multiplied by the cosine of the angle between the outcrop face and the mean paleocurrent direction to determine bar width. The bar length is defined as the 3rd or 4th order surface length across the outcrop multiplied by twice the sine of the angle between the outcrop face and the mean paleocurrent direction (Figs. 2.7A and 2.7B).

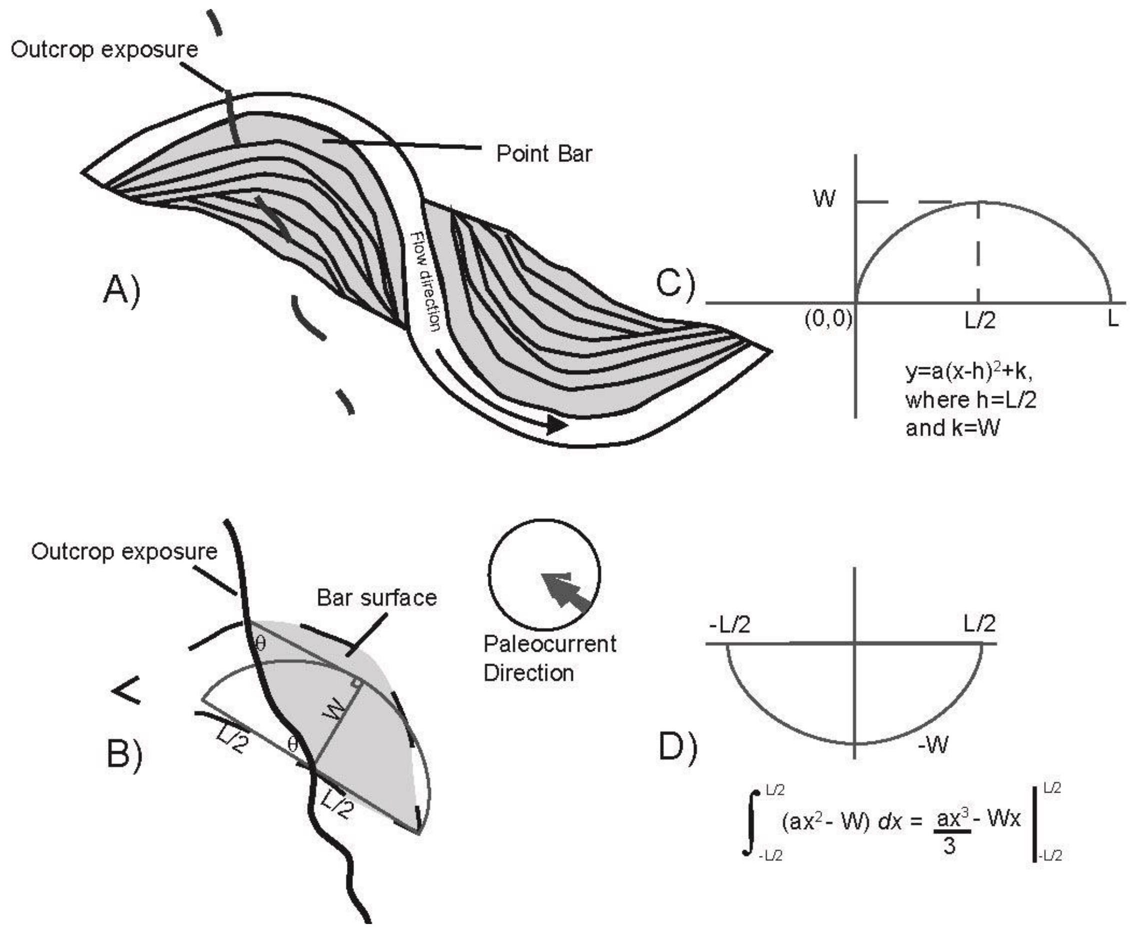

Figure 2.7: The method used in this study to determine point bar and mudstone dimensions from outcop. A) Conceptual orientation of point bar deposits relative to the outcrop exposure. B) Length (L) and width (W) dimensions estimated using the sine of the angular difference in outcrop orientation and palecurrent direction (Ө). C) Determining the leading coefficient (a) for the approximate parabolic shape of a point bar. D) Integrating the parabolic equation to estimate the plan view bar area. The equation was first translated and reflected to simplify the mathematical equation.

2.4 Facies Descriptions and Interpretations

Within the six measured sections, eight facies were distinguished based on lithology, trace fossils, and sedimentary structures (Figs. 2.8 and 2.9). Detailed descriptions of Ferron Sandstone fluvial facies have been extensively documented (Fielding, 2010; Li et al., 2010; Li et al., 2011b; Zhu et al., 2012; Li and Bhattacharya, 2013; Li and Bhattacharya, 2014; Wu and Bhattacharya, 2015; Famubode and Bhattacharya, 2016), a brief description of these facies and their interpretation is presented. A framework of generic facies was used because of the relatively small scale of our study. Many of the facies are not repeated and therefore the facies description is presented with its stratigraphic context.

2.4.1 Facies 1: Planar to Cross-bedded Sandstones

Description: Facies 1 is a light grey to buff coloured fine-upper sandstone. The deposit shows planar laminations at the base of the unit, passing into vague cross-stratification. The contact with the overlying unit is sharp and well defined. Walking the upper surface out 40 m to the west of the study area shows well exposed swaley cross-stratification and abundant marine bioturbation including *Chondrites* and *Ophiomorpha*. These and other unidentified burrows contain minor amounts of mud, thus the NTG of this facies is greater than 0.9.

Interpretation**:** The lack of well-defined structures is interpreted to be due to pervasive bioturbation, suggestive of a marine environment. Swaley cross-bedded fine-upper sandstone combined with the observed marine trace fossils suggests a lower shoreface (Clifton, 2006).

2.4.2 Facies 2: Massive/Bioturbated Sandstones

Description**:** Facies 2 is buff coloured, fine upper sandstone that lacks any visible stratification, and appears structureless (Fig. 2.8A). This facies only occurs above Facies 1 and is 1 to 2 meters thick with abundant root casts on the order of centimeters to 10's of centimeters in length, and shows evidence of oxidation within and around them. There is a sharp erosional contact with the overlying mudstones and sandstones. The NTG is similar to that of Facies 1, greater than 0.9.

Interpretation: The structureless bedding is interpreted as extensive bioturbation in a shoreface deposit (Vakarelov et al., 2012). The abundant root casts are post depositional and are associated with a change in relative sea level. This surface was a semi-consolidated, subaerially exposed sandy paleosol, indicated by the plant root system and high degree of oxidation. This unit was locally described by Li *et al*. (2010) as belonging to Parasequence 4. This surface represents a local interflueve associated with the regional sequence boundary at the base of Sequence 1.

2.4.3 Facies 3: Organic-rich Mudstone

Description: Facies 3 is composed of friable, organic-rich shale with a clay content ranging from 20% to 50%. The colour of this facies ranges from black to reddish brown to dark brownish red (Fig. 2.8B). The base of this mudstone interval shows well-formed, clearly identifiable slickensides and ranges in thickness from 0 to 1.45 m. This facies is absent in several of the measured sections, having been eroded by the overlying channel. Facies 3 directly overlies SB1 (Fig. 2.2) and locally onlaps the valley margin

(Fig. 2.5). NTG values range from 0.1 to 0.3, the values decreasing with increased distance from sandy channel deposits.

Interpretation: The presence of slickensides is evidence of subaerial exposure, and overlies the rooted upper surface of Facies 2. The abundance of organic material laterally adjacent to a channel is interpreted as a flood plain paleosol within the valley (Famubode and Bhattacharya, 2016).

2.4.4 Facies 4: Bentonite

Description: Facies 4 is composed of bentonite. It forms a clay-rich (>50%), unconsolidated layer with an NTG value less than 0.1. Slickensides are identifiable throughout the entire unit (Fig. 2.8C). It is green to brown in colour, and swelling occurs readily with hydration. The bentonite also lies above SB1 (Fig. 2.2) and locally onlaps the valley walls (Fig. 2.5).

Interpretation**:** Slickensides indicate subaerial exposure. The clay material is interpreted as the weathering of a subaerially deposited volcanic ash deposit (Bridge, 2006; Li et al., 2011a; Zhu et al., 2012). The bentonite here looks different from that described in previous studies of the Ferron Sandstone likely due to subaerial deposition. The deposit lies within the organic rich mudstone (Facies 3) floodplain facies and represents an event bed within the valley fill.

2.4.5 Facies 5: Laminated Heteroliths

Description: Facies 5 comprises planar interlaminated mudstones and very fine upper to fine lower sandstones (Fig. 2.8D); with an NTG that ranges from 0.3 to 0.6.

Individual beds vary from 5 to 30 mm in thickness and show both normal and inverse grading separated by sharp contacts with the overlying bed. The facies shows an overall fining upward succession.

Interpretation**:** The millimeter scale alternating sequences of inversely graded mudstones and normal graded silt layers are interpreted as lacustrine deposits. The interbedding of inversely to normal graded facies are typical of hyperpycnites and turbidites respectively, deposited by sediment laden plumes discharged into a water body with lower density (Mulder et al., 2003; Zavala et al., 2006). The rhythmic nature of the facies suggests a longer lived hydrograph (Lamb and Mohrig, 2009). In the context of the associated subaerial deposits, this facies represents a floodplain lake formed within the valley (Bridge, 2006). While channel cut-offs typically produce oxbow lakes in meandering systems (Toonen et al., 2012), tributaries experience damming at the trunk confluence (Kvale and Archer, 2007) as a result of trunk sedimentation and discharge increases. The sheet like morphology and lack of obvious scour also suggest a flooding process by trunk damming, rather than abandonment by autogenic channel cutoff.

2.4.6 Facies 6: Thin Bedded Heteroliths

Description: Facies 6 comprises heterolithic fine lower sandstone interbedded with centimeter scale mudstone layers. Sandstone beds range from 3 cm to 15 cm in thickness, while mudstone layers are less than 4 cm thick. NTG for this facies ranges from 0.6 to 0.8. The prevalent paleocurrent direction is to the NW. Cutting through these layers are well developed root casts (Fig. 2.8E). There is an abundance of coaly fragments and coaly streaks (Fig. 2.8F). Sedimentary structures include planar laminations to cross-bedded ripple lamination, and some soft sediment deformation in the form of load casts.

Interpretation: Bedforms, grain size and muddy inter-beds with soft sediment deformation indicate high sedimentation rates. The root casts indicate a non-marine setting. The association as part of the channel fill suggests a possibly abandoned channel fill within the upper channel deposit (Bridge, 2006; Miall, 2010).

2.4.7 Facies 7: Double Mud-draped Heteroliths

Description: Facies 7 shows the highest ratio of sand to shale among heterolithic facies in this outcrop. It is composed of fine lower to medium lower sandstone, interbedded with ripple laminated heterolithic mudstones. NTG values range from 0.8 in upper and younger channel storeys to 0.9 in lower channel storeys. Sandstone units exhibit dune-scale cross bedding (Fig. 2.9A) with double mud drapes and shows an average current direction of 333 ± 6.4°. Dune scale cross bed bottom sets show tangential terminations, which indicate sinuous crested dunes. The bar accretion direction trends to 060 ± 15 degrees, orthogonal to paleocurrent direction (Fig. 2.5). The average bed thickness is 7.6 cm based on measurements across the outcrop (n=27).

Interpretation**:** The double mud drapes are evidence of diurnal slack tide deposits and indicate tidal processes (Dalrymple, 2010b). The shape and orientation of the dune lee sides suggest a N to NW paleocurrent direction and fluvial process of sediment transport. The lateral accretion of the point bar relative to the average paleocurrent direction indicates that this is a meandering channel. The dunes in this facies are largely unidirectional in the downstream direction. This suggests that the crossbedding is in the direction of the ebb tide.

2.4.8 Facies 8: Rippled Sandstones and Thin Mudstones

Description: The uppermost unit is composed of Facies 8 in all 5 measured sections of the west facing outcrop. It is composed of a heterolithic fine lower to fine upper sandstone, with low amplitude ripple laminations. These sandstone beds are less than 10 cm thick. These units are interbedded with ripple laminated, heterolithic mudstones that range in thickness from 3 mm to 5 cm. NTG values range from 0.6 to 0.8. This facies shows moderate bioturbation with a BI range (Taylor and Goldring, 1993) of 1-2, with vertical escape trace fossils (fugichnia, Fig. 2.9B). In horizontal bedding surfaces, *Haplotichnus* are present alongside deeper *Lockeia* casts (Fig. 2.9C). There are some dinosaur footprints also present (Fig. 2.9D and 2.9E).

Interpretation: This facies was host to various biological activity, including infaunal burrowing organisms and larger theropods. This suggests an environment that remains stable and hospitable, but is subject to episodic sedimentation such as crevasse splays during floods. The theropod prints and *Haplotichnus* indicate a fresh-water, non-marine setting where the water table is near the surface (Hasiotis, 2006). This facies has been interpreted as upper channel fill, as it likely marks the uppermost extent of the channel (Miall, 1988; Miall, 2010).

2.4.9 Facies 9: Channel Mudstones

Description**:** Facies 9 is composed of laterally confined, low amplitude rippled mudstone-rich heterolithic strata. Grainsize ranges from silt to very fine lower sand. These heterolithic mudstones and sandstones are distinguished from heterolithic sandstones (Facies 8) as being composed of a greater proportion of mud to sand, with an NTG of 0.2 to 0.4. Typically they appear dark brown to black, in stark contrast with their interbedded sandstones (Fig. 2.9F).

Interpretation: These channel mudstones are deposited by fluvial and tidal processes that are inherent to a tidally influenced fluvial environments (Thomas et al., 1987; Corbeanu et al., 2004; Lynds and Hajek, 2006) by the process of diurnal slack and ebb tide regimes as previously described. While there is no evidence of flood tidal cross bedding, the flood tide may be responsible for the low amplitude ripple laminated mudstones (Facies 9), and are primarily responsible for the mudstone slack drapes. This indicates that the process of deposition is fluvial dominant and ebb tide enhanced

2.4.10 Facies Summary

Facies descriptions and interpretations are summarized in Table 2.1. A facies diagram was reconstructed (Fig. 2.10) to show the facies distribution and to analyse the organization of mudstone elements.

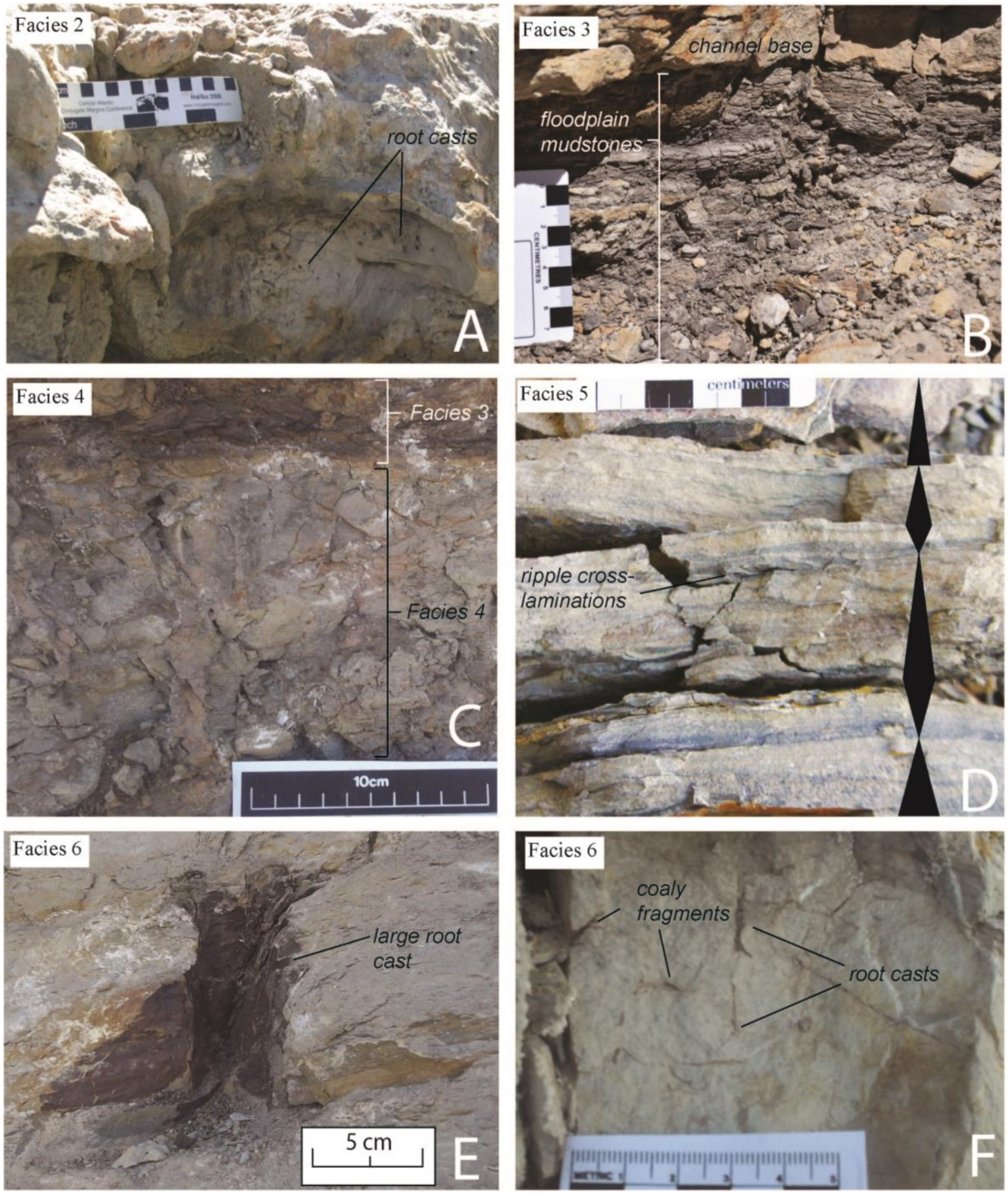

Figure 2.8: A) Massive, bioturbated sandstone with abundant root casts. B) Organic rich mudstone. C) Bentonite layer with overlying mudstone . D) Laminated Heteroliths. Triangles indicate fining direction. Fining upward layers represent turbidites while coarsening upward layers represent hyperpycnites. E) Large root casts truncating ripple laminations in fine lower Sandstone. F) Coaly plant material and root casts in ripple laminated fine lower sandstone.

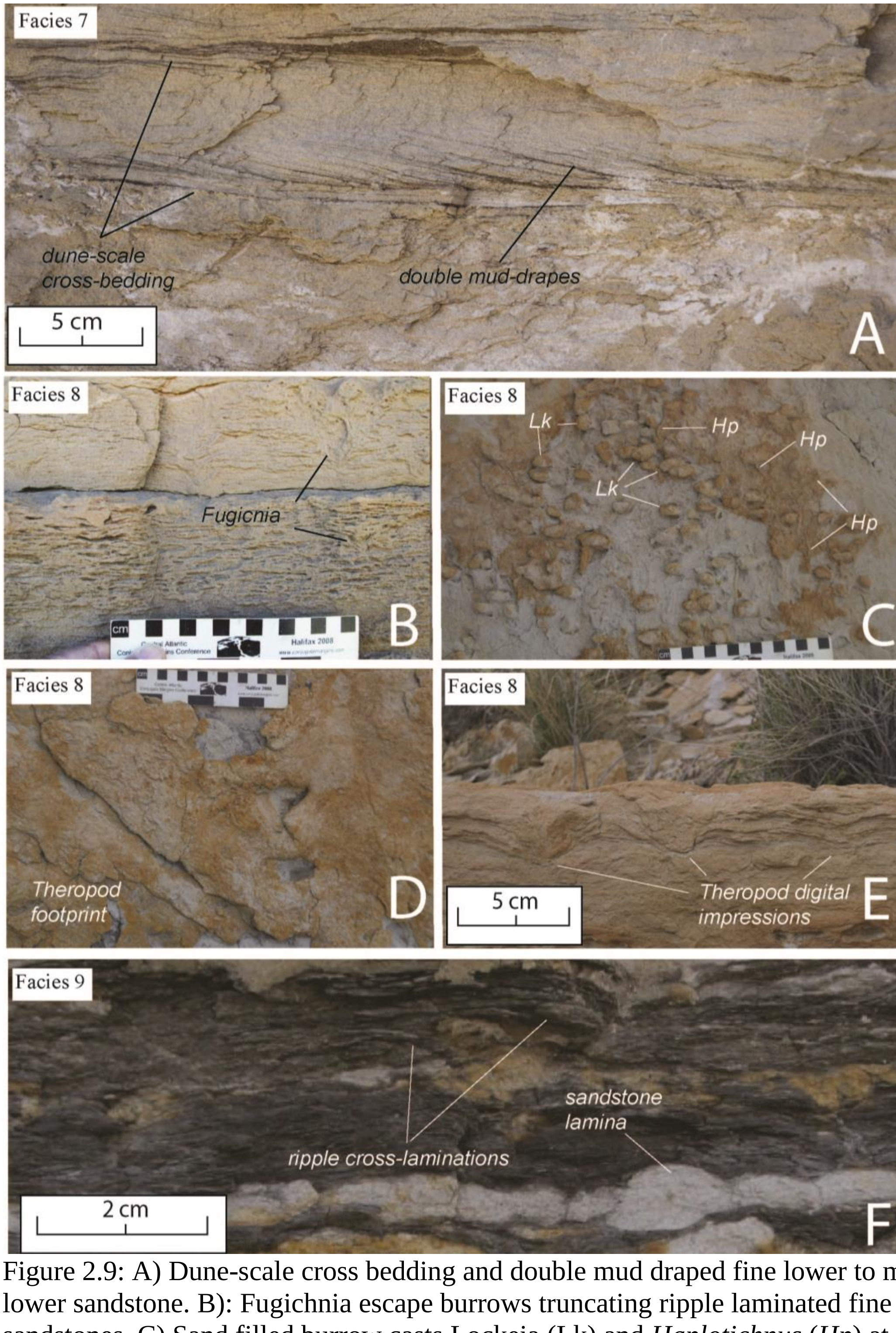

Figure 2.9: A) Dune-scale cross bedding and double mud draped fine lower to medium lower sandstone. B): Fugichnia escape burrows truncating ripple laminated fine upper sandstones. C) Sand filled burrow casts Lockeia (Lk) and *Haplotichnus* (*Hp*) at the base of ripple laminated fine upper sandstones. D) Theropod footprint in plan view, on top surface of ripple laminated sandstone, visible are the 3 digital impressions of a likely

theropod. E) Dinosaur footprint in cross section, apparent from the deformation of rippled lamina in fine upper sandstone. E) Dark brown to black heterolithic mudstones with low amplitude ripples. Interlaminated very fine lower sandstones are lighter in colour and range in thickness from less than 1 mm to 3 cm. The photo shows this facies deposited both above and below Facies 8.

Table 2.1: Facies Summary

Facies	Lithology	Sedimentary Structures	Net to Gross	Biota	Depositional Process	Depositional Environment
1	fine upper sandstone	Planar lamination, vague cross-bedding	> 0.9	Possible bioturbation	Wave dominated	Upper shoreface
2	fine upper sandstone	Massive	> 0.9	Bioturbation	Wave dominated/sub-aerial	Paleosol
3	Organic rich Mudstone	Planar laminations, slickensides	0.1 - 0.3	Plant material	Fluvial/sub-aerial	Flood plain
4	Bentonite Clay	Slickensides	< 0.1		Volcanic	Subaerial
5	Laminated heterolithic vfL to vfU sandstones	Parallel laminations, reverse and normal grading	0.3 - 0.6		Hyperpycnite/ turbidite	Flood plain lake
6	Thin bedded heterolithic fL sandstone and interbedded mudstones	Soft sediment deformation, ripple cross-lamination	0.6 - 0.8	Significant root casts and coaly plant material	Fluvial	Abandoned channel fill and splays
7	Medium bedded heterolithic fL to mL sandstones with interbedded mudstones	Dune scale cross-bedding, double mud drapes	0.8 -0.9		Tidally- influenced fluvial	Coastal plain backwater
8	Medium Bedded heterolithic fL to fU sandstones with thin interbedded mudstones	Low amplitude ripple laminations	0.6 - 0.8	Vertical escape trace fossils, burrow casts, dinosaur footprints	Fluvial	Fluvial upper channel
9	Laminated heterolithic mudstones to vfL sandstones	Low amplitude ripple laminations	0.2 - 0.4	burrow casts	Tidally- influenced fluvial	Tidally influenced fluvial channel

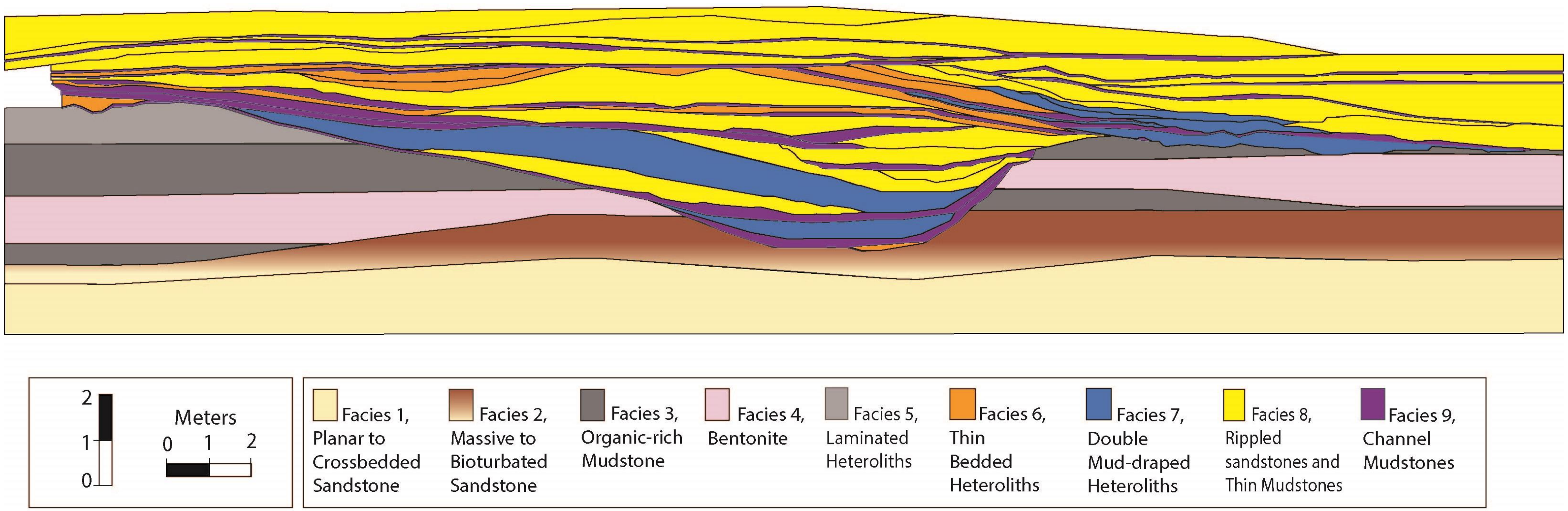

Figure 2.10: Facies diagram showing individual facies distribution within bounding surfaces.

.

2.5 Facies Architecture and bedding diagram

The bedding diagram (Fig. 2.5) represents all major surfaces and architectural elements in the west facing outcrop. The 7th order surface at the base of the outcrop marks the sequence boundary between the younger valley floodplain above (Facies 3), and the older Parasequence 4 marine shoreface below (Facies 2) (Fig. 2.10). The floodplain mudstones (Facies 3) are interbedded with a bentonite layer (Facies 4). This bentonite layer is believed to represent a volcanic ash deposit, as it is bounded above and below by floodplain shales (Facies 3). Locally, this bentonite layer is about 1 m thick and much thicker than the regionally extensive bentonites described by Zhu *et al.* (2012), or Lin *et al.* (2010), which are 10-20 cm thick. The base of the bentonite layer has an offset of 1 m on either side of the incising channel (Facies 6-9) which may be due to differential compaction of the floodplain and bentonite facies (Facies 4), drifting and concentrated accumulation of the ash in the topographic low of the valley. Another explanation is that perhaps the bentonite represents episodic splay deposits from an overloaded fluvial channel at the time of bentonite ash deposition.

The lacustrine deposit (Facies 5) that lies above the floodplain, and is erosionally truncated by the overlying sandstones (Fig. 2.10), is likely a function of damming by the associated trunk channel. This succession of facies consisting of floodplain (Facies 3), lacustrine (Facies 5), and channel deposits (Facies 6-9) is consistent with tributary fills of the early Pennsylvanian in the Illinois Basin (Kvale and Archer, 2007). Kvale and Archer (2007) show the contrast between sandy and gravel filled trunk channels of the Illinois

Basin, and their tributaries, which are filled with muddy lacustrine sediment, due to what they interpret as the “impoundment of the tributary discharge”.

A 6th order erosional surface separates the upper channelized facies from the lacustrine (Facies 5), subaerial, and marine (Facies 1, 2, 3, and 4) below (Figs. 2.5 and 2.10). At the base of the channelized facies, laterally accreting macroforms are bounded by a 5th order surface and internally separated by 3rd and occasional 4th order surfaces, defining the boundary of individual cosets. In this meandering fluvial setting, these coset boundaries define the tops of point bars.

The paleovalley fill is divided into five stacked storeys delineated by 5th order bounding surfaces (Fig. 2.5). Surface 5A onlaps the 6th order surface at the base of the channel. Surface 5B is truncated to the northwest direction on the outcrop, and downlaps towards the southwest, following the pattern of lateral accretion in the lower part of the channel as described in Facies 7. These surfaces are draped by mudstones and heterolithic shales. Surface 5C bounds a bar form, draped with mudstone. Surface 5D is horizontal and truncates surface 5C. The upper northeast part of the outcrop shows surface 5D that truncates 3rd and 4th order surfaces. The 4th order surfaces mark a change in accretion direction.

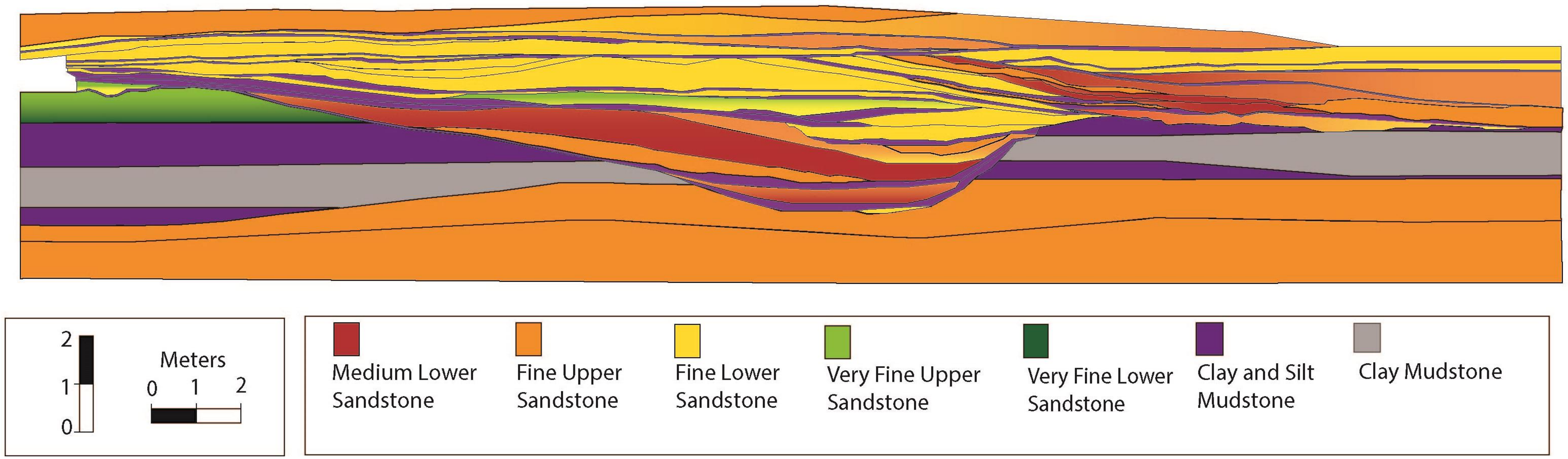

Figure 2.11: Grain size diagram. Varying grain sizes separated by bounding surfaces. Gradational units represent intra-formational variations in grain sizes

2.6 Grainsize Analysis and Mudstone Elements

Figure 2.11 shows the variability and distribution of grain sizes collected from measured sections in the field and mapped across the outcrop. Channel Mudstones were further divided into distinct elements and mapped by channel storey (Fig.2.12). The sand-rich channel deposits have an erosional base with mostly fine upper sandstones and laterally-extensive mud drapes in the lower part of the channel, which are overlain by fine lower sandstones and laterally-extensive mud drapes in the upper channel. Mudstone layers are thicker at the base of the channel fill (10s of cm) but more frequent in the upper part of the channel fill (cm scale) (Fig. 2.12). The NTG sandstone ratio for the channel deposits calculated from measured sections (Fig. 2.11) was 0.84.

The lowest channel deposit has a localized channel lag (Fig. 2.12A) composed of mud chip rip-up clasts. This is overlain by a laterally continuous channel-lining mudstone. The next bar form in this channel fill is a tidally influenced sandstone composed of mL sandstone interbedded with double mud drapes, indicative of tidal processes (Visser, 1980). Another laterally continuous channel-lining mudstone and ripple laminated fine-upper sandstone are the youngest preserved units within this lower channel storey.

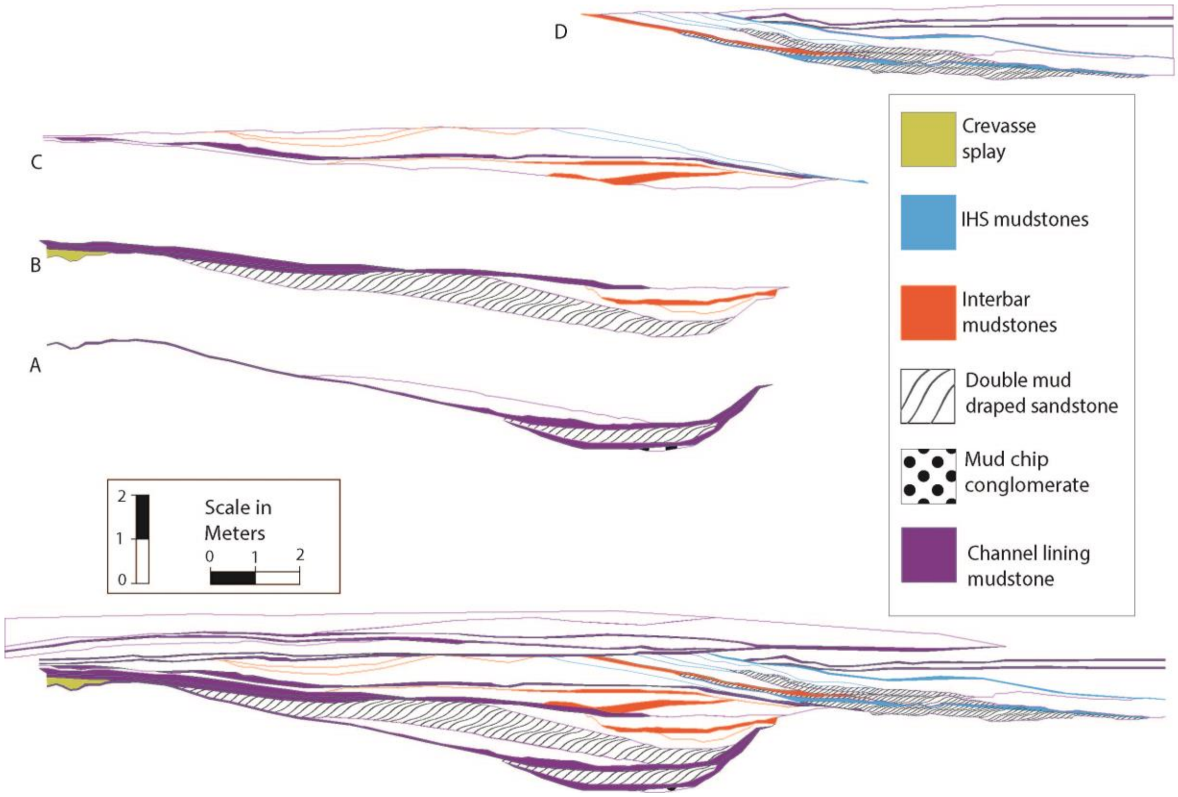

Figure 2.12: Shale map of the study outcrop. Channel stories (A to D) are separated by 5th order surfaces (Fig. 2.5). The individual stories are vertically separated to display the organisation of individual mudstone elements. See text for description.

Mudstones in the coarser-grained second channel storey (Fig. 2.12B) contain a bar with double mud-draped cross strata, overlain by rippled sandstones. These rippled sandstones contain an inter-bar mudstone and are overlain by a channel-lining mudstone. Laterally adjacent to the channel is a silty mudstone deposit containing plant-roots and sediment choked fossilized trees. The underlying barform shows a roll over towards the mudstone consistent with channel levee morphology. The grain size of this thin bedded heterolithic interval (Facies 6) is very-fine upper to fine-lower and therefore does not constitute a mudstone, it is interpreted as a crevasse splay deposit. This storey shows a complete channel height from thalweg to overbank of 2.5 ± 0.1 m.

Similarly, the third channel storey (Fig. 2.12C) shows laterally extensive channel-lining mudstones and abundant inter-bar mudstones. These inter-bar mudstones are often top-truncated by the overlying layers and either pinch out or end abruptly. The youngest preserved channel storey (Fig. 2.12D) deposited several sandstone beds containing lamina-scale double mud drapes, laterally continuous mud-linings, IHS, and inter-bar mudstones. Not seen in this outcrop view (Fig. 2.4A) is a mudstone plug, typical of channel abandonment; however, reconnaissance away from the area shows concave upwards, 3 to 5 m wide and approximately 1 m thick mudstone bodies consistent with channel mud plug morphology (Lynds and Hajek, 2006; Toonen et al., 2012). These mudplugs seem small in comparison to the size of the well preserved point bar deposits (Fig. 2.5). It is likely that this channel remained active beyond the outcrop exposure, but the deposits have not been well preserved.

Mudstone element dimensions can be considered in terms of width perpendicular to flow direction and maximum body thickness (Fig. 2.13). While mudstone linings show no obvious width consistency, they have the greatest width to thickness ratios (w:t) in excess of 100 with a maximum observed ratio of 415 (this study). Inter-bar mudstones scale from 1/3 to 1/2 of the bar width and have a bi-modal distribution that suggest that the ones with higher w:t ratios could represent eroded mudstone linings. IHS deposits tend to span the entire width of the point bar and have an average w:t ratio of 27 and mode of around 20, while double mud draped, dune scale cross bedded sandstone do not exceed ratios of 45.

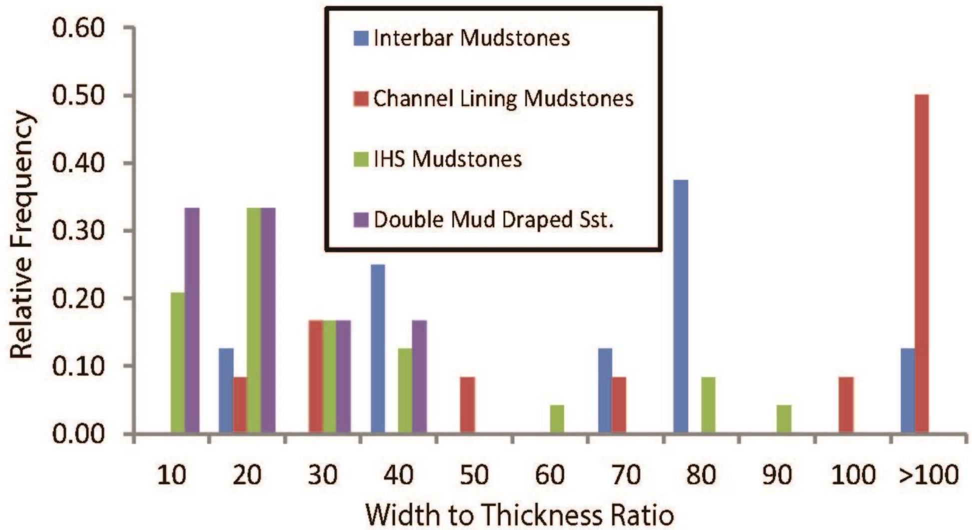

Figure 2.13: Histogram showing the relative frequency of width to thickness ratios (w:t) of mudstone elements (mud chip conglomerate omitted).

Mudstone width and length dimensions are measured relative to the underlying sandstone barform. In this analysis, contiguous mudstones are aggregated to a composite drape if they cover the same 3rd order surface. The mudstone is assumed to have the same morphology as the underlying bar, whereby a length and width can be calculated (Fig. 2.7).

2.7 Paleohydraulic Analysis

Table 2.2: Reference Units

Symbol	Parameter	Units
Q	Water discharge	m^3/s
A	Channel cross sectional area	m^2
$\bar{U}$	Average channel velocity	m/s
s_m	Mean cross-set thickness	m
h_m	Mean dune height	m
β	Mean cross-set thickness/1.8	m
W_{true}	Channel width orthogonal to paleoflow	m
W_{app}	Apparent channel width in outcrop exposure	m
W_b	Bar width orthogonal to paleoflow	m
Δθ	Acute angle between outcrop normal and paleoflow	degrees
H_{bf}	Bankfull flow depth	m
R_h	Hydraulic radius	m
S	slope	m/m
R	Specific gravity of quartz (1.65)	dimensionless
D_{50b}	Median bedload particle diameter	m
u^*_{sf}	Skin friction shear velocity	m/s
Ws	Particle settling velocity for medium sand	m/s
W*	Settling velocity	dimensionless
Re_p	Particle Reynolds number	dimensionless
D*	Dimensionless particle size	dimensionless
ρ_s	Sediment density	kg/m^3
ρ	Density of water at 20°C	kg/m^3
g	Acceleration due to gravity	m/s^2
D	Particle diameter	m
ν	Kinematic fluid viscosity of water at 20°C	m^2/s
n	Manning's *n* coefficient	dimensionless

2.7.1 Workflow

Quantitative estimation of channel discharge (see Table 2 for units) using the cross sectional area (A) and the average velocity ($\bar{U}$) are multiplied to obtain the average discharge (Q) (Bhattacharya and Tye, 2004), wherein:

$$Q = A \times \bar{U} \tag{1}$$

In outcrop, the first and best measure of bankfull flow depth is from facies architectural analysis (Fig. 2.5). The reconstructed channel depth was measured directly from the outcrop where a continuous exposure of channel base to overbank deposit (Fig. 2.12B), shows a preserved channel storey thickness of 2.5 ± 0.1 m from thalweg to the top of the adjacent crevasse splay. This bankfull flow depth (H_{bf}) will be used with channel width to estimate the channel cross-sectional area (A). This estimate is compared with water depth calculated using the average dune cross set thickness in to estimate a mean dune height, which typically scales from 1/10th to 1/6th of flow depth (Bridge and Tye, 2000). Using the mean cross-set thickness (s_m) from channel deposits (Leclair and Bridge, 2001), a mean dune height (h_m) can be estimated given the equation:

$$h_m \approx 5.3\beta + 0.001\beta^2 \text{ where } \beta \approx s_m/1.8 \tag{2}$$

Average cross-set thickness was found to be 7.6 ± 1.0 cm with a standard deviation of 2.7 with all measurements falling within 3 standard deviations of the mean. The mean cross-set thickness relates to a mean dune height (equation 2) of 22.3 ± 2.9 cm. Using empirical relationships for bankfull flow depth and mean dune heights for all types of river dunes (Bridge and Tye, 2000), this translates to a flow depth range of 1.34 ± 0.17 m to 3.29 ± 0.36 m deep. This estimate, while imprecise and independent of river dunes specifically in meandering tidally influenced rivers, is comparable to the bankfull flow depth measured from the observed bar height in the bedding diagram (Fig. 5).

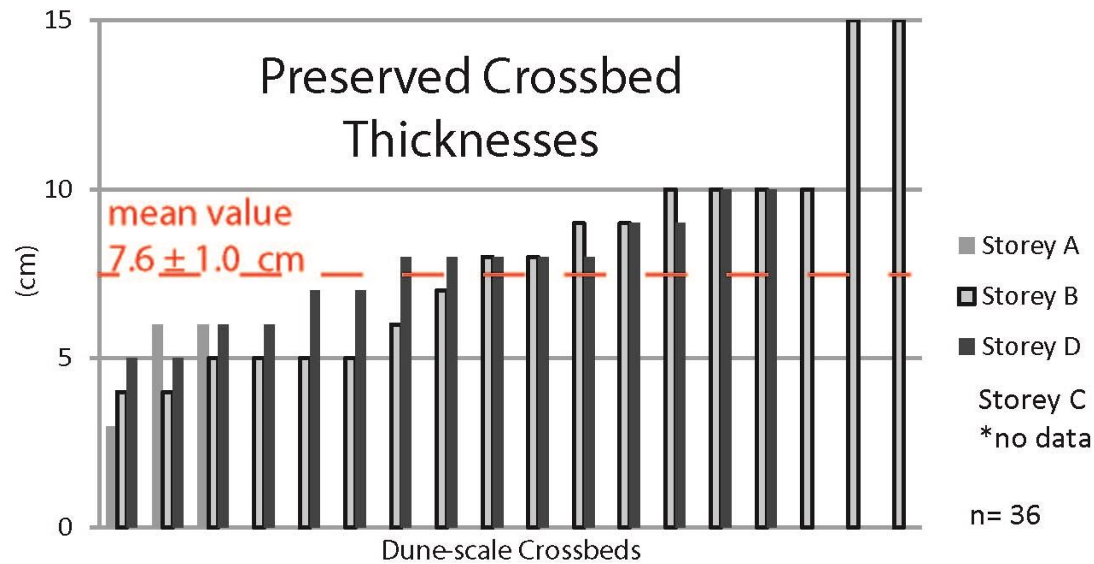

Figure 2.14: Distribution of dune-scale cross-bed thicknesses displayed by channel storey separated by 5th order surfaces (Fig. 2.5).

The overall trend in paleocurrents is towards the northwest (Fig. 2.5) with a mean azimuth of 333 ± 17 ° and a standard deviation of 17°, with all measurements falling within 2 standard deviations of the mean. The west facing outcrop is orientated 044 ± 2° (north) by 224 ± 2° (south). The apparent bar widths are converted to true widths using the formula:

$$W_{bf}=W_{app} \text{ x } \cos(\Delta\theta) \tag{3}$$

In equation 3, W_{bf} is the corrected bankfull channel width, W_{app} is the apparent width in outcrop, and $\Delta\theta$ is the difference between the outcrop orientation (in this case 044 ± 2°) and paleo-flow direction. Figure 2.7 illustrates how data was collected and corrected on dimensions of outcrop bar and mudstone drapes with their associated paleocurrents. Using the premise that point bars typically extends 2/3 of the bankfull channel width (Allen, 1965), and comparing that to empirical relationships relating bankfull width and flow depth (Leeder, 1973; Bridge and Mackey, 1993), the bankfull channel width was determined to be 27.9 ± 2.9 m.

Using the formula for the area of a triangle as an approximation for the cross-sectional area of the channel, the calculation becomes:

$$\text{Area} = ½\, W_{bf} \text{ x } (H_{bf}) \tag{4}$$

This produces an area of 34.9 ± 3.9 m^2. To determine flow velocity using the Manning equation for uniform open channel flow, the hydraulic radius (R_h), and slope (S) must first be derived. The hydraulic radius (R_h) (Vanoni and Brooks, 1957; Van Rijn, 1984) is estimated for trapezoidal and triangular channel geometries using bankfull flow depth from the preserved storey thickness and bankfull channel width given by the equation:

$$R_h = \frac{\text{Area}}{\text{wetted perimeter}} \text{ (meters)} \tag{5}$$

For a wetted perimeter of 30.4 ± 3.3 m the hydraulic R_h = 1.15 ± 0.20. Channel slope can be modelled using the dune scale cross-bedded deposits using a method of paleoslope reconstruction specific to sandy, suspended load dominant rivers (Lynds et al., 2014).

$$S = \frac{RD_{50b}}{H_{bf}} \left(\frac{u^*_{sf}}{W_s} (W^*/\mathrm{Re}_p)^{1/3} \right)^2 \tag{6}$$

$$\text{Where; } \mathrm{Re}_p = \frac{\mathrm{D}_{50b}\sqrt{\mathrm{D}_{50b}Rg}}{v} \tag{7}$$

Equation 6 solves for slope using the specific dimensionless gravity of quartz (R=1.65), the ratio of skin friction shear velocity to particle settling velocity for medium grained sand (u_{sf}^{*} / w_s = 1.6) (Lynds et al., 2014), the dimensionless settling velocity (W^*) and the particle Reynolds number (Re_p) (Parker, 2008; Wilkerson and Parker, 2011). The median particle diameter of the bedload (D_{50b}) in this case is mU sand which ranges from 350 to 500 µm, and the kinematic fluid viscosity of water in m^2/s (ν) at 20˚C is 1.003 x 10^{-6} ± 0.22% (Kestin et al., 1978).

The dimensionless settling velocity, W^*, requires the dimensionless particle size (D^*) (Dietrich, 1982), and is given by the equations:

$$D^* = \frac{(\rho_s - \rho)g\, D^3}{\rho v^2} \tag{8}$$

$$\log W^* = -3.76715 + 1.92944(\log D^*) - 0.09815(\log D^*)^2 - 0.00575(\log D^*)^3 + 0.00056(\log D^*)^4 \tag{9}$$

Equation 8 requires the sediment density of 2650 kg/m^3 (ρ_s), the density of water at a value of 20˚C (ρ), acceleration due to gravity (g), and particle diameter (D). This calculation gives a D* value of 690 to 2011, and a W* (Dietrich, 1982) of 6.67 to 24.83

The slope of this channel is calculated to be 3.8 ± 1.0 x 10^{-4}. Average channel velocity ($\bar{U}$) is calculated using the Manning equation with *n* values of 0.02 to 0.05 for channels in unconsolidated sediment (Chow, 1959):

$$\bar{U} = \frac{1}{n} R_h^{2/3} \sqrt{S} \tag{10}$$

to be between 0.43 ± 0.07 and 1.07 ± 0.19 m/s. These values are plotted on a bedform phase diagram for medium sand (*red*, Fig. 2.15) to test the calculated velocities of this tributary bedforms and compared to those of trunk channels found in the Ferron. At a flow depth of 2.5 ± 0.1 m, dunes form in medium sand at flow velocities between 0.58 and 1.47 m/s (*dashed red*, Fig. 2.15). As no upper flow regime planar laminations are observed in outcrop, the range of flow velocity values predicted by the bedform phase diagram (Rubin and McCulloch, 1980) would favour the calculated flow velocities of 0.58 to 1.26 m/s using the Manning equation and considering the associated uncertainties. Multiplied with the earlier calculated cross-sectional area (equation 4), maximum discharge is estimated to be between 20 ± 2 and 37 ± 8 m^3/s.

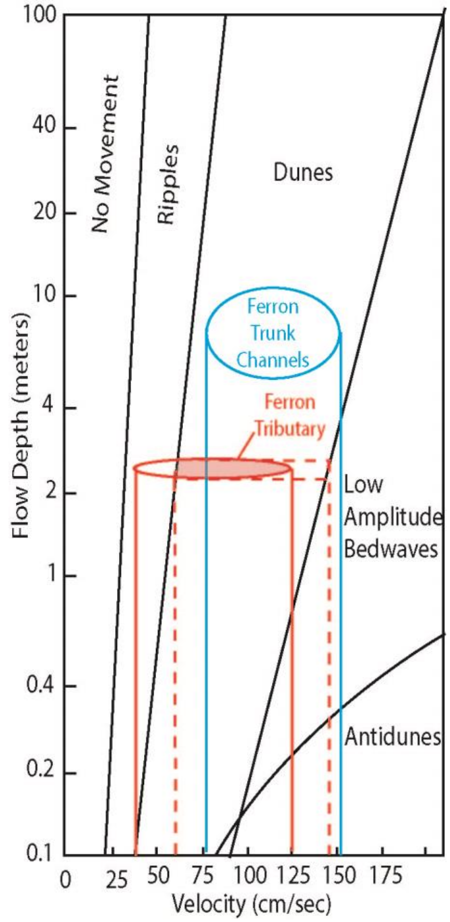

Figure 2.15: Bedform phase diagram for medium sand (0.35 – 0.65 mm) (modified from: Rubin and McCulloch, 1980). Blue: bedforms found in trunk channel deposits plotted by range of flow depths and estimated velocities for Ferron channels (Bhattacharya and Tye, 2004). Red: tributary bedforms found in this study, plotted flow depths observed in outcrop versus calculated velocity ranges possible, given slope estimates. Dashed red: potential velocities for dune scale cross-bedding in medium sand for flow depths ranging from 1.2 m to 3.7 m.

2.7.2 Uncertainties

Any estimation of discharge in ancient systems will involve inherent uncertainties due to the sparse nature of the rock record and the bias that outcrops introduce through the constraints of the exposure available. In this study, we have relied heavily on direct outcrop measurements rather than empirical relationships in an attempt to minimize estimate error. Where we could not, high precision 3D models were used for measurements. Despite this attention to precision, flow depth from levee to thalweg is still approximated to within 10% error (Holbrook and Wanas, 2014) and channel width based on bar width represents a 30% uncertainty that is unavoidable (Bhattacharya et al., 2016). Grain size estimation using a grainsize card in the field can only be estimated as a range in µm representing an uncertainty of up to 17% in these fL to mU deposits used to calculate critical shear stress for velocity values. The effects of grain shape and roundness on settling velocity for the values of D^* reported are only slight for well-rounded, near spherical grains and are most pronounced for flat grains (Dietrich, 1982). Many of the observed grains in outcrop were equant and at least moderately rounded, evident from identifiable grain boundaries which are often occluded by cementation and overgrowths. We have considered this uncertainty and decided that it was likely to be captured within the wider range of uncertainty used in grain diameter estimation. While manning coefficient values of “n” for straight channels range between 0.02 and 0.025 (Chow, 1959), all coefficient values (0.02 – 0.05) of straight and meandering earth lined channels were used to avoid bias introduced with planview reconstruction. The resulting discharge estimates have an uncertainty of ~ 43%.

2.8 Discussion

2.8.1 Geomorphology

The fluvial plan view evolution of these tidally-influenced channel deposits has been reconstructed to show how overtime they build up within a channel belt, the area over which the channel has migrated and its associated floodplain. From paleocurrent data and bedding diagrams, a topographic reconstruction shows the geomorphological evolution (Fig. 2.16). To recreate the planform expression of the outcrop exposure, paleocurrent and accretion surface data was considered with point bar dimensions and projected upstream to conceptualize the resultant structure. This extrapolation of the point bar surface was considered for 2 stages of the channel's evolution (Fig. 2.16). This interpretation is made from the outcrop's 2-D surface and the preservation of laterally continuous mud drapes would suggest that erosion does not play a significant role in controlling the geomorphology of the depositional channel. It is important to mention, that these structural elements, extracted by means of paleocurrent and dimensions from outcrop exposure, mean that this reconstruction is, at best, valid for within 10 meters of the outcrop, that being the average structural dimension of the bars. The reconstruction will therefore reflect the variability within and between channel storeys.

The early stage channel (Fig. 2.16) is made up of a high proportion of steep dune-scale foresets with double mud drapes, denoting a relatively strong tidal signal. This low sinuosity channel exhibits a gently meandering morphology, likely controlled by backwater tidal processes that suggest channels within the backwater have a straighter morphology as they tend to aggrade rather than migrate laterally (Blum et al., 2013). The preservation of continuous bar-draping mudstones suggests that the rate of channel aggradation exceeds the rate of erosion, or channel scour. While there are few paleocurrents observed, the mean paleocurrent of the whole population (n=22) is 333 ± 17° with a standard deviation of 17°. Early stage channel paleocurrents have an average trend of 330 ± 17 ° with a standard deviation of 19°, and later stage channel paleocurrents have an average of 337 ± 19 ° with a standard deviation of 15°. The consistency of paleocurrent data, however sparse, suggests that sinuosity was low . Plan view studies of unconfined channels in the Ferron Sandstone show similar patterns of low to moderate sinuosity. While late stage channel evolution with highly sinuous meanders has been observed (Wang and Bhattacharya, 2018), typically these rivers within a few kilometers of this channel exhibited low to moderate sinuosity, ranging from 1.04 to 1.44 (Bhattacharyya et al., 2015; Wu and Bhattacharya, 2015; Wu et al., 2016; Wang and Bhattacharya, 2018)

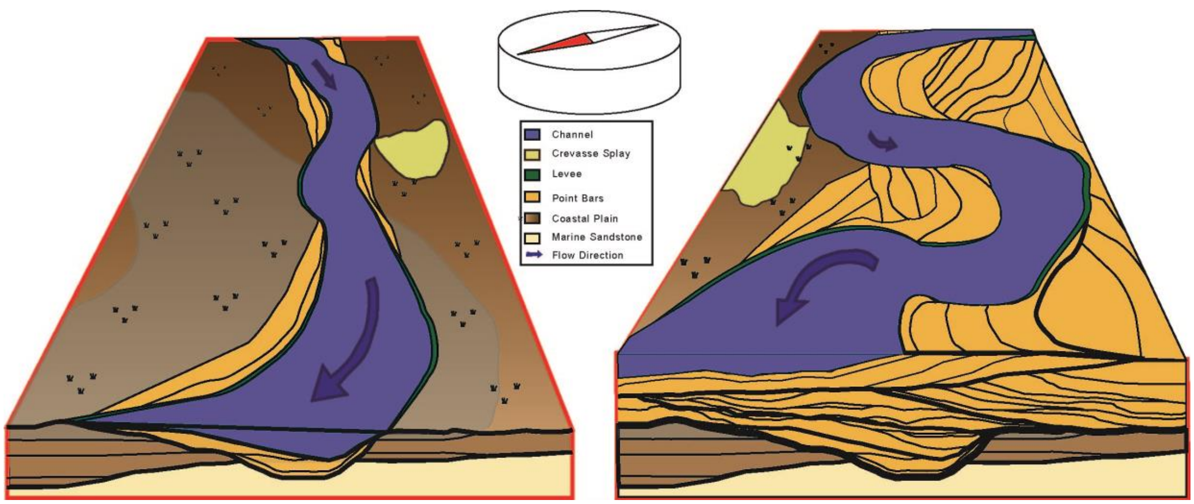

Figure 2.16: Plan view reconstruction of formative tributary valley channels. Early stage *(left)* is characterized by low sinuosity, highly aggradational, tidally-influenced channels. Late stage channels *(right)* have a slightly increased sinuosity and grow by lateral extension and downstream translation.

The later stage channel (Fig. 2.16) is broader, with less relief. The tidal signal is weaker, possibly affected by a moderate increase in sinuosity and the topographic buildup of the channel within the confines of the valley. As the channel aggrades and lifts up within its channel belt within the backwater (Blum et al., 2013), the tidal signal is no longer sufficient to produce double mud drapes. The flow velocity combined with the ebb component of tide oscillations no longer move medium sand, evident from the decrease in grainsize (Fig. 2.11).

Migration of channels within the valley show a paleocurrent progression interpreted to lack either extensive expansion or sinusoidal translation (Willis and Tang, 2010). The implication of this depositional behaviour would be an increase in sand body connectivity. With infrequent 4th order surfaces within bar forms (Fig. 2.5), the paucity of intra-bar erosion may suggest that neither rotational nor translational point bar growth was significant (Durkin et al., 2015), specifically within the Ferron Sandstone backwater limit. 4th order surfaces (Miall, 1985; Durkin et al., 2015; Kimmerle and Bhattacharya, 2018) record intra bar erosion events caused by downstream bar translation and rotation of point bar growth. In this study, 4th order surfaces, characterized by this type of intra-bar erosion (Fig. 2.6), truncate 3rd order surfaces and are found within 5th order surfaces. With the near complete lateral preservation of bar drapes in this study, we do not believe that intra-bar erosion surfaces are being recorded at a higher or lower order, and therefore we interpret this system as aggradational, mildly sinuous and within the effects of the backwater. This may also be affected by the ever-wet nature of the Ferron environment (Famubode and Bhattacharya, 2016), promoting the stable discharge of Ferron rivers and mitigating the erosive nature of drawdown effects (Colombera et al., 2016) and ephemeral river behaviour where channel hydrographs are more variable. Point bar dimensions are estimated from outcrop exposures using the average paleocurrent direction of each bar bounded by a 3rd order surface, the aspect of the outcrop exposure, and the outcrop length of each barform (Figs. 2.7A and 2.7B). A similar method was used to estimate mudstone dimensions in the Ferron Sandstone using a rectangular model (Biber et al., 2017), this conical geometry captures more of the point bar morphology than previously attempted. In this method, the length and width of each bar deposit is estimated and fit to a hyperbolic curve (Fig. 2.7C). The first integral of this curve is then used to estimate the surface area of a given point bar (Fig. 2.7 D).

2.8.2 Trunk, tributary and distributaries within the backwater limit

Sediment routing pathways in a source to sink context (Bhattacharya et al., 2016; Sømme et al., 2009) show the relationship of trunk tributaries to their trunk valleys, and the communication of those trunk valleys to their distributaries (Figure 2.17 A). Trunk tributary valleys are identified as incised channel deposits that run perpendicular to the well-defined main trunk of a system (Posamentier, 2001). In modern systems we recognize trunk tributary valleys in the upper backwater by their characteristic dendritic morphology, orthogonal flow direction, and smaller size relative to their associated trunk. Tributary valleys to the Amazon River valley near Juruti, Brazil have this morphology and are 687 km away from the mouth of the Amazon Delta. With a slope of 2.86×10^{-5} and an average depth of 20 m (Lefavour and Alsdorf, 2005), the Amazon's backwater length is conservatively calculated to be 699 km. This puts the reach of the Amazon near Juruti 10 km within the backwater limit (Fig. 2.17 B). Closer to the tidal signal, the Albert River near Burketown, Australia just 26 km from the coast shows a pattern of erosional side drainages. These drainages were originally recognised as distributaries in the Gulf of Carpentaria (Jones et al., 2003) as they channel water during high tide. These side drainages act as tidal tributaries during low tide and rainfall and may be considered as a tidally-dominated feature (2.17 C), marking a surface of tidal ravinement. Interpretation of 3D time slices acquired in the Gulf of Thailand show how incised tributary channels are preserved in Pleistocene fluvial deposits (Reijenstein et al., 2011). While considerably smaller in size than their associated trunk valley deposit, these features may represent a significant proportion of a fluvial reservoir in their aggregated volume, depending on their size and occurrence frequency along the main trunk valley.

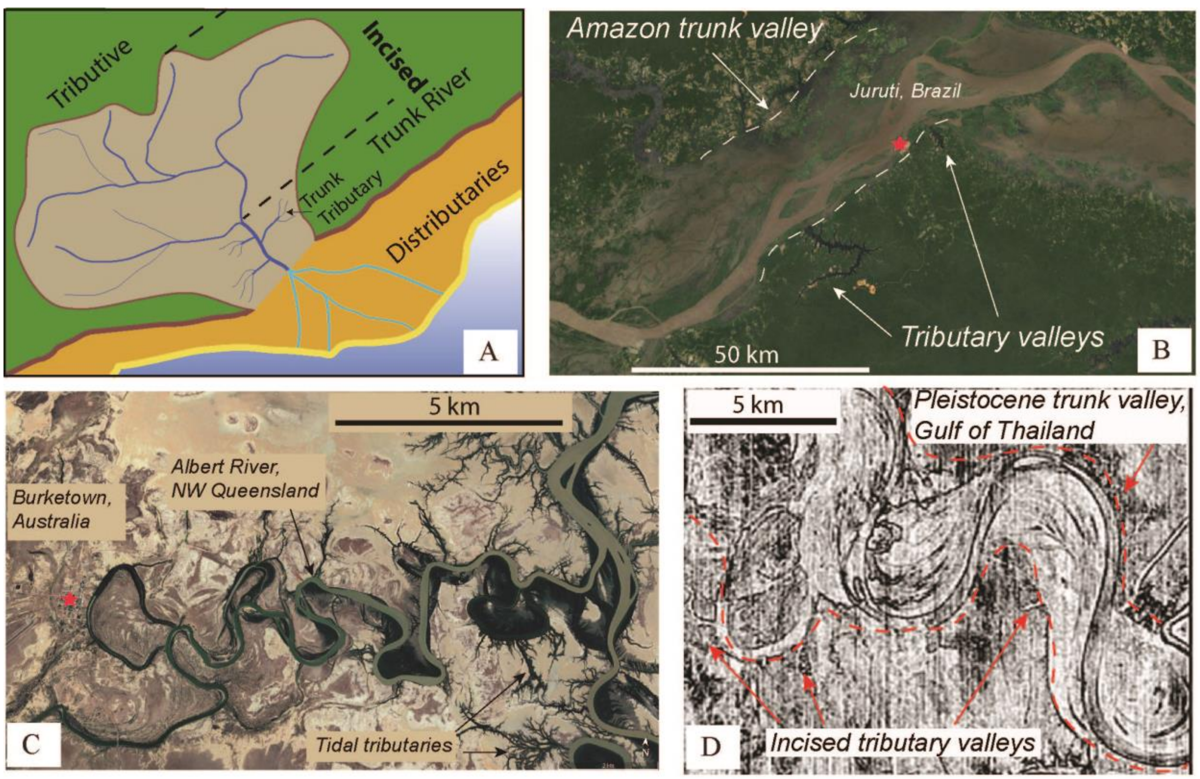

Figure 2.17: A) Channel networks in a S2S system (*modified from* Bhattacharya et al., 2016), are differentiated as being either tributaries, distributive or a trunk channel. Tributaries that directly feed the trunk channel in an orthogonal drainage pattern are considered trunk tributaries. B) Amazon trunk valley within the backwater near Juruti, Brazil. Small tributary valleys are shown relative to the Amazon trunk valley. C) Tidal tributaries that feed the main channel of the Albert River in Queensland, Australia near Burketown. D) Incised tributary valleys in Pleistocene fluvial deposits in the Gulf of Thailand interpreted from seismic time slices (*modified from:* Reijenstein et al., 2011).

A comparison of structural and paleohydraulic elements can help distinguish trunk valley deposits from those of tributary valleys (Table 3). When considering water depth estimates, there is a significant difference in the size of tributary channels compared to that of the published trunk channels (Li et al., 2010; Kimmerle and Bhattacharya, 2018), where trunk channels are up to 7 m deep versus the 2.5 m deep tributary channel. This difference in estimated water depth ranges by a factor of 1.5 to 3.0. Similar structures appear in trunk and tributary channels within the backwater, including dune scale cross-bedding with double mud drapes (Fig. 2.18), laterally extensive muds, and mud chip conglomerates. Li et al. (2010) correlated five distinct fining upwards channel storeys with the largest mud-chip conglomerates at the valley base. Our tributary example also shows four fining upward channel storeys, with the potential for a poorly preserved fifth channel storey at the top (Fig. 2.5). The distinct tidal signal in the form of double mud drapes in both trunk and tributary deposits, as well as *Teredolites* found in trunk channels (Kimmerle and Bhattacharya, 2018) presents the likelihood that this system is well within the FMTZ and likely the lower backwater. As illustrated in the channel reconstruction (Fig. 2.16), the relatively straight channel geometry extrapolated from bedding surfaces and paleocurrents is interpreted to be a function of the lower backwater, which inhibits lateral migration and disallows development of a highly sinuous channel morphology (Fernandes et al., 2016). There are aggradational flood plains with bentonites and relatively narrow channel belts within this tributary valley. The channels show a modest degree of lateral migration and a high degree of aggradation. The behaviour of these channels fit with backwater models that propose channels in the lower backwater tend to lift rather than migrate, resulting in heterogeneous valley fills, not only with a high proportion of mud within the channel belts; but also preservation of flood plains within the valley system.

The paleo-flow velocity and bankfull channel discharge estimates vary by orders of magnitude. Flow velocities in the trunk channels are potentially an order of magnitude greater, as derived from grain size observations. The channel discharge was calculated to be an order of magnitude smaller in the tributary channel than that of the adjacent trunk channel (Kimmerle and Bhattacharya, 2018) using preserved channel fill widths, and 2 orders of magnitude smaller than that of other proximal trunk channels (Li et al., 2010) using empirical channel depth/width ratios.

Table 2.3: Trunk versus Tributary Paleohydraulics

Ferron Sst. Youngest Sequence Valleys (cited)	Estimated water depth (m)	Flow velocity (cm/s)	Channel Discharge (m^3/s)	Slope (m/m)
This study (Tributary)	2.5 ± 0.1	58 – 126	20 – 37	$3.8 \pm 1.0 \times 10^{-4}$
Li and Bhattacharya, 2010	4.3 – 7.1	100 - 160	420 - 1290	-
Kimmerle and Bhattacharya, 2018	3.7 - 6.5	90 - 220	113 - 1255	5.3×10^{-4}
Bhattacharya et al, 2015	4	75 – 230	1300 - 3000	1.4×10^{-3}

Slope estimates are similar within trunk (this study) and adjacent tributary channels (Kimmerle and Bhattacharya, 2018). Ferron Sandstone trunk slope estimates by Bhattacharya et al. (2015) are based on a regional slope, assuming the elevation minima of the valley base would correlate to the slope of initial incision, and therefore of the thalweg of the formative channel. Instead of using a regional slope, Kimmerle and Bhattacharya (2018) calculated reach slopes using grainsize distributions and channel widths and depths from facies architecture analysis (Lynds et al., 2014). This demonstrated that the gradient of any particular reach could differ from that of a region. The tributary slope was calculated using the same method (Lynds et al., 2014).

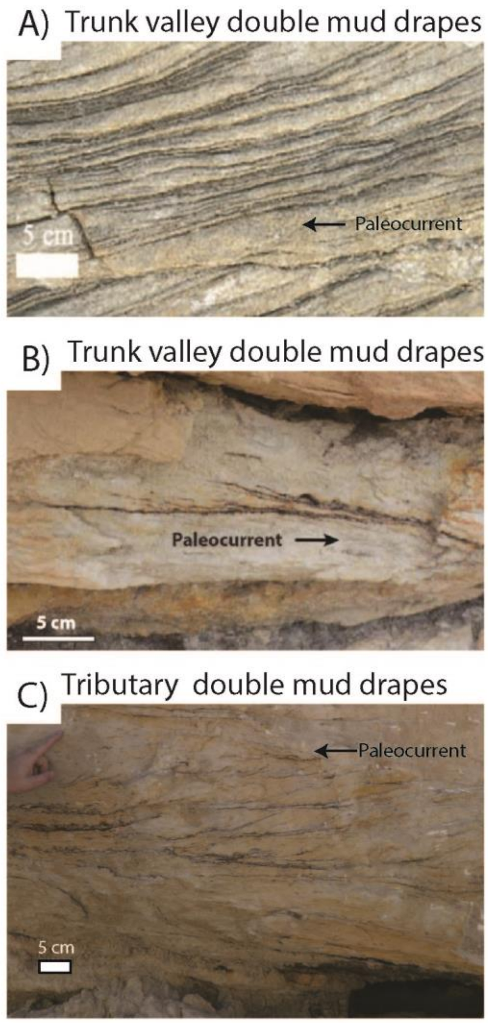

Figure 2.18: Double mud draped, dune scale cross bedding observed in the trunk valleys of A) Li et al. (2010); B) Kimmerle and Bhattacharya (2018); and C) this study.

In general, the trunk valley that feeds the youngest continental deposits of the Ferron Sandstone is described as a piedmont valley composed of multiple terraces (Li et al., 2011a; Li and Bhattacharya, 2013; Kimmerle et al., 2016). Comparing the deposits of this trunk valley, the highly aggradational deposits of floodplain, mud prone tributaries (Kvale and Archer, 2007), and downstream distributary systems (Corbeanu et al., 2004;

Olariu and Bhattacharya, 2006; Ahmed et al., 2014) has potential for valuable insight into predictions of reservoir heterogeneity within the FMTZ. This is dependant not only on what part of the system they are in, but also of their location with respect to the backwater limit, the tidal backwater limit and the bayline, as these factors may control the degree and nature of mud sequestration. In fluvial systems it is critical to determine if a channel is incised (Posamentier, 2001) which we have evaluated on the basis of the depth of the scour or valley surface versus the bankfull channel depth of the deposits contained within it. In the tributary valley of this study we have small channels and flood plains within a much larger erosional surface (factor greater than 2) verifying that this is indeed an incised valley. The distinction of trunk vs distributary channels is made on the basis of size, architecture and paleocurrents on a regional scale. The determination of upper versus lower delta plain distributaries is made by understanding that coastal plain distributaries deposit point bars and are primarily fluvial in nature (Corbeanu et al., 2004; Olariu and Bhattacharya, 2006); while terminal distributaries are dominated by terminal mouth bars (Olariu and Bhattacharya, 2006; Ahmed et al., 2014) and are mostly marine deltaic in nature as they can be the primary source of sediment for the delta front.

2.8.3 Mudstone Dimensions and Conceptual Model

No previous point bar model addresses heterogeneity as a function of backwater or tidal backwater distance. The average aspect ratio of length to width measurements of individual mudstones observed in this study (Fig. 2.19A) is 1.81 ± 0.54. This ratio is consistent with previous work in the Ferron Notom using terrestrial Lidar and relating average mudstone lengths to average mudstone widths of entire channel belts (Biber et al., 2017), where tributary channel belts show an aspect ratio of 1.14 (uncertainty not reported). Any prediction of mudstone dimensions in fluvial deposits is further complicated by backwater processes. We expand the conceptual mudstone model in braided systems (Zaitlin et al., 1994; Willis, 1998; Lynds and Hajek, 2006) to include tidally influenced meandering channel deposits in a tributary valley (Fig. 2.20). Aside from inter-formational mudstones, we include the distribution of those units that host intra-formational mudstones as well. This model retains elements of the idealized channel fill model of Lynds and Hajek (2006), including channel lining mudstones, inter-bar mudstones, IHS, mud plugs and adjacent flood plain splay deposits. While not present in the immediate outcrop area discussed in this study, the potential for mud plugs to occur are dependent on the avulsion susceptibility of the system leading to channel abandonment deposits (Ethridge et al., 1999; Stouthamer and Berendsen, 2001; Tornqvist and Bridge, 2002). Counterpoint bars, previously described as eddy-accretion bars (Smith et al., 2009), were also not observed in the study area, but do occur in the adjacent trunk valley (Kimmerle and Bhattacharya, 2017) and should be included in a general facies model of meandering streams. In the trunk valley, counterpoint bars occur near the valley margin, which is not preserved in this tributary outcrop. This type of deposit would migrate laterally away from the downstream inflection associated with a point-bar deposit. In addition to these units, our meandering channel fill model incorporates the potential for intra-formational mudstones in the form of mud-chip rip-up clast laden sandstones common to basal units of channel fills, and mud draped strata diagnostic of tidal sedimentary environments.

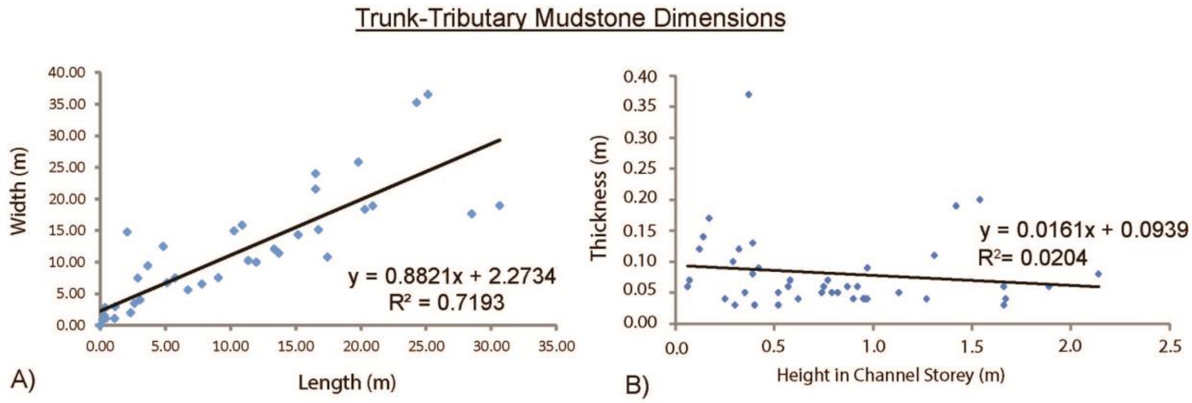

Figure 2.19: Length and width and thickness values for mudstones in the trunk tributary. A) Length to width correlation of mudstone dimensions. B) Mudstone thicknesess taken from measured section and plotted against their height from their respective storey base as defined in the bedding analysis (Fig. 2.5).

These intra-formational mudstones can have a profound impact on the permeability of these units (Miall, 1988; Willis, 1998; Pranter et al., 2007) and will in turn affect the flow characteristics of analogous reservoirs (i.e., tidally- influenced channel belt deposits).

Mudstone thicknesses collected from measured sections (Fig 2.5), are considered relative to their position within their respective channel storeys (Fig. 2.12). The thicker mudstones in this tributary show an affinity for the lower part of the channel (Fig. 2.19B). While it would appear that thicker mudstones tent to be found in the base of the channels no statistical trend is obvious. It is possible that mudstone thickness is controlled by more than just avulsion and autogenic fluvial processes. Thicker basal mudstones are observed in the tide-dominated Fly River Delta of Papua New Guinea, where low-gradient distributary channels deposit cross bedded and rippled sands abruptly overlain by centimeter thick dense fluid muds (Dalrymple et al., 2003a). These fluid muds form at the base of channels in tidal spring cycles and collect in the thalweg, trapped by estuarine dynamics. The observation of larger mudstone thicknesses closer to the channel base in the Ferron tributary may reflect this same spring tide process of fluid mud deposition. While the classic tidal indicator of double mud draped cross-bedding is present in our outcrop, so too are thicker mudstone beds (up to 20 cm) similar to the Cretaceous Bluesky Formation in Alberta, Canada (Mackay and Dalrymple, 2011), formed by low current speeds and higher suspended sediment concentrations. Heterogeneity in this system may therefore reflect velocity instability inherent in estuarine fluvial systems and dynamic suspended sediment concentrations.

Lateral mudstone dimensions in outcrop are an incomplete measurement without consideration to the degree with which the bar is draped and the ratio of draped bars versus undraped bars. To contextualize these mudstones relative to their degree of coverage, we compare trunk, tributary and distributary fluvial systems (Fig. 2.21). In this comparison, there are distinct trends in both the ratio of bars that are draped by mudstones compared with those that are not draped; and the degree or amount of draping. These trends vary considerably from one fluvial component to another in the youngest incised valleys of the Ferron.

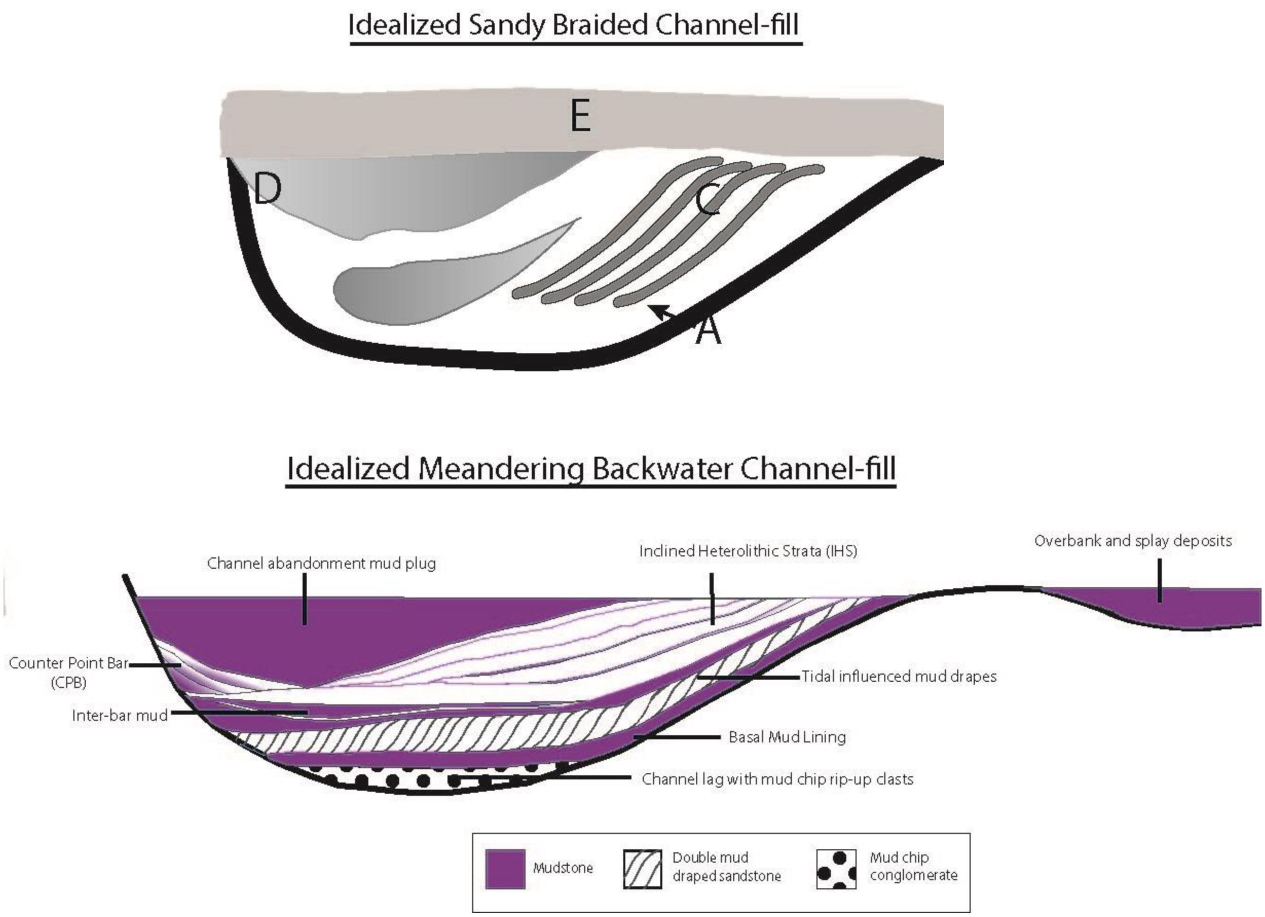

Figure 2.20: Comparison of idealized sandy braided-river channel fill (*modified from:* Lynds and Hajek, 2006) and a meandering backwater channel fill. *(Above)* Idealized channel-fill unit model scaled to paleo- flow depth (pfd). (A) channel-lining muds, (B) interbar muds, (C) inclined heterolithic strata, (D) mud plugs, and (E) flood-plain and overbank deposits. (*Below)* Modified model for mudstone channel fill elements in a tidally influenced tributary channel within the backwater, to include intra-formational mudstone elements such as counter-point bars, Rip-up clasts and double mud draped sedimentary structures.

Terraces in the trunk valley are the least mud prone, both in terms of the proportion of bars that are draped by mudstones and the degree of mudstone coverage. This trend is explained by the dominance of unidirectional flow, despite having a very recognizable tidal influence in outcrop, and characterized as well within the backwater limit (Li et al., 2010; Li and Bhattacharya, 2013; Kimmerle and Bhattacharya, 2017). The lack of drape preservation is likely a result of a strong and stable river hydrograph in an ever-wet climate (Akyuz et al., 2015; Famubode and Bhattacharya, 2016). The micro to meso-tidal setting of the Western Interior Seaway during the Late Cretaceous (Ericksen and Slingerland, 1990) may have affected the trunk rivers to a lesser degree then smaller tributaries, with much lower discharges. Point bars in the trunk channel show little coverage, with more than half of all bars covered by less than 5% of their surface area. 90% of trunk bars are less than 50% covered. The dominant mudstone elements in these trunk deposits include IHS (Li and Bhattacharya, 2013; Biber et al., 2017; Kimmerle and Bhattacharya, 2017), counter point bars (Smith et al., 2009; Kimmerle and Bhattacharya, 2017), mud-chip conglomerates (Li et al., 2010; Zhu et al., 2012; Kimmerle and Bhattacharya, 2017) and lamina-scale double mud drapes and flaser bedding (Li et al., 2010; Li and Bhattacharya, 2013; Kimmerle and Bhattacharya, 2017).

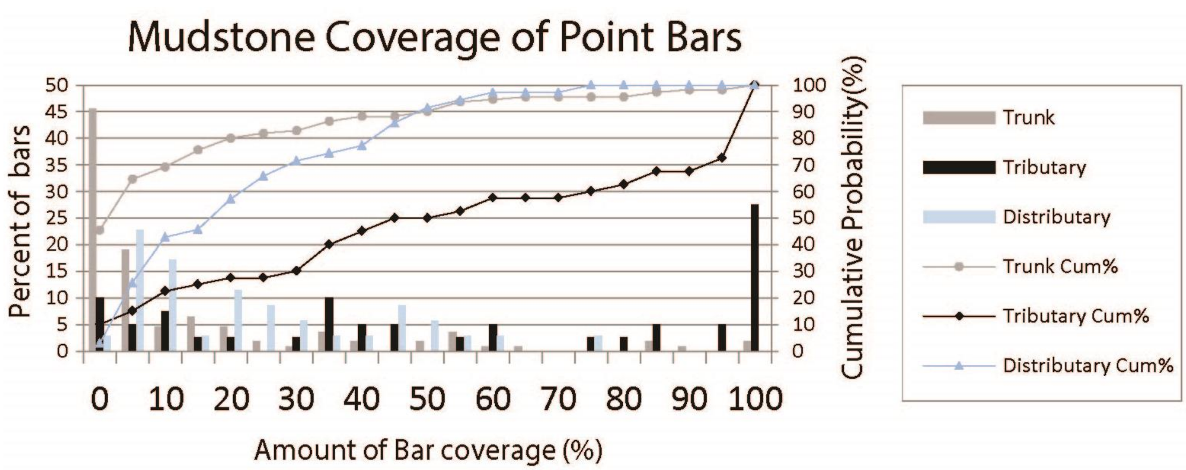

Figure 2.21: Three separate components of a fluvial system are compared within the Ferron Sandstone Member. Trunk channel mudstone dimensions *(grey)* are compiled from Kimmerle and Bhattacharya (2018) and Campbell (2013) for the youngest sequence in the Notom Delta continental strata. Tributary mudstones (*black, this study)* were measured in the field and correlated to the trunk channel described in Kimmerle and Bhattacharya (2018). Distributary mudstone dimensions are reported by Corbeanu et al.

(2004) *(blue)* from the youngest sequence in the Last Chance Delta. Histogram shows normalized values to compare the degree of bar coverage versus the percentage of total bars in each study covered by that amount *(left axis)*. The line graph shows the cumulative amount *(right axis)* at each amount of coverage. See: Supplemental_1.

Upper delta plain distributary channels, which typically experience a greater marine influence than trunk systems, show a slightly greater affinity for mud drape preservation with half of all distributary bars less than 20% covered. 90% of point bars in these distributaries are less than 50% covered. In the context of reservoir characterization, reservoir quality and NTG ratio may be very similar to that of trunk channel deposits, however; mudstone elements differ somewhat. Distributaries in the Ferron Notom and Last Chance Deltas preserve deposits of IHS, mud-chip conglomerates, mud plugs from channel abandonment and lamina scale double mud drapes (Corbeanu et al., 2004; Li and Bhattacharya, 2014). The prevalence of channel abandonment mud plugs is inherent in terminal distributaries (Toonen et al., 2012).

Trunk tributaries show the greatest affinity for mudstone deposition of all three systems. Half of all tributary bars observed in the focus of this study were at least 50% covered by mudstone drapes, with 25% of all tributary point bars being completely covered. Only 10% show no mudstone coverage. Aside from these bar drapes and IHS deposits, dominant mudstone elements include mud linings, inter-bar mudstones and organic rich floodplain shales. This higher mudstone deposition may be a function of marine or backwater influence combined with the effects of the tributary-trunk confluence, as the trunk river may periodically impede tributary flow during periods of high discharge (Kvale and Archer, 2007).

This comparison of tributary, trunk and distributary channels reveals that while distributary systems are the most marine influenced, and may have the thickest mudstone intervals, it is the trunk tributary that has the least point bar connectivity. Tidally-influenced trunk channel sandbodies, may be similar to the distributaries they feed in the lower backwater and bayline. In this regard, outcrop studies are a useful method of predicting analogous reservoir qualities. For calculation of drape area coverage, see: supplemental_1 (supplemental digital file).

2.8.4 Implications for Petroleum Reservoirs

The sequestration of muds in sandy deposits is clearly an impediment to reservoir fluid flow. The observation of thicker mudstones at the base of channels in the FMTZ are counter intuitive, but can be explained by estuarine dynamics of fluid mud accumulation, whereby high concentrations of suspended sediment behave as a psudo-plastic layer moving by gravity and advective processes at the bed interface (Mackay and Dalrymple, 2011). This determination of depositional environment and facies analysis may present a better estimate of reservoir quality then wire log data and core plug tests (Jackson et al., 2005; Nordahl et al., 2005; Massart et al., 2016). The determination of reservoir quality, based on NTG ratios or even mudstone thicknesses from well data, is insufficient to predict connectivity and potential compartmentalization. The tributary valley fill in this study show channel deposits with an apparently high NTG ratio of ~0.7 to 0.8 which would ordinarily imply favourable reservoir permeability (Jackson et al., 2005); however we have shown that despite the volume of shale being quite low, their continuity is quite high. This may reflect conditions of the lower backwater, hence the rivers experience high degrees of aggradation and little in the way of lateral migration, thus less erosion. With the lack of erosion comes more preservation of mud drapes and fewer mud chip conglomerates. In contrast, landward of the backwater, where rivers are free to migrate laterally and tidally influenced, fluid muds are not expected, mud drapes could be stochastically deposited during times of low or waning river discharge and may be additionally preserved as mud chip conglomerates as a result of the next flood cycle.

Even moderate amounts of mudstone coverage may have a great impact on reservoir permeability (Massart et al., 2016). Massart et al. (2016) conclude that while the continuity of mudstone drapes are an important factor for permeability estimates, so are the dune shape and dune foreset-toeset surface geometries. In the case of partial bar coverages, as shown in trunk and upper delta plain distributaries in the Ferron, these parameters may be of greater importance than in the case of our tributary, where total bar coverage is the dominant mode of mud sequestration (Fig. 2.21). For that reason, such tidally-influenced tributaries may represent the lower end of reservoir recovery estimates for what is typical in heterolithic reservoir units of around 15% (Martinius et al., 2005).

While considering useful applications for this study, we focus on the importance to better understand similar reservoir analogues such as the McMurray Formation, Alberta, Canada. Like this study, the McMurray Formation is interpreted to be tidally influenced. The FMTZ environment of deposition is evident from large scale IHS that sequesters laterally continuous mudstone bar drapes, brackish trace fossils and palynology data collected throughout the middle and upper McMurray (Blum, 2017;

Gingras and Leckie, 2017). Unlike our Ferron Sandstone tributary however, the upper and middle McMurray Formation show a fluvial morphology that is highly sinuous, and does not reflect backwater channel behavior. This fundamental inconsistency highlights the need for reassessing fluvial depositional models within backwater reaches. Similar to the Ferron Sandstone tributary, the tidal influenced intervals of the McMurray Formation show abundant lateral mud drapes with rare mud clasts (Nardin et al., 2013). The degree of bar draping in the middle member of the McMurray Formation is highly variable and depends on the degree of tidal influence (Musial et al., 2012; Nardin et al., 2013); however much like the Ferron Sandstone tributary, the majority of mudstone beds in the most tidal influenced facies show complete lateral continuity and may represent similar degrees of point bar coverage (Fig. 20). Extensive work on point bar deposits in the upper backwater show a high sinuosity, continental-scale drainage system(Durkin et al., 2015; Hagstrom et al., 2019; Horner et al., 2019a), whereas the channel deposits in this study drain a far more modest watershed. Despite the McMurray channels being up to three times deeper and having an order of magnitude longer backwater length than the Ferron Sandstone trunk (Martin et al., 2019), there exist similarities in grainsize and lithofacies distribution (Durkin, 2016; Horner et al., 2019b) that may help predict shale drape variability in lower backwater reaches. The lack of seasonality in the Ferron's ever-wet discharge, however, may make this comparison applicable only to the flood-stage deposits of the McMurray, which may have been deposited under much more seasonal climatic conditions (Jablonski and Dalrymple, 2016).

2.9 Conclusions

This study has described a 27.9 ± 2.9 m wide channel deposit within a tidally-influenced trunk-tributary valley fill in the Upper Ferron Sandstone. Through detailed facies architectural analysis, the valley was found to be filled with multi-storey, laterally accreting point bar deposits; forming a 4 to 5 storey incised valley fill. Facies associated with this tidally-influenced tributary valley include floodplain shales, lacustrine heteroliths, and heterolithic fluvial sandstones. Flow depth from bar height approximations and outcrop storey thickness was found to be 2.5 ± 1.0 m, while flood paleodischarge was calculated to be between 20 ± 2 and 37 ± 8 m^3/s. This low discharge and its location within the lower backwater of the FMTZ may explain the complexities of mudstone deposits sequestered in this heterolithic channel deposit. The fluvial style of the meandering channel evolved over time from low sinuosity to moderate sinuosity, interpreted from paleocurrent data and the lack of significant internal erosion within the bar surface architecture, as predicted by the backwater models discussed. The grain size distribution within the channel shows successions of fine upper sandstones with laterally extensive mud drapes and truncated, discontinuous heterolithic beds in the base of the channel, overlain by fine lower sandstones with laterally extensive mud drapes in the upper part of the channel. Mudstone layers and mud drapes are thicker at the base, and thin towards the upper channel.

An improved mudstone dimension model was proposed to include the influence of tidal backwater process. While existing valley models have attempted to predict and explain trunk systems and their associated deposits, a tributary incised valley model still lacks clarification and quantitative constraints. We know that plan view reconstruction can assist in distinguishing trunk from tributary channels, and by association, trunk and tributary valleys. Flow velocity, discharge and slope estimates may also provide insight in distinguishing trunk from tributary fluvial systems within the tidal backwater limit.

Acknowledgements

This paper was written with the generous support of the Susan Cunningham Research Chair at McMaster University, Quantitative Sedimentology Laboratories, with funding from BP, and NSERC.

References

Ahmed, S., Bhattacharya, J.P., Garza, D.E., and Li, Y., 2014, Facies Architecture and Stratigraphic Evolution of A River-Dominated Delta Front, Turonian Ferron Sandstone, Utah, U.S.A: Journal of Sedimentary Research, v. 84, no. 2, p. 97–121, doi: 10.2110/jsr.2014.6.

Akyuz, I., Warny, S., Famubode, O., and Bhattacharya, J.P., 2015, Palynology of the Upper Cretaceous (Turonian) Ferron Sandstone Member, Utah, USA: identification of marine flooding surfaces and Milankovitch cycles in subtropical, ever-wet, paralic to non-marine palaeoenvironments: Palynology, v. 0, no. 0, p. 1–15, doi: 10.1080/01916122.2015.1014525.

Allen, J.R.L., 1965, The sedimentation and palaeogeography of the Old Red Sandstone of

Anglesey, north Wales: Proceedings of the Yorkshire Geological Society, doi: 10.1144/pygs.35.2.139.

Bhattacharya, J.P., Copeland, P., Lawton, T.F., and Holbrook, J., 2016, Estimation of source area, river paleo-discharge, paleoslope, and sediment budgets of linked deep-time depositional systems and implications for hydrocarbon potential: Earth-Science Reviews, v. 153, p. 77–110, doi: 10.1016/j.earscirev.2015.10.013.

Bhattacharya, J.P., and Tye, R.S., 2004, Searching for modern Ferron analogs and application to subsurface interpretation: Regional to Wellbore Analog for Fluvial–Deltaic Reservoir Modeling: the Ferron Sandstone of Utah: American Association of Petroleum Geologists, Studies in Geology 50, p. 39–57.

Bhattacharyya, P., Bhattacharya, J.P., and Khan, S.D., 2015, Paleo-Channel Reconstruction and Grain Size Variability in Fluvial Deposits, Ferron Sandstone, Notom Delta, Hanksville, Utah: Sedimentary Geology, v. 325, p. 17–25, doi: 10.1016/j.sedgeo.2015.05.001.

Biber, K., Khan, S.D., Bhattacharya, J.P., Barton, M.D., and Glennie, C.L., 2017, Quantitative characterization of shales within tidally influenced fluvial valley fill deposits of the Ferron Sandstone, eastern Utah: Implications for hydrocarbon exploration: AAPG Bulletin, v. 101, no. 10, p. 1599–1623, doi: 10.1306/01111715108.

Blum, M.D., 2017, The McMurray Conundrum: CSPG Reservoir, v. 44, no. 2, p. 25–29.

Blum, M., Martin, J., Milliken, K., and Garvin, M., 2013, Paleovalley systems: Insights from Quaternary analogs and experiments: Earth-Science Reviews, v. 116, no. 1, p. 128–169, doi: 10.1016/j.earscirev.2012.09.003.

Bridge, J.S., 2006, Fluvial facies models: recent developments, *in* Posamentier, H.W. and Walker, R.G. eds., Facies Models Revisited: SEPM Special Publication 84, p. 85–168.

Bridge, J.S., and Mackey, S.D., 1993, A theoretical study of fluvial sandstone body dimensions, *in* The Geological Modelling of Hydrocarbon Reservoirs and Outcrop Analogues,.

Bridge, J.S., and Tye, R.S., 2000, Interpreting the dimensions of ancient fluvial channel bars, channels, and channel belts from wireline-logs and cores: AAPG Bulletin, v. 84, no. 8, p. 1205–1228, doi: 10.1306/E4FD4B07-1732-11D7-8645000102C1865D.

Campbell, C.E., 2013, Valley Widening and the Composite Nature of Valley Margin Sequence Boundaries: Evidence from the Neilson Wash Compound Valley Fill, Cretaceous Ferron: University of Houston, 108 p.

Cant, D.J., and Walker, R.G., 1976, Development of a braided-fluvial facies model for the Devonian Battery Point Sandstone, Québec: Canadian Journal of Earth Sciences, v. 13, no. 1, p. 102–119, doi: 10.1139/e76-010.

Chatanantavet, P., Lamb, M.P., and Nittrouer, J. a., 2012, Backwater controls of avulsion location on deltas: Geophysical Research Letters, v. 39, no. 1, p. n/a-n/a, doi:

10.1029/2011GL050197.

Chow, V.T., 1959, Open Channel Hydraulics: McGraw-Hill, New York.

Clifton, H.E., 2006, A reexamination of facies models for clastic shorelines: Facies Models Revisited, , no. 84, p. 293–337, doi: 10.2110/pec.06.84.

Coburn, M.G., Gillespie, J.M., and Coburn, M.G., 2002, performance in a giant oilfield : Kern River field , California A ’: AAPG Bulletin, v. 86, no. 8, p. 1489–1505.

Colombera, L., Shiers, M.N., and Mountney, N.P., 2016, Assessment of Backwater Controls On the Architecture of Distributary-Channel Fills In A Tide-Influenced Coastal-Plain Succession: Campanian Neslen Formation, U.S.A.: Journal of Sedimentary Research, v. 86, no. 5, p. 476–497, doi: 10.2110/jsr.2016.33.

Corbeanu, R.M., Wizevich, M.C., Bhattacharya, J.P., Zeng, X., and McMechan, G. a., 2004, Three-dimensional architecture of ancient lower delta-plain point bars using ground-penetrating radar, Cretaceous Ferron Sandstone, Utah: AAPG Studies in Geology, v. 50, p. 427–449.

Dalrymple, R.W., 2010a, Tidal depositional systems, *in* Dalrymple, R.W. and James, N.P. eds., Facies Models 4, Geological Association of Canada. Geotext, p. 199–208.

Dalrymple, R.W., 2010b, Tidal Depositional Systems, *in* Dalrymple, R.W. and James, N.P. eds., Facies Models 4, p. 201–233.

Dalrymple, R.W., Baker, E.K., Harris, P.T., and Hughes, M.G., 2003, Sedimentology and

Stratigraphy of a Tide-Dominated, Foreland-Basin Delta (Fly River, Papua New Guinea): SEPM Special Publication, v. 76, p. 147–173.

DeCelles, P.G., and Coogan, J.C., 2006, Regional structure and kinematic history of the Sevier fold-and-thrust belt, central Utah: Bulletin of the Geological Society of America, v. 118, no. 7–8, p. 841–864, doi: 10.1130/B25759.1.

Decelles, P.G., Lawton, T.F., and Mitra, G., 1995, Thrust timing, growth of structural culminations, and synorogenic sedimentation in the type Sevier orogenic belt, western United States: Geology, v. 23, no. 8, p. 699–702, doi: 10.1130/0091-7613(1995)023<0699:TTGOSC>2.3.CO;2.

Dietrich, W.E., 1982, Settling Velocity of Natural Particles: Water Resources, v. 18, no. 6, p. 1615–1626.

Durkin, P.R., 2016, The Evolution of Fluvial Meander Belts and Their Product in the Rock Record: University of Calgary.

Durkin, P.R., Hubbard, S.M., Boyd, R.L., and Leckie, D.A., 2015, Stratigraphic expression of intra-point-bar erosion and rotation: Journal of Sedimentary Research, v. 85, p. 1238–1257, doi: 10.2110/jsr.2015.78.

Ericksen, M.C., and Slingerland, R., 1990, Numerical simulations of tidal and wind-driven circulation in the Cretaceous Interior Seaway of North America: Geological Society of America Bulletin, v. 102, no. November, p. 1499–1516.

Ethridge, F.G., Skelly, R.L., and Bristow, C.S., 1999, Avulsion and crevassing in the sandy, braided Niobrara River; complex response to base-level rise and aggradation BT - Fluvial sedimentology VI; proceedings (N. D. Smith & J. Rogers, Eds.): Special Publication of the International Association of Sedimentologists, v. 28, p. 179–191, doi: 10.1002/9781444304213.ch14.

Famubode, O.A., and Bhattacharya, J.P., 2016, Sequence Stratigraphic Analysis of the Youngest Nonmarine Sequence In the Cretaceous Ferron Notom Delta, South Central Utah, U.S.A.: Journal of Sedimentary Research, v. 86, no. 3, p. 168–198, doi: 10.2110/jsr.2016.8.

Fernandes, A.M., Törnqvist, T.E., Straub, K.M., and Mohrig, D., 2016, Connecting the backwater hydraulics of coastal rivers to fluvio-deltaic sedimentology and stratigraphy: Geology, v. 44, no. 12, doi: 10.1130/G37965.1.

Fielding, C.R., 2011, Foreland basin structural growth recorded in the Turonian Ferron Sandstone of the Western Interior Seaway Basin, USA: Geology, v. 39, no. 12, p. 1107–1110, doi: 10.1130/G32411.1.

Fielding, C.R., 2010, Planform and Facies Variability in Asymmetric Deltas: Facies Analysis and Depositional Architecture of the Turonian Ferron Sandstone in the Western Henry Mountains, South-Central Utah, U.S.A.: Journal of Sedimentary Research, v. 80, no. 5, p. 455–479, doi: 10.2110/jsr.2010.047.

Gingras, M.K., and Leckie, D.A., 2017, The Argument for Tidal and Brackish Water Influence in the McMurray Formation Reservoirs: CSPG Reservoir, v. 44, no. 2, p.

21–24.

Hagstrom, C.A., Hubbard, S.M., Leckie, D.A., and Durkin, P.R., 2019, The Effects of Accretion-package Geometry On Lithofacies Distribution in Point-bar Deposits: Journal of Sedimentary Research, v. 89, no. 5, p. 381–398, doi: 10.2110/jsr.2019.23.

Hasiotis, S.T., 2006, Continental trace fossils: SEPM, Tulsa, Oklahoma.

Hill, R.B., 1982, Depositional Environments of the Upper Cretaceous Ferron Sandstone south of Notom, Wayne County: Brinham Young University, Geology Studies, v. 29, p. 59–83.

Holbrook, J., and Wanas, H., 2014, A Fulcrum Approach To Assessing Source-To-Sink Mass Balance Using Channel Paleohydrologic Paramaters Derivable From Common Fluvial Data Sets With An Example From the Cretaceous of Egypt: Journal of Sedimentary Research, v. 84, no. 5, p. 349–372, doi: 10.2110/jsr.2014.29.

Horner, S.C., Hubbard, S.M., Martin, H.K., and Hagstrom, C.A., 2019a, Reconstructing basin-scale drainage dynamics with regional subsurface mapping and channel-bar scaling, Aptian, Western Canada Foreland Basin: Sedimentary Geology, v. 385, p. 26–44, doi: 10.1016/j.sedgeo.2019.03.012.

Horner, S.C., Hubbard, S.M., Martin, H.K., Hagstrom, C.A., and Leckie, D.A., 2019b, The impact of Aptian glacio-eustasy on the stratigraphic architecture of the Athabasca Oil Sands, Alberta, Canada: Sedimentology, p. 1600–1642, doi: 10.1111/sed.12545.

Jablonski, B.V.J., and Dalrymple, R.W., 2016, Recognition of strong seasonality and climatic cyclicity in an ancient, fluvially dominated, tidally influenced point bar: Middle McMurray Formation, Lower Steepbank River, north-eastern Alberta, Canada: Sedimentology, v. 63, no. 3, p. 552–585, doi: 10.1111/sed.12228.

Jackson, M.D., Yoshida, S., Muggeridge, A.H., and Johnson, H.D., 2005, Three-dimensional reservoir characterization and flow simulation of heterolithic tidal sandstones: AAPG Bulletin, v. 89, no. 4, p. 507–528, doi: 10.1306/11230404036.

Jones, B.G., Woodroffe, C.D., and Martin, G.R., 2003, Deltas in the Gulf of Carpentaria, Australia: Forms, Processes and Products: Tropical Deltas of Southeast Asia—Sedimentology, Stratigraphy, and Petroleum Geology, SEPM Spec Pubs 76, v. 76, p. 21–43.

Kestin, J., Sokolov, M., and Wakeham, W. a, 1978, viscosity of liquid water in the range of -8C to 150C: J. Phys. Chem., v. 7, no. 3, p. 1978, doi: 10.1063/1.555581.

Kimmerle, S., and Bhattacharya, J.P., 2018, Facies, Backwater Limits, and Paleohydraulic Analysis of Rivers in a Forced- Regressive, Compound Incised Valley, Cretaceous Ferron Sandstone, Utah, U.S.a.: , no. February, p. 177–200, doi: 10.2110/jsr.2018.5.

Kimmerle, S., and Bhattacharya, J.P., 2017, Facies, Backwater Limits, and Paleohydraulic Analysis within a Forced-Regressive, Compound Incised Valley, Cretaceous Ferron Sandstone, Utah: (In Press),.

Kimmerle, S., Kynaston, D., and Bhattacharya, J.P., 2016, A long-lived compound incised mega-valley in the Cretaceous Ferron Sandstone, Utah [Abstract], *in* American Association of Petroleum Geologists, Annual Convention, Calgary, Canada,.

Kvale, E.P., and Archer, A.W., 2007, Paleovalley fills: Trunk vs. tributary: AAPG Bulletin, v. 91, no. 6, p. 809–821, doi: 10.1306/11060606022.

Lamb, M.P., and Mohrig, D., 2009, Do hyperpycnal-fl ow deposits record river-fl ood dynamics? Geology, v. 37, no. 12, p. 1067–1070, doi: 10.1130/G30286A.1.

Larue, D.K., and Hovadik, J., 2006, Connectivity of channelized reservoirs: a modelling approach: Petroleum Geoscience, v. 12, no. 4, p. 291–308, doi: 10.1144/1354-079306-699.

Leclair, S.F., and Bridge, J.S., 2001, Quantitative Interpretation of Sedimentary Structures Formed By River Dunes: Journal of Sedimentary Petrology, v. 71, no. 5, p. 713–716.

Leeder, M.R., 1973, Fluviatile fining-upwards cycles and the magnitude of palaeochannels: Geological Magazine, doi: 10.1017/S0016756800036098.

Lefavour, G., and Alsdorf, D., 2005, Water slope and discharge in the Amazon River estimated using the shuttle radar topography mission digital elevation model: Geophysical Research Letters, v. 32, no. July, p. 1–5, doi: 10.1029/2005GL023836.

Li, Y., and Bhattacharya, J.P., 2013, Facies-Architecture Study of A Stepped, Forced

Regressvie Compound Incised Valley In the Ferron Notom Delta, Southern Central Utah, U.S.A: Journal of Sedimentary Research, v. 83, no. 3, p. 206–225, doi: 10.2110/jsr.2013.19.

Li, Y., and Bhattacharya, J., 2014, Facies architecture of asymmetrical branching distributary channels: Cretaceous Ferron Sandstone, Utah, USA: Sedimentology, v. 61, no. 5, p. 1452–1483, doi: 10.1111/sed.12104.

Li, W., Bhattacharya, J.P., and Campbell, C., 2010, Temporal Evolution of Fluvial Style in a Compound Incised-Valley Fill, Ferron “Notom Delta”, Henry Mountains Region, Utah (U.S.A.): Journal of Sedimentary Research, v. 80, no. 1994, p. 529–549, doi: 10.2110/jsr.2010.053.

Li, W., Bhattacharya, J., and Zhu, Y., 2011a, Architecture of a forced regressive systems tract in the Turonian Ferron “Notom Delta”, southern Utah, U.S.A.: Marine and Petroleum Geology, v. 28, no. 8, p. 1517–1529, doi: 10.1016/j.marpetgeo.2011.05.004.

Li, W., Bhattacharya, J.P., Zhu, Y., Garza, D., and Blankenship, E., 2011b, Evaluating delta asymmetry using three-dimensional facies architecture and ichnological analysis, Ferron “Notom Delta”, Capital Reef, Utah, USA: Sedimentology, v. 58, no. 2, p. 478–507, doi: 10.1111/j.1365-3091.2010.01172.x.

Lynds, R.M., and Hajek, E. a., 2006, Conceptual model for predicting mudstone dimensions in sandy braided-river reservoirs: AAPG Bulletin, v. 90, no. 8, p. 1273–

1288, doi: 10.1306/03080605051.

Lynds, R.M., Mohrig, D., Hajek, E.A., Heller, P.L., State, W., Survey, G., and Box, P.O., 2014, Paleoslope Reconstruction in Sandy Suspended-Load-Dominant Rivers: Journal of Sedimentary Research, v. 84, p. 825–836, doi: http://dx.doi.org/10.2110/jsr.2014.60.

Mackay, D.A., and Dalrymple, R.W., 2011, Dynamic Mud Deposition in a Tidal Environment : The record of fluid-mud deposition in the Cretaceous Bluesky Formation , Alberta , Canada: Journal of sedimentary Research, v. 81, p. 901–920, doi: 10.2110/jsr.2011.74.

Martin, H.K., Hubbard, S.M., Hagstrom, C.A., Horner, S.C., and Durkin, P.R., 2019, Planform Recognition and Implications of a Cretaceous-age Continental-scale River Avulsion Node in the Western Interior Basin, Alberta, Canada: Journal of Sedimentary Research, v. 89, no. 7, p. 610–628, doi: 10.2110/jsr.2019.37.

Martinius, A.W., Ringrose, P.S., Brostrom, C., Elfenbein, C., Naess, A., and Ringas, J.E., 2005, Reservoir challenges of heterolithic tidal sandstone reservoirs in the Halten Terrace, mid-Norway: Petroleum Geoscience, v. 11, no. 1, p. 3–16, doi: 10.1144/1354-079304-629.

Massart, B.Y.G., Jackson, M.D., Hampson, G.J., Johnson, H.D., Legler, B., and Jackson, C.A.L., 2016, Effective flow properties of heterolithic, cross-bedded tidal sandstones: Part 1. Surfacebased modeling: AAPG Bulletin, v. 100, no. 5, p. 697–

721, doi: 10.1306/02011614221.

Miall, A.D., 1977, A review of the braided-river depositional environment: Earth-Science Reviews, v. 13, no. 1, p. 1–62, doi: 10.1016/0012-8252(77)90055-1.

Miall, A.D., 2010, Alluvial Deposits, *in* Dalrymple, R.W. and James, N.P. eds., Facies Models, 4th Edition, Geological Association of Canada, p. 105–137.

Miall, A.N.D.R.E.W.D., 1985, Architectural-Element Analysis : A New Method of Facies Analysis Applied to Fluvial Deposits: Earth Science Reviews, v. 22, p. 261–308.

Miall, A.D., 1994, Reconstructing Fluvial Macroform Architecture from Two-Dimensional Outcrops: Examples from the Castlegate Sandstone, Book Cliffs, Utah: Journal of Sedimentary Research, v. Vol. 64B, no. 1972, p. 146–158, doi: 10.1306/D4267F78-2B26-11D7-8648000102C1865D.

Miall, A.D., 1988, Reservoir Heterogeneities in Fluvial Sandstones: Lesson From Outcrop Studies.: American Association of Petroleum Geologists Bulletin, v. 72, no. 6, p. 682–697, doi: 10.1306/703C8F01-1707-11D7-8645000102C1865D.

Mossop, G.D., and Flach, P.D., 1983, Deep channel sedimentation in the Lower Cretaceous McMurray Formation, Athabasca Oil Sands, Alberta: Sedimentology, v. 30, no. 4, p. 493–509, doi: 10.1111/j.1365-3091.1983.tb00688.x.

Mulder, T., Syvitski, J.P.M., Migeon, S., Faugères, J.C., and Savoye, B., 2003, Marine hyperpycnal flows: Initiation, behaviorand related deposits. A review: Marine and Petroleum Geology, v. 20, no. 6–8, p. 861–882, doi:

10.1016/j.marpetgeo.2003.01.003.

Musial, G., Reynaud, J.Y., Gingras, M.K., Féniès, H., Labourdette, R., and Parize, O., 2012, Subsurface and outcrop characterization of large tidally influenced point bars of the Cretaceous McMurray Formation (Alberta, Canada): Sedimentary Geology, v. 279, p. 156–172, doi: 10.1016/j.sedgeo.2011.04.020.

Nardin, T., Feldman, H.R., and Carter, B.J., 2013, Stratigraphic architecture of a large-scale point-bar complex in the McMurray Formation: Syncrude's Mildred Lake Mine, Alberta, Canada: Heavy-oil and oil-sand petroleum systems in Alberta and beyond: AAPG Studies in Geology 64, p. 273–311, doi: 10.1306/13371583St643555.

Nieminski, N.M., and Graham, S.A., 2017, Modeling Stratigraphic Architecture Using Small Unmanned Aerial Vehicles and Photogrammetry: Examples From the Miocene East Coast Basin, New Zealand: Journal of Sedimentary Research, v. 87, no. 2, p. 126–132, doi: 10.2110/jsr.2017.5.

Nordahl, K., Ringrose, P.S., and Wen, R., 2005, Petrophysical characterization of a heterolithic tidal reservoir interval using a process-based modelling tool: Petroleum Geoscience, v. 11, no. 1, p. 17–28, doi: 10.1144/1354-079303-613.

Novakovic, D., White, C.D., Corbeanu, R.M., Hammon, W.S., Bhattacharya, J.P., and McMechan, G.A., 2002, Hydraulic effects of shales in fluvial-deltaic deposits: Ground-penetrating radar, outcrop observations, geostatistics, and three-dimensional flow modeling for the Ferron Sandstone, Utah: Mathematical Geology, v. 34, no. 7, p. 857–893, doi: 10.1023/A:1020980711937.

Olariu, C., and Bhattacharya, J.P., 2006, Terminal Distributary Channels and Delta Front Architecture of River-Dominated Delta Systems: Journal of Sedimentary Research, v. 76, no. 2, p. 212–233, doi: 10.2110/jsr.2006.026.

Paola, C., and Mohrig, D., 1996, Palaeohydraulics revisited: Palaeoslope estimation in coarse-grained braided rivers: Basin Research, v. 8, no. 3, p. 243–254, doi: 10.1046/j.1365-2117.1996.00253.x.

Parker, G., 2008, Transport of Gravel and Sediment Mixtures, Chapter 3, Sedimentation Engineering (M. H. Garcia, Ed.): American Society of Civil Engineers, Manuals and Reports on Engineering, Practice.

Posamentier, H.W., 2001, Lowstand alluvial bypass systems : Incised vs . unincised: AAPG Bulletin, v. 10, no. 10, p. 1771–1793.

Pranter, M.J., Ellison, A.I., Cole, R.D., and Patterson, P.E., 2007, Analysis and modeling of intermediate-scale reservoir heterogeneity based on a fluvial point-bar outcrop analog, Williams Fork Formation, Piceance Basin, Colorado: AAPG Bulletin, v. 91, no. 7, p. 1025–1051, doi: 10.1306/02010706102.

Reijenstein, H.M., Posamentier, H.W., and Bhattacharya, J.P., 2011, Seismic geomorphobgy and high-resolution seismic stratigraphy of inner-shelf fluvial, estuarine, deltaic, and marine sequences, Gulf of Thailand: AAPG Bulletin, v. 95, no. 11, p. 1959–1990, doi: 10.1306/03151110134.

Van Rijn, L.C., 1984, Sediment transport, Part II: Suspended load transport: Journal of Hydraulic Engineering, v. 110, p. 1613–1641.

Rubin, D.M., and McCulloch, D.S., 1980, Single and superimposed bedforms: a synthesis of San Francisco Bay and flume observations: Sedimentary Geology, v. 26, no. 1–3, p. 207–231, doi: 10.1016/0037-0738(80)90012-3.

Smith, D.G., Hubbard, S.M., Leckie, D.A., and Fustic, M., 2009, Counter point bar deposits: Lithofacies and reservoir significance in the meandering modern peace river and ancient McMurray formation, Alberta, Canada: Sedimentology, v. 56, no. 6, p. 1655–1669, doi: 10.1111/j.1365-3091.2009.01050.x.

Somme, T.O., Helland-hansen, W., Martinsen, O.J., and Thurmond, J.B., 2009, Relationships between morphological and sedimentological parameters in source-to-sink systems: A basis for predicting semi-quantitative characteristics in subsurface systems: Basin Research, v. 21, no. 4, p. 361–387, doi: 10.1111/j.1365-2117.2009.00397.x.

Stouthamer, E., and Berendsen, H.J. a., 2001, Avulsion Frequency, Avulsion Duration, and Interavulsion Period of Holocene Channel Belts in the Rhine-Meuse Delta, The Netherlands: Journal of Sedimentary Research, v. 71, no. 4, p. 589–598, doi: 10.1306/112100710589.

Taylor, A.M., and Goldring, R., 1993, Description and analysis of bioturbation and ichnofabric: Journal of the Geological Society, v. 150, no. 1, p. 141–148, doi: 10.1144/gsjgs.150.1.0141.

Thomas, R.G., Smith, D.G., Wood, J.M., Visser, M.J., Calverley-Range, E.A., and Koster, E.H., 1987, Inclined heterolithic stratification - terminology, description, interpretation and significance: Sedimentary Geology, v. 53, no. September, p. 123–179, doi: 10.1016/S0037-0738(87)80006-4.

Toonen, W.H.J., Kleinhans, M.G., and Cohen, K.M., 2012, Sedimentary architecture of abandoned channel fills: Earth Surface Processes and Landforms, v. 37, no. 4, p. 459–472, doi: 10.1002/esp.3189.

Tornqvist, T.E., and Bridge, J.S., 2002, Spatial variation of overbank aggradation rate and its influence on avulsion frequency: Sedimentology, v. 49, no. 5, p. 891–905.

Ullah, M.S., Bhattacharya, J.P., and Dupre, W.R., 2015, Confluence Scours Versus Incised Valleys: Examples From the Cretaceous Ferron Notom Delta, Southeastern Utah, U.S.A: Journal of Sedimentary Research, v. 85, no. 5, p. 445–458, doi: 10.2110/jsr.2015.34.

Uresk, J., 1978, Sedimentary Environment of the Cretaceous Ferron Sandstone near Cainville, Utah: Brinham Young University, Geology Studies, v. 26, p. 81–100.

Vakarelov, B.K., Ainsworth, R.B., and MacEachern, J.A., 2012, Recognition of wave-dominated, tide-influenced shoreline systems in the rock record: Variations from a microtidal shoreline model: Sedimentary Geology, v. 279, p. 23–41, doi:

10.1016/j.sedgeo.2011.03.004.

Vanoni, V. a, and Brooks, N.H., 1957, Laboratory Studies of the Roughness and Suspended Load of Alluvial Streams: California Institute of Technology, v. 112, no. 1, p. 130.

Visser, M.J., 1980, Neap-spring cycles reflected in Holocene subtidal large-scale bedform deposits : A preliminary note: Geology, v. 8, no. 11, p. 543–546.

Wang, J., and Bhattacharya, J.P., 2018, Plan-View Reconstruction of Amalgamated Meander Belts, Cretaceous Ferron Sandstone, Notom Delta , South-Central Utah, U . S . A .: Journal of Sedimentary Research, v. 88, no. 1, p. 58–74.

Wilkerson, G. V., and Parker, G., 2011, Physical Basis for Quasi-Universal Relationships Describing Bankfull Hydraulic Geometry of Sand-Bed Rivers: Journal of Hydraulic Engineering, v. 137, no. 7, p. 739–753, doi: 10.1061/(ASCE)HY.1943-7900.0000352.

Willis, B.J., 1998, Permeability structure of a compound valley fill in the cretaceous fall river formation of South Dakota: AAPG Bulletin, v. 82, no. 2, p. 206–227, doi: 10.1306/1D9BC3D1-172D-11D7-8645000102C1865D.

Willis, G.C., 1999, The Utah thrust system - an overview: Geology of Northern Utah and Vicinity, v. 27, p. 1–9.

Willis, B.J., and Tang, H., 2010, Three-Dimensional Connectivity of Point-Bar Deposits: Journal of Sedimentary Research, v. 80, no. 5, p. 440–454, doi:

10.2110/jsr.2010.046.

Wu, C., and Bhattacharya, J.P., 2015, Paleohydrology and 3D Facies Architecture of Ancient Point Bars , Ferron Sandstone, Notom Delta, South-central Utah: Journal of Sedimentary Research, , no. March 2016, p. 399–418, doi: 10.2110/jsr.2015.29.

Wu, C., Ullah, M.S., Lu, J., and Bhattacharya, J.P., 2016, Formation of point bars through rising and falling flood stages: Evidence from bar morphology, sediment transport and bed shear stress: Sedimentology, v. 63, p. 1458–1473, doi: 10.1111/sed.12269.

Zaitlin, B.A., Dalrymple, R.W., and Boyd, R., 1994, The Stratigraphic Organization of Incised-Valley Systems Associated with Relative Sea-Level Change: SEPM Special Publication, v. 51, no. 51, p. 45–60, doi: 10.2110/pec.94.12.0045.

Zavala, C., Ponce, J.J., Arcuri, M., Drittanti, D., Freije, H., and Asensio, M., 2006, Ancient Lacustrine Hyperpycnites: A Depositional Model from a Case Study in the Rayoso Formation (Cretaceous) of West-Central Argentina: Journal of Sedimentary Research, v. 76, no. 1, p. 41–59, doi: 10.2110/jsr.2006.12.

Zhu, Y., Bhattacharya, J.P., Li, W., Lapen, T.J., Jicha, B.R., and Singer, B.S., 2012, Milankovitch-scale sequence stratigraphy and stepped forced regressions of the Turonian Ferron Notom Deltaic Complex, south-central Utah, U.S.A: Journal of Sedimentary Research, v. 82, no. 9, p. 723–746, doi: 10.2110/jsr.2012.63.

CHAPTER 3

FACIES ARCHITECTURE AND TIME STRATIGRAPHIC RELATIONSHIPS OF A CONFINED TRUNK-TRIBUTARY VALLEY FILL AND UNCONFINED FLUVIAL SYSTEM WITHIN THE BACKWATER OF THE TURONIAN FERRON-NOTOM DELTA, UTAH

Abstract

We challenge standard sequence stratigraphic valley models by documenting a tidally-incised, mudstone prone tributary valley fill within the upper backwater limit of the Turonian Notom Delta in the Ferron Sandstone Member, Utah. High resolution 3D photogrammetry models were used to correlate 32 measured sections over a 1 km^2 area of a 20 m deep valley. A GPS survey and GIS geostatistical tools were used to restore the morphology of the trunk-tributary valley floor revealing a surface of tidal ravinement and tidal drainage morphology similar to that found in Pleistocene sediments in the Gulf of Thailand, and modern tidal settings found in northern Australia, and the Memramcook tributary to the Bay of Fundy.

Age dating of bentonite beds confirm previous assumptions of Milankovitch scale sequence duration (15 ± 5 ka) of the youngest sequence in the Ferron-Notom stratigraphy. New methods in $^{40}Ar/^{39}Ar$ dating of sanidine crystals allow re-evaluation of depositional rates and timing of 32 fluvial aggradation cycles and 9 fluvial aggradation cycle-sets bounded by immature paleosols within this fluvial sequence. Chronometric analysis shows that Milankovitch cycles cannot account for the internal complexity of this fluvial

stratigraphy and indicate autogenic control of fluvial aggradation cycle-sets. Fluvial aggradation cycles mapped in outcrop are correlated over 10s to 100s of meters, consistent with lateral floodplain dimensions of the Amazon basin, and are likely autogenically controlled, while climate driven FAC-sets are correlated for up to 10 km along depositional strike.

3.1 Introduction

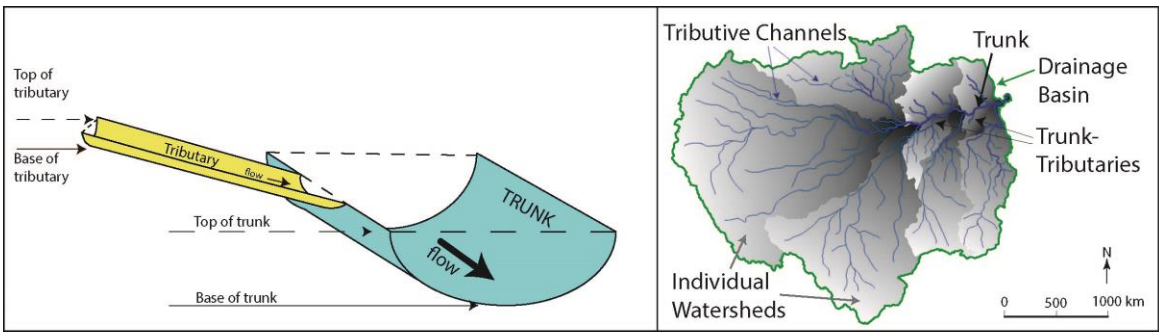

Figure 3.1: Tributary valley concept. Left) Conceptual architecture of a trunk tributary valley or channel feeding an associated trunk. Right) Plan view of tributary drainages in the Amazon drainage basin composed of multiple watersheds (*modified from:* Beighley and Gummadi, 2011). Trunk-tributaries are considered the smaller orthogonal drainages that contribute directly to the trunk stream.

Most incised trunk valleys are flanked by tributary drainages that feed them (Posamentier, 2001; Kvale and Archer, 2007; Reijenstein et al., 2011) and can represent volumetrically significant portions of incised valley fills (Fig. 3.1); however the facies architecture and timing of these valleys are not well documented. The existence of tributary valleys, whose drainage is perpendicular to deeply incised trunk valleys is well documented (Zaitlin et al., 1994; Posamentier, 2001; Ardies et al., 2002; Boyd et al., 2006; Reijenstein et al., 2011; Holbrook and Bhattacharya, 2012; Mattheus and Rodriguez, 2014); and is possibly more prevalent in valley networks during lowstand when wider coastal plains offer a greater potential for drainage convergence by channel capture (Blum and Hattier-womack, 2009; Blum et al., 2013). Given that tributary valleys are ubiquitous components of incised valleys, (Fig. 3.2) they may represent an overlooked component of incised valley petroleum reservoirs (Posamentier, 2001; Ardies et al., 2002; Reijenstein et al., 2011), offering the potential as stratigraphic traps, as in the Lower Cretaceous Chin Coulee and Taber Southeast fields of Alberta Canada (Reel and Campbell, 1985).

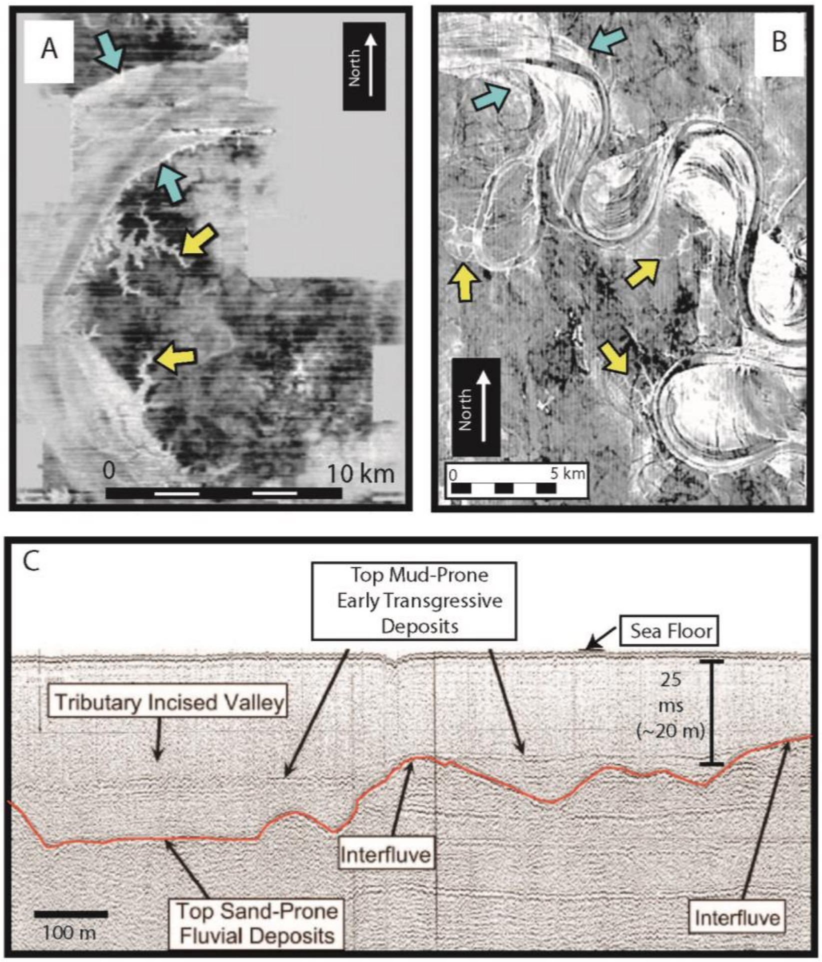

Figure 3.2: Tributary valleys in seismic. A) Seismic time slice (36 ms) of Miocene to Pleistocene sediments on the Java Shelf, northwest offshore Java. Trunk valleys (blue arrows) are interpreted as incised based on the presence of orthogonal, deeply etched tributary valleys (yellow arrows) with dendric drainage patterns (Posamentier, 2001). B) Seismic time slice (160 ms) of Gulf of Thailand continental shelf fluvial deposits. Image shows the differences between the scale and morphology of within valley channel belts (blue arrows) and the associated inced tributary valleys (yellow arrows) (modified from Reijenstein et al., 2011). C) Boomer profile across a tributary valley (Area shown in A) with similar depth and extent to this study (Posamentier, 2001).

The purpose of this study is to investigate a mudstone dominated trunk-tributary valley fill that feeds into a compound trunk valley in the Ferron Sandstone (Li et al., 2010; Li and Bhattacharya, 2013; Ullah et al., 2015; Famubode and Bhattacharya, 2016; Kimmerle and Bhattacharya, 2018) and compare the valley fill floodplain deposits with the unconfined fluvial deposits outside of the valley in a framework of facies analysis and fluvial aggradation cycles. Save for a few studies (Ardies et al., 2002; Kvale and Archer, 2007; Akyuz et al., 2015; Famubode and Bhattacharya, 2016), the nature of tributary fills and their stratigraphic organization remains under–represented in the incised valley literature. Historical models for valley fills assume a valley is cut by fluvial processes and filled first with coarse grained braided fluvial deposits and tidal-fluvial sandstone deposits in late stage valley fill (Shanley and McCabe, 1994; Willis, 1998) or are dominantly estuarine in nature (Dalrymple et al., 2003b). Our study focusses on a floodplain dominated tributary valley fill, interpreted to be in the lower backwater based on previous regional work of Kimmerle and Bhattacharya (2018), that shows convincing evidence of tidal and possibly marine influence.

The lateral margins of trunk valleys, commonly depicted as straight lines (Willis, 1997) because of lack of detail or control, do not convey the complex morphology of a tributary valley confluences that create highly irregular margins. Stratigraphic valleys, which represent the growth of valleys over time, may include rugose margins that reflect different aged terraces formed at different stages, as well as erosional cuts formed at different times resulting in highly complex lateral geometry. Valley floors may also exhibit topographic variations with locally high interflueves forming a surface that is far more complex than an individual channel. The advantage afforded by the outcrops in this study allows us to map extensive continuous lateral exposures in parallel and orthogonal transects across an area similar in size to that of the valley itself, and allows us to document the three-dimensional complexity.

In addition to the basal and lateral complexity, we examine the transition of in- to out-of-valley fluvial successions and revised high resolution chronometric dating to evaluate the time stratigraphic significance of the sequence in order to evaluate the importance of auto versus allogenic controls of valley confined and unconfined fluvial systems. Previous sequence stratigraphic studies suggest a prolonged forced regression, possibly enhanced by tectonic uplift, are the dominant control of valley formation in this system (Fielding, 2011; Li et al., 2011a; Zhu et al., 2012). Superimposed on this are higher-frequency fluvial aggradation cycles that appear to be well below Milankovitch scale frequency, and are either autogenic in nature or allogenic, reflecting a climate cycle of a few thousand years. In order to evaluate allo vs autogenic cyclicity, we evaluate the timescales involved and lateral correlative continuity. Autogenic processes, such as river avulsion and delta lobe switching, tend to be on the scale of 1000s of years for continental scale rivers such as the Mississippi (Aslan et al., 2005), and a few 100s of years for smaller scale rivers (Stouthamer and Berendsen, 2001; Singerland and Smith, 2004) such as the Rhine; and lateral correlation of fluvial cyclicity should extend only as far at the potential deposition of a single river if autogenically controlled.

Distinct lithological differences distinguish Early Pensylvanian sandstone prone trunk valley fills from their mudstone filled tributary valley fills in the Illinois Basin (Kvale and Archer, 2007), hypothesised to be a result of damming of the drainage junction. Our study looks to find similar facies in the Ferron tributary valley fills that may suggest a similar process, and to distinguish this process from backwater effects. Within the FMTZ is the reach of the fluvial system where the base of the channel is below the water surface of the standing body of water at its terminus. This reach, known as the backwater limit (L_b) is defined as the channel depth (h_c) divided by the slope of the channel, (S) (Paola and Mohrig, 1996; Blum et al., 2013), and is susceptible to tidal effects. This limit is further divided in to the upper and lower backwater, expressed as ($0.5L_b$) (Chatanantavet et al., 2012), where the lower backwater inhibits lateral migration and promotes aggradation of fluvial deposits (Blum et al., 2013; Fernandes et al., 2016). Consequently channel belt deposits tend to narrow within the backwater, relative to their distance from the shoreline.

High resolution mapping and facies analysis of a compound incised coastal-plain valley in the Turonian Ferron sandstone documents the deposits of a 7 m deep single thread meandering trunk channel within a 28 m deep valley fill (Kimmerle and Bhattacharya, 2018). This trunk valley shows evidence of three cut and fill cycles over an estimated 60 ka period and has been interpreted to be deposited within 20 km of a 3 to 25 km backwater limit. The range of this uncertainty reflects the local variation of grainsizes in these deposits which are used to calculate slope values, and thereby the backwater length. This calculated estimate of shoreline proximity confirms observations of tidal indicators such as double mud drapes, marine trace fossils and *Teredolites*. Valley fill deposits within 100s of meters of the mapped trunk valley margin reveal paleocurrent and paleohydraulic estimated channel discharges consistent with a tributary to this documented trunk. This study documents the nature and organization of a tidally-influenced tributary valley fill within the backwater limit of the Notom Delta complex of the Ferron Sandstone Member, which forms part of the Upper Cretaceous Mancos Shale

Formation in central Utah, and represents an analogue for tributary valley reservoirs with recognizable tidal signatures.

3.2 Geological Setting, Recent Work, and Study Area

The Mancos Shale Formation was deposited in the mature foredeep basin of the Western Interior Seaway (DeCelles et al., 1995; Willis, 1999; DeCelles and Coogan, 2006) (Fig. 3.3A). Three clastic deltaic wedges comprise the Turonian Ferron Sandstone Member of the Mancos Shale; including the Last Chance, Vernal, and Notom deltas (Uresk, 1978; Hill, 1982; Bhattacharya and Tye, 2004; Corbeanu et al., 2004; Fielding, 2011) (Fig. 3.3B).The Ferron gradationally overlies the Tununk Shale Member, and is sharply bounded above by the Bluegate Shale Member. The Notom Delta is composed of 6 sequences, which are further divided into 18 parasequence sets and 42 parasequences (Li et al., 2011a; Zhu et al., 2012). The lower four sequences are composed of shoreface and heterolithic deltaic facies, while the upper two sequences show incision of lowstand compound incised valleys truncating underlying deltaic and shoreface deposits (Li et al., 2010; Li and Bhattacharya, 2013; Famubode and Bhattacharya, 2016). The youngest incised valley is filled with terrace deposits forming three distinct stages; from youngest to oldest, so named V1, V2, and V3 (Li and Bhattacharya, 2013).

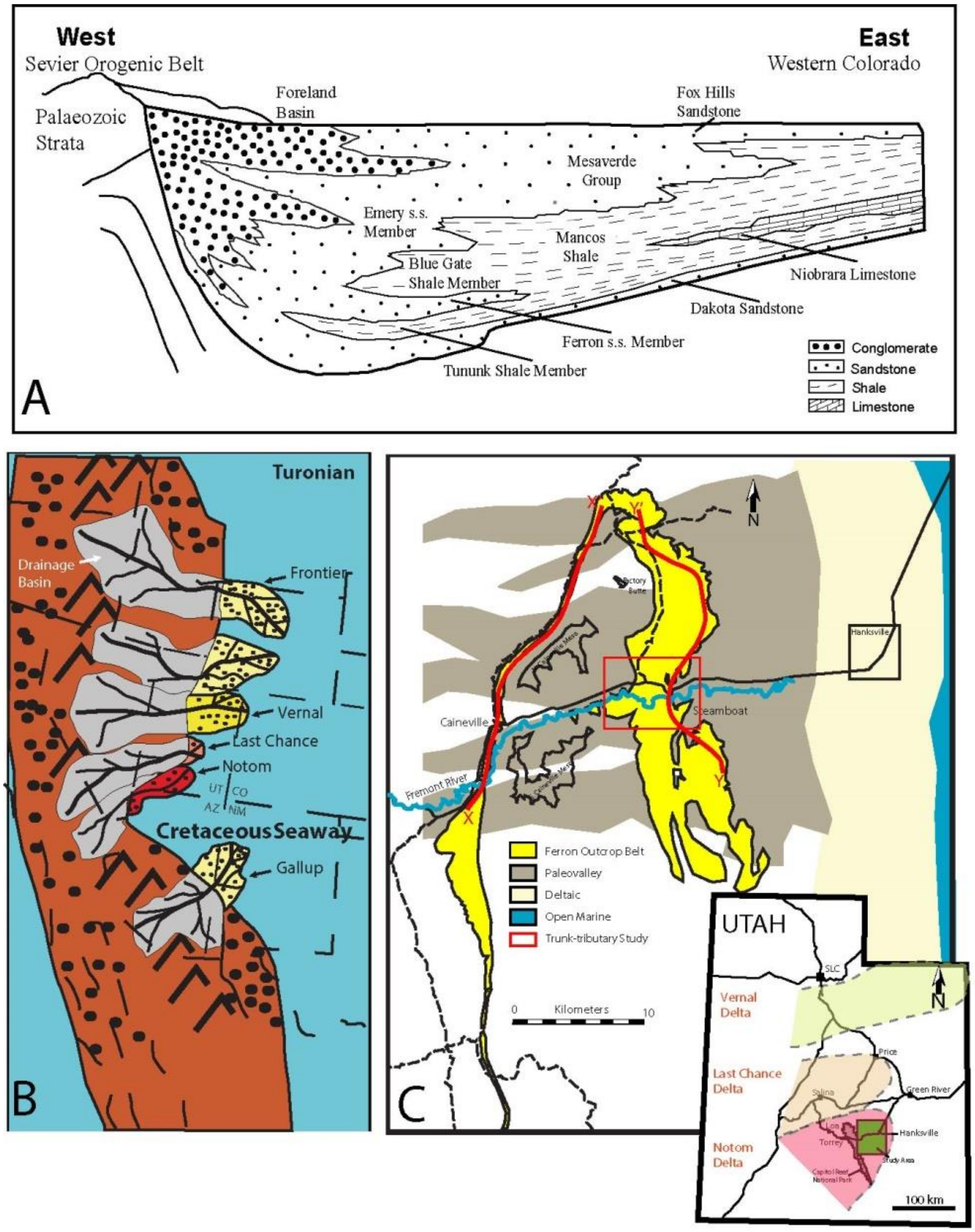

Figure 3.3: Regional setting. A) Regional stratigraphic cross section of the Mancos Shale showing the relative location of the Ferron Sandstone Member, the overlying Bluegate Shale Member, and the underlying Tununk Shale (*Modified from:* Armstrong, 1968). B) The Western Interior Seaway and location of the Notom Delta relative to present day state boundaries *(modified from*: Bhattacharya and Tye, 2004; *Based on:* Gardiner, 2012). C)The study area within Utah (Kimmerle et al., 2016). Cross section locations (Fig. 3.4) are indicated by red lines. The red box indicates the study area satellite photo location (Fig. 3.5).

Recent studies (Li et al., 2010; Fielding, 2011; Zhu et al., 2012) have mapped the extent of the Ferron Notom Delta (Fig. 3.3C) across regional strike and dip cross-sections (Fig. 3.4), indicating several sequence boundaries. The deposit investigated here is stratigraphically located within the youngest sequence of the Notom delta (Li et al., 2010) and is in the uppermost fill of a valley deposit that incises Parasequence 4 of Sequence 2. Our study area (Fig. 3.5) lies directly south of Factory Butte near Hanksville, Utah; and north of the Freemont River. The valley deposit is well exposed and shows multiple stacked channel deposits. Paleocurrent directions (Fig. 3.6) suggest it is a tributary to the main trunk valley system mapped in previous studies (Kimmerle and Bhattacharya, 2018).

The study outcrop comprises marine sandstones from the previous highstand(Li et al., 2010; Zhu et al., 2012), the erosional boundary of the valley incision, confined valley fill deposits, the uppermost deposits of the last Ferron sandstone highstand and the overlying Bluegate Shale Member marked by a major surface of non-deposition. Within the valley deposits and overlying highstand are bentonite deposits that were sampled to test depositional rates and assumptions of Milankovitch-scale frequency within the non-marine stratigraphy. The valley base was surveyed and mapped to show tributary valley morphology and 32 measured sections were made of the kilometer wide valley fill, along with drone photography of the outcrop exposures.

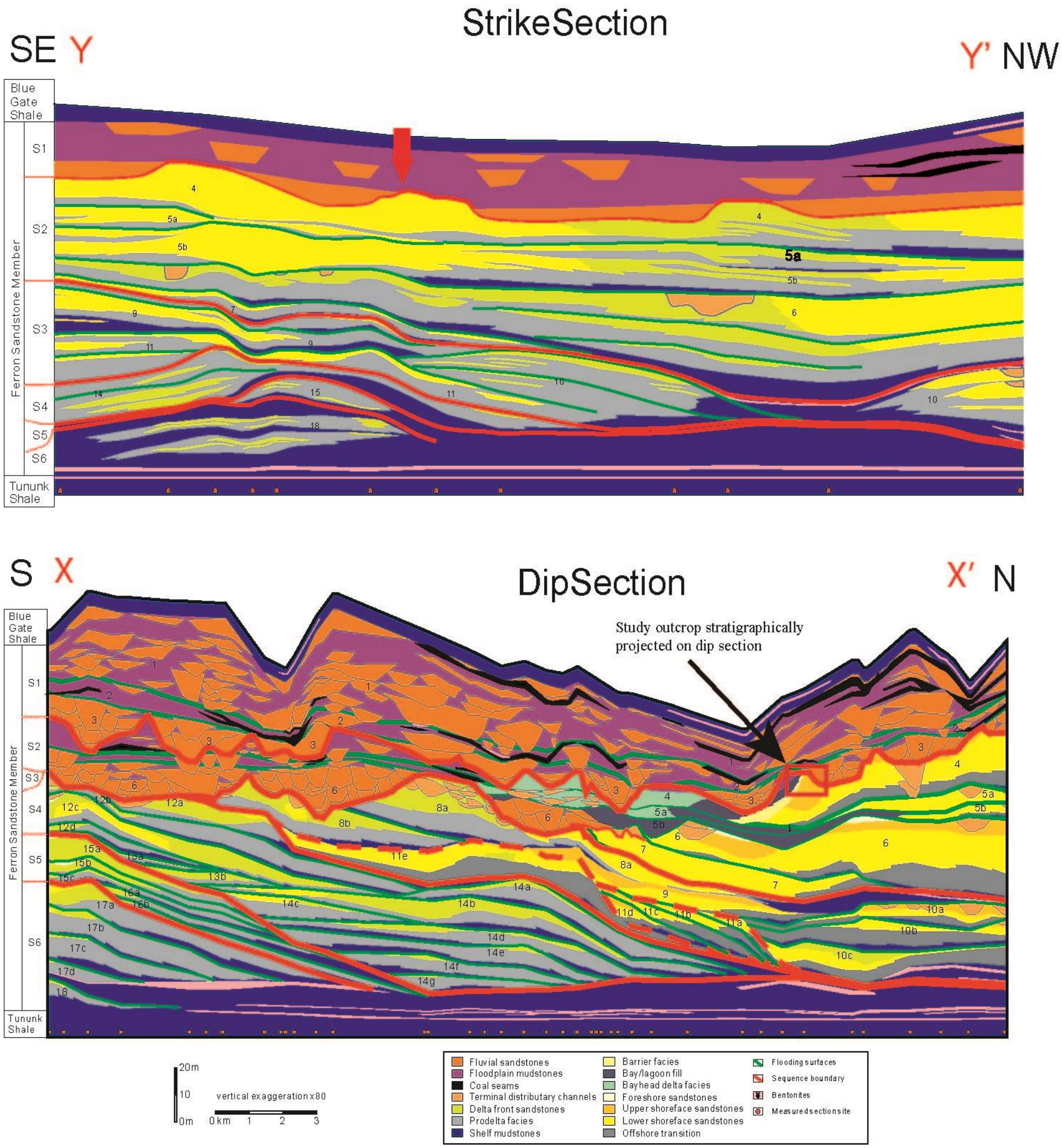

Figure 3.4: Regional correlation. *Above*) Strike cross section Y-Y' in figure 3, showing the study interval. Approximate location of study outcrop is indicated by the red arrow. Focus is on fluvial strata in sequence 1 *(modified from*: Zhu et al, 2012). *Below*) Dip oriented cross section X-X' in figure 3, showing the study interval *(modified from*: Zhu et al, 2012 and Richards, 2018).

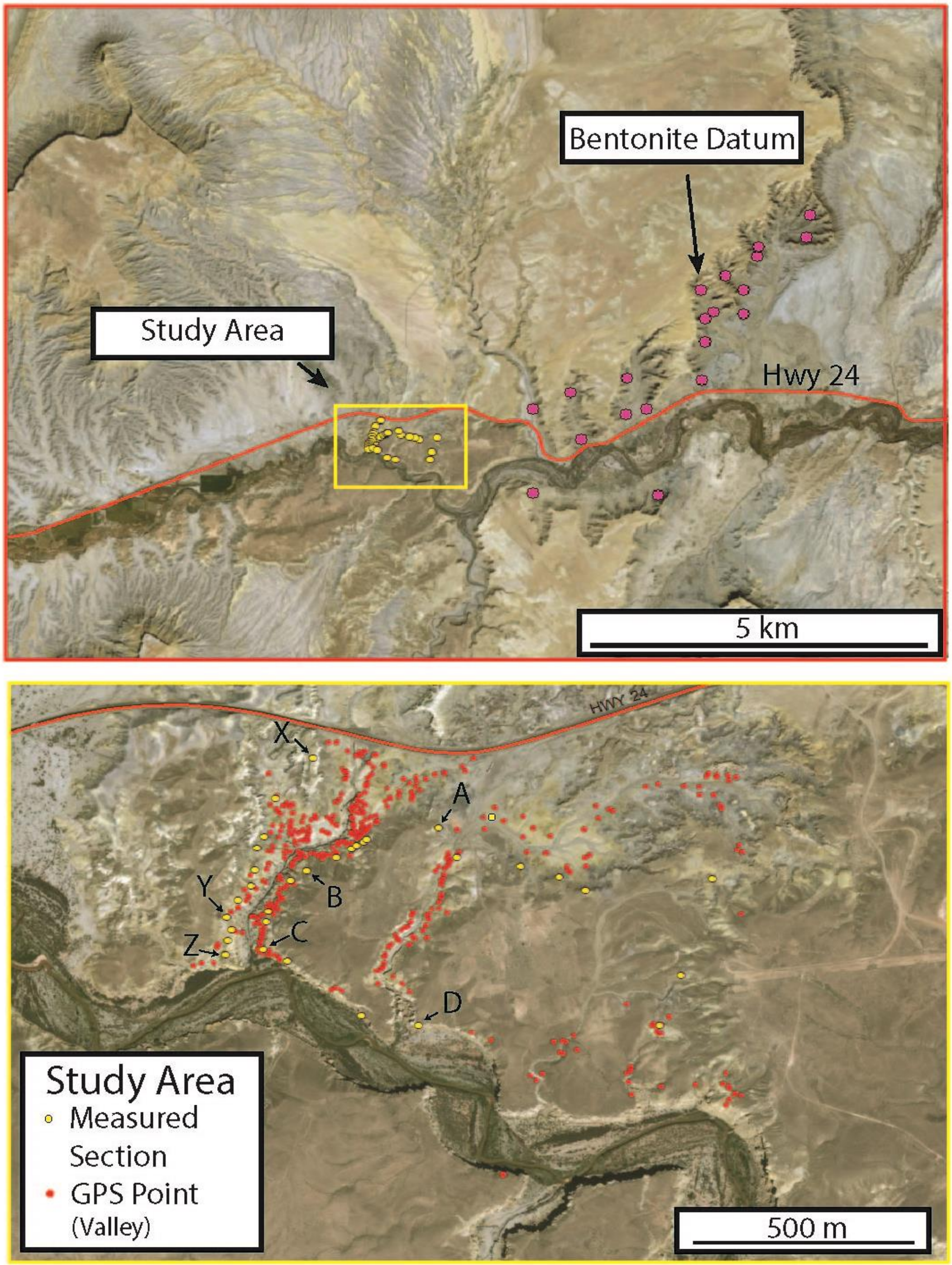

Figure 3.5: Study area. *Above*) Location of red box (Fig. 3.3C) shows measured sections (yellow) relative to bentonite GPS points (pink) used to correct for regional structural tilt (Hilton, 2013). *Below*) Location of yellow box (*above*) with measured sections (yellow) and GPS survey of the trunk tributary valley floor where it is exposed (red).

Much of the valley fill and overlying non-marine stratigraphy is composed of floodplain deposits and paleosols, deposits above the erosional surface that marks the valley floor. The deposits in this study will be presented in a framework of fluvial aggradation cycles (FACs), and fluvial agradation cycle sets (FAC sets) (Prochnow et al., 2006; Atchley et al., 2007; Cleveland et al., 2007; Famubode and Bhattacharya, 2016), and presented in the chronostratigraphic context of bounding bentonite deposition events using $^{40}Ar/^{39}Ar$ dates from sanidine crystals (Zhu et al., 2012). Floodplain entisols, inceptisols and histosols recognized in the field (Bown and Kraus, 1987; Retallack, 1988; Kraus and Aslan, 1999; McCarthy and Plint, 2003; Famubode and Bhattacharya, 2016) represent periods of floodplain non-deposition, and may account for much of the life of this entire sequence in Wheeler space. Previous studies of this sequence identifies three potential sequence boundaries 2 km south of our study area (Famubode and Bhattacharya, 2016) extending another 10 km along strike. With the chronostratigraphic constraints provided by this study, we test the likelihood of higher frequency allogenic cyclicity.

3.3 Methods

Measured sections and facies descriptions include the identification of trace fossils, grain size estimates, sedimentary structures, bioturbation index (BI) (Taylor and Goldring, 1993) and paleocurrent directions. These were made in the field using a Jacob's Staff with an Abney level, hand lens and grainsize card. Estimates of mudstone clay content were made by relative comparison of colour, texture and swelling ratio in the field. Net to gross sandstone volume ratios (NTG) were calculated by multiplying these estimates by their relative thicknesses within measured sections for individual facies and reported as a range to capture facies variability and estimation error.

An SX Blue differential GPS system was used for location accuracy and image control points. A GPS survey of the rooted paleosol surface that defines the incised valley floor collected 677 elevation points and was corrected relative to the structural surface of a regionally extensive bentonite horizon (Zhu et al., 2012) in the overlying Bluegate Shale Member. A previous survey of this bentonite horizon, using 22 elevation points, shows a local structural dip of 0.4 degrees to the north and 1.4 degrees to the west (Hilton, 2013) (Fig. 3.5). The survey data was drift corrected by the instrument and dilution of precision during the survey varied from 1.2 to 1.8. Horizontal accuracy of this survey was averaged at ±0.65m in the horizontal X and Y coordinates and ±0.50 m in the vertical z direction.

Outcrop images were produced by stitching digital camera imagery in photo mosaic software, and by acquiring vertical drone imagery used to create a 3D point cloud and triangular mesh terrain model using Pix4D photogrammetry software. The model was georeferenced using GPS control points collected with the SX Blue system. Vertical accuracy of the model's control points are approximately ±0.60 m in the horizontal, and ±0.45 m in the vertical. This was then used to extract an orthophoto of the outcrop exposures. These outcrop exposures are in an area approximately 0.6 km^2 just south of Hwy 24 between Hanksville and Caineville, Utah. The software model and orthophotos were used to identify and correlate bedding diagrams with the measured sections superimposed.

3.4 Valley Floor Map

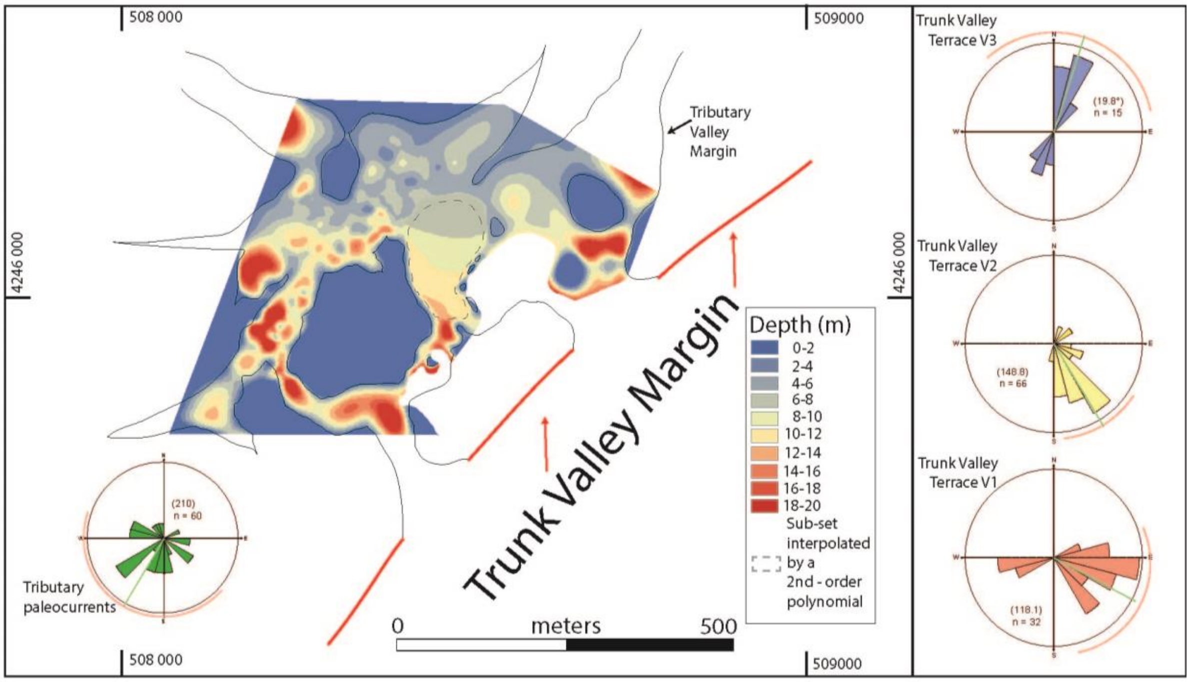

Figure 3.6: Trunk tributary valley floor reconstruction. The depth mapping of this valley is relative to the surveyed interflueve fill elevation. Warmer colours indicated deeper reaches of the valley floor. This surface was generated using 2 separate interpolators. The majority of this depth surface was interpolated using a 3rd derivative spline function, and the region indicated in dashed lines was interpolated using a 2nd order polynomial local interpolation. The red boundary that marks the trunk valley margin is the west most extent of the compound incised trunk valley deposits (*modified from*: Kimmerle and Bhattacharya, 2018). Paleocurrents from measured sections within the trunk tributary valley (green rose plot) are show in contrast with trunk valley paleocurrents (blue, yellow and pink rose plots) for individual terraces.

Based on the collection of 677 individual gps points, resampled to 426 with 1 m resolution in the horizontal (Fig 3.5), this high resolution survey was conducted to interpolate a surface elevation layer using a minimum curvature spline interpolator in Esri

ArcMap 10.2.2 software. Varying the weight of the 3rd derivative of the spline function for values of 0.1, 0.01 and 0.001 had little to no effect on the results of our derived surface. Areas where spline interpolated values exceeded 1.5 times the interquartile range of the survey; a 2nd-order polynomial local interpolator was used to avoid potential artifacts in the results. Valley surfaces were identified by the rooted, iron-stained horizons (Facies 3) and alluvial boulder conglomerate (Facies 4) that makes up the sandstone valley floor (Facies Association 2). The interpolated surface was subtracted from a uniform elevation marked by the maximum corrected elevation observed (Fig 3.6). The resultant depth surface shows a 20 m deep, elongate topographic depression with irregular interflueve “islands”. The deeper areas of the valley are in narrow sections (~50 m wide) proximal to convergences of valley drainage confluences. The wider valley sections (~300 m) show shallower incisions. The studied outcrop extends for 700 to 800 m measured parallel to the trunk valley and 500 to 600 m perpendicular to the trunk valley, margin, covering an area well over 1 km^2; representing over half of the extrapolated tributary valley area.

In a regional context, the maximum depth of incision of this tributary valley is 20 m, while the compound trunk valley show local incision depths of up to 28 m (Li et al., 2010; Li and Bhattacharya, 2013; Kimmerle and Bhattacharya, 2018). The difference in depth may be attributed to the forced regression of tidal incursion that no longer reached the tributary valley, or the difference between the trunk channel depth (~5-7 m) and Tributary depth (~2-4 m) The extent of the regional compound trunk valley spans over 30 by 40 km resulting in an incised area of over 1200 km^2, while the tributary valley likely covers an area less than 5 km^2.

3.5 Facies and Facies Associations

This study has documented 17 sedimentary facies summarized in Table 3.1. These facies are consistent with those previously documented within the Ferron Notom Delta (Fielding, 2010; Li et al., 2010; Fielding, 2011; Zhu et al., 2012; Li and Bhattacharya, 2013; Famubode and Bhattacharya, 2016; Kimmerle et al., 2016). Five facies associations are identified and described.

Table 3.1: Facies Summary

Facies	Lithology	Sedimentary Structures	Net to Gross	Biota	Depositional Process	Depositional Environment
F1	fU sandstone	Planar laminated to Hummocky	> 0.9	_	Wave dominated	middle shoreface
F2	mL to fU sandstone	Trough cross bedded to massive	0.9-0.7	*Ophiomorpha*, *Rhizocorallium*, horizontal burrows	Wave dominated	Upper Shoreface
F3	mL to fine upper sandstone	Vague cross bedding to massive	0.8-0.9	Extensive tabular root system	Subareal exposure of exposed substraight	Coastal paleosol
F4	Cobble to boulder conglomerate	Localized fan shaped conglomerate	0.9 - 0.7	_	Valley wall collapse	Valley margin alluvium
F5	Organic rich Mudstone	Planar laminations, slickensides	0.1 - 0.3	Plant material, soil and root horizons	Near fluvial/sub-aerial	Flood plain
F6	Carbonaceous shale	planar laminated	< 0.1	coaly plant material, significant root horizons	Flooding by fresh water	Wetland, paleosol
F7	Coal	Blocky laminations	n/a	Peat accumulation	Flooding by fresh water	Wetland
F8	Bentonite Clay	Slickensides	< 0.1	_	Volcanic ash deposit	Subaerial

F9	Laminated heterolithic vfL to vfU sandstones	Parallel laminations, reverse and normal grading	0.3 - 0.6	_	Hyperpycnite/ turbidite	Flood plain lake
F10	Mudstone to fine lower sandstone	Massive to ripple laminated	0.4-0.6	fibrous , tabular roots	Unidirectional current	Floodplain, splay overbank
F11	Thin bedded (3-10 cm) heterolithic vfL sst. And interbedded mdst.	Soft sediment deformation, ripple cross-lamination	0.6 – 0.8	Significant root casts and coaly plant material	Fluvial	Abandoned channel fill
F12	Confined Coaly Mudstone Plug	Localized, lenticular coally lamina	< 0.1	Root, plant material	Fluvial abandonment	Abandoned channel fill
F13	Medium bedded (7-25 cm) heterolithic fL to mL sst. With interbedded mdst.	Dune scale cross-bedding, double mud drapes	0.8 -0.9	_	Tidally- influenced fluvial	Lower Backwater
F14	Medium bedded heterolithic (5-20 cm) fL to fU sst. with thin (1 mm - 2 cm) interbedded mdst.	Low amplitude ripple laminations	0.6 - 0.8	fugicnia trace fossils, lockeia, dinosaur footprints	Fluvial	Fluvial channel
F15	Laminated heterolithic mudstones to vfL sandstones	Low amplitude ripple laminations	0.2 - 0.4	lockeia, plant material	Tidally- influenced fluvial	Lower backwater
F16	Thick bedded (25 - 150 cm) fU to granule sst.	Predominantly dune scale cross-bedded	> 0.9	–	Fluvial	Unconfined Fluvial
F17	Shelf Mudstones	Parallel laminated, combined flow, ripple laminated	0.2-0.3	Ammonites, fish scales Inoceramids	Marine	Shelf

3.5.1 Facies Association 1: Marine Shoreface (FA 1)

Description - FA 1 is composed of fU to mL coarsening upwards sandstone that is greater than 15 m thick, which varies with the incision depth of the overlying valley (Fig. 3.7A). Sedimentary structures include trough cross-bedding and hummocky-cross-stratification (HCS) interbedded with heavily bioturbated (BI 4-5) beds with prevalent *Ophiomorpha*, *Rhizocorallium* and several other horizontal burrows. In this area, FA 1 is composed of facies F1 and F2.

Interpretation- The interbedding of HCS with heavily bioturbated beds is typical of lower to middle shoreface deposits (MacEachern et al., 2010) which is consistant with the Cruziana ichnofacies. The trough cross-bedding and medium lower sandstone is evidence of upper shoreface, and likely represents a transitional interval between middle to upper shoreface (Clifton, 2006).

3.5.2 Facies Association 2: Sandy Valley Floor Paleosol (FA 2)

Description- FA 2 is composed of red-stained, oxidized, 1 to 2 m thick fU sandstone with pervasive root casts and vague cross-bedding (F3) (Fig. 3.7B). The roots are well oxidised and exhibit a tabular root morphology (Retallack, 1988). FA 2 is also composed of localised fan-shaped, semi-consolidated boulder conglomerates (F4) along steeper incisions of the valley floor. The boulders are up to 1 m in diameter of their longest axis (Fig 3.7D). The conglomerate is onlapped by mudstones and heterolithic sandstones of the overlying valley fill (FA 3), (Fig. 3.7E.

Interpretation- This sandstone is the uppermost zone of FA1 that was pervasively penetrated by plant roots. Incision of the valley into FA1 left an erosional vacuity that was sub-aerially exposed due to a drop in relative sea level. The extensive root casts and iron-rich mineralization of Facies F3 and the collapse deposits (F4) are evidence that this exposure was of considerable duration and the valley floor was essentially a moderately developed paleosol equivalent to a modern inceptisol (Retallack, 1988; Prochnow et al., 2006).

3.5.3 Facies Association 3: Floodplain Deposits (FA 3)

FA 3 can easily be considered a catch-all for those sediments that are associated with fluvial deposition, but not confined to channels. Herein we describe the facies associated with the floodplain, that we will later subdivide into FACs and correlative FAC sets.

Description- FA 3 is predominantly composed of organic rich mudstones (F5). Silt to clay composition ranges from 70 to 30 percent, and even less in the case of two lower bentonite layers (F8) with a maximum thickness of 1.5 m. Root casts are visible in 20 – 30 cm horizons within this organic mudstone. Columnar siderite concretions also form horizons, with clusters of 5-15 cm diameter masses at certain intervals that extend for 10s of meters laterally. Sand rich deposits (F10) are typically thin beds, less than 20 cm thick and 10s of meters wide, that pinch out laterally, of rippled to massive heterolithic vfL to fL sandstone with abundant plant material and often a rooted top surface. Laterally continuous carbonaceous shales (F6), containing abundant coal fragments, extend for 100s of meters and are 20 to 60 cm thick (Fig. 3.7F). These are capped in most occurrences by 10 to 110 cm thick brown to brownish yellow coal layers (F7) that are also exposed for 100s of meters (Figs. 3.7D, E, F, and G).

Interpretation- The floodplain facies association in this tributary valley shows evidence of stacked moderate to immature paleosols from the rooted horizons and coal forming peat accumulations (F6 and F7). The coal zones in this study are composed of lignite to sub-bituminous ranked coal (Famubode and Bhattacharya, 2016) evident from its typical brown to dark grey colour (Fig 3.7F). The highest rank coal reported in the Ferron

Sandstone is of high volatile A bituminous rank (Lamarre, 1991), suggesting that these coals are immature. Laterally continuous coal layers can be considered as paleosols equivalent to their un-compacted peat thickness, comparable to modern histosols (Retallack, 1988; Famubode and Bhattacharya, 2016).

The columnar siderite concretion clusters (F5) are suggestive of fossilized tree and woody plant remnants. Previous work, focussed on the palynology of these floodplains (Akyuz et al., 2015), demonstrates evidence for an ever-wet climate. This climate would explain the tabular root morphology (F5) similar to modern tropical rainforests (Retallack, 1988). The propensity of ponding in tributary valleys due to effects from the associated trunk channel (Kvale and Archer, 2007) may account for the sheet like lacustrine deposits (Fig. 3.7G) (F9) that are a result of flooding, rather than creating oxbow lakes from channel cut-offs The sandy deposits (F10) are interpreted as crevasse splays, where rooted upper surfaces mark prolonged subaerial exposure between floods.

3.5.4 Facies Association 4: Tidally-Influenced Channel Deposits (FA 4)

Description- This facies association includes all deposits confined by the elongate erosional scour of the channel base of heterolithic sandstone deposits in the valley. The lower sediments in the scour are 7-25 cm thick dune scale cross-bedded fU to Ml sandstones with double mud drapes (Fig. 3.7C) (F13). This facies is interbedded with laminated heterolithic channelized mudstones (F15). The channel mudstones show nearly continuous lateral continuity across bar surfaces within the channels. The channel deposits tend to fine upwards to 5-20 cm thick fL to fU heterolithic sandstones (F14) also interbedded with the heterolithic mudstone facies (F15). Localized vfL sandstones with soft sediment deformation (F11) and coaly mudstones (F12) are present in some of these channel deposits in confined channel top, concave upward lenses.

Interpretation-The dune-scale cross-bedded sandstones with double mud drapes (F11) are interpreted to be produced by alternating diurnal ebb and flood tide cycles (Vakarelov et al., 2012). Continuous mudstone bar drapes are suggestive of lower backwater deposits, which include include decreased lateral migration of point bars, increased erosion of the trunk channel in response to flood stage drawdown, an increase mud sequestration and an increase in lateral continuity of shale drapes (Corbeanu et al., 2004; Chatanantavet et al., 2012; Blum et al., 2013; Colombera et al., 2016; Fernandes et al., 2016). The coaly mudstone fills (F12) may represent stages of channel avulsion and abandonment, leaving behind an organic rich mudstone plug facies, distinguishable from facies F7 by its channelized confinement.

3.5.5 Facies Association 5: Shelf Mudstones (FA 5)

Description- Facies association 5 is composed of silt-rich ripple laminated mudstones (F17). These mudstones are dark gray in colour and weather to blueish gray. Ripples are bi-directional and less than 3 cm in amplitude. Fossils present include abundant ammonites, fish scales and inoceramid shells. The inoceramids are usually found in fragmented pieces along distinct horizons throughout the facies. Within the lower 5 m of facies F17 is a bentonite layer (F8) with a maximum thickness of 30 cm.

Interpretation- FA5 is interpreted as a shelf mudstone, the base of which marks a regional unconformity separating the Ferron Sandstone Member below from the Bluegate Shale Member above. The bentonite in the lower part of the Bluegate Shale is regionally extensive and shows little topographic relief, and was therefore used as the regional datum for this study.

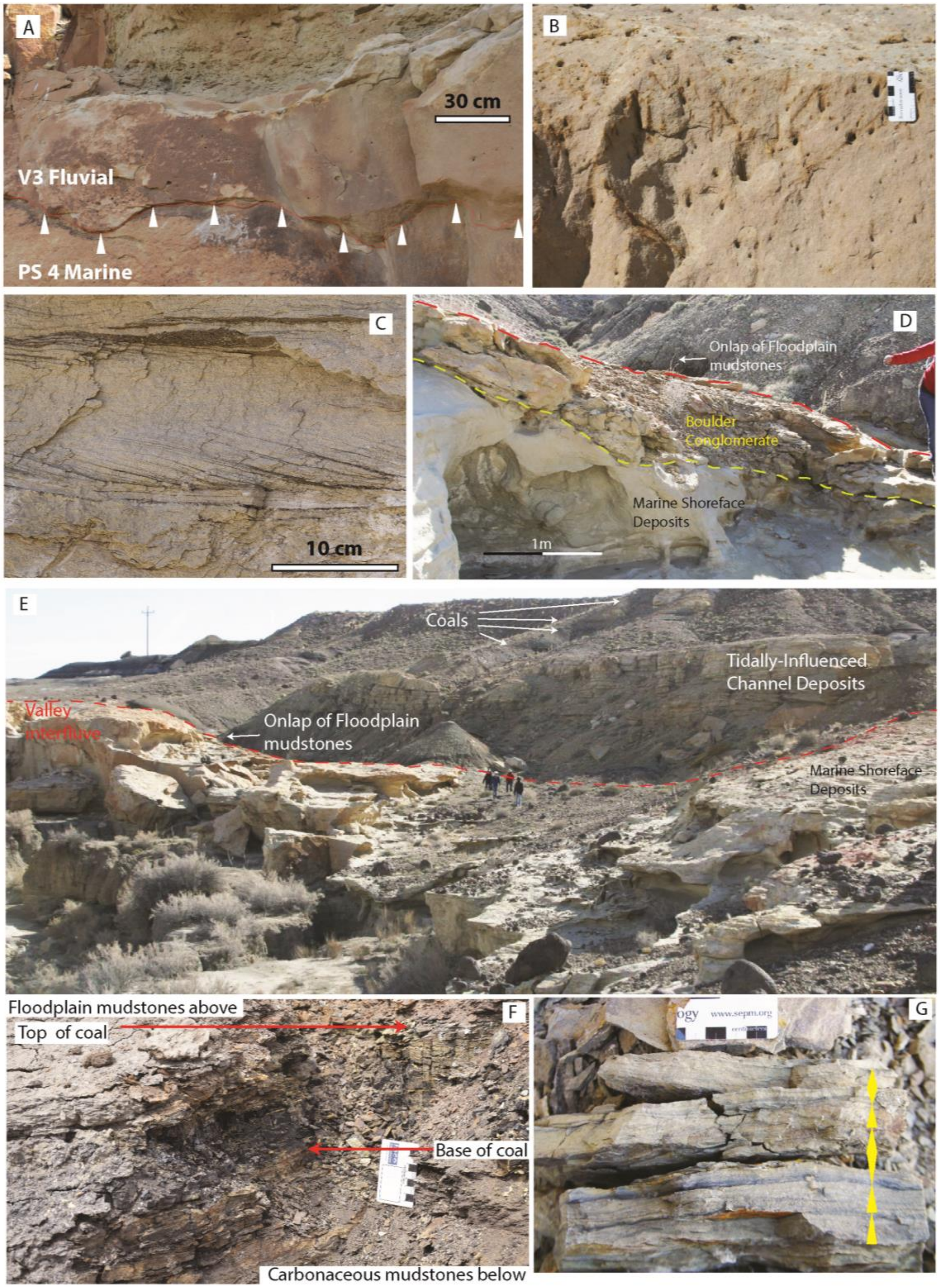

Figure 3.7: Trunk tributary facies. A) Underlying PS4 shoreface (FA1) (*modified from:* Kimmerle and Bhattacharya, 2018). B) Sandy paleosol composed of a coarsening

upwards medium lower to fine upper sandstone with vague hummocky cross-bedding disrupted by abundant oxidised plant root casts (FA3). B) A fan shaped boulder conglomerate (F4) overlying marine sandstone deposits of the incised Parasequence 4 shoreface (Fig. 4) onlapped by the floodplain mudstones (F5) of the trunk tributary valley. C) Wide view of the stratal relationships of the incised shoreface (FA 1) deposits creating valley interflueves and a valley floor (FA 2) onlapped by floodplain mudstones (FA 3) with overlying tidally-influenced heterolithic channel sandstones (FA 4) and interbedded mudstone and coal layers (FA 3). D) Coal layer (F7) capping carbonaceous mudstones (F6) and overlain by organic rich floodplain mudstones (F5). E) Lacustrine mudstones with interlaminated rippled very fine lower sandstones showing normal and inverse grading, interpreted as turbidic and hyperpicnal flow deposits in a floodplain lake environment.44

3.6 FACs, FAC-Sets and Paleosol Development.

FACs are decimeter to meter thick fluvial deposits bounded below by a paleosol and above by either a paleosol or an erosional surface of fluvial deposition, such as a channel scour or splay. The division of FACs is independent of interpretation, but rather is related to the recognition of paleosol development based on the presence of rooted surfaces, soil maturity and lithologic changes in vertical succession (Kraus and Aslan, 1999; Prochnow et al., 2006; Cleveland et al., 2007; Famubode and Bhattacharya, 2016) (Fig. 3.8). This study maps out 32 distinct FACs that can be correlated over 10s to 100s of meters (Figs. 3.9, 3.10 (*lower*) and 3.11(*lower*) in blue). FAC sets (Figs. 3.10 (*lower*) and 3.11(*lower*) in red) are recognised as meter to 10’s of meter thick stacked FACs that are bounded by paleosols of increased paleosol maturity (Prochnow et al., 2006; Atchley et al., 2007; Cleveland et al., 2007; Famubode and Bhattacharya, 2016), in this study coal layers represent equivalents to modern histosols. Closely spaced measured sections (Fig. 3.5) were used to correlate laterally extensive coal layers, FACs, FAC sets and channel belts (Figs. 3.9, 3.10,and 3.11). These coals and their correlative horizons form the bounding framework for most of the FAC-sets . The stacked FACs are grouped into 9 FAC sets with a remnant FAC above the highest coal capping FAC Set 9. A summary of FAC-set dimensions (Table 3.2) and a description of each FAC set is presented.

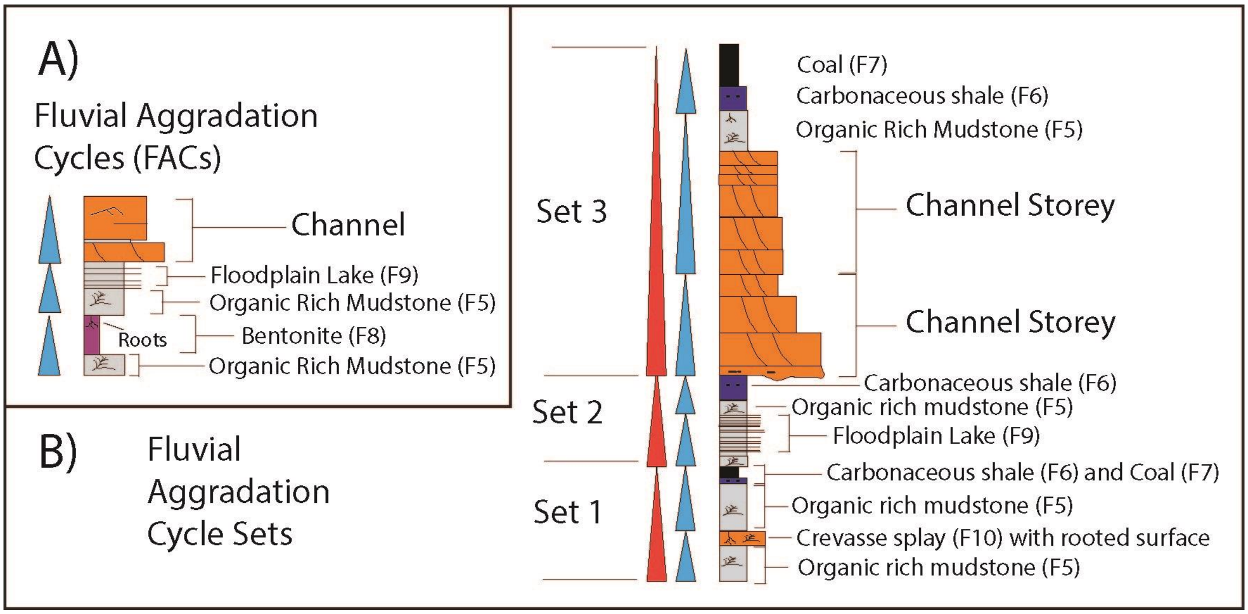

Figure 3.8: Fluvial aggradation framework. A) Fluvial aggradation cycles (FACs) shown here illustrate how these cycles are recognized in measured sections. The first cycle is capped by a rooted paleosol in a bentonite layer and marks a prolonged time of non-deposition. The second FAC is top truncated by a fluvial channel and therefore is bounded below by a paleosol and above by a channel scour. The third cycle is the autogenic progression of channel erosion and fill that precedes avulsion or abandonment. B) Fluvial aggradation cycle sets (FAC sets) group stratal hierarchies of increasing paleosol maturity. In this instance, FAC sets are capped by coal zones in Sets 1 and 3, and represent significantly more mature paleosol horizons than that of the upper surface of the next FAC. The upper surface of FAC-Set 2 is the basal surface of the lowest channel story in FAC-Set 3.

Table 3.2: FAC-set Summary

FAC Set	Max Number of FACs	Max Thicknes of Floodplain Deposits (mm)	Max Thicknes of Coal Deposits (mm)
1	1	1950	-
2	5	5240	-
3	4	1400	250
4	4	730	1100
5	4	1240	560
6	3	1360	580
7	3	2490	360
8	3	3410	350
9	5	5270	760

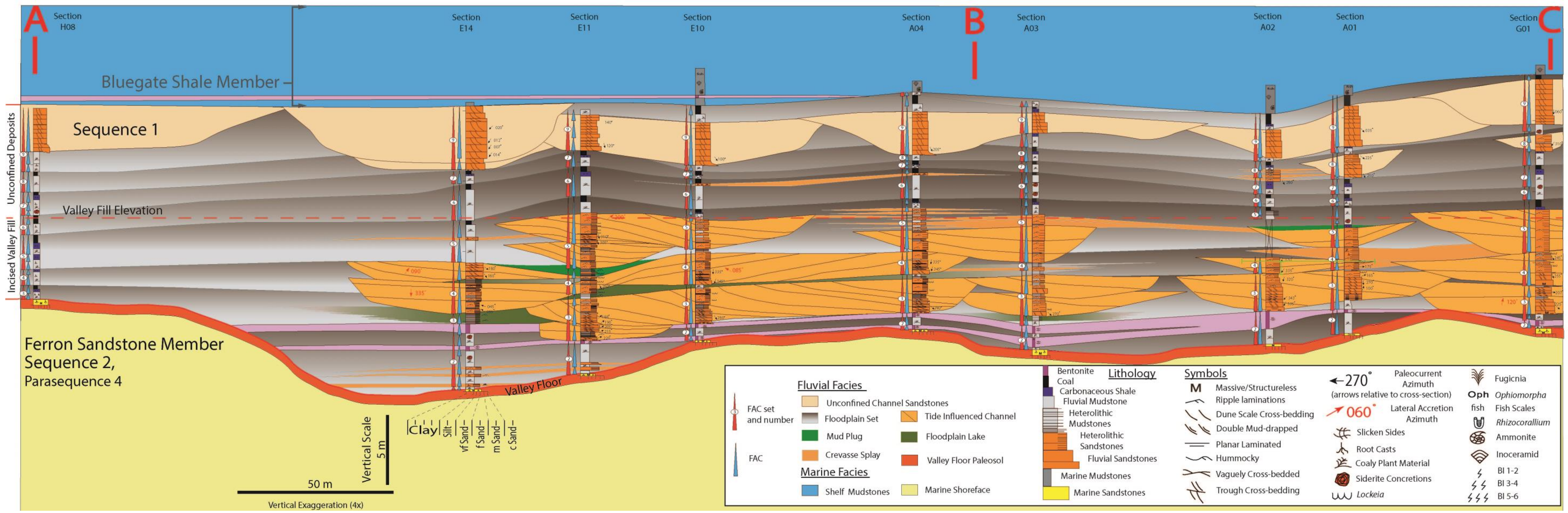

Figure 3.9: Cross section A-B-C (north-south). Stratigraphic cross section of the trunk tributary valley at locations marked A, B and C (Fig. 3.5) showing the correlation of measured sections and the stacking of FACs (blue triangles) and FAC sets (red triangles). The valley fill elevation (dashed red) marks the highest elevation of the valley floor (Fig. 3.6) separating incised valley fill from unconfined fluvial deposits. See text for description.

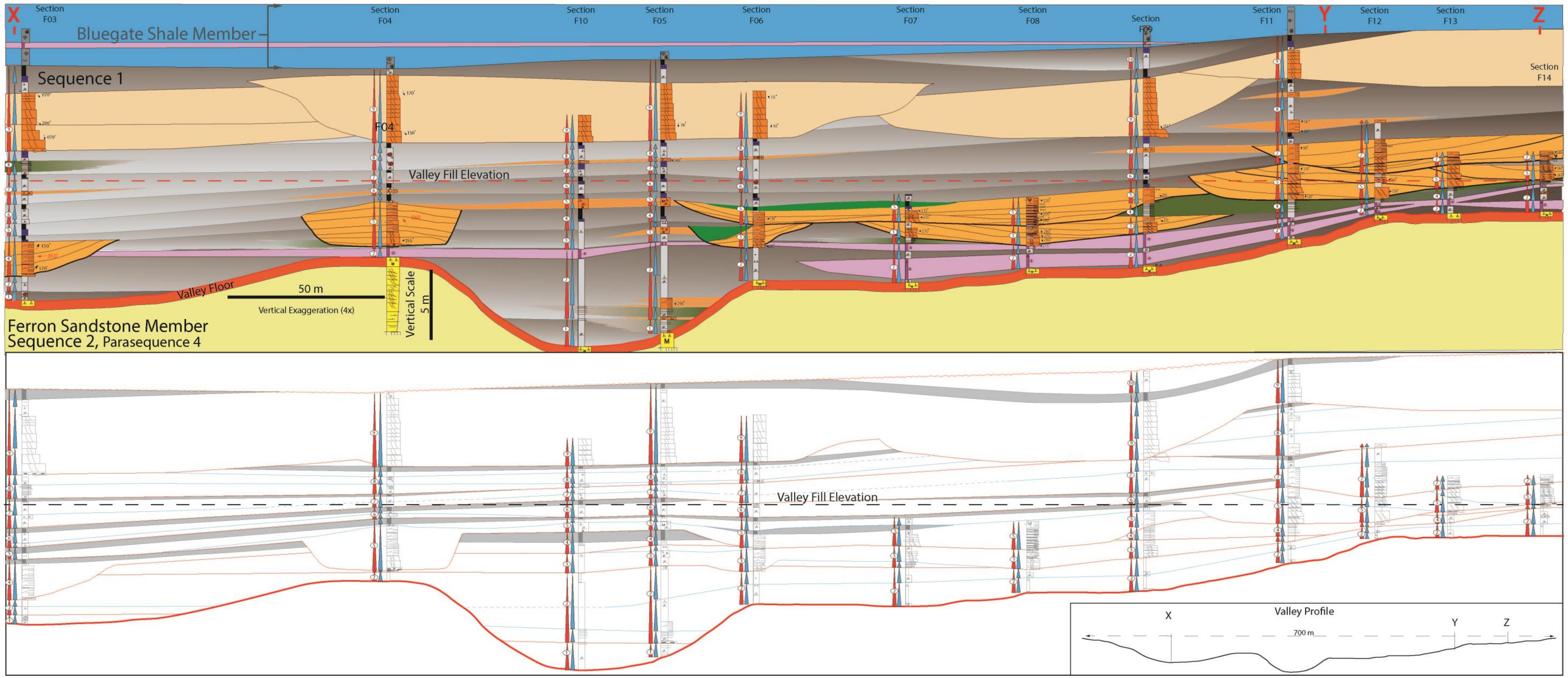

Figure 3.10: Cross section X-Y-Z (north-south). Stratigraphic cross-section of the trunk tributary valley at locations marked X, Y and Z (Fig. 3.5). The lower section correlates FACs and FAC sets of cross section X-Y-Z above. Individual FAC's are correlated 10s to 100's of meters while FAC sets identified by coal layers at the top of most sets, are continuous throughout the study area and may be correlated several kilometers away.

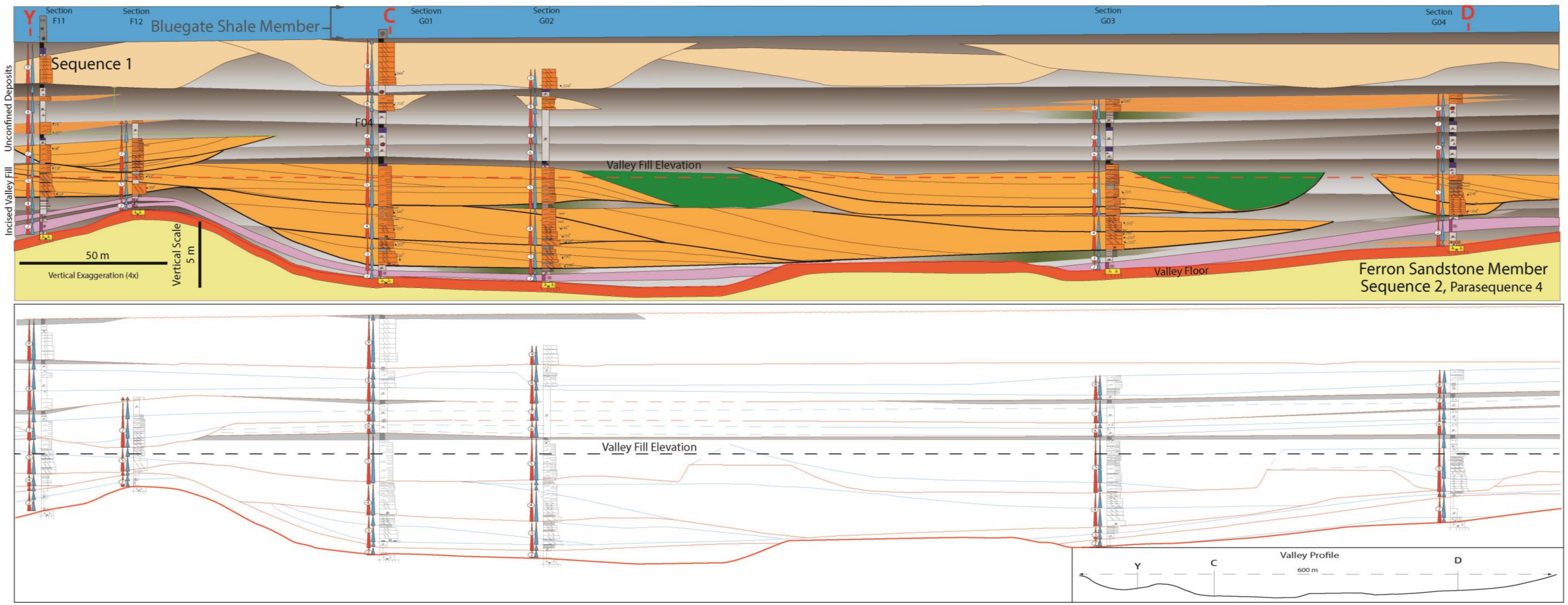

Figure 3.11: Cross section Y-C-D (west-east). Stratigraphic cross section of the trunk tributary valley at locations marked Y, C and D (Fig. 3.5), with FAC and FAC-set correlation below.

3.6.1 FAC-Set 1

FAC Set 1 (Figs. 3.9 and 3.10) marks the earliest deposition of floodplain deposits in the valley and varies in thickness from 0.35 to 1.95 m. It is composed of organic rich mudstones (F5) and lacustrine siltstones (F9). Remarkable is the lack of fluvial channel deposits at the base of this mud lined, kilometer scale valley. FAC-Set 1 is capped by the first occurrence of sandstone and in the northern extent of correlation X-Y-Z (Figs. 3.9, section E14 and Figure 3.12, sections F05 and F10) by a siderite concretion cluster; and is everywhere overlain by FAC-Set 2.

3.6.2 FAC-Set 2

This FAC-set is distinctive as having the earliest occurrence of vfU to fL sandstone in the form of crevasse splays (F10), and 2 laterally extensive bentonite layers (F8) that drape most of the exposed valley surface (Figs. 3.9, 3.10,and 3.11). Ranging in thickness from 0.57 to 5.56 m in measured sections, it onlaps the valley floor in more shallowly incised areas, such as the northern edge of cross-section A-B-C (Fig. 3.9), and has an average thickness of 2.00 m in measured sections. This set is composed of up to 5 recognizable FACs identified from rooted surfaces, and well preserved lower tree bases and upper root systems. The top of FAC-Set 2 is the weathered upper surface of the second bentonite layer, with a soil colour of 10YR6/1, a well preserved tabular root horizon and abundant slickensides. This surface may be analogous to a modern vertisol or inceptisol. The lateral continuity of these 0.15 to 1.50 m clay rich bentonite layers suggests an absence of significant fluvial channels.

3.6.3 FAC-Set 3

FAC-Set 3 is characterized as the first occurrence of heterolithic fU to mL sandstone with interbedded mudstone channel stories (FA4) and the earliest occurrence of a coal horizon (Fig. 3.9, section H08). This set ranges from 0.11 to 3.85 m in thickness where preserved, and is heavily incised by overlying channels. It is composed of 3 distinct FACs, including evidence of 2 preserved stacked channel stories in a 350 ± 35 m wide channel belt confined within the valley, whose floodplains are composed primarily of organic rich mudstones (F5) and lacustrine heteroliths (F9), and which onlap FAC-Set 2 (Fig. 3.10, sections F11-F12). The average of all channel paleocurrent directions in this set is 241 degrees with a standard deviation (σ) of 55. The set is capped by a 0.25 m coal layer that is only present in cross-section A-B-C (Fig 3.9), as it pinches out to the west in cross-section X-Y-Z (Fig 3.10) and was potentially deposited, although eroded away by overlying channels in cross-section Y-C-D (Fig 3.11). This coal shows paleosol development, however discontinuous, consistent with a histosol. FAC-Set 3 is erosionally truncated by FAC-Set 4 and even FAC-Set 5 in the deepest channel scours.

3.6.4 FAC-Set 4

This set is 0.32 to 3.76 m thick where present in measured sections, and is locally eroded away by FAC-Set 5, as shown in correlation X-Y-Z (Fig. 3.10, sections F06-F08). This FAC-set is composed of 2 FACs including 2 distinct heterolithic fL to mU sandstone channel storeys (FA4) (Fig. 3.9, section E14) and floodplain paleosol horizons (F5). The lower floodplain cycle is capped by a weekly rooted entisol. The confined channels in this set have an average paleocurrent of 234 degrees and σ=96. Channel belts formed in this

FAC set range in width from 35 m to 450 ± 25 m. Floodplain deposits are composed of organic rich mudstones (F5), lacustrine heteroliths (F9) and an increase in crevasse splay facies (F10) than observed in earlier FAC-sets. FAC-Set 4 is capped by a 1.10 m coal layer and upper histosol, the thickest observed in this valley.

3.6.5 FAC-Set 5

FAC-Set 5 deeply incises FAC-Set 4 (Fig. 3.10, sections F06 – F14) and is the thickest continuous FAC-set within the valley, ranging from 0.83 to 5.22 m, and an average of 2.64 meters thick. Composed of 4 FACs bounded by rooted entisols and histosols, FAC-Set 5 marks the earliest set to aggrade above the valley margin. This set contains 2 stacked channel stories, the lower being confined and the upper storey being semi-confined by the valley margin. Heterolithic fL to mL sandstone channel deposits have an average paleocurrent of 222 degrees and σ=84, with channel belts ranging from 52 ± 10 to 430 ± 35 m wide . FAC-Set 5 channels incise lower FAC-Set 4 and 5 floodplain facies (FA4). Floodplain deposits are primarily composed of organic rich mudstones (F5) with minor crevasse splay sandstones (F10). This set is capped by the most laterally extensive coal layer, which can be correlated through the entire study area, however it is incised by FAC-Set 7. FAC-Set 5 is the last FAC-set to be fully confined by the mapped tributary valley.

3.6.6 FAC-Set 6 and 7

Composed entirely of floodplain deposits (FA3), FAC-Set 6 shows no evidence of channel sandstones, only a 125 m wide crevasse splay, as shown in cross-section A-B-C

(Fig. 3.9, section F04). This mudstone dominated FAC-set has 3 FACs, each capped by a moderately rooted entisiol or coal histosol. There is no evidence of channel fill deposits in FAC-Set 6 from cross-sections A-B-C, X-Y-Z, and Y-C-D (Figs. 3.9, 3.10 and 3.11). It is erosionally truncated by FAC-Set 7 channels (Fig. 3.10, sections F11-F14), and completely missing in some areas. Where present, it ranges from 0.76 to 2.63 m thick, and is capped by a 0.20 to 0.32 m thick coal layer. The coal capping FAC-Set 6 is also eroded by FAC-Set 7 channel scours and pinches out within correlation Y-C-D (Fig. 3.11, sections G01-G03). FAC-set 7 is composed of 3 FACs defined by a rooted entisol, 2 localized stacked channel deposits (FA 4) (Fig. 3.10, sections F11 –F14), and capped by a coal layer histosol that pinches out to a carbonaceous shale. The set ranges in thickness from 0.57 where it is completely floodplain deposits, to 3.56 m at the deepest channel fill. The average channel paleocurrent was 147 degrees (insufficient data to determine σ). The floodplain associated with FAC-set 7 (FA3) is composed primarily of organic rich mudstones (F5) with subordinate splay facies (F10) proximal to the channel deposit and is capped by a 3.20 m thick coal that pinches out in the study area. FAC-Set 7 channels incise lower FAC-Set 3 and 4 floodplains.

3.6.7 FAC-Set 8 and 9

FAC-Set 8 shows similar floodplain composition (F5 and F10) with limited lacustrine facies (F9) (Fig. 3.10, section F03), and has few isolated single storey unconfined channels (F16) filled with fU to cL sandstones that do not truncate FAC-Set 7 below (Fig 3.9, sections A01 and G01). FAC-Set 8 ranges in thickness from 0.23 to 3.79 m with a 3.45 m coal layer and is erosionally truncated by FAC-Set 9 above, which shows laterally continuous, amalgamated mL to cU channel sandstones (F16) that erosionally overlie FAC-Set 8, and FAC-Set 7 where 8 is completely incised (Fig 3.9, section E14 and E11; Fig 3.10, section F09). The sandstones in FAC-Set 9 represent the coarsest grained deposits in this study. FAC-Set 9 has 3 associated FACs, with 2 channel stories and is capped by an organic rich mudstone (F5) and 0.75 m thick coal layer. Channel storeys range from 1.65 to 4.75 m thick in measured sections and have an average paleocurrent direction of 135 degrees and σ=107. The set is bounded above by shelf mudstone facies of the Bluegate Shale (F17), and in places organic rich mudstones (F5) and shelf mudstones above.

3.7 FAC and FAC-Set Interpretation

The valley floor, identified by its rooted surface and conglomerates, represents a major basinward shift of facies from fully marine to a sub-aerially exposed non-marine environment. Based on the regional stratigraphy (Li et al., 2011a; Zhu et al., 2012) this represents a major sequence boundary. The rooted surface and conglomerates are evidence of a major hiatus in deposition, potentially recording the falling stage systems tract. The FAC-Sets 1 and 2 show no channel sandstones across the valley within the constraints of our cross-sections (Figs. 3.9, 3.10,and 3.11). As the valley floor survey shows complete coverage of the study area (Fig. 6), the most likely source of the floodplain sediment bounded by the valley floor to the bentonite layers is the associated trunk channel. This includes the heterolithic lacustrine facies (F9) and splay deposits (F10). The mudstone strata in the lowest parts of this valley shows a distinct difference in valley fills from those documented elsewhere in the Ferron Notom, which are composed of terrace forming sandstones that directly onlap valley margins or older terrace deposits (Li et al., 2010; Zhu et al., 2012; Campbell, 2013; Ullah et al., 2015; Kimmerle and Bhattacharya, 2018). The muddy valley fill of FAC-sets 1 and 2 may therefore represent the early lowstand systems tracts.

FAC-Sets 3, 4 and 5 show evidence of channel reoccupation and aggradation and moderate lateral migration. The floodplains of these sets show a greater proportion of floodplain lacustrine deposits (F9). This observation may be attributed to the effects of trunk valley channels on their trunk tributaries (Kvale and Archer, 2007) as they can cause damming of subordinate drainages due to the higher flow dynamics of trunk channels, trunk channel bar migration, and possible backwater effects (Colombera et al., 2015; Fernandes et al., 2016). FAC-Sets 4 and 5 are more sandstone prone than other sets within the confines of the valley scour and have a greater diversity of paleocurrents. The amalgamation of channel belts and the re-incision of channels (Figs. 3.9, 3.10,and 3.11) creates a higher density of amalgamated fluvial bodies and are suggestive of aggradational valley fill architecture (Wright and Marriott, 1993) in the context of the underlying, more isolated fluvial geometry of FAC-Set 3. With such a diversity of paleocurrents it is possible that either avulsion is more frequent or that this FAC-set incorporates multiple drainage feeder channels within the valley. Notable is the paucity of lacustrine facies in FAC-Set 5, which comprised a significant contribution to earlier floodplain deposition. We interpret FAC-Sets 4 and 5 as a late lowstand to early transgressive systems tract that marks the last FAC-set to be completely confined in the trunk tributary valley.

FAC-Set 6 is deposited above the fill elevation of the trunk tributary valley and extends beyond our study area. The dominance of floodplain facies (FA 3) may indicate avulsion of the tributary or that of the trunk channel in the unconfined floodplain. The stacked channels in FAC-Set 7 (Fig. 3.10, sections F11 - F14) suggest a Late-transgressive systems tract to early Highstand, supported by the paucity of unconfined channel deposits, and the lack of tidal-influence in FAC-Set 8. The amalgamated fluvial channels of FAC-Set 9, therefore is interpreted as the late highstand.

It would it be unlikely to have a continuous succession of out-of-valley floodplain deposits representing a single FAC, as the river should avulse periodically. This has implications for the area of lateral floodplain deposition. This area would define the width of the area of active deposition at any given time in a Ferron river. While FACs in this study are identified on the basis of laterally extensive paleosols, indicating a break in fluvial deposition or fluvial non-deposition, we question the potential lateral dimensions for a fluvial system to deposit sediment onto its floodplain, as depicted in Figures 3.10 (*lower*) and 3.11 (*lower*). Previous floodplain studies have considered the entire mudstone belt surrounding a river channel as its floodplain, extending at times in excess of 10's of kilometers (Behrensmeyer et al., 1995). Modelling and satellite imagery studies integrating paleohydraulic data with modern floodplain widths suggest that the width of an active floodplain scales to the dimensions of its feeder channel (Gross and Small, 1998; Beighley and Gummadi, 2011). Figure 3.12 plots the relationship of Amazon basin floodplain lateral widths (W_f) with bankfull discharge (Q_b), bankfull width (W_b) and channel depth (d_c) of the respective river. We plot paleohydraulic values for Ferron rivers from this study and published values along data trends from the Amazon basin to test our assumptions of how far we could potentially correlate fluvial deposits and hence, FACs (Li et al., 2010; Li and Bhattacharya, 2013; Wu and Bhattacharya, 2015; Bhattacharya et al., 2016; Famubode and Bhattacharya, 2016; Kimmerle and Bhattacharya, 2018; Wang and Bhattacharya, 2018). Much of the data regarding bankfull channel width (W_f) is empirically derived from width to depth relationships, however it does suggest that it may be possible to correlate our study with that of Famubode and Bhattacharya (2016), 2 km south in Sweetwater Wash for the laterally extensive FACs that lie above the valley margin. It would be unlikely however to assume lateral continuity of FACs over the 10 km correlation of that study, as documented Ferron rivers are typically 50 – 200 m wide, 1-7 m deep with discharges of less than 1500 m^2/s. For a river to extend its floodplain even 5 km, it would require a Ferron river to have twice its typical width, three times its maximum observed depth and an order of magnitude greater discharge. These scalling relationships imply a significant difference between a stratigraphic floodplain and the autogenic floodplain deposit of an active channel.

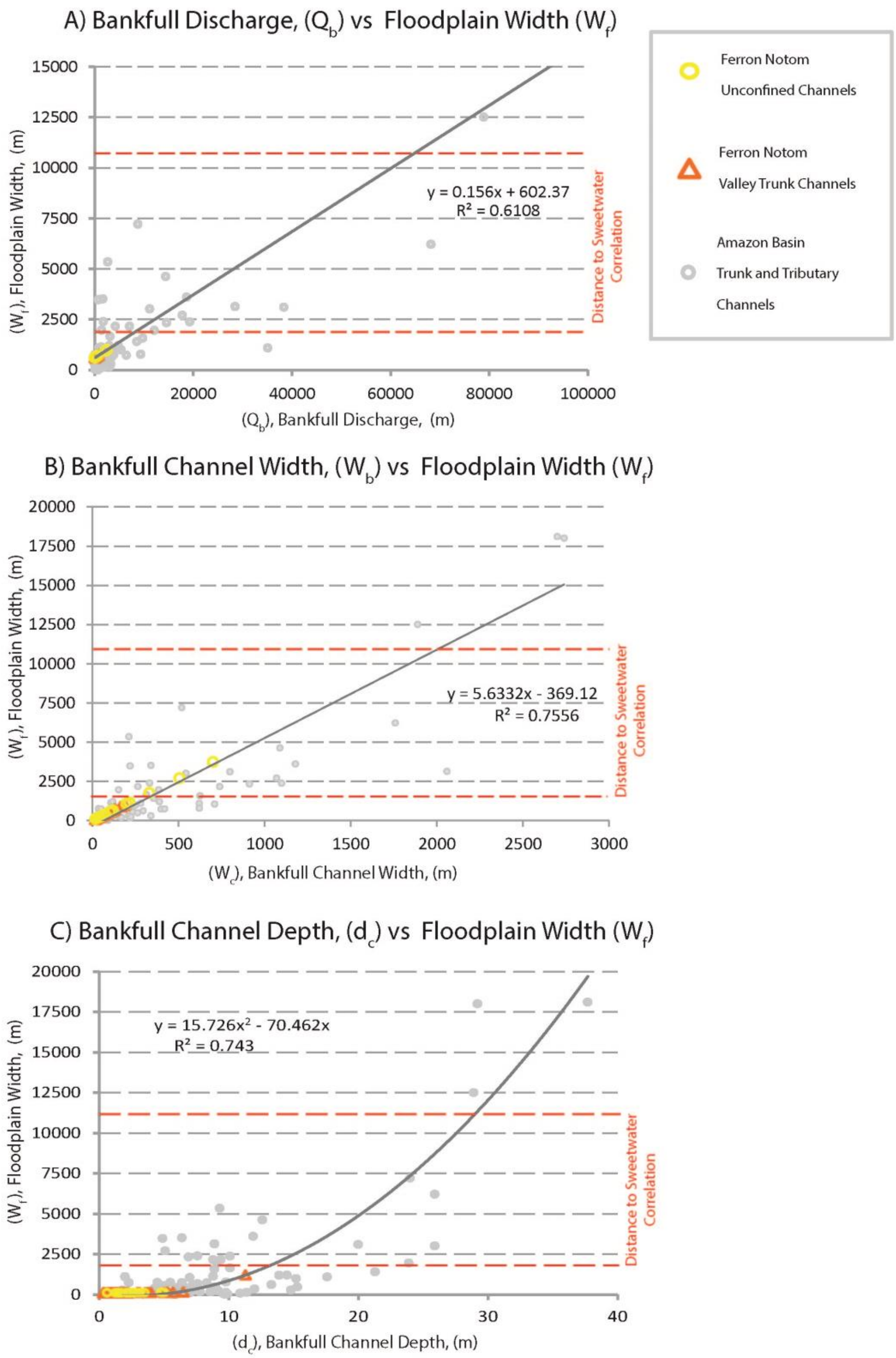
A) Bankfull Discharge, (Q_b) vs Floodplain Width (W_f)
Ferron Notom
Unconfined Channels
Ferron Notom
Valley Trunk Channels
Amazon Basin
Trunk and Tributary
Channels
y = 0.156x + 602.37
R² = 0.6108
Distance to Sweetwater Correlation
(W_f), Floodplain Width, (m)
(Q_b), Bankfull Discharge, (m)
B) Bankfull Channel Width, (W_b) vs Floodplain Width (W_f)
y = 5.6332x - 369.12
R² = 0.7556
Distance to Sweetwater Correlation
(W_f), Floodplain Width, (m)
(W_c), Bankfull Channel Width, (m)
C) Bankfull Channel Depth, (d_c) vs Floodplain Width (W_f)
y = 15.726x² - 70.462x
R² = 0.743
Distance to Sweetwater Correlation
(W_f), Floodplain Width, (m)
(d_c), Bankfull Channel Depth, (m)

Figure 3.12 (*previous page*): Scalling relationships of bankfull discharge (Q_b), bankfull channel width (W_f), and bankfull channel depth (d_c) to the lateral width of the floodplain associated with that channel in the Amazon Basin (Beighley and Gummadi, 2011). Error bars are not shown for purposes of clarity, average error values for Q_b are 100%, for W_f are 20% and for d_c are <5%. Ferron Notom valley trunk channels and unconfined channels are plotted relative to Amazon data trends. The 2 km distance to the outcrop location in Sweetwater and its distal correlated end 10 km along strike are shown (dashed red lines).

The constraints on lateral floodplain widths suggest that many of the correlations in this study may overestimate the lateral continuity of an individual FAC (Figs. 3.10 (*lower*) and 3.11(*lower*). While lap-out and erosive truncations of these surfaces are evident (Fig. 3.10), closer spaced measured sections may reveal a more fragmentary and discontinuous surface of deposition adjacent to the active channel. This lack of lateral correlation potential suggests that FAC are autogenic and shorter lived as the relatively immature paleosols suggest.

Correlation of FAC-sets (Fig. 3.13) show convincing similarity in coal layer cyclicity and each show a total of 9 preserved FAC-sets. These sets are similar in thickness and consistant in the total sequence thickness, suggesting that our FAC-sets are laterally extensive over kilometers to 10's of kilometers.

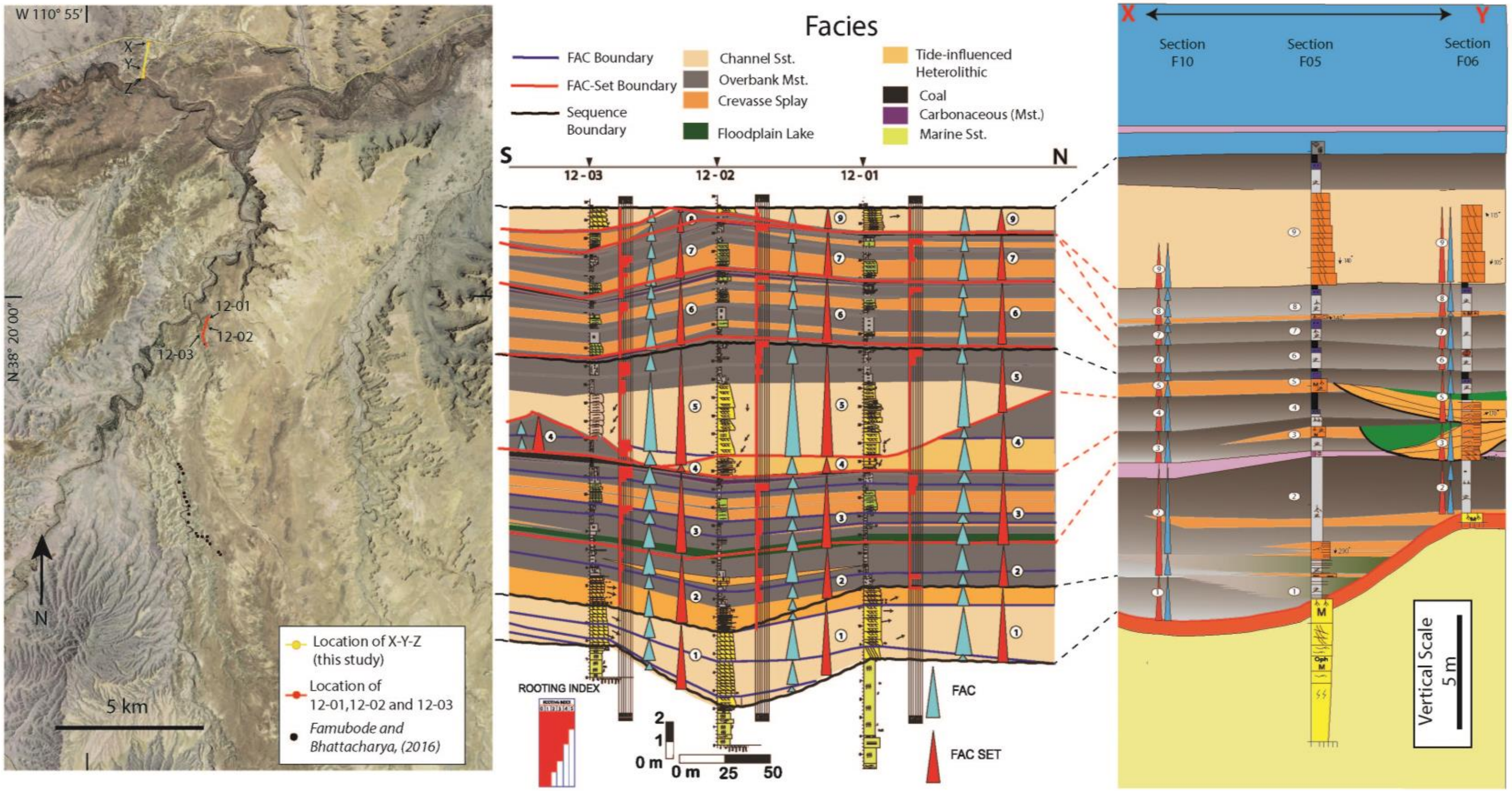

Figure 3.13: Correlation of the FACs and FAC-sets in our study area (*left and right*) to previous observations of FACs 10 km south of our outcrop (*middle*) (*modified from:* Famubode and Bhattacharya, 2016). Both correlations show a similar number of FACs, FAC-sets and channel patterns. The southern outcrop (*middle*) shows evidence of marine flooding horizons, which gave rise to the interpretation of multiple sequence boundaries no present in the northern outcrop.

3.8 Discussion

3.8.1 Backwater Controls and shoreline Proximity

Channel belt widths have been shown to decrease relative to their associated channel width within the backwater (Fernandes et al., 2016). Using data from the Mississippi and Rhine River systems (Fig. 3.14A), channel belt width to channel width ratios can be plotted along a regression to calculate their distance from the shoreline scaled to their backwater length. To determine the relevant backwater influences and whether this trunk tributary lies within the upper or lower backwater (Chatanantavet et al., 2012) we must isolate backwater conditions within the associated trunk channel at or near the confluence of these valleys. Trunk terraces 300 - 800 m from our study area in the adjacent valley have been documented (Kimmerle and Bhattacharya, 2018) and analysed for channel depths, channel widths, channel belt widths and slope values, consistent with estimate methods of Lynds *et al*., (2014). Three stacked valley terraces, so named V1 (youngest), V2 and V3, are identified with their corresponding geometries and backwater estimates. These valley terraces and the trunk tributary channel belt width to channel width ratios reveal distances of 5.1 to 19.4 km from the shoreline (Fig. 3.14B), along with their changes in elevation relative to sea level (Table 3.3). This method suggests that this trunk tributary valley does lie within the backwater calculated by Kimmerle and Bhattacharya, (2018). The original fall in sea level is determined by the basinward shift in facies and valley incision depths of 28 m (Kimmerle and Bhattacharya, 2018), less the height of a single channel story of 3.0 to 7.1 m (Li et al., 2010; Kimmerle and Bhattacharya, 2018). Subsequent changes in sea level are considered using calculated slope estimates and intermediate backwater lengths. Shoreline distance estimates suggest that V3 was a falling stage terrace, V2 a lowstand and V1 a transgressive valley fill.

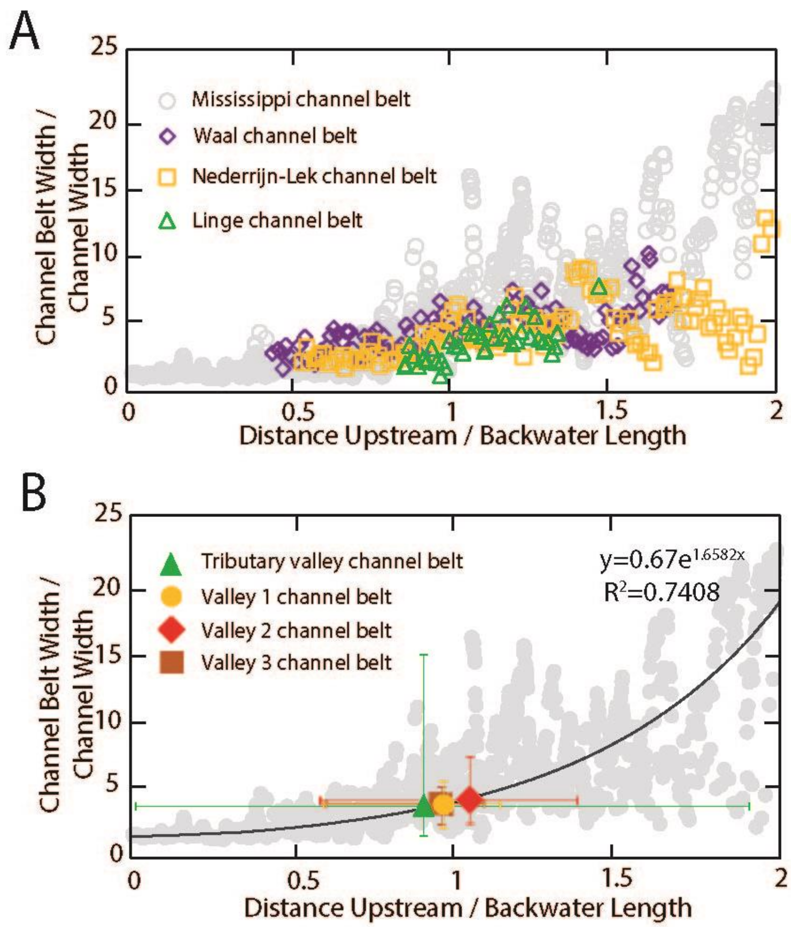

Figure 3.14: Backwater Scaling. A) Dimensionless scaling of fluvio-deltaic channel belts in the Mississippi and Rhine River System with respect to their location within the backwater (Fernandes et al., 2016). B) Valley terraces from a Ferron -Notom compound incised valley system (Kimmerle and Bhattacharya, 2018) and its tributary valley (this study) plotted along an exponential regression of the Mississippi/Rhine data (gray).

The deeper incisions of the valley found in cross-section A-B-C (Fig. 3.9) and X-Y-Z (Fig. 3.10) show elongate radial troughs or rills radiating perpendicular to the trunk valley (Kimmerle and Bhattacharya, 2018). With almost no sandstone onlapping the valley floor, we infer that this valley was not cut by a series of terrace forming scours, rather the valley base morphology suggest that this was cut by a process of tidal ravinement (Reijenstein et al., 2011). Similar features of tidal drainage patterns (Fig. 3.15) have been observed in Pleistocene fluvial deposits in the Gulf of Thailand (Reijenstein et al., 2011), in the modern Van Dieman Inlet of the Gulf of Carpentaria, Australia (Jones et al., 2003), and adjacent to the Memramcook River, New Brunswick. This interpretation implies that this valley was at one time within the tidal range and would therefore be within a distance to the coastline equivalent to the tidal range divided by the channel slope, which would define the tidal backwater, and be subject to variable intensities of neap-spring tide cycles (Dalrymple, 2010b). A 2 m tidal range with a an estimated trunk slope of $5x10^{-4}$ (Kimmerle and Bhattacharya, 2018) could propagate upstream <5km. With a calculated backwater length of ~20km (Kimmerle and Bhattacharya, 2018), the observation of tidal scour indicates this valley was in the lower backwater during the falling stage.

Table 3.3: Backwater Dimensions for V1, V2, and V3

Valley	Backwater length (km)*	Distance from coastline (km)	Slope*	Elevation M.A.S.L. (m)	Δ in Sea Level (m)
1	11.1 - 20.3	5.1 ± 4.5	0.00053	2.7	-2.7 ± 2.4
2	11.7 - 24.9	19.4 ± 9.1	0.00026	5.4	1.0 ± 1.7
3	2.9 - 7.6	14.8 ± 11.3	0.00033	4.4	-21 ± 5.0

The tidal drainage morphology of the trunk-tributary valley floor may support the interpretation that this valley was cut during the falling stage by tidal process, rather than by channel incision through the adjacent interflueves. This suggests that over time, shoreline, and therefore the tides, moved farther away, leaving this valley exposed during the late falling stage to early lowstand, explaining the depositional hiatus, valley floor paleosol and root development on the valley margin. Li *et al*., (2013) suggests that this compound valley was formed during a stepped, forced regression in which initially the shoreline moved further away during the evolution of the valley, as supported by our interpretation. As the valley is flooded, the shoreline moved landward once more, depositing tidally-influenced fluvial deposits in late stage valley fill. The overlying deposits of fluvial channels, floodplain deposits and laterally extensive coal layers may represent highstand, suggesting a complete cycle of sea level fall and rise.

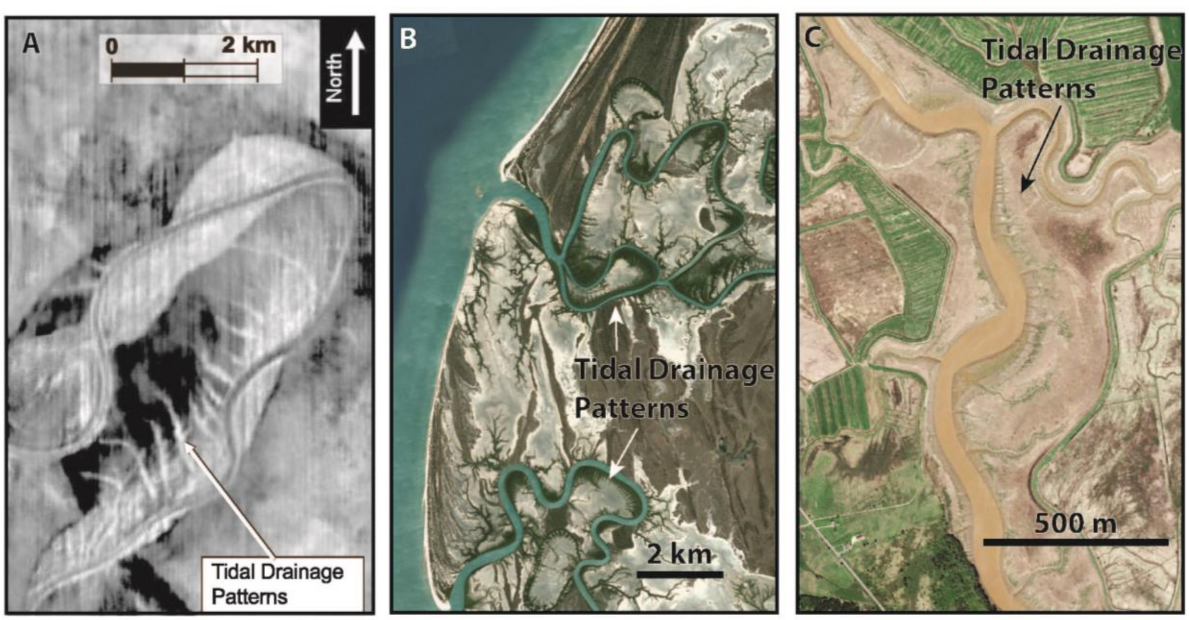

Figure 3.15: Analogues for tidal ravinement morphology. A) Seismic time slice of the

downstream limit of Pleistocene fluvial channels in the Gulf of Thailand (*modified from:* Reijenstein et al., 2011). B) Aerial photo tidal drainage near Van Dieman Inlet, Gulf of Carpentaria (*modified from:* Jones et al., 2003). C) Google Earth image of tidal drainage features along the Memramcook River near Dorchester, New Brunswick; a tributary of the Bay of Fundy.

3.8.2 Wheeler Analysis, Sedimentation Rates and Chronostratigraphy

Sanidine crystals extracted from bentonite layers collected during regional mapping of the Ferron Notom (Zhu et al., 2012) have been re-analysed (along with a new sample taken at the base of the valley in this study) using improved $^{40}Ar/^{39}Ar$ dating methods (Jicha et al., 2016). The results of this analysis are summarized in Table 3.4. The position of the upper bentonite (sample B4) and the bentonite found at the top of Sequence 3 (Sample B3) is shown on Figure 3.16. The time difference between these samples amounts to around 20 Ka, and chronometrically constrains the deposition of 2 sequences, with the highstand systems tract for Sequence 1 unaccounted for. Extrapolating for a 5 to10 Ka highstand duration, which conforms to the resulting temporal scale of Sequence 2 from the constraining bentonite dates; we infer a youngest chronometric value for the uppermost Ferron-Notom continental deposits of 91.13 Ma.

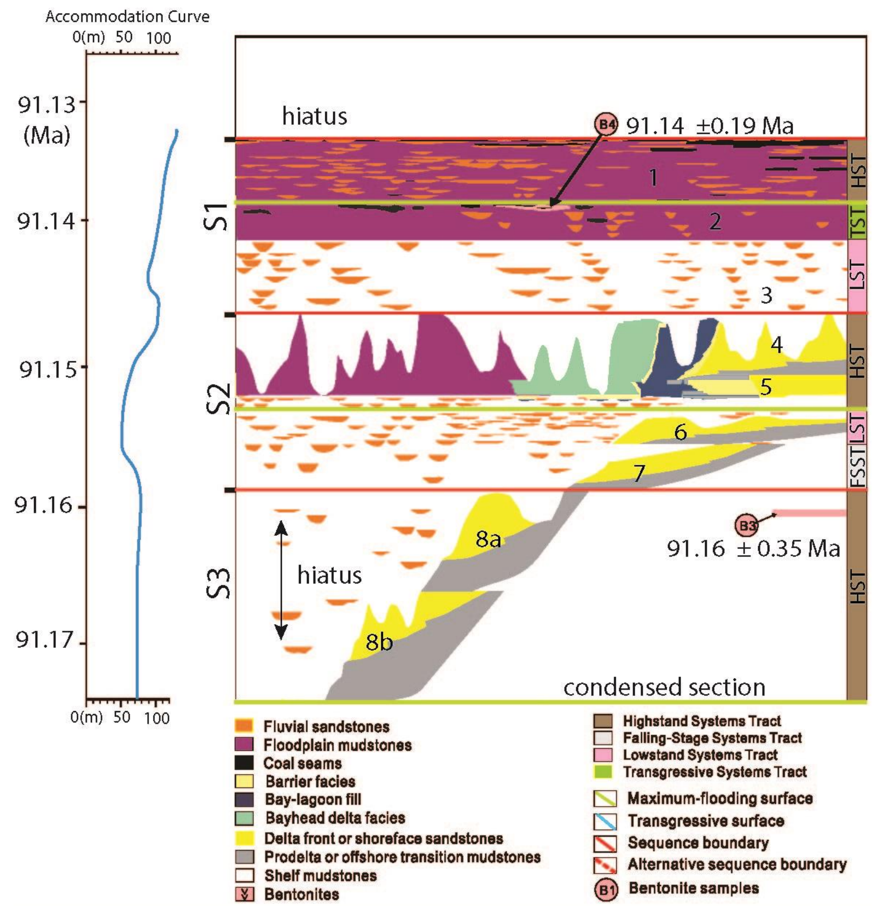

Figure 3.16: Wheeler diagram of Sequence 1 and 2 of the Ferron-Notom (*modified from:* Zhu et al., 2012)**.** Chronostratigraphic relationships of valley erosion and fluvial deposition are considered to be diachronous accross a compound valley surface. The locations of bentonite samples with their reported chronometric values are shown. These dates form the basis for the timeline on the vertical axis. The location of sample B1 at the base of the Ferron on the condensed section at the top of the Tununk Shale Member is not shown.

<u>Table 3.4: $^{40}Ar/^{39}Ar$ dating of Sanidine Crystals from Bentonite Beds</u>

	Previous Analysis			This Study		
Sample #	n	MSWD	Weighted Mean AGE (Ma) ± 2s	n	MSWD	Weighted Mean AGE (Ma) ± 1σ
UH-BHA-B4	8 of 8	0.84	90.64 ± 0.25	13 of 26	0.64	91.14 ± 0.19
FN-BHt				16 of 16	1.42	91.15 ± 0.11
UH-BHA-B3	12 of 14	1.05	90.69 ± 0.34	6 of 15	0.20	91.16 ± 0.36
UH-BHA-B1	13 of 13	0.69	91.25 ± 0.77	27 of 30	1.35	91.90 ± 0.12

The correlation diagram defined by points X-Y-Z (Fig. 3.10) is placed in Wheeler space (Fig. 3.17) using a combination of the described chronostratigraphic surfaces, estimated hiatus periods inferred from paleosol maturity (Retallack, 1988; Kraus and Aslan, 1999; Prochnow et al., 2006; Cleveland et al., 2007) and published sedimentation rates of floodplain and peat accumulations (Table 3.5)(Anderson, 1964; Hickey, 1980; Rahmani and Flores, 1984; Bown and Kraus, 1987; Smith, N et al., 1989; Staub and Esterle, 1994; Neuzil, 1997; Walker et al., 1997; Bristow, 1999; Hensel et al., 1999; Kraus and Aslan, 1999; Bridge, 2006; Bourgoin et al., 2007; Aalto et al., 2008; Gautier et al., 2010; Famubode and Bhattacharya, 2016). Using the observed maturity of paleosols in this study to infer the duration of subaerial exposure, we identify 3 common types; entisols, which take between 100 and 600 years to develop, inceptisols that require 600 to 4000 years, and histosols, which are determined based on decompacted peat thicknesses (Table 3.5). Sediment accumulations are calculated by maximum thicknesses at the FAC level and assume a uniform sedimentation rate for the purpose of Wheeler analysis. Floodplain sediment thicknesses (Table 3.2) are decompacted 16% (Hensel et al., 1999) to account for the difference in the initial porosity of floodplain muds of around 36% (Nadon and Issler, 1997) and the preserved porosity of floodplain mudstones of around 20% (Hammer et al., 2010). Coal thicknesses are decompacted to peat thicknesses at a ratio of 2.2:1(Nadon, 1998; Famubode and Bhattacharya, 2016). We vary the timing of deposition to reflect floodplain sedimentation rates that range from 1.1 mm/a representative of the Rhone Delta (Hensel et al., 1999); to 6 mm/a similar to a system like the Rio Beni or the Fly-Strickland rivers (Aalto et al., 2008; Gautier et al., 2010). Peat accumulation rates are assumed to be somewhere between the global average of 1.7 mm/a (Rahmani and Flores, 1984) and the tropical swamps of Borneo and Sumatra at 4.8 mm/a (Anderson, 1964; Neuzil, 1997).

Table 3.5: Floodplain and Peat Accumulation Rates

Sediment Mud	Location	Accumulation rates (mm/a)	Source
Peat	Borneo	4.8	*Anderson, 1964*
Peat	Clarkes Fork Basin	0.39	*Hickey, 1980*
Peat	Fort Union Powder River	0.15	*Rahmani and Flores, 1981*
Peat	Global average	1.72	*Rahmani and Flores, 1981*
Peat	Sumatra	6 - 13	*Neuzil, 1997*
Peat	Sarawak, East Malaysia	1.4	*Staub and Esterle, 1994*
Peat	Modern Tropical Deltas	2.5	*Famubode and Bhattacharya, 2016*
Floodplain Muds	Willwood Fm, Big Horn Basin	0.3 - 0.7	*Bown and Kraus, 1987*
Floodplain Muds	Saskachewan River	2.5	*Smith et al., 1989*
Floodplain Muds	Grand River, Ontario	0.5 - 0.7	*Walker, 1997*
Floodplain Muds	Mississippi Delta	1 - 10	*Kraus and Aslan, 1999*
Floodplain Muds	Rhone Delta, FR	1.1 - 1.2	*Hensel et al., 1999*
Floodplain Muds	Amazon River, BR	1.2 - 1.9	*Maurice-Bourgouin et al., 2007*
Floodplain Muds	Rio Beni, Bolivia	3 - 6	*Gautier et al., 2010*
Floodplain Muds	Fly-Strickland, New Guinnea	7	*Aalto et al., 2008*

The chronostratigraphic implications of considering the uncertainty in sedimentation rates and duration of pedogenesis are summarized in Table 3.6. The immaturity of the paleosol horizons in this trunk tributary valley fill and the overlying unconfined floodplain suggests that sedimentation was somewhat continuous over this 10 to 20 Ka long sequence. Floodplain sedimentation and peat accumulation rates were high, consistent with modern tropical peat deposits. Figure 3.17 combines the interpretation of FAC-sets with the age dating of chronostratigraphic surfaces and the time occupied by sedimentation, while the hiatuses represent periods of pedogenic soil development. The assumptions that were made regarding sedimentation rates, which were shown to be consistent with bentonite age dates, support previous estimates of FACs depositing in 25-2000 a and FAC-sets depositing in 240 -14,000 a (Famubode and Bhattacharya, 2016), but suggest that fluvial sequences may deposit in half as much time as the previously interpreted range of 20, 000 -40,000 a. Correlation of FAC-sets described by Famubode and Bhattacharya (2016) and those identified in this study show similar FAC-sets, FACs and channel geometries (Fig. 3.13). Our age dating suggests that previously interpreted fluvial sequences within this interval are 5 to 10 ka in duration as opposed to 20 – 40 ka. The timing of FAC-sets are therefore on the scale of 1000s of years. These frequencies are too slow for continental scale drainages to avulse (Aslan et al., 2005) let alone smaller scale rivers like the Ferron. The lateral extent of the FAC–sets suggest that it may be too large to be deposited by a single river, and combined with a timescale of 1000s of years; it may represent fluvial responses to higher frequency allogenic forcing of climatic cycles (Schumm and Etheridge, 1994).

Table 3.6: Sedimentation and Paleosol Development Scenarios

Conditions	Floodplain Accumulation Rate (mm/a)	Peat Accumulation Rate (mm/a)	Paleosol Duration (a)	Sequence 1 Duration (Ka)
Low sedimentation/ max pedogenesis	1.1	1.7	600 - 4000	40.2
Low sedimentation/ min pedogenesis	1.1	1.7	100 - 600	32.9
High sedimentation/ max pedogenesis	6.0	4.8	600 - 4000	17.1
High sedimentation/ min pedogenesis	6.0	4.8	100-600	8.2

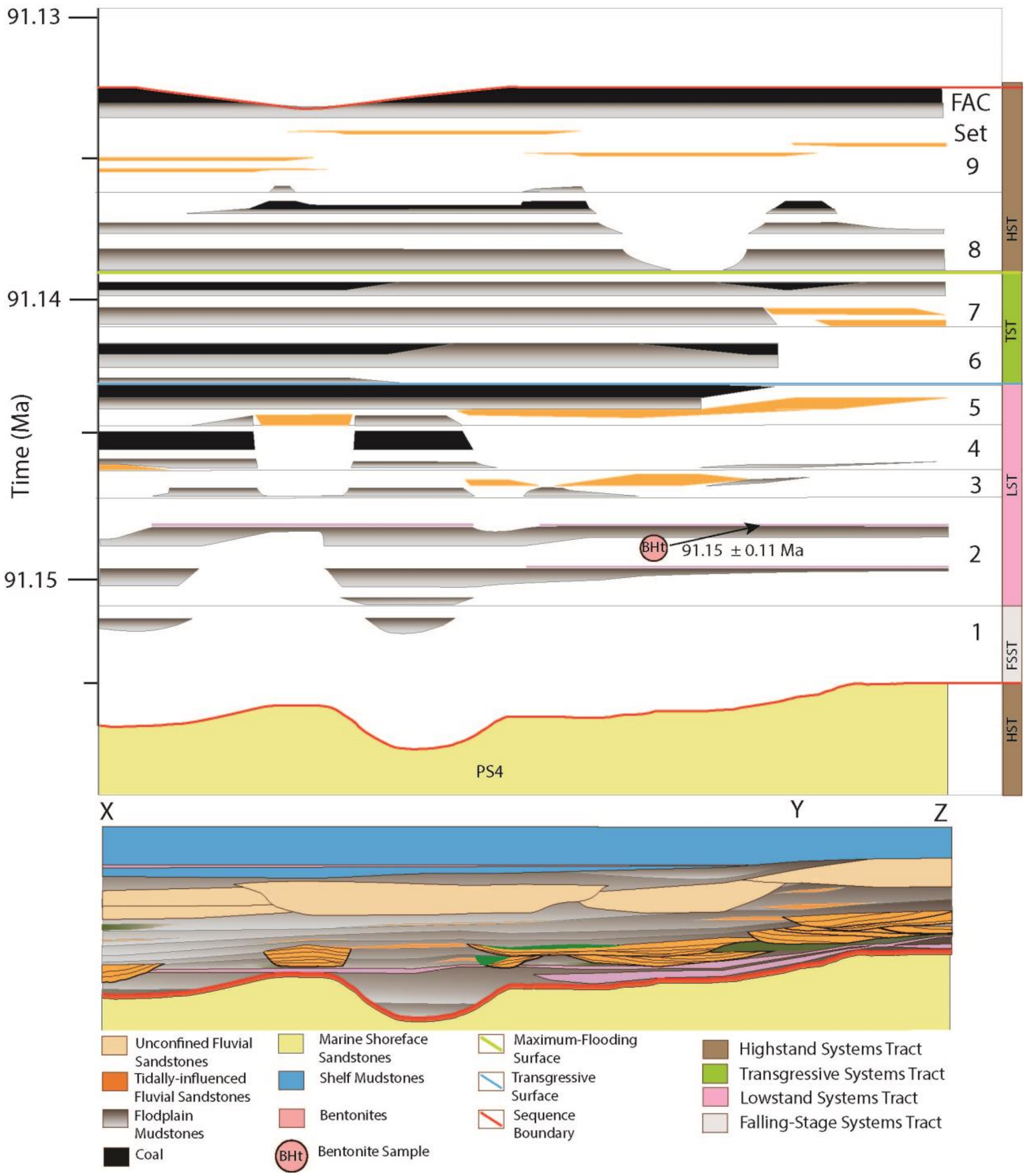

Figure 3.17: The evolution of our trunk-tributary valley shown in Wheeler space at correlation X-Y-Z. Uppermost surface and the valley floor take their timing from Figure 15, while the intermediate sample BHt (Table 3.4) supports our interpretation of a 10 – 20 ka fluvial sequence.

Both the calculation of accumulation time and sanidine chronometry agree that previous Wheeler analyses of this sequence (Li and Bhattacharya, 2013; Famubode and Bhattacharya, 2016; Kimmerle and Bhattacharya, 2018) have overestimated the period of this sequence by a factor of between 3 and 5. In the case of Famubode and Bhattacharya (2016), this overestimation was perhaps due to the identification of dinocyst-rich horizons indicating multiple marine flooding surfaces. Multiple flooding surfaces would suggest multiple parasequence boundaries. Consequently, either higher frequency cycles in relative sea level have been overlooked in our study; or evidence of Milankovitch scale cyclicity has been previously misinterpreted within the youngest sequence of the Ferron-Notom fluvial deposits, and a single rise and fall of sea level may account for the entire stratigraphy of Sequence 1. Our shortened evaluation of timing calls into question any similarity between the cyclicity of FAC-sets and marine parasequences and is evidence that the processes responsible for FACs are likely autogenic in nature while FAC-sets may represent high frequency allogenic factors, including climate.

3.8.3 Tidally-Influenced Incised Trunk-Tributary Valley Model

While the existence of trunk- tributary valleys has been widely noted, few studies have discussed or documented the nature of their formation, morphology and fill. Valley networks in the Basal Quartz of the Western Canadian Basin show tributary junction scours (Ardies et al., 2002; Boyd et al., 2006), which implies a convergence of channels, however it is not clear which is tributary and which trunk. The work by Kvale and Archer (2007) in the the Illinois Basin document that the trunk valleys tend to be filled with medium to coarse grained fluvial sandstones with pebble conglomerates at the base of channels. In contrast, the Illinois Basin tributary valleys are filled with conodont and brachiopod prone mudstones and laminated siltstones interpreted to be of tidal origin. This juxtaposition suggests different stages of filling and highlights the need to understand the sequential stages of valley filling and the effect of tidal processes in these deposits. In contrast to Kvale and Archer (2007), our study shows more fluvial dominated fill with tidally-influenced deposits and perhaps even tidal mediation or reworking, but little evidence of direct marine incursion, such as in the transgressive valley fill of the Illinois Basin. Occurances of lacustrine interpreted deposits in the tributary valley of this study suggest that damming may be a significant depositional process in tributaries.

Our observations challenge our understanding of standard sequence stratigraphic and valley fill facies models. Sequence stratigraphic valley models predict fluvial excavation of an elongate topographic low that is considerably deeper than the channel that fills it (Zaitlin et al., 1994). The topographic low is first filled by braided fluvial deposits with tidal tidally-influenced deposits in the upper, late stage fill (Shanley and McCabe, 1994). In this study we show an ovate to radial branching topographic low (Fig. 3.6) that lacks channelized scour morphology. While many of the aspects of this tributary valley satisfy the definitions of an incised valley, in that it is much deeper than the rivers that feed it; the valley floor does not appear to be cut by rivers and shows evidence that it was cut by tidal processes (Reijenstein et al., 2011). The valley floor is almost entirely covered by floodplain mudstones, and show tidally-influenced fluvial sandstones being deposited later. Estuarine and drowned valley models predict a fully marine outer segment at the distal end of the valley with wave to tidal influenced sand barriers

(Dalrymple et al., 2003b), where we show confluence with a fluvial to tidally influenced trunk valley (Fig. 3.6) (Kimmerle and Bhattacharya, 2018).

3.9 Conclusions

We document the depositional facies of an incised trunk-tributary valley and the youngest depositional sequence within the upper backwater of the Cretaceous Notom delta in the Ferron Sandstone. Despite their recognition in several well correlation and seismic studies, we address the lack of detailed facies description and bedding analysis of these ubiquitous valleys. Using high resolution GPS data and geostatistical interpolation tools, we have mapped the spatial extent and geomorphology of this 1 km^2 valley floor and constrained the thickness of valley fill to be 20 ± 0.5m. Channel belt to channel width ratios of the tidally-influenced fluvial sandstones that fill this valley are consistant with this trunk-tribulary being in the lower backwater of the Notom Delta, and valley floor morphology is consistant with modern seismic imaged tidal drainage patterns.

Our study identifies 17 distinct lithofacies and 5 facies associations in the underlying shoreface, valley fill, and overlying fluvial deposits not confined by the valley. The trunk-tributary valley fill is dominated by floodplain facies consisting of organic-rich mudstones, floodplain lake deposits and floodplain paleosols with subordinate deposits of tidally-influenced channel facies, and minor coal and carbonaceous shale facies.

Using a framework of fluvial aggradation cycles (FACs) we correlate 32 FACs grouped into 9 fluvial aggradation cycle sets (FAC-sets) over a 1 km^2 study area, and to a previous study over 10 Km away. Autogenic floodplain deposits of channels in this study are unlikely to correlate distances greater than a few hundred meters, and do not extend greater than a kilometer or two across the stratigraphic floodplain of the Sequence 1 Highstand.

Sanidine $^{40}Ar/^{39}Ar$ dating of bentonite horizons have constrained the valley cutting, filling and overtopping stages to a duration of 15 ± 5 Ka, consistent with high frequency Milankovitch scale periodicity, but well short of the previously assumed 100 Ka time scale. High frequency Milankovitch cycles are therefore unlikely to control FACs or FAC-sets in our study

Acknowledgements

This paper was written with the generous support of the Susan Cunningham Research Chair at McMaster University, Quantitative Sedimentology Laboratories, with funding from BP, Ecopetrol, INPEX and NSERC. Extraction preparation of sanidine grains from bentonite samples for chronometric dating was done by Nick Randazzo and Greg Hemon.

References

Aalto, R., Lauer, J.W., and Dietrich, W.E., 2008, Spatial and temporal dynamics of sediment accumulation and exchange along Strickland River floodplains (Papua New Guinea) over decadal-to-centennial timescales: Journal of Geophysical Research: Earth Surface, v. 113, no. 1, p. 1–22, doi: 10.1029/2006JF000627.

Akyuz, I., Warny, S., Famubode, O., and Bhattacharya, J.P., 2015, Palynology of the Upper Cretaceous (Turonian) Ferron Sandstone Member, Utah, USA: identification of marine flooding surfaces and Milankovitch cycles in subtropical, ever-wet, paralic to non-marine palaeoenvironments: Palynology, v. 0, no. 0, p. 1–15, doi: 10.1080/01916122.2015.1014525.

Anderson, J.A.R., 1964, Structure and development of the peat swamps of Sarawak and Brunei: Journal of Tropical Geography, v. 18, p. 7–16.

Ardies, G.W., Dalrymple, R.W., and Zaitlin, B.A., 2002, Controls on the geometry of incised valleys in the Basal Quartz unit (Lower Cretaceous), Western Canada Sedimentary Basin: Journal of Sedimentary Research, v. 72, no. 5, p. 602–618, doi: 10.1306/032101720602.

Armstrong, R.L., 1968, Sevier orogenic belt in Nevada and Utah: Geological Society of America Bulletin, v. 79, no. 3, p. 429–458.

Aslan, a., Autin, W.J., and Blum, M.D., 2005, Causes of River Avulsion: Insights from the Late Holocene Avulsion History of the Mississippi River, U.S.A.: Journal of Sedimentary Research, v. 75, no. 4, p. 650–664, doi: 10.2110/jsr.2005.053.

Atchley, S.C., Nordt, L.C., and Dworkin, S.I., 2007, Eustatic Control on Alluvial Sequence Stratigraphy: A Possible Example from the Cretaceous-Tertiary Transition of the Tornillo Basin, Big Bend National Park, West Texas, U.S.A.: Journal of Sedimentary Research, v. 74, no. 3, p. 391–404, doi: 10.1306/102203740391.

Behrensmeyer, A.K., Willis, B.J., and Quade, J., 1995, Floodplains and Paleosols of Pakistan Neogene and Wyoming Paleogene Deposits: A Comparative Study: Palaeogeography, Palaeoclimatology, Palaeoecology, v. 115, p. 37–60.

Beighley, R.E., and Gummadi, V., 2011, Developing channel and floodplain dimensions with limited data: A case study in the Amazon Basin: Earth Surface Processes and Landforms, v. 36, no. 8, p. 1059–1071, doi: 10.1002/esp.2132.

Bhattacharya, J.P., Copeland, P., Lawton, T.F., and Holbrook, J., 2016, Estimation of source area, river paleo-discharge, paleoslope, and sediment budgets of linked deep-time depositional systems and implications for hydrocarbon potential: Earth-Science Reviews, v. 153, p. 77–110, doi: 10.1016/j.earscirev.2015.10.013.

Bhattacharya, J.P., and Tye, R.S., 2004, Searching for modern Ferron analogs and application to subsurface interpretation: Regional to Wellbore Analog for Fluvial–Deltaic Reservoir Modeling: the Ferron Sandstone of Utah: American Association of Petroleum Geologists, Studies in Geology 50, p. 39–57.

Blum, M.D., and Hattier-womack, J., 2009, Climate change, sea-level change, and fluvial sediment supply to deepwater systems, *in* Kneller, B., Martinsen, O.J., McCaffrey, B. ed., External Controls on Deep Water Depositional Systems: Climate, Sea-Level, and Sediment Flux: SEPM Special Publication, SEPM Special Publication, p. 15–39.

Blum, M., Martin, J., Milliken, K., and Garvin, M., 2013, Paleovalley systems: Insights from Quaternary analogs and experiments: Earth-Science Reviews, v. 116, no. 1, p.

128–169, doi: 10.1016/j.earscirev.2012.09.003.

Bourgoin, L.M., Bonnet, M.P., Martinez, J.M., Kosuth, P., Cochonneau, G., Moreira-Turcq, P., Guyot, J.L., Vauchel, P., Filizola, N., and Seyler, P., 2007, Temporal dynamics of water and sediment exchanges between the Curuaí floodplain and the Amazon River, Brazil: Journal of Hydrology, v. 335, no. 1–2, p. 140–156, doi: 10.1016/j.jhydrol.2006.11.023.

Bown, T.M., and Kraus, M.J., 1987, Integration of channel and floodplain suites. I. Developmental sequence and lateral relations of alluvial paleosols.: Journal of Sedimentary Petrology, v. 57, no. 4, p. 587–601, doi: 10.1306/212F8BB6-2B24-11D7-8648000102C1865D.

Boyd, R., Dalrymple, R.W., and Zaitlin, B. a, 2006, Estuarine and incised-valley facies models: Special Publication - Society for Sedimentary Geology, v. 84, no. 84, p. 171–235, doi: 10.2110/pec.06.84.0171.

Bridge, J.S., 2006, Fluvial facies models: recent developments, *in* Posamentier, H.W. and Walker, R.G. eds., Facies Models Revisited: SEPM Special Publication 84, p. 85–168.

Bristow, C.S., 1999, Gradual avulsion, river metamorphosis and reworking by underfit streams; a modern example from the Brahmaputra River in Bangladesh and a possible ancient example in the Spanish Pyrenees BT - Fluvial sedimentology VI; proceedings (N. D. Smith & J. Rogers, Eds.): Special Publication of the International

Association of Sedimentologists, v. 28, p. 221–230, doi: 10.1002/9781444304213.ch17.

Campbell, C.E., 2013, Valley Widening and the Composite Nature of Valley Margin Sequence Boundaries: Evidence from the Neilson Wash Compound Valley Fill, Cretaceous Ferron: University of Houston, 108 p.

Chatanantavet, P., Lamb, M.P., and Nittrouer, J. a., 2012, Backwater controls of avulsion location on deltas: Geophysical Research Letters, v. 39, no. 1, p. n/a-n/a, doi: 10.1029/2011GL050197.

Cleveland, D.M., Atchley, S.C., and Nordt, L.C., 2007, Continental Sequence Stratigraphy of the Upper Triassic (Norian Rhaetian) Chinle Strata, Northern New Mexico, U.S.A.: Allocyclic and Autocyclic Origins of Paleosol-Bearing Alluvial Successions: Journal of Sedimentary Research, v. 77, no. 11, p. 909–924, doi: 10.2110/jsr.2007.082.

Clifton, H.E., 2006, A reexamination of facies models for clastic shorelines: Facies Models Revisited, , no. 84, p. 293–337, doi: 10.2110/pec.06.84.

Colombera, L., Mountney, N.P., and McCaffrey, W.D., 2015, A meta-study of relationships between fluvial channel-body stacking pattern and aggradation rate: Implications for sequence stratigraphy: Geology, v. 43, no. 4, p. 283–286, doi: 10.1130/G36385.1.

Colombera, L., Shiers, M.N., and Mountney, N.P., 2016, Assessment of Backwater

Controls On the Architecture of Distributary-Channel Fills In A Tide-Influenced Coastal-Plain Succession: Campanian Neslen Formation, U.S.A.: Journal of Sedimentary Research, v. 86, no. 5, p. 476–497, doi: 10.2110/jsr.2016.33.

Corbeanu, R.M., Wizevich, M.C., Bhattacharya, J.P., Zeng, X., and McMechan, G. a., 2004, Three-dimensional architecture of ancient lower delta-plain point bars using ground-penetrating radar, Cretaceous Ferron Sandstone, Utah: AAPG Studies in Geology, v. 50, p. 427–449.

Dalrymple, R.W., 2010, Tidal Depositional Systems, *in* Dalrymple, R.W. and James, N.P. eds., Facies Models 4, p. 201–233.

Dalrymple, R.W., Zaitlin, B.A., and Boyd, R., 2003, Estuarine facies models; conceptual basis and stratigraphic implications; discussion and reply: Journal of Sedimentary Research, v. 62, no. 6, p. 1130–1146, doi: 10.1306/d4267f50-2b26-11d7-8648000102c1865d.

DeCelles, P.G., and Coogan, J.C., 2006, Regional structure and kinematic history of the Sevier fold-and-thrust belt, central Utah: Bulletin of the Geological Society of America, v. 118, no. 7–8, p. 841–864, doi: 10.1130/B25759.1.

Decelles, P.G., Lawton, T.F., and Mitra, G., 1995, Thrust timing, growth of structural culminations, and synorogenic sedimentation in the type Sevier orogenic belt, western United States: Geology, v. 23, no. 8, p. 699–702, doi: 10.1130/0091-7613(1995)023<0699:TTGOSC>2.3.CO;2.

Famubode, O.A., and Bhattacharya, J.P., 2016, Sequence Stratigraphic Analysis of the Youngest Nonmarine Sequence In the Cretaceous Ferron Notom Delta, South Central Utah, U.S.A.: Journal of Sedimentary Research, v. 86, no. 3, p. 168–198, doi: 10.2110/jsr.2016.8.

Fernandes, A.M., Törnqvist, T.E., Straub, K.M., and Mohrig, D., 2016, Connecting the backwater hydraulics of coastal rivers to fluvio-deltaic sedimentology and stratigraphy: Geology, v. 44, no. 12, doi: 10.1130/G37965.1.

Fielding, C.R., 2011, Foreland basin structural growth recorded in the Turonian Ferron Sandstone of the Western Interior Seaway Basin, USA: Geology, v. 39, no. 12, p. 1107–1110, doi: 10.1130/G32411.1.

Fielding, C.R., 2010, Planform and Facies Variability in Asymmetric Deltas: Facies Analysis and Depositional Architecture of the Turonian Ferron Sandstone in the Western Henry Mountains, South-Central Utah, U.S.A.: Journal of Sedimentary Research, v. 80, no. 5, p. 455–479, doi: 10.2110/jsr.2010.047.

Gardiner, 1995, Tectonic and eustatic controls on the stratal architecture of mid-Cretaceous strati- graphic sequences, central western interior foreland basin of North America.

Gautier, E., Brunstein, D., Vauchel, P., Jouanneau, J.M., Roulet, M., Garcia, C., Guyot, J.L., and Castro, M., 2010, Channel and floodplain sediment dynamics in a reach of the tropical meandering Rio Beni (Bolivian Amazonia): Earth Surface Processes and

Landforms, v. 35, no. 15, p. 1838–1853, doi: 10.1002/esp.2065.

Gross, L.J., and Small, M.J., 1998, River and floodplain process simulation for subsurface characterization: Water Resources Research, v. 34, no. 9, p. 2365–2376, doi: 10.1029/98WR00777.

Hammer, E., Mørk, M.B.E., and Næss, A., 2010, Facies controls on the distribution of diagenesis and compaction in fluvial-deltaic deposits: Marine and Petroleum Geology, v. 27, no. 8, p. 1737–1751, doi: 10.1016/j.marpetgeo.2009.11.002.

Hensel, P.E., Jr, J.W.D., Pont, D., Henselt, P.F., and Day, J.W., 1999, Wetland Vertical Accretion and Soil Elevation Change in the Rhône River Delta , France : The Wetland Vertical Accretion and Soil Elevation Change in the Rh6ne River Delta , France : The Importance of Riverine Flooding: Journal of Coastal Research, v. 15, no. 3, p. 668–681.

Hickey, L.J., 1980, Early Cenozoic Paleontology and Stratigraphy of the Bighorn Basin, Wyoming, 1880-1980: University of Michigan, Papers on Paleontology, v. 24, p. 33–50.

Hill, R.B., 1982, Depositional Environments of the Upper Cretaceous Ferron Sandstone south of Notom, Wayne County: Brinham Young University, Geology Studies, v. 29, p. 59–83.

Hilton, B., 2013, 3D Allostratigraphic Mapping and Facies Heterogeneity of a Compound, Tributary Incised Valley System, Turonian Ferron Sandstone, Notom

Delta, South-Central Utah [MS thesis]: University of Houston, 136 p.

Holbrook, J.M., and Bhattacharya, J.P., 2012, Reappraisal of the sequence boundary in time and space: Case and considerations for an SU (subaerial unconformity) that is not a sediment bypass surface, a time barrier, or an unconformity: Earth-Science Reviews, v. 113, no. 3–4, p. 271–302, doi: 10.1016/j.earscirev.2012.03.006.

Jicha, B.R., Singer, B.S., and Sobol, P., 2016, Re-evaluation of the ages of 40 Ar/ 39 Ar sanidine standards and supereruptions in the western U.S. using a Noblesse multi-collector mass spectrometer: Chemical Geology, v. 431, p. 54–66, doi: 10.1016/j.chemgeo.2016.03.024.

Jones, B.G., Woodroffe, C.D., and Martin, G.R., 2003, Deltas in the Gulf of Carpentaria, Australia: Forms, Processes and Products: Tropical Deltas of Southeast Asia—Sedimentology, Stratigraphy, and Petroleum Geology, SEPM Spec Pubs 76, v. 76, p. 21–43.

Kimmerle, S., and Bhattacharya, J.P., 2018, Facies, Backwater Limits, and Paleohydraulic Analysis of Rivers in a Forced- Regressive, Compound Incised Valley, Cretaceous Ferron Sandstone, Utah, U.S.a.: , no. February, p. 177–200, doi: 10.2110/jsr.2018.5.

Kimmerle, S., Kynaston, D., and Bhattacharya, J.P., 2016, A long-lived compound incised mega-valley in the Cretaceous Ferron Sandstone, Utah [Abstract], *in* American Association of Petroleum Geologists, Annual Convention, Calgary, Canada,.

Kraus, M.J., and Aslan, A., 1999, Palaeosol Sequences in Floodplain Environments: A Hierarchical Approach: Palaeoweathering, Palaeosurfaces and Related Continental Deposits, , no. 27, p. 303–321, doi: 10.1002/9781444304190.ch12.

Kvale, E.P., and Archer, A.W., 2007, Paleovalley fills: Trunk vs. tributary: AAPG Bulletin, v. 91, no. 6, p. 809–821, doi: 10.1306/11060606022.

Lamarre, R.A., 1991, Coalbed Methane Production from Previous Ferron Coals at Buzzard Bench Field, Utah, *in* Chidsey, T.C., Adams, R.D., and Morris, T.H. eds., AAPG Studies in Geology No. 50: Regional to Wellbore Analog for Fluvial-Deltaic Reservoir Modeling, p. 551–558.

Li, Y., and Bhattacharya, J.P., 2013, Facies-Architecture Study of A Stepped, Forced Regressvie Compound Incised Valley In the Ferron Notom Delta, Southern Central Utah, U.S.A: Journal of Sedimentary Research, v. 83, no. 3, p. 206–225, doi: 10.2110/jsr.2013.19.

Li, W., Bhattacharya, J.P., and Campbell, C., 2010, Temporal Evolution of Fluvial Style in a Compound Incised-Valley Fill, Ferron "Notom Delta", Henry Mountains Region, Utah (U.S.A.): Journal of Sedimentary Research, v. 80, no. 1994, p. 529–549, doi: 10.2110/jsr.2010.053.

Li, W., Bhattacharya, J., and Zhu, Y., 2011, Architecture of a forced regressive systems tract in the Turonian Ferron "Notom Delta", southern Utah, U.S.A.: Marine and

Petroleum Geology, v. 28, no. 8, p. 1517–1529, doi: 10.1016/j.marpetgeo.2011.05.004.

MacEachern, J.A., Pemberton, S.G., Gingras, M.K., and Bann, K.L., 2010, Ichnology and Facies Models, *in* Dalrymple, R.W. and James, N.P. eds., Facies Models 4, Geological Association of Canada. Geotext, p. 19–58.

Mattheus, C.R., and Rodriguez, A.B., 2014, Controls On Lower-Coastal-Plain Valley Morphology and Fill Architecture: Journal of Sedimentary Research, v. 84, no. 4, p. 314–325, doi: 10.2110/jsr.2014.30.

McCarthy, P.J., and Plint, A.G., 2003, Spatial variability of palaeosols across Cretaceous interfluves in the Dunvegan Formation, NE British Columbia, Canada: Palaeohydrological, palaeogeomorphological and stratigraphic implications: Sedimentology, v. 50, no. 6, p. 1187–1220, doi: 10.1111/j.1365-3091.2003.00600.x.

Nadon, G.C., 1998, Magnitude and timing of peat-to-coal compaction: , p. 727–730.

Nadon, G.C., and Issler, D.R., 1997, The Compaction of Floodplain Sediments: Timing, Magnitude and Implications: Geoscience Canada, v. 24, no. 1, p. 37–43.

Neuzil, S.G., 1997, Onset and rate of Peat and Carbon accumulation in four domed ombrogenous peat deposits, Indonesia, *in* Rieley, J.O. and Page, S.E. eds., Biodiversity and Sustainability in Peatlands - Proceedings of the International Symposium on Tropical Peatlands, Palangka Raya, Indonedia, Samara Publishing, Cardigan, p. 55–72.

Paola, C., and Mohrig, D., 1996, Palaeohydraulics revisited: Palaeoslope estimation in coarse-grained braided rivers: Basin Research, v. 8, no. 3, p. 243–254, doi: 10.1046/j.1365-2117.1996.00253.x.

Posamentier, H.W., 2001, Lowstand alluvial bypass systems : Incised vs . unincised: AAPG Bulletin, v. 10, no. 10, p. 1771–1793.

Prochnow, S.J., Atchley, S.C., Boucher, T.E., Nordt, L.E.E.C., and Hudec, M.R., 2006, The influence of salt withdrawal subsidence on palaeosol maturity and cyclic fluvial deposition in the Upper Triassic Chinle Formation : Castle Valley , Utah: Sedimentology, v. 53, no. 6, p. 1319–1345, doi: 10.1111/j.1365-3091.2006.00821.x.

Rahmani, R.A., and Flores, R.M., 1984, Sedimentology of Coal and Coal-Bearing Sequences, *in* Rahmani, R.A. and Flores, R.M. eds., IAS Spec. Pubs. 7, Blackwell Scientific, London, p. 411.

Reel, C.L. (RPI/Colorado), and Campbell, C.V. (RPI/ C.L.., 1985, Chin Coulee Field—a Stratigraphic Trap in Lower Cretaceous Fluvial Valley-Fill Sandstones: ABSTRACT: AAPG Bulletin, v. 69, p. 300.

Reijenstein, H.M., Posamentier, H.W., and Bhattacharya, J.P., 2011, Seismic geomorphobgy and high-resolution seismic stratigraphy of inner-shelf fluvial, estuarine, deltaic, and marine sequences, Gulf of Thailand: AAPG Bulletin, v. 95, no. 11, p. 1959–1990, doi: 10.1306/03151110134.

Retallack, J.G., 1988, Field recognition of paleosols: Geological Society of America

Special Paper, v. 29, no. 216, p. 1–20, doi: 10.1130/SPE216-p1.

Richards, B.H., 2018, Stratigraphy of the Fluvial-To-Marine Transition Zone Associated With a Forced- Regressive Compound Incised-Valley System in the Turonian Ferron Notom Delta ,: , no. March, p. 311–326, doi: 10.2110/jsr.2018.17.

Schumm, S.A., and Etheridge, F.E., 1994, Origin, evolution and morphology of fluvial valleys, *in* Incised-Valley Systems: Origin and Sedimentary Sequence, p. 11–27.

Shanley, K.W., and McCabe, P.J., 1994, Perspectives on the sequence stratigraphy of continental strata: American Association of Petroleum Geologists Bulletin, v. 78, no. 4, p. 544–568, doi: 10.1306/BDFF9258-1718-11D7-8645000102C1865D.

Singerland, R., and Smith, N.D., 2004, River Avulsions and Their Deposits: Annual Review of Earth and Planetary Sciences, v. 32, no. 1, p. 257–285, doi: 10.1146/annurev.earth.32.101802.120201.

Smith, N, D., Cross, T, A., Dufficy, J, P., and Clough, S, R., 1989, Anatomy of an avulsion: Sedimentology, , no. 36, p. 1–23.

Staub, J.R., and Esterle, J.S., 1994, Peat-accumulating depositional systems of Sarawak, East Malaysia: Sedimentary Geology, v. 89, no. 1–2, p. 91–106, doi: 10.1016/0037-0738(94)90085-X.

Stouthamer, E., and Berendsen, H.J. a., 2001, Avulsion Frequency, Avulsion Duration, and Interavulsion Period of Holocene Channel Belts in the Rhine-Meuse Delta, The Netherlands: Journal of Sedimentary Research, v. 71, no. 4, p. 589–598, doi:

10.1306/112100710589.

Taylor, A.M., and Goldring, R., 1993, Description and analysis of bioturbation and ichnofabric: Journal of the Geological Society, v. 150, no. 1, p. 141–148, doi: 10.1144/gsjgs.150.1.0141.

Ullah, M.S., Bhattacharya, J.P., and Dupre, W.R., 2015, Confluence Scours Versus Incised Valleys: Examples From the Cretaceous Ferron Notom Delta, Southeastern Utah, U.S.A: Journal of Sedimentary Research, v. 85, no. 5, p. 445–458, doi: 10.2110/jsr.2015.34.

Uresk, J., 1978, Sedimentary Environment of the Cretaceous Ferron Sandstone near Cainville, Utah: Brinham Young University, Geology Studies, v. 26, p. 81–100.

Vakarelov, B.K., Ainsworth, R.B., and MacEachern, J.A., 2012, Recognition of wave-dominated, tide-influenced shoreline systems in the rock record: Variations from a microtidal shoreline model: Sedimentary Geology, v. 279, p. 23–41, doi: 10.1016/j.sedgeo.2011.03.004.

Walker, I.J., Desloges, J.R., Crawford, G.W., and Smith, D.G., 1997, Floodplain formation processes and archaeological implications at the Grand Banks site, lower Grand River, southern, Ontario: Geoarchaeology, v. 12, no. 8, p. 865–887, doi: 10.1002/(sici)1520-6548(199712)12:8<865::aid-gea3>3.0.co;2-3.

Wang, J., and Bhattacharya, J.P., 2018, Plan-View Reconstruction of Amalgamated Meander Belts, Cretaceous Ferron Sandstone, Notom Delta , South-Central Utah, U .

S . A .: Journal of Sedimentary Research, v. 88, no. 1, p. 58–74.

Willis, B.J., 1997, Architecture of fluvial-dominated valley-fill deposits in the Cretaceous Fall River Formation: Sedimentology, v. 44, no. 4, p. 735–757, doi: 10.1046/j.1365-3091.1997.d01-48.x.

Willis, B.J., 1998, Permeability structure of a compound valley fill in the cretaceous fall river formation of South Dakota: AAPG Bulletin, v. 82, no. 2, p. 206–227, doi: 10.1306/1D9BC3D1-172D-11D7-8645000102C1865D.

Willis, G.C., 1999, The Utah thrust system - an overview: Geology of Northern Utah and Vicinity, v. 27, p. 1–9.

Wright, P. V., and Marriott, S.B., 1993, The sequence stratigraphy of fluvial depositional systems: the role of floodplain sediment storage: Sedimentary Geology, v. 86, no. 3–4, p. 203–210, doi: 10.1016/0037-0738(93)90022-W.

Wu, C., and Bhattacharya, J.P., 2015, Paleohydrology and 3D Facies Architecture of Ancient Point Bars , Ferron Sandstone, Notom Delta, South-central Utah: Journal of Sedimentary Research, , no. March 2016, p. 399–418, doi: 10.2110/jsr.2015.29.

Zaitlin, B.A., Dalrymple, R.W., and Boyd, R., 1994, The Stratigraphic Organization of Incised-Valley Systems Associated with Relative Sea-Level Change: SEPM Special Publication, v. 51, no. 51, p. 45–60, doi: 10.2110/pec.94.12.0045.

Zhu, Y., Bhattacharya, J.P., Li, W., Lapen, T.J., Jicha, B.R., and Singer, B.S., 2012, Milankovitch-scale sequence stratigraphy and stepped forced regressions of the

Turonian Ferron Notom Deltaic Complex, south-central Utah, U.S.A: Journal of Sedimentary Research, v. 82, no. 9, p. 723–746, doi: 10.2110/jsr.2012.63.

CHAPTER 4

PALEOGEOGRAPHIC RECONSTRUCTION AND PROVENANCE ANALYSIS OF A COMPOUND VALLEY, TURONIAN FERRON SANDSTONE, UTAH.

ABSTRACT

This study evaluates the nature and provenance of valley fills to test assumptions made by valley models and their rather simplistic conceptual morphology. The compound incised valley of the Ferron-Notom delta's youngest non-marine sequence in the Turonian Mancos Shale Formation was found to have been filled at times by sediment from the Mogollon Highlands of Arizona to the southwest, and at other times by sediment from the Sevier Thrust Front to the northwest. Previously, the Ferron-Notom delta was assumed to have been fed by a single axial trunk river. Trunk valley terraces show detrital zircon assemblages and QmFLt detrital modes typical of transverse drainages sourced from Sevier thrust sheets. The resulting 40 km wide compound incised valley is a result of the cutting and filling of more than one trunk channel.

Radically revised paleogeographic mapping shows an evolution of valley incision and filling that combines the provenance of individual valley terraces with stratigraphic valley dimensions and paleocurrents. This evolution suggests how high frequency Milankovitch scale cyclicity (~10 - 20 ka) may control the interplay of sedimentation between axial and transverse drainage within a valley fill sucession. This more complex paleogeography of the Ferron Notom, with reference to Quaternary analogues, shows multiple rivers fed by multiple drainages.

Our study offers one of the highest resolution detrital zircon data sets published for an incised valley network, with a total zircon sample size of 2953 concordant dates. Overlying terraces were sampled at 4 locations confining a topographic valley area of ~100 km^2. Inter-valley terrace samples were independently analysed to test detrital zircon assemblage variability and confirm provenance interpretations.

4.1 INTRODUCTION

The commonly used definition of an incised valley as an elongate topographic low (Van Wagoner et al., 1990; Zaitlin et al., 1994; Boyd et al., 2006) may be somewhat misleading, as they commonly have extremely complicated margins and evolve to form increasingly mature dendritic tributive patterns that cover a degradational landscape defined by a circular to ovate shaped drainage basin. The concept of a valley as an elongate feature may only represent a segment of a given area, given the fractal nature of landscapes with complex topology. This simplified definition may not adequately describe the frondescent morphology depicted in outcrop and well correlation examples such as the Ferron Sandstone Member of the Mancos Shale Formation (Li et al., 2010; Zhu et al., 2012; Li and Bhattacharya, 2013; Kimmerle and Bhattacharya, 2018), the Pensylvanian Morrow Formation in Oklahoma (Bowen et al., 2003) or the Lower Mannville Group (Ardies et al., 2002; Zaitlin, 2002) and Dunvegan Alloformation (Plint, 2002) in Alberta, Canada. Quaternary examples, particularly from 3D seismic imagery, show far more complexity with much of the incised area owing to tributary drainages (Posamentier, 2001; Reijenstein et al., 2011). This becomes important in mapping ancient incised valleys and the paleogeography of their drainage networks. Much of the emphasis on incised valley models is on relatively simplistic systems that correlate directly with their better understood conformable marine deposit equivalents (Posamentier and Vail, 1988; Zaitlin et al., 1994; Boyd et al., 2006), despite the well know complexities of incised valley network morphologies (Posamentier, 2001; Plint, 2002; Blum and Hattier-womack, 2009; Reijenstein et al., 2011; Blum et al., 2013). Recent studies in valley morphology have looked at factors that influence drowned valleys and their fill based on their shape, due to factors such as faulting, coastal location relative to littoral drift and tidal contidions (Menier et al., 2006; Chaumillon and Weber, 2013). This study will focus on valley morphology landward of the bayline, to the apex of the main trunk channel.

The problem with the geomorphic versus stratigraphic expression of incised valleys is complicated by the fact that they may be formed over long periods of time, resulting in the formation of terraces and interflueves (McCarthy and Plint, 2003; Li et al., 2010; Li and Bhattacharya, 2013), where the resulting total valley incision does not represent any topographic feature that ever existed at any point in time (Strong and Paola, 2008; Holbrook and Bhattacharya, 2012). The focus of this paper is to map the laterally extensive outcrop exposures of incised valleys in the Ferron Sandstone Member of the Mancos Shale Formation in comparison to Quaternary examples in order to produce more realistic planview representations of an ancient valley system. The importance of accurately restoring the degradational landscape lies in the potential underestimation of incised valley deposit volumes as potential hydrocarbon reservoirs.

Implicit in incised valley models is that downstream incised valleys are fed by a single trunk river. Given the fact that incised valleys are dominated by tributive networks, and therefore tributary valleys (Drost and Keller, 1989; Posamentier, 2001; Kvale and Archer, 2007); it follows that downstream incised valleys may be fed by multiple trunks with separate sources of sediment. As drainage systems scale to larger areas, individual tributaries may be more accurately classified as trunk systems in their own right, such as the Ganges-Bramaputra, Red River-Mississippi or the Colorado-Trinity-Brazos Rivers. If the hinterland drainage sources of these separate trunks are spatially distinct, then provenance analysis could be used to resolve the relative importance of deposits from distinct drainages within the same stratigraphic valley through time.

We test these assumptions regarding valley drainage configurations by sampling Ferron Sandstone outcrops for detrital zircon (DZ) populations and constituent abundances within ten incised valley terrace deposits at four locations in our study area. The DZ populations from our study will be compared to similar sampling done on the Straight Cliffs Formation in the Kaiparowits Plateau of Southern Utah that highlight the complex interplay of basin axial and transverse drainage systems that flowed into the Cretaceous Cordilleran foreland basin (Lawton et al., 2009; Szwarc et al., 2014; Primm et al., 2018). Several other studies on source terrains have also documented DZ age distributions in the exposed landscape of the Turonian North American craton (Amato et al., 2008; Dickinson and Gehrels, 2008b; Dickinson and Gehrels, 2008a; Dickinson and Gehrels, 2010b; Dickinson and Gehrels, 2010a; Amato and Mack, 2012; Amato, 2019). In the case of fluvial deposits draining into the Western Interior Basin of Southern Utah, potential sources are the Mogollon highlands of Arizona, the active thrust sheets of the Sevier Thrust Front in West and North Utah, and the Cordilleran Magmatic Arc in California and Nevada

4.2 PREVIOUS WORK ON THE FERRON

The Turonian Ferron Sandstone Member of the Mancos Shale Formation overlies the Tununk Shale Member and is bounded above by the Bluegate Shale Member north of the Henry Mountains in southeastern Utah. The Notom Delta is one of three clastic wedges within the Ferron, along with the Last Chance and Vernal Deltas (Fig. 4.1); and is composed of 6 sequences, which are further divided into 18 parasequence sets and 42 parasequences (Li et al., 2011a; Zhu et al., 2012) (Fig. 4.2). The lower four sequences are composed of shoreface and heterolithic deltaic facies, while the upper two sequences have incised valley fills truncating underlying deltaic and shoreface deposits (Li et al., 2010; Li and Bhattacharya, 2013; Famubode and Bhattacharya, 2016). The youngest incised valley deposits have been documented by several previous studies (Fielding, 2010; Li et al., 2010; Zhu, 2010; Li et al., 2011a; Zhu et al., 2012; Campbell, 2013; Hilton, 2013; Li and Bhattacharya, 2013; Ullah et al., 2015; Biber et al., 2017; Kimmerle and Bhattacharya, 2018) describing three distinct episodes of terraced cut and valley filling, so named V3 (oldest), V2 and V1 (youngest). These valley terraces were differentiated and loosely correlated based primarily on their grainsize, sedimentary structures and depositional onlap relationships. The valley network of this youngest sequence spans a distance of over 40 km north to south and 30 km east to west, incising a coastal plain composed of shoreface deposits of the older sequence. Paleogeographic reconstruction of the older (Sequence 2) incised valley interpreted a single axial drainage that flowed to the northeast (Zhu, 2010; Ahmed et al., 2014). A similar axial drainage system was assumed for Sequence 1, as the entire Notom delta progrades basinward (Li et al., 2011a; Zhu et al., 2012; Li and Bhattacharya, 2013).

Previous studies of the Ferron Sandstone suggests that the Ferron-Notom Delta was fed by a single Notom trunk river (Zhu, 2010; Li et al., 2011b; Zhu et al., 2012; Li and Bhattacharya, 2013; Ullah et al., 2015) and is responsible for multiple episodes of cut-and-fill over a time span of 60 ka to 100 ka (Li and Bhattacharya, 2013; Famubode and Bhattacharya, 2016; Kimmerle and Bhattacharya, 2018) making it a relatively long lived compound incised valley system that covers over 1200 km^2. Tectonic influence may also play a role as inferred from subtle stratigraphic geometries to the south (Fielding, 2010). Basin-wide correlations have suggested that this single Ferron trunk channel is part of a larger avulsive system (Garrison and Van Den Bergh, 2004) that began by depositing the Tibet Canyon Member of the Straight Cliffs Formation in the Kaiparowits Plateau, then prograded northeast to deposit the Ferron-Notom Delta (Fig. 4.3A). Depositionthen shifted northward to the Last Chance Delta of the Ferron Sandstone (Garrison and Van den Bergh, 2004) and Smokey Hollow Member of the Straight Cliffs and then transgressed back to The Kaiparowits, depositing the John Henry Member of the Straight Cliffs.

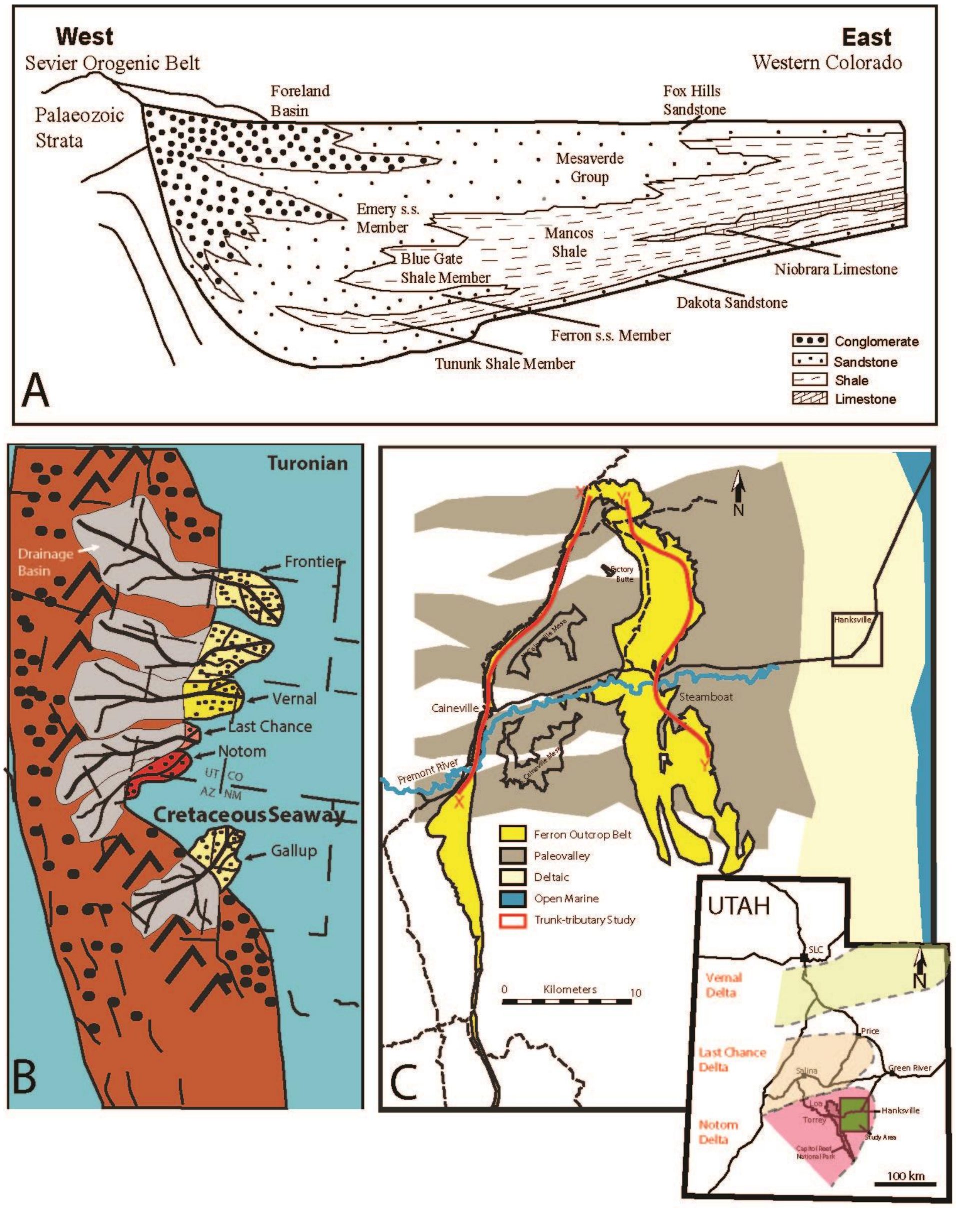

Figure 4.1: A) Regional stratigraphic cross section of the Mancos Shale showing the relative location of the Ferron Sandstone Member, the overlying Bluegate Shale Member, and the underlying Tununk Shale (*Modified from:* Armstrong, 1968). B) The Western Interior Seaway and location of the Notom Delta relative to present day state boundaries *(modified from*: Bhattacharya and Tye, 2004; *Based on:* Gardiner, 2012). C)The study area within Utah (Kimmerle and Bhattacharya, 2018). Cross section locations (Fig. 2) are indicated by red lines.

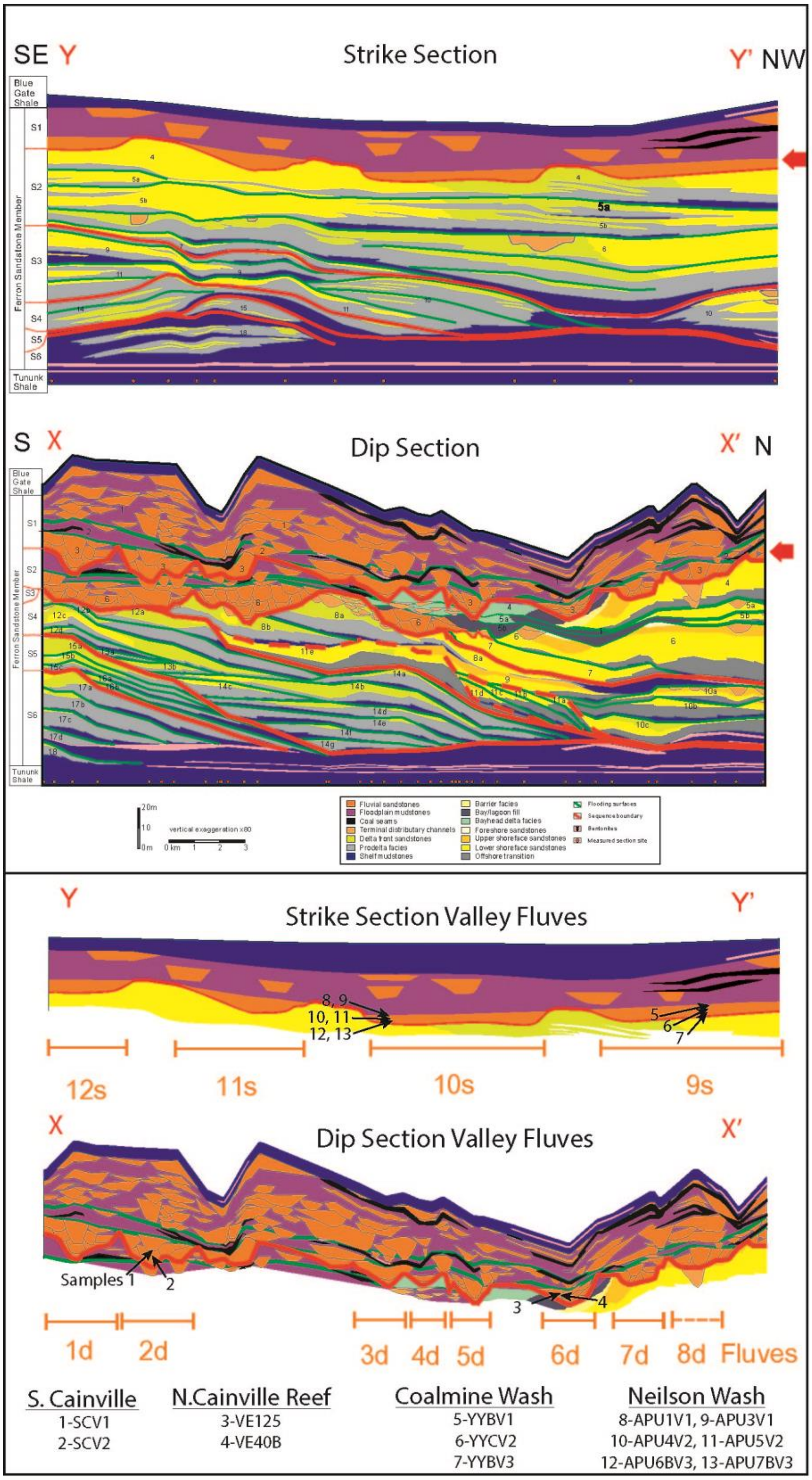
SE Y
Strike Section
Y' NW
Dip Section
S X
X' N
Strike Section Valley Fluves
Y
Y'
12s
11s
10s
9s
Dip Section Valley Fluves
X
X'
Samples 1
1d
2d
3d
4d
5d
6d
7d
8d
Fluves
S. Cainville
1-SCV1
2-SCV2
N.Cainville Reef
3-VE125
4-VE40B
Coalmine Wash
5-YYBV1
6-YYCV2
7-YYBV3
Neilson Wash
8-APU1V1, 9-APU3V1
10-APU4V2, 11-APU5V2
12-APU6BV3, 13-APU7BV3

Figure 4.2 (*preceding page*): *Upper*) Strike cross section Y-Y' in figure 3, showing the study interval. Approximate location of study outcrop is indicated by the red arrow. Focus is on fluvial strata in sequence 1 *(modified from*: Zhu et al, 2012). Dip oriented cross section X-X' in figure 3, showing the study interval *(modified from*: Zhu et al, 2012 and Richards, 2018). *Lower*) Location of 13 samples taken from 10 separate valley terraces (black numbered) and identified valley flueves (orange numbered).

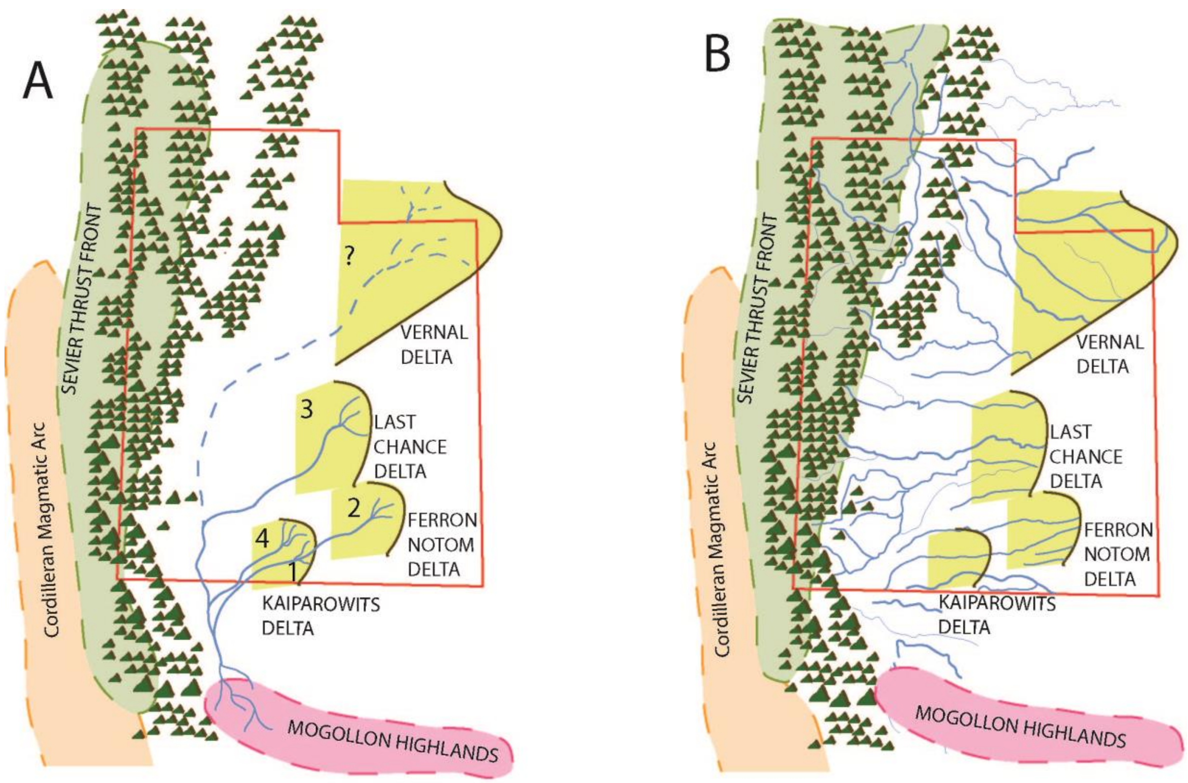

Figure 4.3: Ferron paleogeography models relative to modern state boundaries, Cordilleran, Sevier Thrust Front and Mogollon Highland terrains (*modified from:* Ryer, 2004). A) Avulsive single trunk drainage model described by Garrison and van den Burg (2004), that with migrating deposition foci. Deposition of the Vernal delta is inferred in this model, but never explicitly defined. B) Modern Andean eastern drainage in Equador superimposing the Andes on the Sevier Thrust Front in Utah. This figure shows the likelihood of multiple trunk rivers feeding the various deltaic complexes (Ryer and Lovekin, 1986).

In contrast, the Ferron drainage system was compared to that of the Peruvian Andes (Ryer, 2004) due to its proximity to the Sevier Thrust Front at the time of deposition (Fig 4.3B). This analogue would combine elements of piedmont type incised valleys with those of coastal plains apparent from the incision of underlying shoreface deposits. The resultant delta could be more analogous to the Colorado – Brazos – Trinity Quaternary valley system (Blum and Hattier-womack, 2009; Blum et al., 2013) (Fig. 4.4) which is similar in scale and deposits sediment from separate drainage basins, with contrasting sediment signals. With the use of high resolution provenance analysis combined with the established sequence stratigraphy, we will determine if sufficient sediment source disparity exists between adjacent valley flueves and between valley terraces within the same compound valley fill. Once provenance is determined, paleogeography of the incised valleys can be framed within the context of source, direction and timing (Fig. 4.5). The resulting paleogeographic mapping will rely primarily on correlating between regional strike and dip correlations of the stratigraphic compound valley (Li et al., 2010; Zhu et al., 2012) (Fig. 4.2) in order to recreate the topographic valley flueves that existed at each stage of valley terrace deposition (V3, V2 and V1), and will address the more simplistic valley morphology of previous studies.

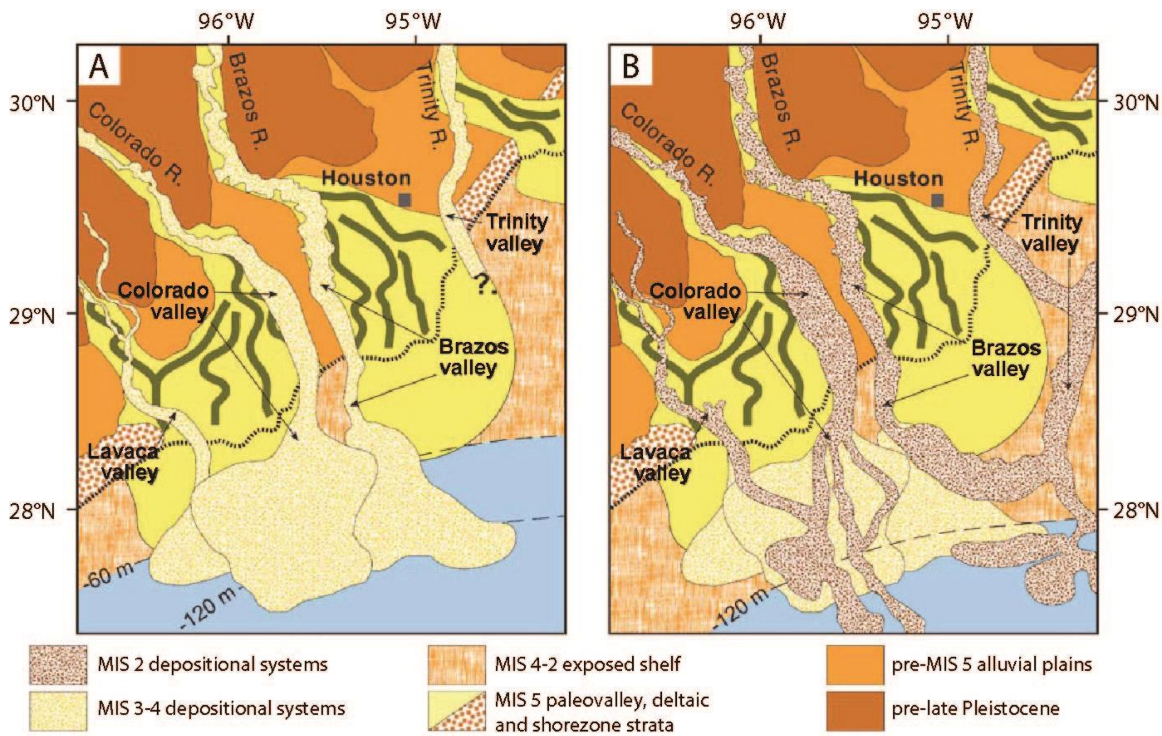

Figure 4.4: Colorado – Brazos – Trinity paleovalley system during MIS4-2 glacial Period (Blum and Aslan, 2006; Blum et al., 2013) A) Position of valleys during falling stage as the Quaternary valleys erode into the coastal plain. B) Lowstand configuration of valleys that have coalesced to fill the more seaward valley reaches with a composite fill.

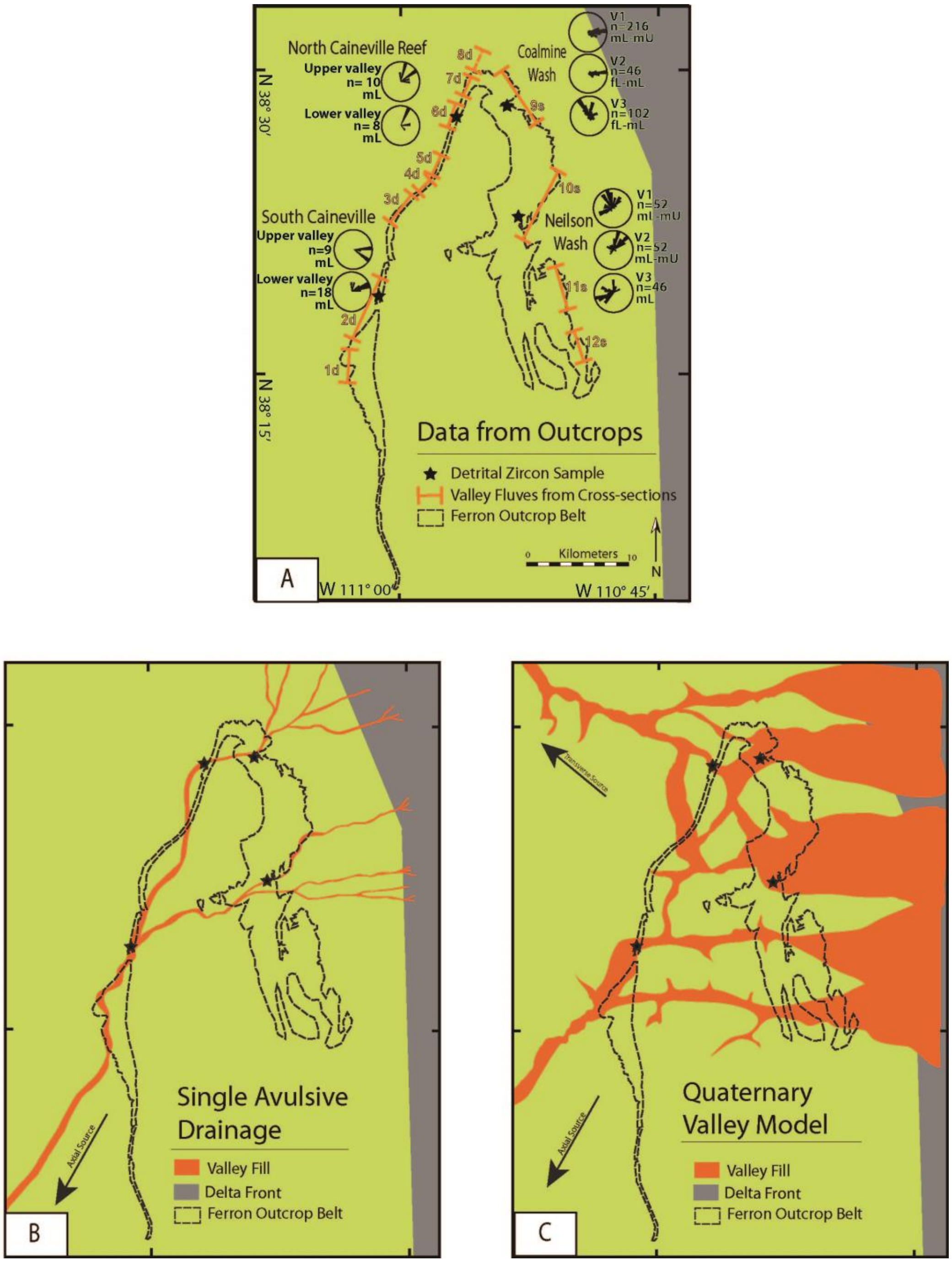

Figure 4.5: A) A summary of the data used to reconstruct valley paleogeography including paleocurrents, dominant grainsize and stratigraphic valley flueves (numbered) taken from regional strike and dip cross sections (Fig. 2). B) Valley model assuming a single avulsive axial trunk drainage that connects dip section valley flueves by threading in and out of the outcrop profile as proposed by Zhu, (2010). C) Valley model of incision

and fill based on multiple drainage souces and coalecence of valley flueves similar to the Quaternary Brazos-Colorado-Trinity valley models in the Gulf Coast of Texas.

4.3 METHODS

Samples were taken from the field at locations previously described as compound incised valley terraces (Zhu et al., 2012; Li and Bhattacharya, 2014; Ullah et al., 2015). Stratigraphic correlation in the original dip-section of Zhu *et al.* (2012) were never divided into the V3, V2 and V1 terrace framework as the compound nature of the valleys were not fully realised at the time. We used 3D photogrammetric models from drone photography and Pix4D software to identify 2 valley terraces (upper and lower) in the North Caineville Reef and South Caineville outcrops (Fig. 4.6 A and B). Identification of barform surfaces and valley bases were made on the basis of bedding surface hierarchy and grain size observations.

In order to minimize the effects of hydraulic sorting (Garzanti et al., 2009; Ibañez-Mejia et al., 2018) , all samples taken were at the lowest identifiable cross-set of the lowest barform that did not include any elements of the thalweg, such as rip-up clasts, channel lag deposits or confluence scour fills (Ullah et al., 2015). This protocol was designed to capture sediment representative of the formative channel provenance of each terrace. The samples were processed for 30 μm thin sections for petrographic analysis and U-Pb ratios of detrital zircon grains extracted and mounted for quadrupole laser ablation-inductively coupled plasma-mass spectrometry (LA-ICP-MS) according to methods specified by Matthews and Guest (2017).

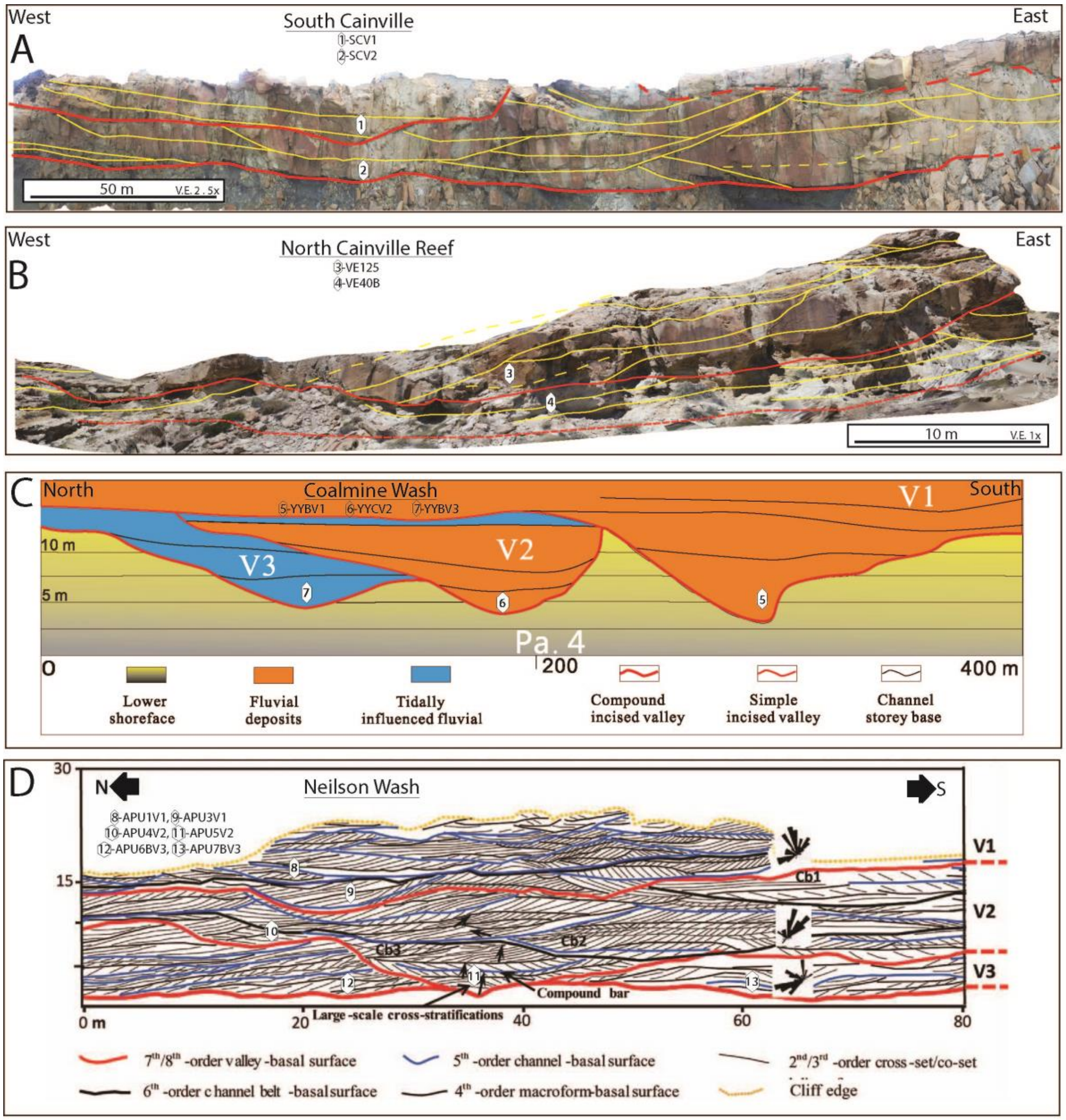

Figure 4.6: Sample locations at the four outcrops in our study area (Fig. 5A). A) Extruded orthopane of a 3D model in Pix4D software of South Caineville outcrop with locations of samples SCV1 and SCV2. Barform surfaces (yellow) are truncated by valley erosion surfaces (red). B) Orthopane of North Caineville Reef outcrop with locations of samples VE125 and VE40B. C) Graphical representation of the valley terraces V1, V2, and V3 (*modified from:* Li and Bhattacharya, 2013) in Coalmine Wash. Samples YYBV1, YYCV2 and YYBV3 were taken at the lowest cross-bedded sandstone in each terrace above the thalweg deposit. D) Bedding diagram of terraces V1, V2 and V3 (*modified from:* Ullah et al., 2015) in Neilson Wash with the locations of samples APU1V1, APU3V1, APU4V2, APU5V2, APU 6BV3 AND APU7BV3. Redundant samples were

taken of each terrace deposit at this outcrop and were separated vertically by the height of a channel storey.

Laser ablation beam diameter was 22 μm chosen based on a 95% best fit, at a frequency of 10 Hz for a duration of 15 s to a pit depth of 12 μm. We used 6 calibration materials within the ablation sequence (Matthews and Guest, 2017) and corrected for instrumental and mass fractionation, removal of laser induced elemental fractionation and calculated all best age integrations and error measurements using Iolite software (Paton et al., 2010) with VisualAge data reduction scheme (Petrus and Kamber, 2012). All zircon data was visualized and statistical analysis processed using detritalPy toolset in Python (Sharman et al., 2018). See: Supplemental_2 for a list of all detrital zircon data used in this study.

Provenance ternary diagrams were created in excel (Zahid and Barbeau, 2012) from petrographic point counts of thin sections using an n= 400 sample and a 0.5 mm step size. Paleogeography was interpreted by georeferencing incised valley correlations and paleocurents using ESRI ArcMap software.

4.4 RESULTS

4.4.1 Detrital-Zircon U-Pb Populations

Detrital zircon samples were taken from valley fill deposits at each study location (Fig. 4.6). A total of 3900 grains were analysed from 13 samples, and produced 2953 concordant age measurements (≤10% discordant). The age measurements were organized into 6 populations (*A* - *F*) based on terrain ages from parent assemblages in order to correlate a detrital source signal. Relative age measurement errors ranged from 0.6 to

31.5%, with an average relative error of 3.1% for all grains. Additionally 2 samples were collected from shallow marine deposits in the upper and lower sections of the Vernal Delta yielding 263 and 287 concordant ages respectively. These Vernal samples are not included in the descriptions below, but will be used for basin wide context.

Population A: Cordilleran Magmatic Arc 300-86 Ma. This population is composed of Permian to contemporaneous Cretaceous aged grains and makes up 12% of all concordant grains, ranging in relative abundance from 5 to 19% of each sample. The cumulative distribution of all 2953 grains reveals key population peaks at 90, 148 and 245 Ma, with the most dominant at 90 Ma. These grains are sourced in the volcanically active western margin (Dickinson and Gehrels, 2010b; Laskowski et al., 2013; Szwarc et al., 2014; Primm et al., 2018; Pettit et al., 2019) of the basin and have travelled either by transverse drainage trends or by airfall. Regional Ferron-Notom stratigraphy (Fig. 4.2) shows multiple extensive bentonite layers from volcanic ash deposits (Li et al., 2012; Zhu et al., 2012), which suggests that airfall zircons may play greater importance in the 90 Ma peak than in similar aged zircon populations within the Western Interior Basin (Szwarc et al., 2014; Primm et al., 2018).

Population B: Appalachian-Ouachita and Whicita Mountains 900-300 Ma. Zircon ages from Neoproterozoic to the end of the Pennsylvanian vary from 5 to 32 % by sample with an average of 17% for all grains. Most prominent peaks are at 419 and 590 with a subordinate peak at 367. These grains are primarily sourced from the eroding Sevier Thrust Front (Dickinson and Gehrels, 2010a; Szwarc et al., 2014; Pettit et al., 2019). This population includes recycled zircons from the Wichita Mountains and accreted peri-Gondwanan terranes with zircons from the Appalachian-Ouachita Cordillera that were deposited on the western passive margin of Laurentia. Jurassic eolianties composed of these sediments are exposed along several thrust fronts at the time of the Ferron-Notom deposition (Willis, 1999; Szwarc et al., 2014), particularly are the Paxton, Canyon Range, Pavant, Blue Mountain and Wah Wah thrust sheets.

Population C: Grenvillian 1300-900 Ma. Zircon dates from Late Mesoproterozoic make up 22% of all grains in this study and vary from 9 to 33% by sample. This population is dominated by a prominent peak at 1060 Ma with smaller peaks at 1020 and 1132, consistant with timing of the Late Ottawan and Shawinigan events of the Grenville orogeny (Rivers et al., 2003; Dickinson and Gehrels, 2010b; Pettit et al., 2019). This population is present in both Sevier thrust sheet sources within Jurassic eolianites and as sedimentary overburden of Mogollon highland signals (Dickinson et al., 2010; Laskowski et al., 2013; Szwarc et al., 2014; Pettit et al., 2019).

Population D: Anorogenic Plutons 1550-1300 Ma. Early Mesoproterozoic zircons range in relative abundance from 8 to 15% and average 12% abundance for all grains, with a single prominent peak at 1378 Ma. This age signal represents batholiths formed by continental magmatism and drainage input from the mid-continental granite-rhyolite province (Thomas et al., 1984; Amato et al., 2011; Blum and Pecha, 2014; Pettit et al., 2019). This signal is present throughout the Sevier thrust belt and Mogollon highlands and does not vary greatly between samples.

Population E: Yavapai-Mazatzal 1850-1550 Ma. Late Paleoproterozoic zircons range from 12 to 53% relative abundance with an average of 33% and show the greatest variation of all population groups between samples. In our study, this population shows a single peak at 1677 Ma. While present in both Sevier and Mogollon Highland sources (Dickinson and Gehrels, 2010a; Laskowski et al., 2013; Szwarc et al., 2014; Pettit et al., 2019), the Mogollon signal is dominated by Yavapai-Mazatzal basement, while the Sevier Thrust Sheet shows a more dilute signal, suggesting a more recycled history.

Population F: Archean-Wopmay 3735-1850 Ma. All grains up to and including the early Paleoproterozoic make up only 4% of the total dataset. Samples range from 0 - 7% abundance with no significant peak. This population is the least abundant in all 13 samples and likely represents multiple cycles of reworking.

4.4.2 Provenance Interpretation Groups

Ages were plotted on probability density plots and cumulative frequency plots for all 13 samples (Fig. 4.7). Visual inspection of these plots suggested 2 main groups in the data that diverge significantly at around 40% of their cumulative distribution. These samples were plotted using multidimensional scaling (MDS), to visualize the similarity or dissimilarity between samples (Fig. 4.8). MDS uses a pairwise comparison of samples within a distance matrix that maps the euclidean distance between any two points (Vermeesch, 2013). The result is that similar samples plot close together and dissimilar samples will plot farther away.

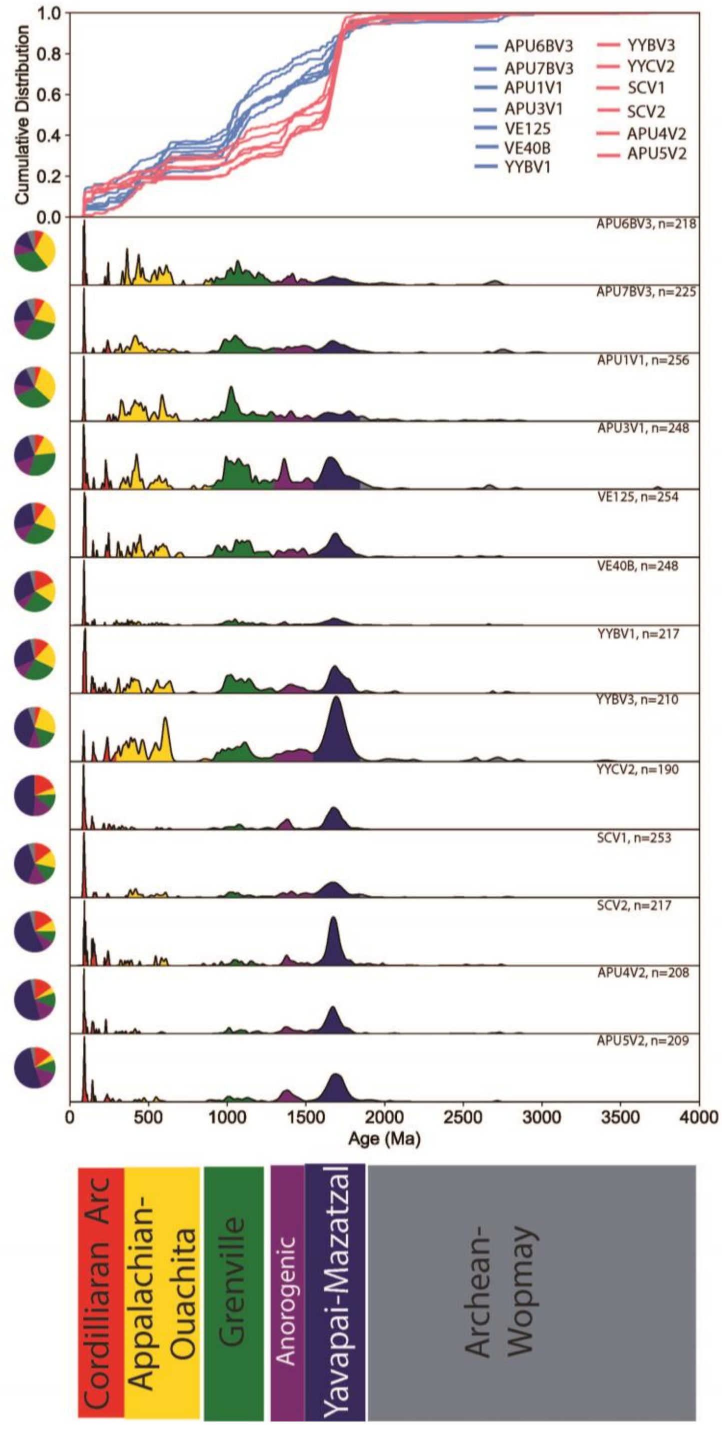

Figure 4.7: Ages from detrital zircons samples taken from the Ferron-Notom Sequence 1 incised valleys (Figs 4.2 and 4.6). The relative probability plots (N=13, n= 2953) for each sample with the cumulative distribution grouped by similarity (pink – blue) above. Pie charts on the left show the normalized population of each sample. Redundant samples

show consistency with each paired sample, while V1, V2 and V3 terraces at different locations do not. Some valley flueves also show samples from both groups See: Supplemental_2.

We use the Kolgomorov-Smirnov (K-S) p-value to test the null hypothesis (Table 4.1) that both are random samples and are taken from populations with the same distribution (Laskowski et al., 2013) within a 95% confidence interval ($p \geq 0.05$). Criticism of this method of correlation is due to its dependence on sample size and the fact that mathematical testing does not prove that samples are identical, only that either they are in fact different or that the difference is indistinguishable (Vermeesch, 2013; Vermeesch, 2018). These concerns are addressed in the following ways. First, by insuring a consistent large initial sample set (n=300) before the data reduction. Second, all samples are analyzed and processed under the same conditions, such that pairwise comparisons are only done on the Ferron-Notom samples from this study. Third, we use this test only to verify trends in similarity between samples that we observe in MDS.

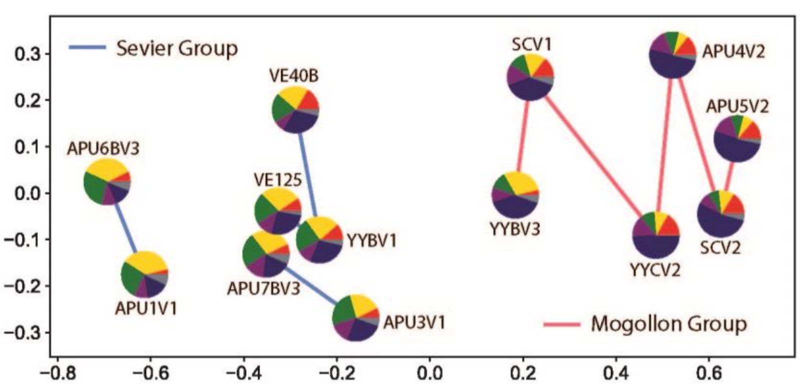

Figure 4.8: Multi-dimensional scaling (MDS) plot of the Ferron-Notom samples. Lines connect nearest neighbours, as defined by the K-S D_{max} statistic. Line colour (pink – blue) suggests the provenance group membership.

K-S pairwise test of the cumulative fraction plots identifies the maximum vertical deviation of sample plots, known as the statistic D_{max}. Samples with the most similar cumulative distributions will have the lowest D_{max} value, with identical samples $D_{max} = 0$ (Table 4.2). Included in the MDS analysis (Fig. 4.8) is the results of the lowest D_{max} value for all samples, where lines are coloured by provenance interpretation group membership determined from MDS and K-S p-value, and identify the greatest similarity between samples. Having satisfied that all members of a given provenance group show statistical similarity with at least one other member (Table 4.1) we propose at least 2 distinct provenance interpretation groups.

Potential source MDS analysis is shown in the context of our samples (Fig. 4.9), which includes the Mogollon Highlands of Arizona to the southwest of our study area, and the Sevier Thrust Front (STF) to the east. Data from the Mogollon sourced Straight Cliffs Formation (Lawton et al., 2014; Szwarc et al., 2014; Primm et al., 2018), Mesosoic Eaolianites (Dickinson and Gehrels, 2010a) on the Colorado Plateau and samples directly from the Mogollon Highlands (Amato et al., 2008; Amato et al., 2011; Amato and Mack, 2012; Amato, 2019) are plotted in Figure 4.9. Both upper and lower valley terraces in South Caineville show a Mogollon source, while both upper and lower terraces in North Caineville are Sevier. This may imply that all the deposits in their respective valley flueves share a similar provenance signal. The outcrops in Coalmine and Neilson Wash however show different detrital sources within the same valley flueve. This could indicate a certain degree of stream capture or channel convergence has occurred. The same groups are confirmed by the paired samples in Neilson Wash, suggesting that sedimentation may not have been the result of concurrent drainages, but rather consecutive deposits within the same compound valley, as the statistical similarity allows the samples to belong to one group but not both. If this were a case of concurrent sedimentation, then one would expect a mixed signal to show similarity with both groups.

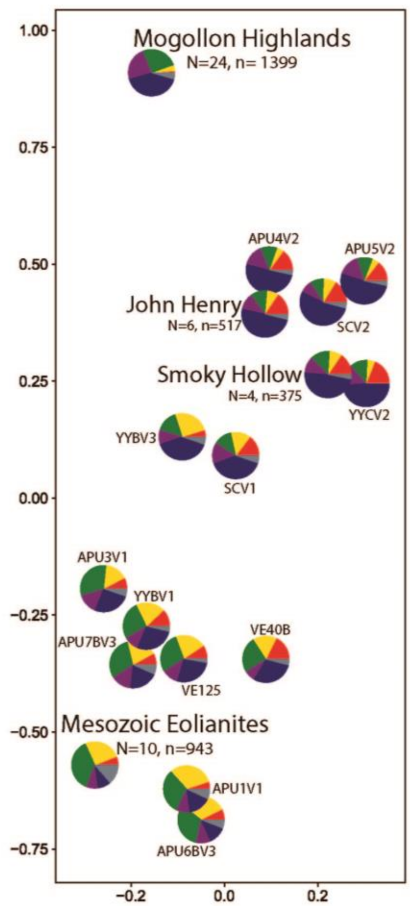

Figure 4.9: MDS plot of likely sources including the Mesozoic eolianites of the Sevier Thrust Sheets on the Colorado Plateau, the John Henry and Smokey Hollow Members of the Straight Cliffs Formation, and the Mogollon Highlands.

Table 4.1: Kolgomorov-Smirnov p-value for Ferron Notom valley terrace samples

Sample ID	n	APU6BV3	APU7BV3	APU1V1	APU3V1	VE125	VE40B	YYBV1	YYBV3	YYCV2	SCV1	SCV2	APU4V2	APU5V2
APU6BV3	218	1	0.0358978	0.7531595	0.0012141	0.0354197	0.0087396	0.0149486	3.69E-08	2.94E-12	1.12E-10	4.75E-16	3.63E-16	4.17E-17
APU7BV3	225	0.0358978	1	0.0825391	0.4932939	0.9254701	0.0852005	0.5817197	0.000619	6.24E-06	0.0002188	2.29E-10	7.71E-09	8.61E-10
APU1V1	256	0.7531595	0.0825391	1	0.0004798	0.0189811	0.0184389	0.0606217	5.66E-07	6.88E-11	2.59E-09	3.99E-14	3.00E-15	1.49E-16
APU3V1	248	0.0012141	0.4932939	0.0004798	1	0.1234041	0.0169496	0.1796006	0.0035005	0.0001618	0.0008222	2.89E-08	1.01E-07	1.42E-07
VE125	254	0.0354197	0.9254701	0.0189811	0.1234041	1	0.0797213	0.7346312	0.0025373	4.38E-06	0.000151	4.72E-09	4.71E-09	7.43E-10
VE40B	248	0.0087396	0.0852005	0.0184389	0.0169496	0.0797213	1	0.2284731	0.0064656	8.04E-06	0.0002964	3.36E-08	2.97E-08	3.48E-09
YYBV1	217	0.0149486	0.5817197	0.0606217	0.1796006	0.7346312	0.2284731	1	0.0143115	4.58E-05	0.0009528	7.35E-07	1.06E-07	1.41E-08
YYBV3	210	3.69E-08	0.000619	5.66E-07	0.0035005	0.0025373	0.0064656	0.0143115	1	0.0245109	0.0704541	0.0304958	0.0164123	0.0079051
YYCV2	190	2.94E-12	6.24E-06	6.88E-11	0.0001618	4.38E-06	8.04E-06	4.58E-05	0.0245109	1	0.0967927	0.2259567	0.2545853	0.1951912
SCV1	253	1.12E-10	0.0002188	2.59E-09	0.0008222	0.000151	0.0002964	0.0009528	0.0704541	0.0967927	1	0.0008473	0.0648069	0.009932
SCV2	217	4.75E-16	2.29E-10	3.99E-14	2.89E-08	4.72E-09	3.36E-08	7.35E-07	0.0304958	0.2259567	0.0008473	1	0.5725896	0.1723159
APU4V2	208	3.63E-16	7.71E-09	3.00E-15	1.01E-07	4.71E-09	2.97E-08	1.06E-07	0.0164123	0.2545853	0.0648069	0.5725896	1	0.0761311
APU5V2	209	4.17E-17	8.61E-10	1.49E-16	1.42E-07	7.43E-10	3.48E-09	1.41E-08	0.0079051	0.1951912	0.009932	0.1723159	0.0761311	1

Kolgomorov-Smirnov p-values > 0.05 indicate that we cannot reject the null hypothesis that these samples are taken from the same population. Any pair is coloured (blue or pink) according to the cluster with which it cannot be rejected from. Two non-overlapping clusters are shown.

Table 4.2: Kolgomorov-Smirnov Dmax for Ferron Notom valley terrace samples

Sample ID	n	APU6BV3	APU7BV3	APU1V1	APU3V1	VE125	VE40B	YYBV1	YYBV3	YYCV2	SCV1	SCV2	APU4V2	APU5V2
APU6BV3	218	0	0.1330887	0.0614249	0.1765315	0.1295601	0.1511912	0.1481842	0.2849279	0.3616127	0.3137034	0.4016827	0.4074629	0.4189456
APU7BV3	225	0.1330887	0	0.1140104	0.075681	0.0495188	0.1142832	0.0730364	0.1904762	0.2449123	0.1933773	0.3179314	0.2956624	0.3115577
APU1V1	256	0.0614249	0.1140104	0	0.1798135	0.1336122	0.1348286	0.1205537	0.252567	0.3282484	0.2803391	0.3621112	0.3810096	0.3969049
APU3V1	248	0.1765315	0.075681	0.1798135	0	0.1041402	0.1370968	0.1008065	0.1650538	0.2066638	0.1744071	0.2759217	0.2692308	0.2661483
VE125	254	0.1295601	0.0495188	0.1336122	0.1041402	0	0.1120142	0.0626474	0.168279	0.2418152	0.191295	0.2878733	0.2911872	0.3040161
VE40B	248	0.1511912	0.1142832	0.1348286	0.1370968	0.1120142	0	0.0956221	0.156874	0.237309	0.1854679	0.2747696	0.2788462	0.2945864
YYBV1	217	0.1481842	0.0730364	0.1205537	0.1008065	0.0626474	0.0956221	0	0.1502304	0.2267039	0.1787946	0.2580645	0.2773618	0.293211
YYBV3	210	0.2849279	0.1904762	0.252567	0.1650538	0.168279	0.156874	0.1502304	0	0.1466165	0.1192923	0.1382488	0.1496795	0.1604694
YYCV2	190	0.3616127	0.2449123	0.3282484	0.2066638	0.2418152	0.237309	0.2267039	0.1466165	0	0.1166632	0.1023769	0.1005061	0.1066986
SCV1	253	0.3137034	0.1933773	0.2803391	0.1744071	0.191295	0.1854679	0.1787946	0.1192923	0.1166632	0	0.1801607	0.1210854	0.1504057
SCV2	217	0.4016827	0.3179314	0.3621112	0.2759217	0.2878733	0.2747696	0.2580645	0.1382488	0.1023769	0.1801607	0	0.0749956	0.1059467
APU4V2	208	0.4074629	0.2956624	0.3810096	0.2692308	0.2911872	0.2788462	0.2773618	0.1496795	0.1005061	0.1210854	0.0749956	0	0.1236198
APU5V2	209	0.4189456	0.3115577	0.3969049	0.2661483	0.3040161	0.2945864	0.293211	0.1604694	0.1066986	0.1504057	0.1059467	0.1236198	0

Kolgomorov-Smirnov Dmax values indicated the maximum separation in the cumulative frequency (Fig. 4.7) for each pairwise comparison. The highlighted comparison (blue or pink) indicates the least different neighbor.

4.4.3 Regional Samples

The 13 Ferron-Notom samples were classified by DZ provenance group as either Notom Mogollon or Notom Sevier, referring to their respective delta and source. These detrital assemblages were compared to 2 samples taken from the upper and lower Vernal Delta; and published sources for the Last Chance fluvial deposits and Kaiparowits Plateau's John Henry and Smokey Hollow members of the Straight Cliffs Formation (Fig. 4.10). This analysis suggests that similarity exists between the Notom Mogollon and Straight Cliffs sources, and between the Notom Sevier, Vernal and Last Chance Deposits.

Figure 4.10 (*following page*): MDS plot, Cumulative frequency and relative probability plots of data from the Vernal, Last Chance, Notom and Kaiparowitz (Straight Cliffs). MDS analysis shows 2 distinct DZ assemblage groups, one that is distinctly Mogollon sourced including the Straight Cliffs and Notom Mogollon samples, while the suggests a Sevier source.

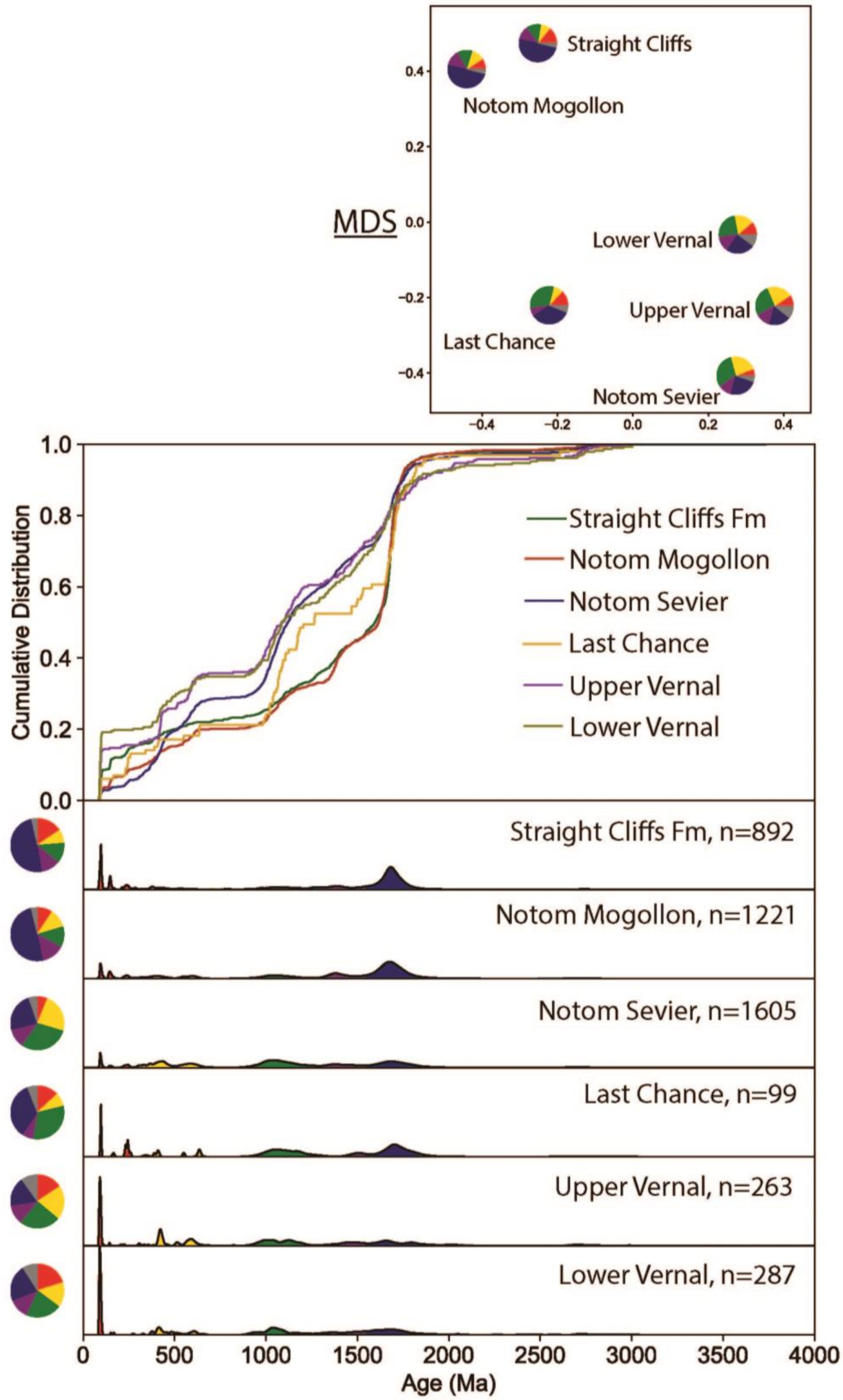

MDS
Straight Cliffs
Notom Mogollon
Lower Vernal
Upper Vernal
Last Chance
Notom Sevier
Cumulative Distribution
Straight Cliffs Fm
Notom Mogollon
Notom Sevier
Last Chance
Upper Vernal
Lower Vernal
Straight Cliffs Fm, n=892
Notom Mogollon, n=1221
Notom Sevier, n=1605
Last Chance, n=99
Upper Vernal, n=263
Lower Vernal, n=287
Age (Ma)

4.4.4 Petrography

Detrital modal analyses for 10 of the 13 Ferron-Notom samples were conducted, representing each of the valley terraces in this study. Point counts from thin sections were compiled (Table 4.3) and grouped according to the results of the interpreted provenance groups from the detrital zircon analysis (Fig.4.8) to test if our MDS and K-S analysis is supported by provenance trends in the resulting rock classification (Dickinson, 1985; Suczek and Ingersoll, 1985; Weltje, 2006; Zahid and Barbeau, 2012). The most abundant grain constituents were monocrystalline quartz, followed by potassium feldspar (orthoclase and microcline) and sedimentary lithic fragments. Monocrystalline quartz grains were often fractured and rimmed with smectite and other clay minerals. The orthoclase fraction of the K-feldspar was very altered and in some instances mostly dissolved. Where possible it was distinguished based on recognition of Carlsbad twinning, low birefringence, a characteristic grungy texture and biaxial optical figures. The sedimentary lithic fragments were dominated by mudstone clasts and recycled quartz sandstones (Fig. 4.11), likely from the abundant Jurassic eoliantites in the Sevier thrust sheets to the west. Detrital assemblage analyses (Fig.4.12) show that the Sevier group shows a predominantly recycled signature (Dickinson, 1985; Weltje, 2006) with some samples showing mixed characteristics, possibly from the underlying incised strata. The Mogollon group, with a greater average percentage of feldspars than lithic grains, displays a more continental provenance also with samples that tend towards a mixed signal. This mixed signal in valley terraces is expected according to cut and cover models of valley incision (Strong and Paola, 2008; Holbrook and Bhattacharya, 2012), where the valley fill will contain sediment from the underlying lithology as it widened through time; yet each terrace is still dominated by the sediment signal sourced from its headwaters.

Table 4.3: Modal point-count relative abundances (%)

Sample ID	Outcrop	Q_m	Q_p	Q_t	P	K	F	L_{sm}	L_{vm}	L	L_t	M	ϕ	DZ Group
APU6BV3	Neilson Wash, *V3*	61	1	62	3	15	18	16	7	23	24	-	5%	Sevier
APU1V1	Neilson Wash, *V1*	65	0	65	1	10	11	18	5	23	23	-	3%	Sevier
VE125	N. Caineville Reef, *upper valley*	58	1	59	1	13	14	26	2	28	29	-	4%	Sevier
VE40B	N. Caineville Reef, *lower valley*	59	1	60	2	17	19	14	8	22	23	-	6%	Sevier
YYBV1	Coalmine Wash, *V1*	63	1	64	1	14	15	10	3	13	14	1%	7%	Sevier
YYBV3	Coalmine Wash, *V3*	63	1	64	3	24	27	11	3	14	15	-	1%	Mogollon
YYCV2	Coalmine Wash, *V2*	62	1	63	1	24	25	12	2	14	15	-	3%	Mogollon
SCV1	South Caineville, *upper valley*	62	2	64	2	24	26	4	6	10	12	1%	3%	Mogollon
SCV2	South Caineville, *lower valley*	67	1	68	5	23	28	10	3	13	14	-	3%	Mogollon
APU4V2	Neilson Wash, *V2*	60	1	61	3	23	26	14	2	16	17	-	3%	Mogollon

Samples are separated into outcrop locations and sequential valley terraces. All detrital values are reported as normalized percentages (Qm = monocrystalline quartz, Qp = polycrystalline quartz, Qt = total quartz = Qm + Qp, P = plagioclase, K = potassium feldspar, F = total feldspar = P + K, Lsm = sedimentary and meta sedimentary lithic fragments, Lvm = volcanic and metavolcanic lithic fragments, Lt = total lithic fragments = Lsm + Lvm + Qp). Porosity (Φ) and total abundance of micas (M) are relative to total point counts (n > 400) for each sample.

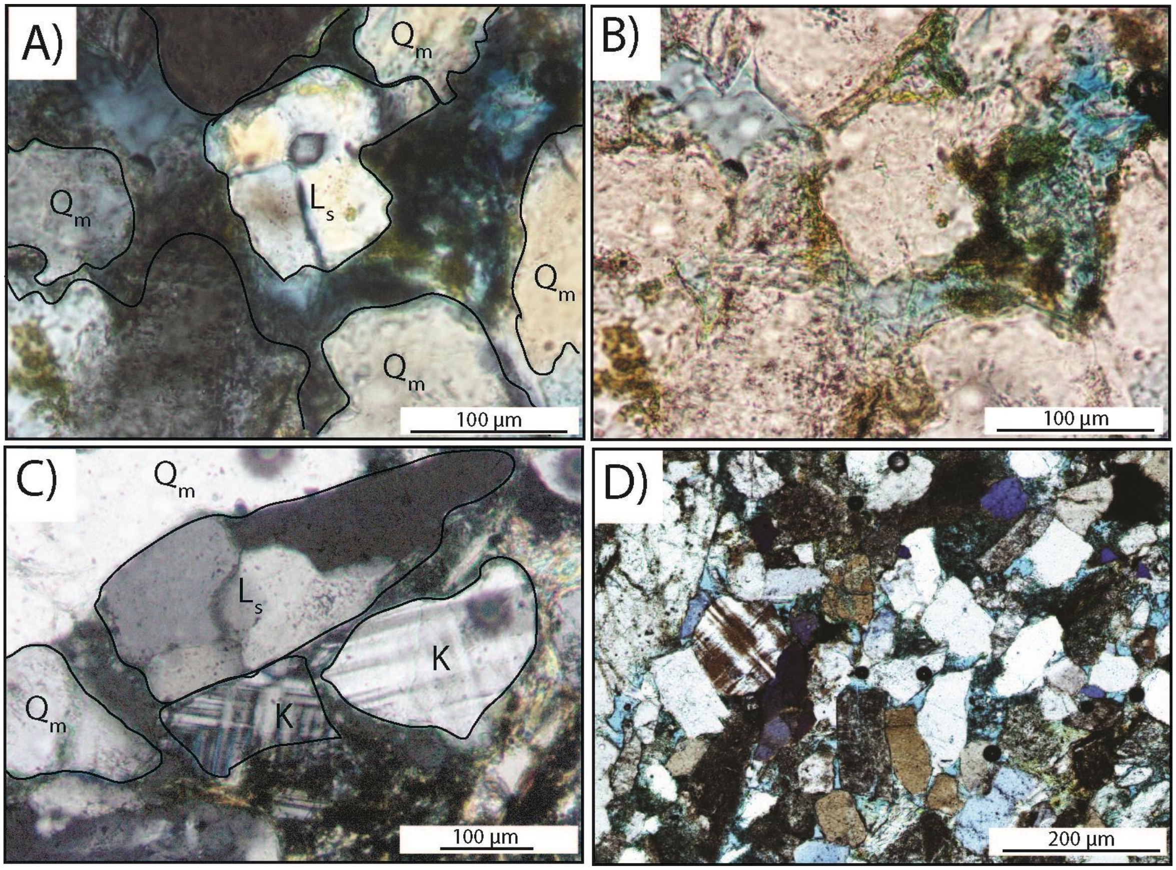

Figure 4.11: 30 µm thick thin sections of detrital grains. A) Sevier sourced sample APU3V1 composed of dominantly monocrystalline quarts (Q_m) grains with subordinate sedimentary lithic grains, likely composed of detrital eolianite sandstone grains (Ls) shown under cross-polars. B) same field of view as A), in plane polarized light. C) Mogollon sourced sample YYBV3 with significant constituents of potassium feldspar (K) grains and interclast clay minerals under cross-polars. D) Sample APU6BV3 showing mostly angular Q_m grains with significant porosity (light blue). (Dark circles are air bubbles in the epoxy).

The Straight Cliffs Formation shows similar trends in detrital grain composition as the Notom Mogollon group. Lower Smokey Hollow intervals show a distinctly recycled orogen signal while Middle Smokey Hollow and Lower John Henry members have a more continental block signal (Primm et al., 2018). The mean value shows a system that may at times be supplied from a Mogollon source and at others, a Sevier source, much like the Notom. Last Chance detrital grains (Chidsey, 2001) suggest a stronger recycled signal than that of the Notom Sevier group (Fig. 4.12). This result is counter to the cumulative DZ distribution (Fig. 4.10) which suggested a mixing of axial and transverse sources; however this may have been biased due to its low sample population.

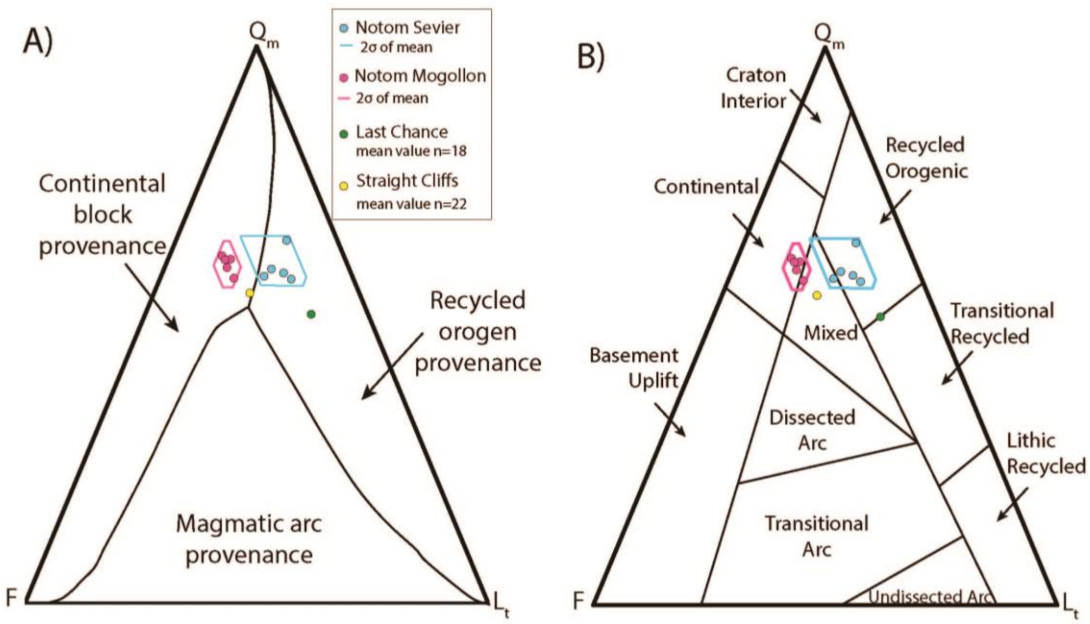

Figure 4.12: Ternary diagrams by depositional groups distinguishing between Ferron-Notom valley fill deposits with a Sevier source and a Mogollon source. Left and right show classification schemes by Weltje, (2006), and Dickinson, (1985), respectively. Averaged values for the Ferron Last Chance deltas (Chidsey, 2001) are compared with samples from Straight Cliffs lower John Henry Member and lower and middle Smokey Hollow members to the results of this study(Primm et al., 2018). (no Ferron Vernal data available).

<u>4.4.5 Incised Valley Evolution and Paleogeography</u>

Paleogeographic reconstruction of the Sequence 1 incised valley system was mapped from 125 paleocurrent measurements (Fielding, 2010; Li et al., 2010; Zhu et al., 2012; Hilton, 2013; Ullah et al., 2015; Famubode and Bhattacharya, 2016; Kimmerle and Bhattacharya, 2018), each assigned specific valley terrace membership and grouped by provenance. The interpreted drainage system honours the valley margins correlated by previous studies (Li et al., 2010; Zhu et al., 2012; Li and Bhattacharya, 2013), as well as paleocurrent locations, provenance and incorporates concepts of valley widening and channel straightening within the backwater (Chatanantavet et al., 2012; Blum et al., 2013). A calculated backwater length of 14 ± 10 km (Kimmerle and Bhattacharya, 2018) was used to estimate the location of the bayline through time relative to backwater and tidal signitures observed in outcrop (Li et al., 2010; Campbell, 2013; Hilton, 2013; Ahmed et al., 2014; Kimmerle and Bhattacharya, 2018). Grainsize is also noted at our sample locations, and we assume a general trend of finer material being deposited downstream in our valley flueve correlations. As DZ control is evenly distributed within four locations, valley morphology is based primarily on flow direction and favor eastward-flowing, Quaternary style geometries. For simplicity of interpretation, valley fill deposits have been assigned a representative colour: blue for Sevier and pink for Mogollon sources (Fig. 4.13).

Incised Valley V3 Terraces

Description-The oldest valley terrace deposits, V3, shows differing provenances (Fig. 4.13A). North Caineville Reef and Neilson Wash samples show a Sevier DZ signal suggesting transverse drainage from the northern part of the outcrop belt. Grainsize variation shows predominantly cU to granule sandstone in North Caineville Reef, and mostly mL sandstone in Neilson Wash (Li et al., 2010; Hilton, 2013; Ullah et al., 2015; Kimmerle and Bhattacharya, 2018). South Caineville and Coalmine Wash have a Mogollon sourced provenance, which would imply an axial drainage sourced from the south west, and varies in grainsize from mU-mL sandstone in South Caineville (Zhu et al., 2012) to fL to mL sandstone in Coalmine Wash (Li and Bhattacharya, 2013).

Interpretation-The timing of these valley fills creates a challenging geometry, as V3 deposits of the axial valley must cross the transverse valley in order to be contiguous from the southwest to the northeast of the study area. The V3 terrace in Coalmine Wash (Sample YYBV3) shows the greatest similarity with the Mogollon source, yet is the closest of this subset to the Sevier group, perhaps suggesting some mixing of the two sources. If these valleys were consecutive, then a stepped lowering of baselevel may explain the sucession of an axial valley over a transverse valley (Fig 4.13B) with associated valley coalescence and stream capture (Schumm and Etheridge, 1994; Blum and Hattier-womack, 2009) particularly in the valley networks between North Caineville Reef and Coalmine Wash. A stepped forced regression is consistent with Notom delta models and previous work on the incised valleys in Coalmine Wash (Li et al., 2011a; Campbell, 2013; Li and Bhattacharya, 2013) where V3 falling-stage terraces have been interpreted.

Incised Valley V2 Terraces

Description- North Caineville Reef and South Caineville locations show only two stacked terraces with two 6^{th} order surfaces (Miall, 1994) therefore sequential timing of each terrace is not certain. The youngest valley fill in North Caineville Reef is predominantly mL to mU sandstone, and provenance suggests a Sevier Thrust Front source. V2 in Coalmine Wash is fL to mL with tidally influenced inclined heterolithic deposits in the upper valley fill (Li and Bhattacharya, 2013) and a Mogollon provenance. The youngest valley fill in South Caineville is Mogollon sourced and has a grainsize of mL-mU sandstone. Mogollon sourced V2 terrace in Neilson Wash grainsize is much more heterolithic, ranging from mudstone to mU sandstone and shows distinct marine and tidal influence (Campbell, 2013; Hilton, 2013; Kimmerle and Bhattacharya, 2018). The incision in Neilson Wash and Coalmine Wash made by V2 is locally the deepest incision of the three terraces (Li et al., 2010; Hilton, 2013; Li and Bhattacharya, 2013; Ullah et al., 2015). Dominant paleotransport direction is to the northeast in Coalmine Wash and Neilson Wash outcrops. (Fig. 4.5A)

Interpretation- The V2 Mogollon provenance in Coalmine Wash, Neilson Wash and South Caineville indicates that the axial drainage is now the dominant sediment source. The youngest valley fill in North Caineville Reef is not likely active at this time, as the valleys east of this location do not show Sevier sediments. The marine and tidal influence in these deposits, along with the deeper valley incisions, may indicate that either this is a lowstand terrace or tectonic forcing and subtle slope changes have affected the drainage in this part of the basin and Sevier sourced valley fills have shifted north as a result (Fig. 4.13C).

Incised Valley V1 Terraces

Description- As the youngest mL to mU sandstone valley fill in North Caineville Reef was excluded from the V2 drainage network, we assume that it feeds the more distal terraces at the Coalmine Wash and Neilson Wash locations. Coalmine Wash V1 valley fills are predominantly mL-mU sandstone, while Neilson Wash V1 terraces are composed of fL-mL sandstones with increasing heterogeneity and tidal influence in the upper part of the deposits (Li et al., 2010; Li and Bhattacharya, 2013; Kimmerle and Bhattacharya, 2018). The transverse drainage has resumed its previous sediment dispersal pattern during V3 deposition, and the axial drainage no longer reaches the study area. Paleotransport direction shows no change in Coalmine Wash, and little change (<45 degrees) in Neilson Wash.

Interpretation- V1 terraces show a re-establishment of transverse drainage in this area, possibly as a result of baselevel rise (Fig. 4.13D). Combined with the absence of the axial drainage component, we interpret this valley fill as late transgression; an interpretation supported by the increase in tidal influence in the upper part of these deposits. Consequently we assume any unconfined fluvial highstand sediments out of the valley will retain the same provenance and transverse drainage dominance as the transgressive V1 valley fill.

Regional paleogeography, implied by axial trunk-only depositional models (Garrison and Bergh, 2006; Zhu, 2010; Ahmed et al., 2014), seem unlikely, given the valley width and complex geometry of valley flueves in the study area (Fig. 4.2). The avulsion of rivers is typically most influenced by backwater controls, which are not likely to reach to the extent of a ~400 km avulsion node; the distance between the Kaiparowits and Last Chance deltas at the foot of the Cordilleran mountains. Even continental scale drainages, such as the Mississippi, have not recorded avulsions greater than 200 km in the last 10,000 years (Aslan et al., 2005) and is therefore an unsuitable analog for the Ferron. The Andean drainage pattern (Ryer and Lovekin, 1986) allows for a more realistic drainage and valley incisions patterns, as it assumes that no Ferron delta is fed only by a single far reaching trunk (Fig. 4.3A), rather it is the contributive amalgamation of several smaller local drainages (Fig. 4.3B) and this model seems to better fit our provenance data.

Provenance analysis shows that valley terraces have at least 2 main sources of sediment in the Ferron Notom and suggests multiple sources in the Straight Cliffs Formation of the Kaiparowits Plateau. The limited DZ data and petrographic evidence from the Last Chance suggests a singular Sevier source; and similarly with the samples collected from the Vernal. This evidence further implies that the avulsion model of a single axial trunk river (Fig. 4.5B) is unlikely.

Figure 4.13 (*following page*): Paleogeographic reconstruction of a degradational landscape a three episode of valley terrace formation in the youngest Ferron-Notom sequence. A) Early falling stage V3 terraces sourced from separate axial and transverse drainages feeding incised valley trunks with different DZ assemblages and Q_mFL_t signatures. B) Late falling stage shows valley coalescence of Sevier trunk incised valleys filled with Mogollon sourced sediment. C) Complete drainage capture of all valleys by Mogollon axial drainage during lowstand. D) Transgressive stage valley fill by transverse Sevier trunk drainage and Sevier dominance of late compound valley fill.

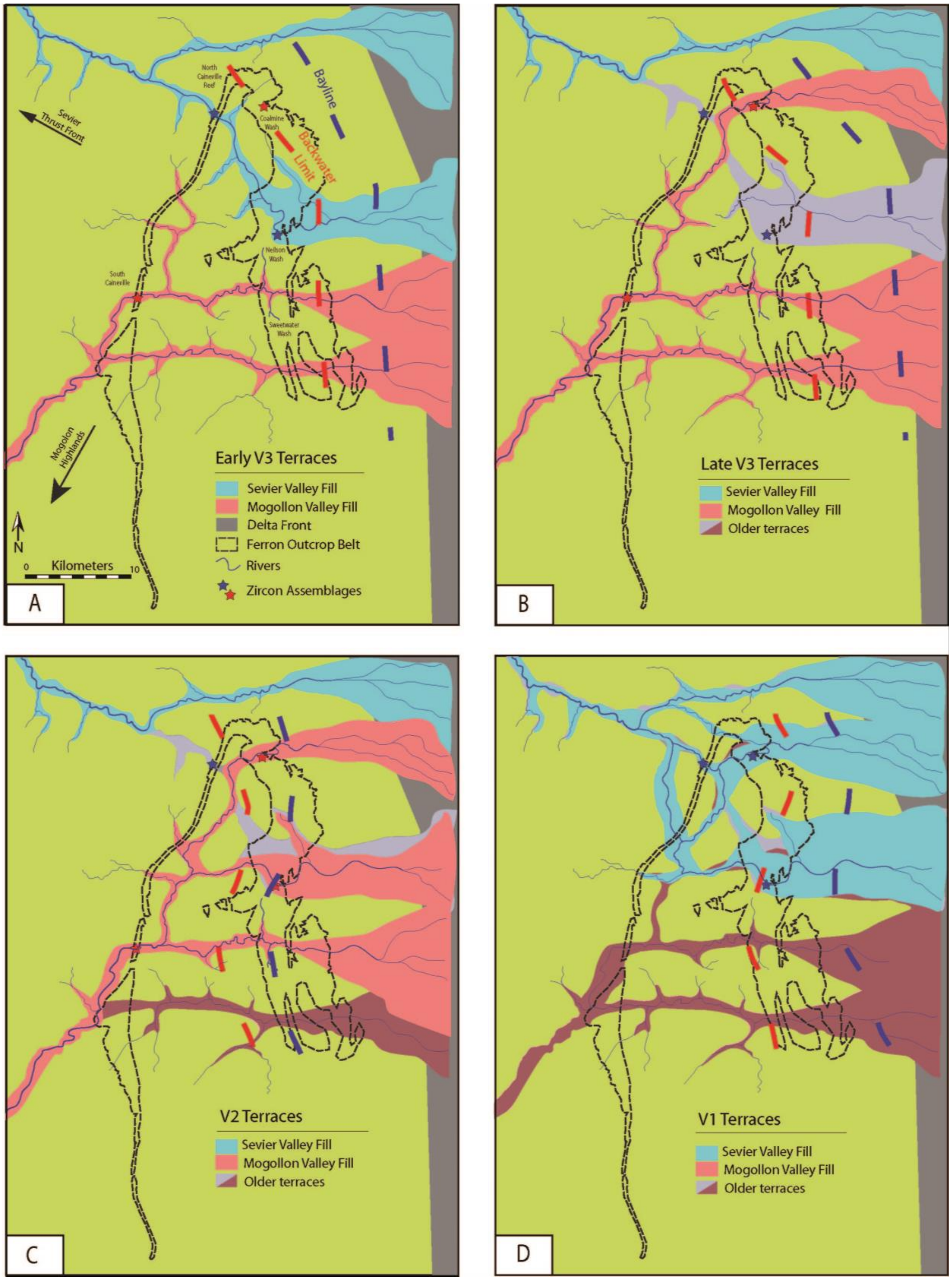
North Caineville Reef
Coalmine Wash
Bayline
Backwater Limit
Sevier Thrust Front
Nellson Wash
South Caineville
Sweetwater Wash
Mogolon Highlands
Early V3 Terraces
Sevier Valley Fill
Mogollon Valley Fill
Delta Front
Ferron Outcrop Belt
Rivers
Zircon Assemblages
N
0 Kilometers 10
A
Late V3 Terraces
Sevier Valley Fill
Mogollon Valley Fill
Older terraces
B
V2 Terraces
Sevier Valley Fill
Mogollon Valley Fill
Older terraces
C
V1 Terraces
Sevier Valley Fill
Mogollon Valley Fill
Older terraces
D

4.5 Discussion

4.5.1 Valley Morphology

The incised valley networks of the Cretaceous Dunvegan Formation (Plint, 2002) and Lower Pennsylvanian Morrow formation (Bowen et al., 2003), mapped from the correlation of well logs, show far more complex valley geometries than those depicted by simplistic valley models previously discussed. These valleys include tributary junctions of adjacent feeder valley networks that are separated by interflueve "islands" while still interpreted to drain a single watershed, and are mapped to show far more interflueve than valley. Valleys in the Lower Mannville Formation in Alberta, particularly in the Horsefly, Bantry-Alderson-Taber (BAT) and Ellerslie Sandstones, show much wider valley systems with smaller interflueves (Ardies et al., 2002; Zaitlin, 2002). This is likely due to the long lifespan of these valleys that reflect significant tectonic control (Zaitlin, 2002). The location of strike-slip faults are primarily responsible for modern incised valley morphology along the French Atlantic coast (Menier et al., 2006; Chaumillon and Weber, 2013). Eustatically controlled incised valley systems, however, may exhibit cyclicity on a much shorter timescale of 10-100 ka (Broecker and van Donk, 1970; Berger, 1978; Markonis and Koutsoyiannis, 2013) than those that are tectonically controlled; and are susceptible to factors such as stream capture (Schumm and Etheridge, 1994) and valley convergence with changes in baselevel (Wescott, 1993; Blum and Hattier-womack, 2009).

The Ferron Notom valleys (Fig. 4.13) reflect much of the tributive radiating network morphology seen in the Lower Mannville, without any obvious strike-slip control of the French valleys. The planform expression of the topographic valley at each stage of terrace formation (V3, V2 and V1) show a progressively degrading landscape of fragmentary interflueves and valleys. We interpret the valley fill deposits of distinctly different sources as originating from vastly different directions before it reaches the last 40 km of the coastal plain. We propose that the west-east trending valleys converge and eventually coalesce, likely due to backwater influences as the resulting valleys widen. Ferron compound valleys should therefore be considered analogous to the Colorado-Brazos-Trinity valleys, as they share much in the way of scale, transverse drainage dominance and are sourced by multiple drainage basins (Fig. 4.4).

Maximum incision depth of the compound Ferron Notom valley reaches aproxiamtely 29 m (Li et al., 2010; Li and Bhattacharya, 2013; Kimmerle and Bhattacharya, 2018). Assuming an average width of ~40 km, this coastal plain incised valley shows width to thickness ratios greater than those of the Trinity, Rhine and Po and is most similar to that of the Colorado in Texas (Gibling, 2006; Blum et al., 2013).

4.5.2 Wheeler Analysis and Chronostratigraphy

Sanidine crystals extracted from bentonite layers collected during regional mapping of the Ferron Notom (Zhu et al., 2012) have been re-analysed, along with the new sample taken at the base of the valley in this study, using improved $^{40}Ar/^{39}Ar$ dating methods (Jicha et al., 2016). The results of this analysis are summarized in Table 4. The position of the upper bentonite (sample B4) and the bentonite found at the top of Sequence 3 (Sample B3) are shown in context with the regional sequence stratigraphic dip oriented cross section (Fig 4.14). The time difference between these samples amounts to around 20 Ka, and chronometrically constrains the deposition of 2 sequences with the highstand systems tract for Sequence 1 unaccounted for. Extrapolating for a 5 to10 ka highstand duration in Sequence 1, which conforms to the timing of the Sequence 2 highstand, we infer a duration of 10 to 15 ka for Sequence 1 and a youngest chronometric value for the uppermost Ferron-Notom fluvial deposits of 91.13 Ma.

Table 4.4: Bentonite Dates

	Previous Analysis			This Study		
			Weighted Mean			Weighted Mean
Sample #	n	MSWD	AGE (Ma) ± 2s	n	MSWD	AGE (Ma) ± 1σ
UH-BHA-B4	8 of 8	0.84	90.64 ± 0.25	13 of 26	0.64	91.14 ± 0.19
FN-BHt				16 of 16	1.42	91.15 ± 0.11
UH-BHA-B3	12 of 14	1.05	90.69 ± 0.34	6 of 15	0.20	91.16 ± 0.36
UH-BHA-B1	13 of 13	0.69	91.25 ± 0.77	27 of 30	1.35	91.90 ± 0.12

Chronometric values for bentonite extracted sanidines that correlate with stratigraphic surfaces (Fig. 4.14). Values reported as Previous Analysis were published by Zhu *et al.* (2012). These values are shown with our new results.

Our Ferron-Notom 40 km wide valley took less than 15 ka to cut and fill, and represents a feature larger than a single trunk channel could produce in a higher frequency stratigraphic sequence, likely requiring more than one trunk valley to create. This feature may have been produced by the convergence and change from an axial to transverse drainage system within the fluvial succession as a result of baselevel fluctuations. The paleogeographic evolution discussed above was previously assumed to have occurred over timescales approaching 100 ka, consistent with the longest Milankovitch wavelength

(Li and Bhattacharya, 2013; Famubode and Bhattacharya, 2016; Kimmerle and Bhattacharya, 2018). Recent geochronology now suggests a 10 - 15 ka timeframe, which is consistent with a eustatic control and may rule out a tectonic influence, as the drainage changes from transverse to axial and back to transverse dominated are likely too high frequency.   Tectonic control typically operates on a 100,000 year timescale in a greenhouse setting (Vakarelov et al., 2006), while bentonite dates constrain our time frame to at least an order of magnitude higher frequency.

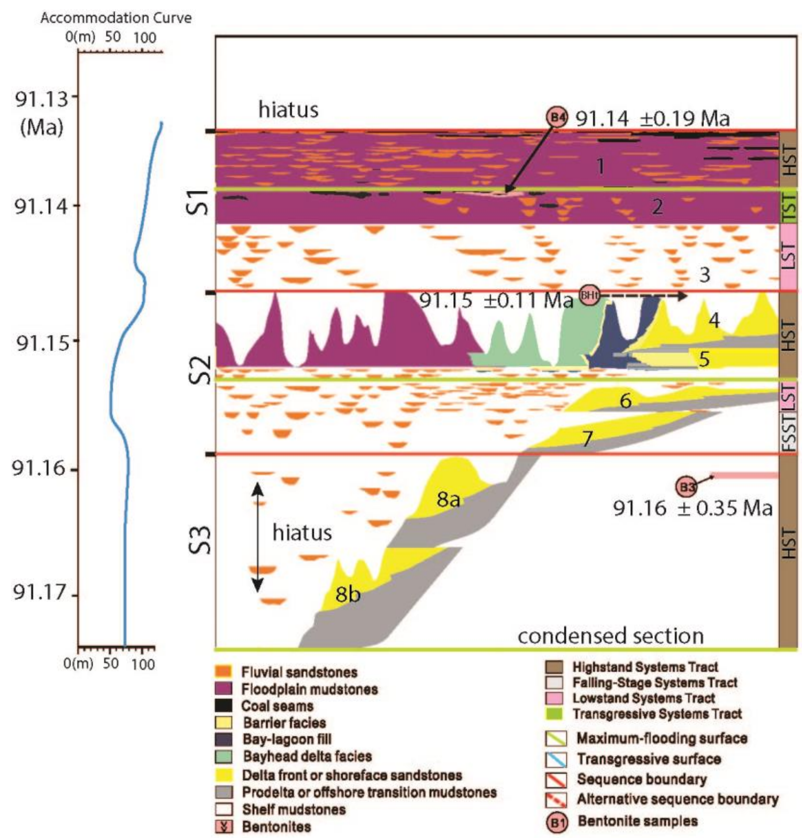

Figure 4.14: Wheeler diagram of Sequence 1 and 2 of the Ferron-Notom (*modified from:* Zhu et al., 2012)**.** Chronostratigraphic relationships of valley erosion and fluvial deposition are considered to be diacronous accross a compound valley surface. The locations of bentonite samples with their reported chronometric values are shown. These dates form the basis for the timeline on the vertical axis.

Changes in baselevel translate upstream to knickpoint exposure and erosion as channels reacquire profile equilibrium within the coastal prism. In the Ferron Notom Sequence 1 compound valley, widening appears to be controlled by a combination of knickpoint exposure, the convergence of multiple trunk rivers and possibly differences in drainage basin configurations. With a maximum incision depth of 28 m, closer watershed sources will experience a greater change in slope profile than those whose headwaters are farther away. This would exert a greater influence on the Sevier sourced trunk channels, who's headwaters are a few hundred kilometers away to the northwest, than the Mogollon sourced channels, who's headwaters span more than 3 times that distance away. The evolution of valley fill provenance from Sevier to Mogollon to Sevier shown in Neilson Wash in Figure 4.13 may therefore express preferential drainage due to changes in slope.

4.5.3 Source to Sink implications for Degradational Landscapes

Sequence 1 compound incised valley of the Ferron-Notom non-marine deposits shows a much wider and degraded landscape then predicted by previous valley incision models (Posamentier et al., 1988; Shanley and McCabe, 1994; Boyd et al., 2006). Assuming the shortest duration for baselevel fluctuation interpreted from our chronometric dating, it seems anomalously wide when compared with other valley systems (Gibling, 2006; Blum et al., 2013) which include Quaternary examples with a similar semi-consolidated coastal plain substrate. It is possible that the interplay and alternation of axial and transverse trunk valleys may create a regional composite scour that does not require multiple rises and falls in base level or landward knickpoint migration (Holbrook and Bhattacharya, 2012). Instead, the degraded landscape created by the convergence of two or more trunk valley incisions and their fills, produces a compound valley that is larger than could be produced by either trunk channel on its own.

Distinct differences in grainsize, lithology and fluvial style between valley terraces V1, V2, and V3 in the Ferron-Notom non Marine strata were previously interpreted to be a result of changes in baselevel, slope, discharge and therefore backwater effects (Li et al., 2010; Li and Bhattacharya, 2013; Kimmerle and Bhattacharya, 2018). While these factors do play a significant role, we wish to stress that this compound valley likely represents the convergence of at least two separate trunk systems based on provenance analysis in source to sink estimations. Any use of sediment budget analysis, such as the BQART model (Syvitski et al., 2007) or similar methods that estimate upstream catchment dimensions, assumes that axial trunk rivers supply all sediment sequestered in the channel fill. Transverse drainages and their related catchment basins are not considered in such estimates and may represent additional sources of mass imbalance.

4.6 Conclusions

Ten incised valley terraces were sampled in the youngest non-marine sequence of the Turonian Notom Delta of the Ferron Sandstone Member, Mancos Shale Formation. Detrital zircon assemblages of these samples revealed two distinct provenance groups, likely originating from separate axial and transverse drainages. Redundant sampling of other bar deposits within three of these terraces confirmed that inter-group variability did not affect our interpretation of group membership. Petrographic classification of the same samples confirmed statistical similarity of our samples and each terrace provenance group membership.

We conclude that the Ferron incised valleys in our study were filled with sediment from a Mogollon Highland axial drainage source flowing to the northeast and a Turonian Sevier Thrust Front transverse drainage source flowing to the southeast. Paleogeographic reconstruction of an incised trunk network using provenance groups and GIS to map paleocurrents within documented valley margins, has shown the complex morphology of such a system including much more fragmentary and discontinuous interflueves. The source of the sediment within the valley is not uniform throughout the entire compound valley fill, but is consistent within individual valley terraces at the same location. In that sense, the resulting fill may be predictable given the stratigraphic context of its systems tract and the regional context of its drainage.

Reginal provenance analysis disagrees with drainage models that suggest avulsion of a single axial trunk river avulsion was responsible for cyclical changes in depositional focus, resulting in the Kaiparowits, Notom and Last Chance Deltas. Remapping this compound valley assuming more complex drainages with reference to Quaternary analogues shows a radically revised paleogeography suggesting several coeval rivers along strike.

Acknowledgements

This paper was written with the generous support of the Susan Cunningham Research Chair at McMaster University, Quantitative Sedimentology Laboratories, with funding from BP, and NSERC.

References

Ahmed, S., Bhattacharya, J.P., Garza, D.E., and Li, Y., 2014, Facies Architecture and Stratigraphic Evolution of A River-Dominated Delta Front, Turonian Ferron Sandstone, Utah, U.S.A: Journal of Sedimentary Research, v. 84, no. 2, p. 97–121, doi: 10.2110/jsr.2014.6.

Amato, J.M., 2019, Detrital zircon ages from Proterozoic, Paleozoic, and Cretaceous clastic strata in southern New Mexico, U.S.A.: Rocky Mountain Geology, v. 54, no. 1, p. 19–32, doi: 10.24872/rmgjournal.54.1.19.

Amato, J.M., Boullion, A.O., Serna, A.M., Sanders, A.E., Farmer, G.L., Gehrels, G.E., and Wooden, J.L., 2008, Evolution of the Mazatzal province and the timing of the Mazatzal orogeny: Insights from U-Pb geochronology and geochemistry of igneous and metasedimentary rocks in southern New Mexico: Bulletin of the Geological Society of America, v. 120, no. 3–4, p. 328–346, doi: 10.1130/B26200.1.

Amato, J.M., Heizler, M.T., Boullion, A.O., Sanders, A.E., Toro, J., McLemore, V.T., and Andronicos, C.L., 2011, Syntectonic 1.46 Ga magmatism and rapid cooling of a gneiss dome in the southern Mazatzal province: Burro Mountains, New Mexico: Bulletin of the Geological Society of America, v. 123, no. 9–10, p. 1720–1744, doi:

10.1130/B30337.1.

Amato, J.M., and Mack, G.H., 2012, Detrital zircon geochronology from the Cambrian-Ordovician Bliss Sandstone, New Mexico: Evidence for contrasting grenville-age and cambrian sources on opposite sides of the Transcontinental Arch: Bulletin of the Geological Society of America, v. 124, no. 11–12, p. 1826–1840, doi: 10.1130/B30657.1.

Ardies, G.W., Dalrymple, R.W., and Zaitlin, B.A., 2002, Controls on the geometry of incised valleys in the Basal Quartz unit (Lower Cretaceous), Western Canada Sedimentary Basin: Journal of Sedimentary Research, v. 72, no. 5, p. 602–618, doi: 10.1306/032101720602.

Armstrong, R.L., 1968, Sevier orogenic belt in Nevada and Utah: Geological Society of America Bulletin, v. 79, no. 3, p. 429–458.

Aslan, a., Autin, W.J., and Blum, M.D., 2005, Causes of River Avulsion: Insights from the Late Holocene Avulsion History of the Mississippi River, U.S.A.: Journal of Sedimentary Research, v. 75, no. 4, p. 650–664, doi: 10.2110/jsr.2005.053.

Berger, A.L., 1978, Long-Term Variations of Daily Insolation and Quaternary Climatic Changes: Journal of the atmospheric sciences, v. 35, p. 2362–2367.

Bhattacharya, J.P., and Tye, R.S., 2004, Searching for modern Ferron analogs and application to subsurface interpretation: Regional to Wellbore Analog for Fluvial–Deltaic Reservoir Modeling: the Ferron Sandstone of Utah: American Association of

Petroleum Geologists, Studies in Geology 50, p. 39–57.

Biber, K., Khan, S.D., Bhattacharya, J.P., Barton, M.D., and Glennie, C.L., 2017, Quantitative characterization of shales within tidally influenced fluvial valley fill deposits of the Ferron Sandstone, eastern Utah: Implications for hydrocarbon exploration: AAPG Bulletin, v. 101, no. 10, p. 1599–1623, doi: 10.1306/01111715108.

Blum, M.D., and Aslan, A., 2006, Signatures of climate vs. sea-level change within incised valley-fill successions: Quaternary examples from the Texas GULF Coast: Sedimentary Geology, v. 190, no. 1–4, p. 177–211, doi: 10.1016/j.sedgeo.2006.05.024.

Blum, M.D., and Hattier-womack, J., 2009, Climate change, sea-level change, and fluvial sediment supply to deepwater systems, *in* Kneller, B., Martinsen, O.J., McCaffrey, B. ed., External Controls on Deep Water Depositional Systems: Climate, Sea-Level, and Sediment Flux: SEPM Special Publication, SEPM Special Publication, p. 15–39.

Blum, M., Martin, J., Milliken, K., and Garvin, M., 2013, Paleovalley systems: Insights from Quaternary analogs and experiments: Earth-Science Reviews, v. 116, no. 1, p. 128–169, doi: 10.1016/j.earscirev.2012.09.003.

Blum, M., and Pecha, M., 2014, Mid-cretaceous to paleocene North American drainage reorganization from detrital zircons: Geology, v. 42, no. 7, p. 607–610, doi: 10.1130/G35513.1.

Bowen, D.W., Weimer, P., Benson, B.D., Scott, A., Gillis, S., Mathews, R., Strife, S., and Pearl, M., 2003, Regional sequence stratigraphic setting and reservoir geology of Morrow incised-valley sandstones (lower Pennsylvanian), eastern Colorado and western Kansas of the manuscript benefited from the reviews: AAPG Bulletin, v. 5, no. 5, p. 781–815, doi: 10.1306/01150301131.

Boyd, R., Dalrymple, R.W., and Zaitlin, B. a, 2006, Estuarine and incised-valley facies models: Special Publication - Society for Sedimentary Geology, v. 84, no. 84, p. 171–235, doi: 10.2110/pec.06.84.0171.

Broecker, W.S., and van Donk, J., 1970, Insolation Changes, Ice Volumes, and the O18 in Deep-Sea Cores: Reviews of Geophysics and Space Physics, v. 8, no. 1, p. 169–198.

Campbell, C.E., 2013, Valley Widening and the Composite Nature of Valley Margin Sequence Boundaries: Evidence from the Neilson Wash Compound Valley Fill, Cretaceous Ferron: University of Houston, 108 p.

Chatanantavet, P., Lamb, M.P., and Nittrouer, J. a., 2012, Backwater controls of avulsion location on deltas: Geophysical Research Letters, v. 39, no. 1, p. n/a-n/a, doi: 10.1029/2011GL050197.

Chaumillon, E., and Weber, N., 2013, Spatial Variability of Modern Incised Valleys on the French Atlantic Coast: Comparison between the Charente and the Lay–Sèvre Incised Valleys: Incised Valleys in Time and Space, p. 57–85, doi: 10.2110/pec.06.85.0057.

Chidsey, T.C., 2001, Geological and Petrophysical Characterization of the Ferron Sandstone for 3-D Simulation of a Fluvial-Deltaic Reservoir (U. G. Survey, Ed.): U.S. Department of Energy Contract No. DE-AC22-93BC14896.

Dickinson, W.R., 1985, Interpreting Provenance Relations from Detrital Modes of Sandstones, *in* Provenance of Arenites,.

Dickinson, W.R., and Gehrels, G.E., 2010a, Insights into North American Paleogeography and Paleotectonics from U-Pb ages of detrital zircons in Mesozoic strata of the Colorado Plateau, USA: International Journal of Earth Sciences, v. 99, no. 6, p. 1247–1265, doi: 10.1007/s00531-009-0462-0.

Dickinson, W.R., and Gehrels, G.E., 2008a, Sediment delivery to the Cordilleran foreland basin: Insights from U-Pb ages of detrital zircons in Upper Jurassic and Cretaceous strata of the Colorado Plateau: American Journal of Science, v. 308, no. 10, p. 1041–1082, doi: 10.2475/10.2008.01.

Dickinson, W.R., and Gehrels, G.E., 2010b, Synoptic Record in Space and Time of Provenance Relations for Mesozoic Strata in South-Central Utah from U-Pb Ages of Detrital Zircons: Geology of South Central Utah, v. 39, p. 178–193.

Dickinson, W.R., and Gehrels, G.E., 2008b, U-Pb Ages of Detrital Zircons in Relation to Paleogeography: Triassic Paleodrainage Networks and Sediment Dispersal Across Southwest Laurentia: Journal of Sedimentary Research, v. 78, no. 12, p. 745–764, doi: 10.2110/jsr.2008.088.

Dickinson, W.R., Gehrels, G.E., and Marzolf, J.E., 2010, Detrital zircons from fluvial Jurassic strata of the Michigan basin: Implications for the transcontinental Jurassic paleoriver hypothesis: Geology, v. 38, no. 6, p. 499–502, doi: 10.1130/G30509.1.

Drost, J.B., and Keller, S.J., 1989, Development of the Mississippian- Pennsylvanian Unconformity in Indiana: Indiana Geological Survey Occasional Paper, v. 55, p. 11.

Famubode, O.A., and Bhattacharya, J.P., 2016, Sequence Stratigraphic Analysis of the Youngest Nonmarine Sequence In the Cretaceous Ferron Notom Delta, South Central Utah, U.S.A.: Journal of Sedimentary Research, v. 86, no. 3, p. 168–198, doi: 10.2110/jsr.2016.8.

Fielding, C.R., 2010, Planform and Facies Variability in Asymmetric Deltas: Facies Analysis and Depositional Architecture of the Turonian Ferron Sandstone in the Western Henry Mountains, South-Central Utah, U.S.A.: Journal of Sedimentary Research, v. 80, no. 5, p. 455–479, doi: 10.2110/jsr.2010.047.

Gardiner, 1995, Tectonic and eustatic controls on the stratal architecture of mid-Cretaceous strati- graphic sequences, central western interior foreland basin of North America.

Garrison, J.R., and Bergh, T.C.V. Van Den, 2006, Effects of sedimentation rate, rate of relative rise in sea level, and duration of sea-level cycle on the filling of incised valleys: examples of filled and “overfilled” incised valleys from the upper Ferron Sandstone, Last Chance Delta, east-central Utah:

Garrison James R., and Van den Bergh, T.C.V., 2004, High-resonlution depositional sequence stratigraphy of the Upper Ferron sandstone Last Chance Delta: an application of coal-zone stratigraphy: AAPG Studies in Geology, v. 50, p. 125–192.

Garzanti, E., Andò, S., and Vezzoli, G., 2009, Grain-size dependence of sediment composition and environmental bias in provenance studies: Earth and Planetary Science Letters, v. 277, no. 3–4, p. 422–432, doi: 10.1016/j.epsl.2008.11.007.

Gibling, M.R., 2006, Width and Thickness of Fluvial Channel Bodies and Valley Fills in the Geological Record: A Literature Compilation and Classification: Journal of Sedimentary Research, v. 76, no. 5, p. 731–770, doi: 10.2110/jsr.2006.060.

Hilton, B., 2013, 3D Allostratigraphic Mapping and Facies Heterogeneity of a Compound, Tributary Incised Valley System, Turonian Ferron Sandstone, Notom Delta, South-Central Utah [MS thesis]: University of Houston, 136 p.

Holbrook, J.M., and Bhattacharya, J.P., 2012, Reappraisal of the sequence boundary in time and space: Case and considerations for an SU (subaerial unconformity) that is not a sediment bypass surface, a time barrier, or an unconformity: Earth-Science Reviews, v. 113, no. 3–4, p. 271–302, doi: 10.1016/j.earscirev.2012.03.006.

Ibañez-Mejia, M., Pullen, A., Pepper, M., Urbani, F., Ghoshal, G., and Ibañez-Mejia, J.C., 2018, Use and abuse of detrital zircon U-Pb geochronology-A case from the Río Orinoco delta, eastern Venezuela: Geology, v. 46, no. 11, p. 1019–1022, doi: 10.1130/G45596.1.

Jicha, B.R., Singer, B.S., and Sobol, P., 2016, Re-evaluation of the ages of 40 Ar/ 39 Ar sanidine standards and supereruptions in the western U.S. using a Noblesse multi-collector mass spectrometer: Chemical Geology, v. 431, p. 54–66, doi: 10.1016/j.chemgeo.2016.03.024.

Kimmerle, S., and Bhattacharya, J.P., 2018, Facies, Backwater Limits, and Paleohydraulic Analysis of Rivers in a Forced- Regressive, Compound Incised Valley, Cretaceous Ferron Sandstone, Utah, U.S.a.: , no. February, p. 177–200, doi: 10.2110/jsr.2018.5.

Kvale, E.P., and Archer, A.W., 2007, Paleovalley fills: Trunk vs. tributary: AAPG Bulletin, v. 91, no. 6, p. 809–821, doi: 10.1306/11060606022.

Laskowski, A.K., Decelles, P.G., and Gehrels, G.E., 2013, Detrital zircon geochronology of Cordilleran retroarc foreland basin strata, western North America: Tectonics, v. 32, no. 5, p. 1027–1048, doi: 10.1002/tect.20065.

Lawton, T.F., Bradford, I.A., Vega, F.J., Gehrels, G.E., and Amato, J.M., 2009, Provenance of Upper Cretaceous-Paleogene sandstones in the foreland basin system of the Sierra Madre Oriental, northeastern Mexico, and its bearing on fluvial dispersal systems of the Mexican Laramide Province: Bulletin of the Geological Society of America, v. 121, no. 5–6, p. 820–836, doi: 10.1130/B26450.1.

Lawton, T.F., Schellenbach, W.L., and Nugent, A.E., 2014, Late Cretaceous Fluvial-Megafan and Axial-River Systems In the Southern Cordilleran Foreland Basin: Drip

Tank Member of Straight Cliffs Formation and Adjacent Strata, Southern Utah, U.S.A: Journal of Sedimentary Research, v. 84, no. 5, p. 407–434, doi: 10.2110/jsr.2014.33.

Li, Y., and Bhattacharya, J.P., 2013, Facies-Architecture Study of A Stepped, Forced Regressvie Compound Incised Valley In the Ferron Notom Delta, Southern Central Utah, U.S.A: Journal of Sedimentary Research, v. 83, no. 3, p. 206–225, doi: 10.2110/jsr.2013.19.

Li, Y., and Bhattacharya, J., 2014, Facies architecture of asymmetrical branching distributary channels: Cretaceous Ferron Sandstone, Utah, USA: Sedimentology, v. 61, no. 5, p. 1452–1483, doi: 10.1111/sed.12104.

Li, W., Bhattacharya, J.P., and Campbell, C., 2010, Temporal Evolution of Fluvial Style in a Compound Incised-Valley Fill, Ferron "Notom Delta", Henry Mountains Region, Utah (U.S.A.): Journal of Sedimentary Research, v. 80, no. 1994, p. 529–549, doi: 10.2110/jsr.2010.053.

Li, W., Bhattacharya, J., and Zhu, Y., 2011a, Architecture of a forced regressive systems tract in the Turonian Ferron "Notom Delta", southern Utah, U.S.A.: Marine and Petroleum Geology, v. 28, no. 8, p. 1517–1529, doi: 10.1016/j.marpetgeo.2011.05.004.

Li, W., Bhattacharya, J.P., and Zhu, Y., 2012, Stratigraphic uncertainty in sparse versus rich data sets in a fluvial-deltaic outcrop analog: Ferron Notom delta in the Henry

Mountains region, southern Utah: AAPG Bulletin, v. 96, no. 3, p. 415–438, doi: l0.1306/05231110192.

Li, W., Bhattacharya, J.P., Zhu, Y., Garza, D., and Blankenship, E., 2011b, Evaluating delta asymmetry using three-dimensional facies architecture and ichnological analysis, Ferron "Notom Delta", Capital Reef, Utah, USA: Sedimentology, v. 58, no. 2, p. 478–507, doi: 10.1111/j.1365-3091.2010.01172.x.

Markonis, Y., and Koutsoyiannis, D., 2013, Climatic Variability Over Time Scales Spanning Nine Orders of Magnitude: Connecting Milankovitch Cycles with Hurst-Kolmogorov Dynamics: Surveys in Geophysics, v. 34, no. 2, p. 181–207, doi: 10.1007/s10712-012-9208-9.

Matthews, W.A., and Guest, B., 2017, A Practical Approach for Collecting Large-n Detrital Zircon U-Pb Data sets by Quadrupole LA-ICP-MS: Geostandards and Geoanalytical Research, v. 41, no. 2, p. 161–180, doi: 10.1111/ggr.12146.

McCarthy, P.J., and Plint, A.G., 2003, Spatial variability of palaeosols across Cretaceous interfluves in the Dunvegan Formation, NE British Columbia, Canada: Palaeohydrological, palaeogeomorphological and stratigraphic implications: Sedimentology, v. 50, no. 6, p. 1187–1220, doi: 10.1111/j.1365-3091.2003.00600.x.

Menier, D., Bonnet, S., Reynaud, J., Guillocheau, F., Guennoc, P., Proust, J., Tessier, B., and Goubert, E., 2006, Basement Control on Shaping and Infilling of Valleys Incised at the Southern Coast of Brittany, France: Incised Valleys in Time and Space, p. 37–

55, doi: 10.2110/pec.06.85.0037.

Miall, A.D., 1994, Reconstructing Fluvial Macroform Architecture from Two-Dimensional Outcrops: Examples from the Castlegate Sandstone, Book Cliffs, Utah: Journal of Sedimentary Research, v. Vol. 64B, no. 1972, p. 146–158, doi: 10.1306/D4267F78-2B26-11D7-8648000102C1865D.

Paton, C., Woodhead, J.D., Hellstrom, J.C., Hergt, J.M., Greig, A., and Maas, R., 2010, Improved laser ablation U-Pb zircon geochronology through robust downhole fractionation correction: Geochemistry, Geophysics, Geosystems, v. 11, no. 3, doi: 10.1029/2009GC002618.

Petrus, J.A., and Kamber, B.S., 2012, VizualAge: A Novel Approach to Laser Ablation ICP-MS U-Pb Geochronology Data Reduction: Geostandards and Geoanalytical Research, v. 36, no. 3, p. 247–270, doi: 10.1111/j.1751-908X.2012.00158.x.

Pettit, B.S., Blum, M., Pecha, M., McLean, N., Bartschi, N.C., and Saylor, J.E., 2019, Detrital-Zircon U-Pb Paleodrainage Reconstruction and Geochronology of the Campanian Blackhawk–Castlegate Succession, Wasatch Plateau and Book Cliffs, Utah, U.S.A.: Journal of Sedimentary Research, v. 89, no. 4, p. 273–292, doi: 10.2110/jsr.2019.18.

Plint, a. G., 2002, Paleovalley systems in the Upper Cretaceous Dunvegan Formation, Alberta and British Columbia: Bulletin of Canadian Petroleum Geology, v. 50, no. 2, p. 277–296, doi: 10.2113/50.2.277.

Posamentier, H.W., 2001, Lowstand alluvial bypass systems : Incised vs . unincised: AAPG Bulletin, v. 10, no. 10, p. 1771–1793.

Posamentier, H.W., Jervey, M.T., and Vail, P.R., 1988, Eustatic Controls on Clastic Deposition I-Conceptual Framework: Special Publications of the SEPM, , no. 42, p. 125–154, doi: 10.2110/pec.88.01.0109.

Posamentier, H.W., and Vail, P.R., 1988, Eustatic Controls on Clastic Deposition II — Sequence and System Tract Models: SEPM, Spec. Publ., , no. 42, p. 125–154.

Primm, J.W., Johnson, C.L., and Stearns, M., 2018, Basin-axial progradation of a sediment supply driven distributive fluvial system in the Late Cretaceous southern Utah foreland: Basin Research, v. 30, no. 2, p. 249–278, doi: 10.1111/bre.12252.

Reijenstein, H.M., Posamentier, H.W., and Bhattacharya, J.P., 2011, Seismic geomorphobgy and high-resolution seismic stratigraphy of inner-shelf fluvial, estuarine, deltaic, and marine sequences, Gulf of Thailand: AAPG Bulletin, v. 95, no. 11, p. 1959–1990, doi: 10.1306/03151110134.

Richards, B.H., 2018, Stratigraphy of the Fluvial-To-Marine Transition Zone Associated With a Forced- Regressive Compound Incised-Valley System in the Turonian Ferron Notom Delta ,: , no. March, p. 311–326, doi: 10.2110/jsr.2018.17.

Rivers, T., Ketchum, J., Indares, A., and Hynes, A., 2003, The High Pressure belt in the Grenville Province: architecture, timing, and exhumation: Canadian Journal of Earth Sciences, v. 39, no. 12, p. 1847, doi: 10.1139/e02-904.

Ryer, T.A., 2004, The Ferron Sandstone -- Overview and Reservoir Analog, *in* AAPG Studies in Geology No. 50, p. 2–38.

Ryer, T.A., and Lovekin, J.R., 1986, Upper Cretaceous Vernal Delta of Utah--Depositional or Paleotectonic Feature?, *in* Peterson, J.A. ed., Paleotectonics and sedimentation in the Rocky Mountain region, United States: AAPG Memoir 41, p. 497–510.

Schumm, S.A., and Etheridge, F.E., 1994, Origin, evolution and morphology of fluvial valleys, *in* Incised-Valley Systems: Origin and Sedimentary Sequence, p. 11–27.

Shanley, K.W., and McCabe, P.J., 1994, Perspectives on the sequence stratigraphy of continental strata: American Association of Petroleum Geologists Bulletin, v. 78, no. 4, p. 544–568, doi: 10.1306/BDFF9258-1718-11D7-8645000102C1865D.

Sharman, G.R., Sharman, J.P., and Sylvester, Z., 2018, detritalPy: A Python-based toolset for visualizing and analysing detrital geo-thermochronologic data: The Depositional Record, v. 4, no. 2, p. 202–215, doi: 10.1002/dep2.45.

Strong, N., and Paola, C., 2008, Valleys That Never Were: Time Surfaces Versus Stratigraphic Surfaces--Discusion: Journal of Sedimentary Research, v. 80, no. 1, p. 4–5, doi: 10.2110/jsr.2010.007.

Suczek, C.A., and Ingersoll, R. V, 1985, Petrology and Provenance of Cenozoic Sand From the _, U: v. 55, no. 3, p. 340–346.

Syvitski, J.P.M., Milliman, J.D., The, S., January, N., Syvitski, J.P.M., and Milliman, J.D., 2007, Geology , Geography , and Humans Battle for Dominance over the Delivery of Fluvial Sediment to the Coastal Ocean: Journal of Geology, v. 115, no. 1, p. 1–19.

Szwarc, T.S., Johnson, C.L., Stright, L.E., and McFarlane, C.M., 2014, Interactions between axial and transverse drainage systems in the Late Cretaceous Cordilleran foreland basin: Evidence from detrital zircons in the Straight Cliffs Formation, southern Utah, USA: Bulletin of the Geological Society of America, v. 127, no. 3–4, p. 372–392, doi: 10.1130/B31039.1.

Thomas, J.J., Shuster, E., and Bickford, Mk.E., 1984, A Terrane of 1,350 to 1,400 m.y. old silicic volcanic and plutonic rocks in the buried Proterozoic of the mid-continent and in the Wet Mountains , Colorado: GSA Bulletin, v. 95, no. 10, p. 1150–1157.

Ullah, M.S., Bhattacharya, J.P., and Dupre, W.R., 2015, Confluence Scours Versus Incised Valleys: Examples From the Cretaceous Ferron Notom Delta, Southeastern Utah, U.S.A: Journal of Sedimentary Research, v. 85, no. 5, p. 445–458, doi: 10.2110/jsr.2015.34.

Vakarelov, B.K., Bhattacharya, J.P., and Nebrigic, D.D., 2006, Importance of high-frequency tectonic sequences during greenhouse times of Earth history: Geology, v. 34, no. 9, p. 797–800, doi: 10.1130/G22348.1.

Vermeesch, P., 2018, Dissimilarity measures in detrital geochronology: Earth-Science Reviews, v. 178, no. July 2017, p. 310–321, doi: 10.1016/j.earscirev.2017.11.027.

Vermeesch, P., 2013, Multi-sample comparison of detrital age distributions: Chemical Geology, v. 341, p. 140–146, doi: 10.1016/j.chemgeo.2013.01.010.

Van Wagoner, J.C., Mitchum, R.M., Campion, K.M., and Rahmanian, V.D., 1990, Siliciclastic Sequence Stratigraphy in Well Logs , Cores , and Outcrops : Concepts for High-Resolution Correlation of Time and Facies: The American Association of Petroleum Geologists, Tulsa, Oklahoma.

Weltje, G.J., 2006, Ternary sandstone composition and provenance: An evaluation of the “Dickinson model”: Geological Society Special Publication, v. 264, no. 1, p. 79–99, doi: 10.1144/GSL.SP.2006.264.01.07.

Wescott, W., 1993, Geomorphic Thresholds and Complex Response of Fluvial Systems--Some Implications for Sequence Stratigraphy: AAPG Bulletin, v. 77, no. 7, p. 1208–1218.

Willis, G.C., 1999, The Utah thrust system - an overview: Geology of Northern Utah and Vicinity, v. 27, p. 1–9.

Zahid, K.M., and Barbeau, D.L., 2012, Constructing Sandstone Provenance and Classification Ternary Diagrams Using An Electronic Spreadsheet: Journal of Sedimentary Research, v. 82, no. 2, p. 131–132, doi: 10.2110/jsr.2012.12.

Zaitlin, B.A., 2002, Depositional styles in a low accommodation foreland basin setting: an example from the Basal Quartz (Lower Cretaceous), southern Alberta: Bulletin of Canadian Petroleum GeologyCanadian, v. 50, no. 1, p. 31–72.

Zaitlin, B.A., Dalrymple, R.W., and Boyd, R., 1994, The Stratigraphic Organization of Incised-Valley Systems Associated with Relative Sea-Level Change: SEPM Special Publication, v. 51, no. 51, p. 45–60, doi: 10.2110/pec.94.12.0045.

Zhu, Y., 2010, Sequence Stratigraphy and Facies Architecture of the Cretaceous Ferron Notom Delta Complex, South-Central Utah, U.S.A.: 160 p.

Zhu, Y., Bhattacharya, J.P., Li, W., Lapen, T.J., Jicha, B.R., and Singer, B.S., 2012, Milankovitch-scale sequence stratigraphy and stepped forced regressions of the Turonian Ferron Notom Deltaic Complex, south-central Utah, U.S.A: Journal of Sedimentary Research, v. 82, no. 9, p. 723–746, doi: 10.2110/jsr.2012.63.

CHAPTER 5

CONCLUSIONS

5.1 Research Conclusions

This research has successfully demonstrated the complex nature of confined and unconfined fluvial deposits within the backwater limit of an ancient system. In examining a tidally-influenced trunk-tributary valley fill channel deposit in the Upper Ferron Sandstone, we document the paleohydraulics, facies and bedding architecture of an under-represented heterolithic reservoir analogue. An improvement in the model of mudstone dimensions has been to include the influence of tidal backwater process. The paucity of research in tributary systems and their associated deposits is addressed by the quantitative constraints and facies descriptions presented here. Five tributary channel mudstone elements were identified and compared with trunk and distributary channels within the backwater limit of the Ferron Sandstone, showing evidence of relatively poor vertical connectivity within backwater tributaries.

Using high resolution photogrammetry models and GPS survey, a trunk-tributary valley was mapped in the lower backwater of the Ferron-Notom delta coastal plain. Basal valley morphology is consistent with modern tidal drainage patterns. Detailed facies architecture of the tributary valley fill identified 17 distinct lithofacies and 5 facies associations in the underlying shoreface, valley fill, and overlying fluvial deposits not confined by the valley. The trunk-tributary valley fill is dominated by floodplain facies consisting of organic-rich mudstones, floodplain lake deposits and floodplain paleosols with subordinate deposits of tidally-influenced channel facies, and minor coal and carbonaceous shale facies. 32 FACs were correlated within 9 FAC-Sets in a floodplain dominated valley fill. FACs were correlated a distance of 100s of meters, while FAC Sets were correlated over 5 km, and suggest allogenic processes on a sub-Milankovitch timescale.

Provenance analysis of ten incised valley terraces revealed two distinct provenance groups, likely originating from separate axial and transverse drainages. Paleogeographic mapping of the regional compound incised valley demonstrates the deposition of two trunk channels in the same trunk valley by processes of stream capture and valley coalescence, forming fragmentary and discontinuous interflueves within a degradational landscape. This morphology challenges the simple elongate morphology defined by incised valley models and challenges single-source assumptions of their drainages. Basin-wide provenance analysis disagrees with drainage models that suggest axial trunk river avulsion is responsible for cyclical changes in depositional focus, resulting in all three wedges of the Ferron Sandstone.

Chronostratigraphic analysis reveals the youngest incised valley sequence duration to be between 10,000 to 20,000 years. The multiple trunk system, ever-wet climate and stepped regressive nature of base level changes has created this laterally extensive, compound incised valley, and may explain why this 40 km by 40 km valley does not conform to traditional models.

5.2 Future Work

Based on the findings of this work, certain questions remain as to the distinct facies within tributive backwater systems and models of valley evolution, and the following research is proposed.

Mircrofossil analysis using foraminifera and thecamoebian indicators in environment of deposition analysis in ancient rock is still a nacent branch of micropaleontology(Patterson et al., 1985; Mccarthy et al., 1995; Scott et al., 2004), however is being used more frequently in mud prone deposits. The tributary valley fill in this study, dominated by floodplain mudstones, is an excellent candidate for this type of biostratigraphy, and could potentially confirm interpretations made regarding ponding in these tributaries as a result of trunk valley damming. Biostratigraphic changes may also reveal cryptic horizons in floodplain successions that mark individual FAC deposits.

A good deal of this research relies on current assumptions made regarding floodplain dimensions (Beighley and Gummadi, 2011). There is as yet no well-established relationship of channel dimensions to lateral floodplain width. Future work would look at systems that can identify the immediate floodplain deposits of an adjacent active channel rather than the stratigraphic floodplain, which may contain older deposits, thereby exaggerating the distance.

The work on drainage reconstruction and paleogeography in this study presented has been a first step in resolving the complex network of Sequence 1 valleys. Provenance of the underlying shoreface may show complex DZ signal mixing and help resolve other trunk drainages within the samples already collected. Sequence 2 valleys have previously been interpreted similarly to the original avulsive trunk model (Ahmed et al., 2014), and were based on outcrops with preservation of the fluvial to marine transition. Such work would tie the findings of the non-marine stratigraphy in this thesis to well established marine sequence stratigraphic framework, and lay the foundations for direct temporal and spatial correlations between fluvial and deltaic deposits.

References

Ahmed, S., Bhattacharya, J.P., Garza, D.E., and Li, Y., 2014, Facies Architecture and Stratigraphic Evolution of A River-Dominated Delta Front, Turonian Ferron Sandstone, Utah, U.S.A: Journal of Sedimentary Research, v. 84, no. 2, p. 97–121, doi: 10.2110/jsr.2014.6.

Beighley, R.E., and Gummadi, V., 2011, Developing channel and floodplain dimensions with limited data: A case study in the Amazon Basin: Earth Surface Processes and Landforms, v. 36, no. 8, p. 1059–1071, doi: 10.1002/esp.2132.

Blum, M., Martin, J., Milliken, K., and Garvin, M., 2013, Paleovalley systems: Insights from Quaternary analogs and experiments: Earth-Science Reviews, v. 116, no. 1, p. 128–169, doi: 10.1016/j.earscirev.2012.09.003.

Boyd, R., Dalrymple, R.W., and Zaitlin, B. a, 2006, Estuarine and incised-valley facies models: Special Publication - Society for Sedimentary Geology, v. 84, no. 84, p. 171–235, doi: 10.2110/pec.06.84.0171.

Burke, K., 1990, Importance of the geological record in understanding global change: Global and Planetary Change, v. 3, no. 3, p. 193.

Chatanantavet, P., Lamb, M.P., and Nittrouer, J. a., 2012, Backwater controls of avulsion location on deltas: Geophysical Research Letters, v. 39, no. 1, p. n/a-n/a, doi: 10.1029/2011GL050197.

Colombera, L., Shiers, M.N., and Mountney, N.P., 2016, Assessment of Backwater Controls On the Architecture of Distributary-Channel Fills In A Tide-Influenced Coastal-Plain Succession: Campanian Neslen Formation, U.S.A.: Journal of Sedimentary Research, v. 86, no. 5, p. 476–497, doi: 10.2110/jsr.2016.33.

Dalrymple, R.W., Zaitlin, B.A., and Boyd, R., 2003, Estuarine facies models; conceptual basis and stratigraphic implications; discussion and reply: Journal of Sedimentary Research, v. 62, no. 6, p. 1130–1146, doi: 10.1306/d4267f50-2b26-11d7-8648000102c1865d.

Durkin, P.R., Hubbard, S.M., Boyd, R.L., and Leckie, D.A., 2015, Stratigraphic expression of intra-point-bar erosion and rotation: Journal of Sedimentary Research, v. 85, p. 1238–1257, doi: 10.2110/jsr.2015.78.

Horner, S.C., Hubbard, S.M., Martin, H.K., and Hagstrom, C.A., 2019, Reconstructing basin-scale drainage dynamics with regional subsurface mapping and channel-bar scaling, Aptian, Western Canada Foreland Basin: Sedimentary Geology, v. 385, p. 26–44, doi: 10.1016/j.sedgeo.2019.03.012.

Jicha, B.R., Singer, B.S., and Sobol, P., 2016, Re-evaluation of the ages of 40 Ar/ 39 Ar sanidine standards and supereruptions in the western U.S. using a Noblesse multi-collector mass spectrometer: Chemical Geology, v. 431, p. 54–66, doi: 10.1016/j.chemgeo.2016.03.024.

Kimmerle, S., and Bhattacharya, J.P., 2018, Facies, Backwater Limits, and Paleohydraulic Analysis of Rivers in a Forced- Regressive, Compound Incised Valley, Cretaceous Ferron Sandstone, Utah, U.S.a.: , no. February, p. 177–200, doi: 10.2110/jsr.2018.5.

Li, C., 2006, Incised-Valley-Fill Sequences in Sediment-Rich Deltas and Estuaries : Case Studies From China: Incised Valleys in Time and Space, , no. 85, p. 1–20.

Li, Y., and Bhattacharya, J.P., 2013, Facies-Architecture Study of A Stepped, Forced Regressvie Compound Incised Valley In the Ferron Notom Delta, Southern Central Utah, U.S.A: Journal of Sedimentary Research, v. 83, no. 3, p. 206–225, doi: 10.2110/jsr.2013.19.

Li, W., Bhattacharya, J.P., and Campbell, C., 2010, Temporal Evolution of Fluvial Style in a Compound Incised-Valley Fill, Ferron “Notom Delta”, Henry Mountains Region, Utah (U.S.A.): Journal of Sedimentary Research, v. 80, no. 1994, p. 529–549, doi: 10.2110/jsr.2010.053.

Matthews, W.A., and Guest, B., 2017, A Practical Approach for Collecting Large-n Detrital Zircon U-Pb Data sets by Quadrupole LA-ICP-MS: Geostandards and

Geoanalytical Research, v. 41, no. 2, p. 161–180, doi: 10.1111/ggr.12146.

Mccarthy, F.M.G., Collins, E.S., Mcandrews, J.H., Kerr, H.A., Scott, D.B., Medioli, F.S., Mccarthy, F.M.G., Collins, E.S., Mcandrews, J.H., Kerr, H.A., Scott, D.B., and Medioli, F.S., 1995, A Comparison of Postglacial Arcellacean (" Thecamoebian ") and Pollen Succession in Atlantic Canada , Illustrating the Potential of Arcellaceans for Paleoclimatic Reconstruction: Journal of Paleontology, v. 69, no. 5, p. 980–993.

Patterson, R.T., MacKinnon, K.D., Scott, D.B., and Medioli, F.S., 1985, Arcellaceans (“thecamoebians”) in small lakes of New Brunswick and Nova Scotia; modern distribution and Holocene stratigraphic changes: The Journal of Foraminiferal Research, v. 15, no. 2, p. 114–137, doi: 10.2113/gsjfr.15.2.114.

Scott, D.B., Schafer, C.T., and Medioli, F.S., 2004, Monitoring in Costal Environments Using Foraminifera and Thecamoebian Indicators: Cambridge University Press, Cambridge.

Shanley, K.W., and McCabe, P.J., 1994, Perspectives on the sequence stratigraphy of continental strata: American Association of Petroleum Geologists Bulletin, v. 78, no. 4, p. 544–568, doi: 10.1306/BDFF9258-1718-11D7-8645000102C1865D.

Strong, N., and Paola, C., 2008, Valleys That Never Were: Time Surfaces Versus Stratigraphic Surfaces--Discusion: Journal of Sedimentary Research, v. 80, no. 1, p. 4–5, doi: 10.2110/jsr.2010.007.

Ullah, M.S., Bhattacharya, J.P., and Dupre, W.R., 2015, Confluence Scours Versus

Incised Valleys: Examples From the Cretaceous Ferron Notom Delta, Southeastern Utah, U.S.A: Journal of Sedimentary Research, v. 85, no. 5, p. 445–458, doi: 10.2110/jsr.2015.34.

Visser, M.J., 1980, Neap-spring cycles reflected in Holocene subtidal large-scale bedform deposits : A preliminary note: Geology, v. 8, no. 11, p. 543–546.

Vitousek, P.M., 1997, Human Domination of Earth’s Ecosystems: Science, v. 277, no. 5325, p. 494–499.

Zaitlin, B.A., Dalrymple, R.W., and Boyd, R., 1994, The Stratigraphic Organization of Incised-Valley Systems Associated with Relative Sea-Level Change: SEPM Special Publication, v. 51, no. 51, p. 45–60, doi: 10.2110/pec.94.12.0045.

Zhu, Y., Bhattacharya, J.P., Li, W., Lapen, T.J., Jicha, B.R., and Singer, B.S., 2012, Milankovitch-scale sequence stratigraphy and stepped forced regressions of the Turonian Ferron Notom Deltaic Complex, south-central Utah, U.S.A: Journal of Sedimentary Research, v. 82, no. 9, p. 723–746, doi: 10.2110/jsr.2012.63.

APPENDIX

Digital Supplemental Files:

Supplemental_1 is an excel.xlsx file showing the bar drape workflow from outcrop and published cross-section data.

Supplemental_2 is a repository in all detrital zircon data used in this study.